Summer 2014

Technology, science, and environtmental impact of a novel Cu-Ag core-shell solderless interconnect system

Milea Joy Kammer
Purdue University

Recommended Citation

Kammer, Milea Joy, "Technology, science, and environtmental impact of a novel Cu-Ag core-shell solderless interconnect system" (2014). *Open Access Dissertations*. 303.
https://docs.lib.purdue.edu/open_access_dissertations/303

Graduate School Form
(Revised /)

PURDUE UNIVERSITY
GRADUATE SCHOOL
Thesis/Dissertation Acceptance

This is to certify that the thesis/dissertation prepared

By Milea Joy Kammer

Entitled
TECHNOLOGY, SCIENCE, AND ENVIRONTMENTAL IMPACT OF A NOVEL CU-AG
CORE-SHELL SOLDERLESS INTERCONNECT SYSTEM

For the degree of Doctor of Philosophy

Is approved by the final examining committee:

Carol A. Handwerker

Eric P. Kvam

Fu Zhao

John E. Blendell

To the best of my knowledge and as understood by the student in the Thesis/Dissertation Agreement, Publication Delay, and Certification/Disclaimer (Graduate School Form 32), this thesis/dissertation adheres to the provisions of Purdue University's "Policy on Integrity in Research" and the use of copyrighted material.

Approved by Major Professor(s): Carol A. Handwerker

Approved by: David Bahr 09/01/2014

Head of the Graduate Program Date

TECHNOLOGY, SCIENCE, AND ENVIRONTMENTAL IMPACT OF A NOVEL CU-AG CORE-SHELL SOLDERLESS INTERCONNECT SYSTEM

A Dissertation
Submitted to the Faculty
of
Purdue University
by
Milea Joy Kammer

In Partial Fulfillment of the
Requirements for the Degree
of
Doctor of Philosophy

December 2014
Purdue University
West Lafayette, Indiana

THIS DISSERTATION IS DEDICATED TO MY INCREDIBLE FATHER,

DR. DANIEL RAY KITTLE.

YOU INSPIRED ME TO GO FOR MY DREAMS. I LOVE YOU DAD.

ACKNOWLEDGEMENTS

Personal Acknowledgements

I would like to start by saying how particularly grateful I am to my advisor, Prof. Carol Handwerker for all of her support and guidance throughout these projects. I am truly grateful for having the opportunity to work with her. Over the years, her confidence in my knowledge and abilities has truly changed my level of technical confidence.

I would also like to acknowledge the help provided by group members, Prof. John Blendell, Dr. Pylin Sarobol, Dr. Wei-Shun Chen, Dr. Ying Wang, and Luthfia Syarbaini for our many discussions, theory reviews, and suggested next steps throughout this entire project. A special thank you for the amazing friendship and support from the Drs. Dubelman, Steven and Meredith, I wouldn’t have made it without you to lean on.

Finally, and most importantly, I would like to thank my husband, Matthew, for patiently supporting me throughout this process. And my parents, Dan and Vicky, for always believing in me and encouraging me. I could have never made it this far without your love and support.

Funding Acknowledgements

This research would not have been possible without my collaborations with Alan Rae, TPF Enterprises, Speedline Technologies, and Heraeus.

I also gratefully acknowledge the NSF IGERT on Sustainable Electronics (DGE 1144843) and Air Force ManTech grant FA8650-10-M-5120 and the SBIR program for support of this research.

TABLE OF CONTENTS

Page

Page

LIST OF TABLES

Table Page

LIST OF FIGURES

Figure Page

ABSTRACT

Kammer, Milea Joy. Ph.D., Purdue University, December 2014. Technology, Science, and Environmental Impact of a Novel Cu-Ag Core-Shell Solderless interconnect System. Major Professor: Carol Handwerker.

Tin-based solder is ubiquitous in microelectronics manufacturing and plays a critical role in electronic packaging and attachment. While manufacturers of consumer electronics have made the transition to the use of lead-free solder, there are still a variety of reliability issues associated with these lead-free alternatives, particularly for high performance, high reliability applications. Because of these performance short-comings, researchers are still searching for a material, an alloy, or a unique alternative that can meet the thermal, mechanical, and electrical requirements for conventional reflow solder applications. In an effort to produce a more reliable alternative, Kim et al. proposed the low-temperature (200°C) sintering of copper-silver core-shell particles as a viable solderless interconnect technology. This technology is based on the silver atoms from the shell diffusing by surface diffusion to form sintered necks between copper particles, and therefore dewetting most of the copper surfaces. This study presents a 3-fold, in-depth evaluation of this Cu-Ag core-shell lead-free solderless interconnect technology focusing on solder paste

development and prototyping, silver thin film stress relaxation and dewetting kinetics, and the environmental impacts associated with this new technology.

First, an evaluation of the starting particle consistency and sintered compact mechanical properties determined that a specific core-shell particle geometry (1μm average core diameter and 10nm shell thickness) outperformed other combinations, exhibiting the highest modulus and yield strengths in sintered compacts, of 620 MPa and 40-60 MPa respectively. In particular, yield strengths for sintered compacts are similar to those reported for Sn-3.5Ag-0.75Cu (a commonly used lead-free solder) for the same strain rate. Following particle evaluations, the development of a functioning flux formulation was a key factor in the creation of a viable drop-in replacement. The processing of the final flux/particle paste combination was optimized at a commercial test facility for printing on test boards containing a wide variety of pad shapes, sizes, and pitches and thus, validated the ability of the Cu-Ag core-shell paste to be a drop-in replacement for traditional solder paste using conventional manufacturing techniques.

The second study addresses the fundamental mechanisms behind interconnect formation. An assessment of the kinetics and microstructure evolution during silver thin film dewetting and defect formation provides essential materials science knowledge to understand and control the functionality of the Cu-Ag core-shell system. From an interrupted annealing study used to quantify dewetting kinetics, a range of surface diffusion coefficients were calculated from the experimental results, assuming that surface diffusion controlled dewetting.

The two order of magnitude range in calculated diffusion coefficient demonstrates that the diffusion-limited kinetic models traditionally used to quantify hillock and hole growth kinetics during thin film relaxation and dewetting do not apply to the dewetting of Ag films. The presence of interface-limited kinetics was then validated through the non-uniform growth of individual hillocks over time.

Lastly, an environmental assessment compares the impacts associated with the manufacturing and materials for the Cu-Ag core-shell particle system and SAC 305, the most commonly used lead-free solder alloy that contains 96.5% tin, 3% silver, and 0.5% copper. By comparing the impacts on global warming, acidification, eutrophication, ozone depletion, ecotoxicity, smog, carcinogenics, non-carcinogenics, and respiratory effects associated with each technology, the environmental advantages and disadvantages of each system are clearly communicated. By utilizing this information and the versatility of the core-shell system, possible methods for reducing impacts of the Cu-Ag core-shell system are addressed in order to reduce its environmental footprint.

This multidimensional assessment provides a comprehensive validation in terms of technology, science, and environmental impacts of the Cu-Ag core-shell interconnect technology as a viable drop-in replacement for lead-based and lead-free solders for microelectronic manufacturing.

CHAPTER 1. INTRODUCTION AND DISSERTATION STRUCTURE

1.1 Introduction

Solder paste is abundant in microelectronics manufacturing and plays a critical role in packaging and attachment. Manufacturers of consumer electronics have recently made the transition to the use of lead-free solder. However, there are still a variety of well-known reliability issues associated with current lead-free solders, used in consumer electronic manufacturing. Therefore, researchers are still searching for a material, an alloy, or a unique alternative that can meet the thermal, mechanical, and electrical needs for conventional die attach and reflow solder applications. [1-8]

This dissertation presents a multidimensional approach in developing and assessing a lead-free solderless interconnect technology that is based on the use of a Cu-Ag core-shell particle system. The evaluation of the system is 3-fold and will focus on solder paste development and prototyping, the fundamental science behind the interconnect formation mechanism, and the environmental impacts associated with this new technology. This comprehensive evaluation will provide a complete assessment of the Cu-Ag core-shell particle system as a viable drop-in replacement for traditional solder Pb-free solder paste.

1.2 Dissertation Structure

As afore mentioned, this dissertation presents a three tiered approach to assessing the viability of the sintering of Cu-Ag core-shell particles as a replacement for traditionally used lead-free solders in electronics manufacturing. First, the study focuses on the technology development. The creation of a functional drop-in replacement solder paste prototype will be presented. Evaluation of a variety of particle configurations and the development of a functioning flux formulation will be key factors in the creation of a viable technology. Second, the study addresses the fundamental mechanism behind interconnect formation. An assessment of silver thin film dewetting, orientation relationships, and defect formation provides essential materials science to understand and control the functionality of the Cu-Ag core-shell system. Lastly, an environmental assessment compares the impacts associated with manufacturing and materials for both the Cu-Ag core-shell particle system and SAC 305, a commonly used lead-free solder alloy that contains 96.5 % tin, 3% silver, and 0.5% copper. This assessment defines the benefits associated with the proposed lead-free solderless interconnect technology.

1.3 Overview

In the last ten years the electronics industry has converted from the traditionally used lead-tin solder to lead-free alternatives due to the ROHS directive established by the European Union.[9] Due to materials property differences between lead-free alternatives and traditional leaded solders, this transition has been accompanied by processing and reliability challenges.[10] The lead-free alternatives most frequently used in electronics manufacturing are tin-silver-copper (SAC) solder alloys. Several major concerns with this lead-free alternative include the 20°C increase in required processing temperature over Pb-Sn eutectic, the anisotropic nature of the solidification, and the increased differences in thermal expansion between the solder joint and printed circuit board (PCB) pads or component leads.[10]

In an effort to produce a more reliable alternative, Kim et al. proposed the use of copper-silver core-shell particles as a sintered solderless interconnect.[11] Upon annealing of copper-silver core-shell particles, the silver shells dewet the surface of the copper particles and silver atoms diffuse to the particle-particle contact regions creating sintered necks between the particles. A schematic representation of this interconnect formation process and the structural evolution can be seen in Figure 1.

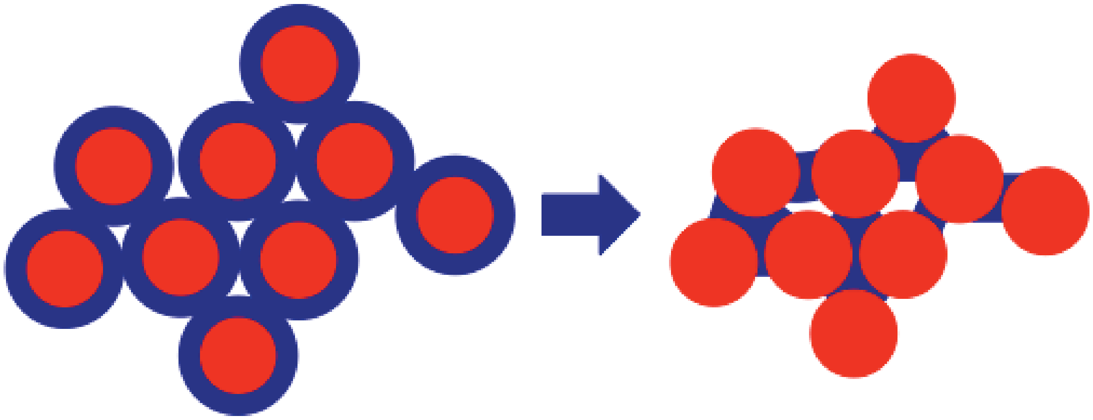

Figure 1. A schematic representation of the structure change of the copper-silver core-shell system during annealing. Red - copper, Blue - silver

Kim et al. used energy filtered transmission electron microscopy (EFTEM) to confirm this interconnect formation mechanism as seen in Figure 2. These results show that in this silver-coated copper particle system, the surface diffusivity of the silver shell is much faster than that of copper at the lower processing temperature used (220°C). Their work demonstrates that diffusion is the fundamental mechanism by which this core-shell system creates mechanically and electrically stable interconnects. However, they did not address the development of the particles into a usable system for electronics manufacturing. The technology chapter of this dissertation addresses the development and fabrication of a functional solder paste from these core-shell powders.

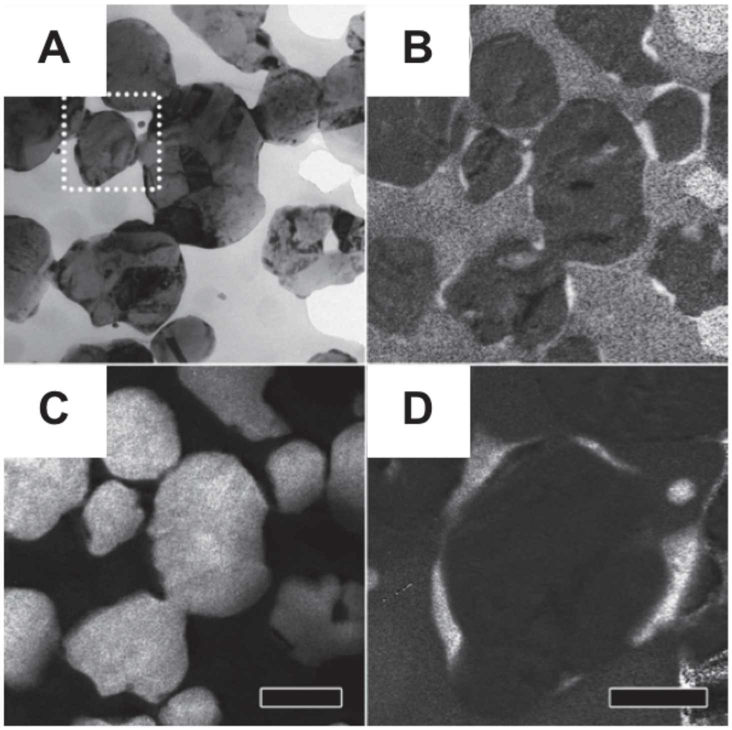

Figure 2. TEM and EFTEM images of Cu–Ag particles after annealing at 220 °C: (A) TEM image, (B) Ag ratio map of area A, (C) Cu elemental map of area A, (D) Ag ratio map of white box area within area A. Scale bars: (A), (B), and (C) have the same scale of 300 nm and (D) is 100 nm. Reproduced with permission from [S. J. Kim, E. A. Stach, and C. A. Handwerker, Fabrication of conductive interconnects by Ag migration in Cu–Ag core-shell nanoparticles. Applied Physics Letters **96,** 144101 (2010).]. Copyright [2010], AIP Publishing LLC.

Along with the development of a prototype solder paste; it is crucial to understand the mechanisms by which the silver films dewet the polycrystalline copper seeds to form necks. Understanding the fundamental mechanisms will allow for optimization of the dewetting process and may result in the ability to engineer particle configurations that can meet specific manufacturing needs. The science chapter of this dissertation addresses sources of thin film stress, mechanisms of thin film stress relaxation and dewetting, and the associated defect structures. In order to better understand dewetting and stress relaxation by defect formation in thin silver films, a variety of silver films on silicon substrates were studied. While the formation of silver necks between copper particles by sintering was seen experimentally by Kim et al., there were many areas of film stability and characterization left unaddressed. A better understanding of the factors that influence silver thin film dewetting structures and kinetics will allow for the possibility of tailoring both the material system (particle size, film thickness, polycrystallinity and texture) and annealing parameters (time, temperature) to create solder pastes that can meet a variety of processing requirements for temperature and dwell time/ process thermal profile dictated by different applications.

The movement to replace lead-based solders with lead-free was made solely based on the elimination of lead, which is known to be toxic. There are, however, more dimensions to life cycle impact than human toxicity. Therefore, there is a need to confirm that a potential solder alternative is in-fact more environmentally friendly (less harmful to the environment in terms of toxicity, acidification, etc.) than the technology it is intended to replace. The impacts of a technological transition should be openly evaluated, minimized through potential changes in materials and manufacturing and acknowledged when introducing a new technology to the public. One way of scientifically quantifying the environmental impacts associated with a product and its production is by performing a Life Cycle Assessment (LCA).

The environmental impact chapter of this dissertation contains a comparative LCA of the environmental impacts associated with the materials and manufacturing of using the Cu-Ag core-shell technology and a traditional lead-free solder, SAC305. By comparing the impacts on global warming, acidification, eutrophication, ozone depletion, ecotoxicity, smog, carcinogenics, non-carcinogenics, and respiratory effects associated with each technology. The environmental advantages and disadvantages of each system are clearly communicated and possible methods for reducing impacts of the Cu-Ag core-shell system are addressed in order to reduce its environmental footprint.

The multidimensional assessment presented in this dissertation covers the development of a sintering-based solderless core-shell interconnect technology. This work provides an evaluation of silver thin film stress relaxation focusing on dewetting, and defect formation, the impact of these relaxation processes on the performance of the Cu-Ag core-shell technology, and a comparative LCA evaluating the environmental advantages and disadvantages of the proposed system. This approach allows for a comprehensive understanding of the potential for the Cu-Ag core-shell particle system to be implemented as a viable drop-in replacement for lead-based and lead-free solders for microelectronic manufacturing.

CHAPTER 2. TECHNOLOGY

2.1 Technology Introduction

2.1.1 Solder and Electronics Manufacturing

Solder paste has been and continues to be ubiquitous in microelectronics manufacturing, playing a critical role in packaging and attachment. Historically, Sn-Pb alloys have been used as low melting point, inexpensive, reliable solders for component attachment in electronics manufacturing. In 2006, the Restriction of Hazardous Substances (RoHS) directive was established by the European Union, and restricted the use of Pb in electronics. [9] The result of this restriction of Pb was the transition to using a variety of Pb-free Sn-rich solders. Although manufacturers of consumer electronics have successfully made the transition to the use of lead-free solder for surface mount reflow soldering and wave solder of through-hole assemblies, there are still a variety of well-known reliability issues associated with current Sn-Ag-Cu (SAC) lead-free solders, widely used in consumer electronic manufacturing. Therefore, researchers are still searching for a material, an alloy, or a unique alternative technology that can meet the thermal, mechanical, and electrical needs for conventional die attach and reflow solder applications.[1-8]

2.1.2 Reflow Soldering

Solder is commonly available in a variety of forms including wires, bars, and pastes. There are a variety of soldering methods for attaching components to printed circuit boards. For example, hand, wave, vapor phase, and reflow soldering. As surface mount packaging technology (SMT) became the standard, reflow soldering has become one of the most popular techniques for bulk soldering. [12] Solder paste is typically used in reflow soldering applications.

In the reflow soldering process solder paste is deposited onto the pads of a printed circuit board through a screen-printing process. The board and paste are then transferred into a pick-and-place machine where the desired components are put in place on the tacky solder paste; the tacky solder paste temporarily holds components in place on a printed circuit board. Lastly, the entire assembly is then passed through a reflow oven typically containing 4 well-controlled temperature regimes: preheat, thermal soak, reflow, and cooling. This controlled heating and cooling process melts the solder alloy, burns off the organics contained within the solder paste and permanently attaches the component lead to the board pad without overheating components, which can cause permanent damage. An example of a typical reflow profile for Sn-Pb solder can be seen in Figure 3. The preheat zone determines the thermal ramp rate, typically somewhere between 2-3 °C/s. This temperature ramp rate must be well controlled in order to minimize component damage from thermal shock. In the preheat zone the solvents contained within the solder paste begins to evaporate and the thermal ramp rate will be critical in ensuring that evaporation is complete.

The thermal soak zone is the regime where activation of many of the flux components takes place. In this zone a 60-120 second temperature exposure is used to initialize oxide reduction and flux activation. The temperature of the thermal soak zone is determined by the components within the flux. The temperature must be high enough to reach the activation temperatures for each flux component but not too high as to cause the molten metal to splatter as the flux components vaporize. After exposure to the thermal soak zone, all components, regardless of size or shape, should be relatively the same temperature throughout, minimizing differences in thermal behavior across the board. The reflow zone, where the maximum temperature is achieved, follows the thermal soak zone. The maximum temperature is an important consideration in designing a reflow profile and is typically 20-40 °C above the liquidus temperature of the solder alloy. However, this value is also limited by the components associated with the assembly of interest. Throughout this high temperature regime the flux reduces surface tension, promoting wetting of the solder metal with the metal leads and pads. In this zone, the actual soldering, or metallurgical bonding of component lead to pad occurs. The last temperature zone is the cooling zone. In the cooling zone the entire assembly is gradually cooled to room temperature. During cooling the solder joints solidify. [13,14]

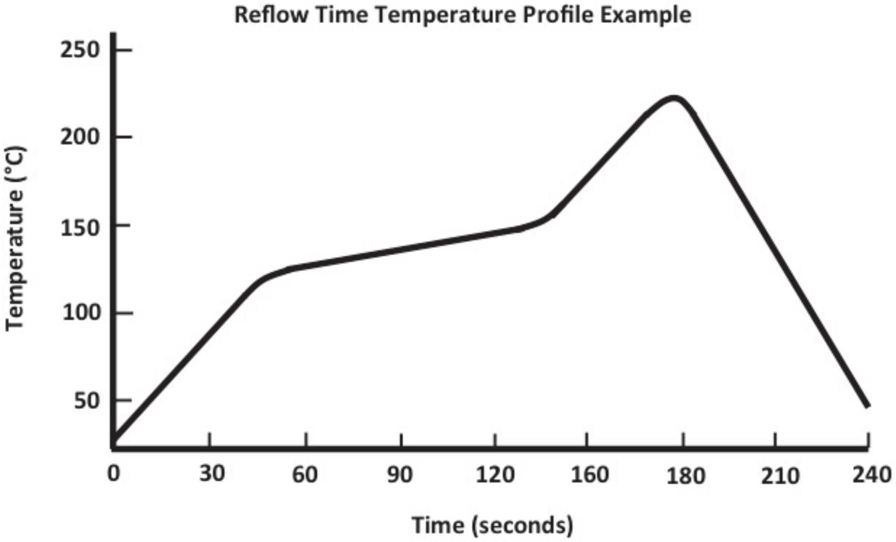

Figure 3. Schematic of the general thermal profile for reflow soldering of Sn-Pb solder paste

2.1.3 Solder Paste

Solder paste is composed of both metallic particles, often referred to as solder balls, and flux which contains rosins, thickener, and solvents. Typical solder particles contained within solder paste are on the order of 40 microns. [15] The flux component of a solder paste suspends the metal particles in a carrier material. The components of solder paste flux provide improved particle, lead, and pad reactivity through oxide reduction. The components of the flux also determine the solder paste storage shelf life due to the volatile solvents.

2.1.4 Lead-Tin Solder

There is a broad range of available compositions for Sn/Pb solders. The majority of Sn/Pb solder compositions exhibit a pasty range between the solidus and liquidus temperatures as seen in the phase diagram in Figure 4. All compositions are solid at and below 183°C. Lower tin content reduces product cost, increases the pasty region, raises the liquidus temperature and decreases wettability. Therefore, compositions with greater lead content are more desirable for electronic manufacturing applications such as reflow and wave soldering. Compositions with a low melting point and short freezing range are ideal. Because of this, eutectic 63/37 and 60/40, with its 5-degree freezing range are traditionally chosen for these applications. [15,16]

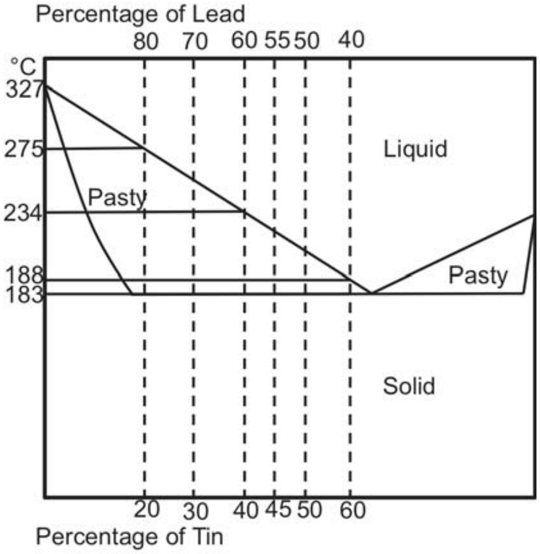

Figure 4. Schematic Sn/Pb phase diagram showing compositions and melting temperatures for a variety of solder pastes with different compositions.

2.1.5 Lead-Free Alternatives

2.1.5.1 Solder Alloy-Based Option

The electronics industry has evaluated a wide range of potential solder alloys to act as a Pb-free alternative over the years. There are a variety of factors to consider when evaluating possible alloy compositions including, melting temperatures, wetting properties, thermal expansion, electrical conductivity, mechanical behavior under stresses, corrosion, oxidation, manufacturability, and cost. [17-20] Of key importance is the processing temperature required to undergo traditional surface mount and wave soldering processes. Processing temperatures should be lower than 230°C in order to avoid damage to the components attached to the PCB. There are broad ranges of Pb-free options currently in use including binary, ternary, and even quaternary alloys of a variety of metals. Currently, Sn-Ag-Cu (SAC) lead-free solder alloys dominate the consumer electronics manufacturing industry. Specifically, Sn-3.0Ag-0.5Cu (SAC 305), with a reflow temperature of approximately 240 °C, has dominated the market to date.

2.1.5.2 Solid Particle-Based Option

In the search for lead free alternatives that will meet the current industry standards for both processing conditions and performance, many research groups have investigated non-solder-based (non-melting) methods of interconnect formation. The sintering of particle systems has been proposed as alternative method to produce interconnects with higher mechanical stability, lower processing temperatures, and more isotropic properties than Pb-free solder alloys. Nano-scale particles, mixed metal powders of larger sizes and non-spherical shapes, and core-shell particle systems have all been proposed as viable alternatives. The majority of these alternatives focus on the use of silver and copper. A key advantage for all Ag- and Cu-based technologies is in the reduction of thermal expansion mismatch. Minimization of the thermal expansion mismatch within the interconnect system is an important factor in reducing joint stress and therefore increasing thermo-mechanical fatigue resistance. The thermal expansion coefficient (CTE) of each constituent will be a key factor in fatigue due to the thermo-mechanical cycling that an interconnect will undergo during electronic use. The CTE's of Ag and Cu are 18 and 17(10^{-6}/°C) respectively. The CTE's of Ag and Cu are significantly lower than both Pb-Sn eutectic solder, ~24 (10^{-6}/K) [21] and SAC 305, ~21 (10^{-6}/K) [22]. The reduced thermal expansion mismatch of Cu-Ag technologies leads to increased fatigue resistance and thermo-mechanical stability.

There are a wide variety of commercially available single phase nano-silver solder systems that function over a broad range of processing temperatures (300-960°C), and particle geometries. Similarly, copper nanoparticle sintering has been proposed as a interconnect alternative. However, the systems' need for a removable capping layer to mitigate oxidation have led to challenges in development of sintered Cu nanoparticle interconnects. Along with this complication, the nanoparticle interconnect system can continue to evolve after initial joint formation is created due to the diffusion-based formation mechanism. Diffusion may continue to occur when the system is exposed to subsequent heating during storage or usage and resulting in weakening of joints. [23-25] Kim et al. identified low temperature sintering of Cu-Ag core-shell particles as a viable interconnect formation method. In this proposed system, the fast surface diffusion of the thin silver shell results in sintering of the system creating a network of micrometer or sub-micrometer copper particles connected by silver necks. The use of a combination of limited amounts of Ag and Ag surface diffusion as the connection formation mechanism results in little shrinkage during sintering and produces mechanically stable interconnects that are resistant to further coarsening. [11]

In light of its promise, the focus of this study is in transforming the concept of Cu-Ag core-shell particle sintering into a viable technology by formulating a paste that can be dispensed and sintered to form reliable interconnects. Critical performance factors include: core-shell particle sintering kinetics, the mechanical properties of the porous interconnect system, and paste performance, including flux stability, printability/dispensability, and adhesion. Variables under our control include core particle size, silver to copper ratio, shell thickness, particle size distribution and agglomeration, flux formulation, particle loading, paste fabrication, and processing temperature/sintering thermal profile. All of these factors affect optimal particle-flux combination for a commercially viable paste. The order of optimization required first, synthesis and characterization of the starting core-shell powders, followed by mechanical characterization of sintered interconnects from the powders. Using powders for which the interconnects showed acceptable as-sintered strengths, pastes were formulated using 26 common flux constituents (10 solvents, 10 rosins, 5 thickeners, and 1 acid additive) and characterized with respect to typical paste characteristics, such as rheology, mixability, flux stability, weight loss during annealing, and adhesion to the substrate after sintering. Through the experiments presented here, a copper-silver core-shell particle system using a typical solder paste particle loading of 50-volume percent [15] and a 1 μm core-shell particle size is shown to be a viable replacement for solder pastes currently deposited via printing or jetting and used for reflow soldering and die attach. As a guide to future studies, the effect of reducing the core-shell particle size on sintering kinetics was also evaluated in order to estimate the particle sizes needed for producing sintered connections at lower assembly temperatures and shorter sintering times than reported here.

2.2 Technology Experimental Plan and Characterization

2.2.1 Physical Properties of Core-Shell Particles

Three different configurations of Cu-Ag core-shell particles were synthesized for this study, (Ames Goldsmith, Glens Falls NY) as seen in Table 1. Particle nomenclature used here identifies the average diameter (1μm = 10; 0.5 μm = 05) and weight percent silver (10wt% = 10; 5wt%=05). (i.e., PAC 1005 particles have a 1μm average particle diameter and 5 weight percent silver). Assuming uniform shell coverage, shell thicknesses were calculated using the known volumes, silver assays, and bulk densities. Previous TEM examination of similar core-shell particles established that these are reasonable estimates of shell thickness. [11]

Table 1. Diameter and weight percent silver for the particle configurations

Name	PAC0505	PAC1005	PAC1010
Avg. Diameter (μm)	0.5	1	1
Weight % Ag	5	5	10
Ag Shell Thickness (nm)	4	9	17

The degree of particle agglomeration was assessed from measurements of tap density. Particle size distribution, surface area, and silver assay were determined using a Microtrac S-3000 laser diffraction analyzer at Ames Goldsmith. The particle size distribution measurements were compared with particle sizes and distributions obtained by scanning electron microscopy (SEM - FEI XL-40).

2.2.2 Mechanical Properties of Sintered Compacts

The mechanical properties of sintered powder compacts of the three particle configurations were studied via uniaxial compression tests. Approximately 1 g of powder was compressed in a 0.25-inch diameter die using a pressure of 70 MPa creating samples with a 1:1 height to diameter ratio. Powder compacts were annealed for 20 minutes at 200°C, 225°C, and 250°C in a tube furnace with a forming gas (95%N, 5%H) atmosphere. Compression tests were performed on two compacts for each processing condition using an MTS Sintech 30/D at a head displacement rate of 2×10^{-5} m/s using a flat plate compression head, resulting in a strain rate of 3.4×10^{-3} s^{-1}.

2.2.3 Flux Formulation

The flux component of a solder paste suspends the metal particles in a carrier, allowing for the system to be printed and/or jetted. Flux provides increased particle, lead, and pad surface reactivity by removing or inhibiting formation of surface oxide, promotes particle-particle interactions during flux evaporation, and determines storage shelf life. Fluxes were formulated using the rosins, solvents, thickeners and acid activators listed in Table 2. Rosins are used to control both rheology and surface activity of particles and substrates. Solvents with different vapor pressures control the evaporation of the flux during printing and annealing and promote interparticle contact. Thickeners are used to achieve the desired rheological properties for paste dispensing and component attachment and acid activators promote sintering by increasing the flux activity. [26,27] For flux development, solvents and rosin(s) for each composition were mixed and heated to between 80-120°C until dissolution occurred and the system appeared transparent. The mixture was cooled to ~50 °C. Thickener(s) and acid(s) were then added to the 50 °C mixture as it was stirred vigorously. The final flux formulations were allowed to cool to room temperature overnight before particle incorporation. The specific flux formulations are described in detail in the results and discussion section.

Table 2. Flux components investigated

Material	**Function**
Diethylene Glycol Dibutyl Ether	Solvent
Tridecyclalcohol	Solvent
Dipropylene Glycol (DPG)	Solvent
Methyl Ethyl Ketone	Solvent
i-propanol	Solvent
Cellosolve	Solvent
Butyl Cellosolve	Solvent
Terpineol	Solvent
N Methyl Pyrrolidone	Solvent
Teckros D85	Rosin
Teckros D95	Rosin
Pinecrystal KE-604	Rosin
Teckros D140	Rosin
R101 Rosin Ester	Rosin
SL102 Rosin Ester	Rosin
Teckros HX	Rosin
Teckros RL60	Rosin
Teckros RL	Rosin
Troythix XYZ	Thickener
Succinic Acid	Acid Activator
Adipic Acid	Acid Activator
Malonic Acid	Acid Activator

2.2.4 Paste Formulation

Based on the mechanical properties of sintered compacts formed without flux, PAC1005 powder was selected as the optimized powder for flux formulation. In order to achieve 50-volume percent loading, approximately 2 g of powder and 0.5 g of flux were combined for the paste formulation trials. Four paste development studies were performed with over 50 total flux formulations, with the down selection criteria for the first matrix being flux rheology, the second being particle wettability and paste rheology and the second being flux residues and weight loss after sintering. The final matrix of 9 pastes were qualitatively evaluated using a 5 point scale ease of the mixing, relative adherence to the substrate as printed, and relative adherence to the substrate after annealing. From these three studies, two paste formulations were identified for quantitative manufacturability testing, including paste rheology, printability, and promotion of neck formation.

2.2.5 Rheology and Printability

The fabrication of a viable paste relies heavily on a flux that provides shear-thinning paste rheology, a non-corrosive environment for the resulting interconnect, and an acceptable shelf life, while also promoting interparticle and substrate bonding. The rheological behavior was evaluated using a TA Instruments AR-G2 Controlled Stress Rheometer with a plate-on-plate geometry. Approximately 0.5 mL of pastes with 53.3 vol% loading was used for the rheology measurements.

Printability of the down-selected pastes was evaluated at Speedline Technologies Inc., using an MPM stencil printer, for comparison with commercial Pb-free solder pastes. The squeegee speed and pressure were optimized to ensure uniform coverage for a variety of pad shapes, sizes, and pitches.

2.3 Results and Discussion

2.3.1 Physical Properties of Core-Shell Particles

Particle characterization results for the three powders are reported in Table 3, and the morphologies of the as-received core-shell particles in Figure 5. The data and images for PAC0505 (with a nominal average particle size of 0.5μm) show that PAC0505 is highly agglomerated. The average PAC0505 particle size from SEM imaging is 0.69 μm, while the average measured by laser diffraction is 1μm with a particle size distribution that is the same as the 1μm powders. The difference in average particle size measured by SEM and laser diffraction is due to agglomeration. The PAC0505 powder also has a low tap density packing factor of 0.38 as compared with packing factors of 0.50, 0.54, and 0.6 for PAC1005, PAC1010, and the theoretical packing factor, respectively [28]. The theoretical packing factor describes the limiting relative density of equal size spheres vibrated in a container to promote packing. The low tap density of PAC0505 is another indication of agglomeration. Surface area measurements for PAC0505 showed a slightly lower surface area than estimated based on calculations for spherical 0.5μm particles. This difference in surface are is not unexpected given the degree of agglomeration, that is, the particle agglomerates.

Both PAC1005 and PAC1010 showed significantly less agglomeration when compared with PAC0505, with a D50 of 1 μm for both powders. The surface areas for both PAC1005 and PAC1010 were approximately 50% greater than estimated based on calculations for spherical particles with a 1μm average diameter. This increase in measured surface area is due to the non-spherical nature of the particles. As seen in Figure 5, all particle formulations contain well-defined facets as well as concave and convex surface features. The combination of rough and faceted surfaces results in surface area measurements well above the theoretical values. Overall, PAC1005 and PAC1010 exhibited expected properties in terms of particle size distribution, packing, and surface area, suggesting minimal agglomeration.

Table 3. Density, surface area, and particle size distribution data for the three particle configurations

	PAC0505	PAC1005	PAC1010
Tap Density (g/cm^3)	3.5	4.6	4.9
Packing Factor (tap density/theoretical density)	0.38	0.51	0.54
Measured Surface Area (m^2/g)	1.16	0.91	0.95
Calculated Surface Area – Nominal diameter, Spherical particles (m^2/g)	1.33	0.66	0.66
D10 (μm)	0.6	0.6	0.6
D50 (μm)	1	1	1
D90 (μm)	2.2	1.9	2
Particle Size from SEM Analysis - Avg. (St Dev.) (μm)	0.69 (0.24)	0.74 (0.21)	0.79 (0.22)
Silver Assay (%)	5.1	5.0	9.6

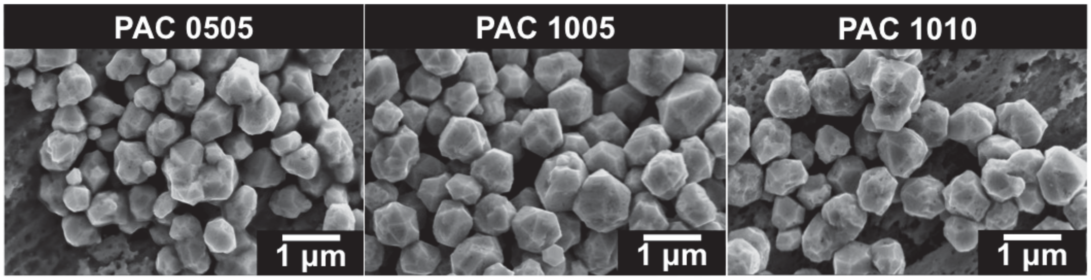

Figure 5. SEM image of (A) PAC0505, (B) PAC1005, and (C) PAC1010 showing faceted, non-spherical particles

In each particle configuration, particle pairs were present that appeared to have formed necks prior to annealing. These particle pairs resulted from agglomeration prior to the Ag coating process, i.e., particle pairs are coated forming a single, Ag-coated, dumbbell-shaped particle, as seen in Figure 6a. After sintering, the neck morphologies of dumbbell structures are distinguishable from neck formation between two individual core-shell particles as seen by comparing Figures 6a and 6b, thus allowing for identification of necks formed only by the sintering process.

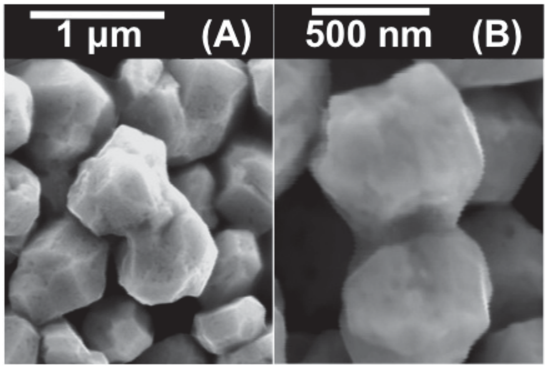

Figure 6. SEM images showing the structure differences between (a) a particle-pair dumbbell and (b) a sintered neck

2.3.2 Sintering of Core-Shell Particles

In the development of a viable technology, there are many practical considerations that must be examined. For example, processing times should be fast enough to be make it acceptable to manufacturers, there should be a sufficiently wide process window to enable reliable, reproducible results, and the resulting properties of the sintered interconnect should be more than sufficient for the intended applications. These are all controlled by the kinetics of neck formation as a function of particle geometry, particle packing, annealing temperature and time.

Since the core-shell particles sinter predominantly by Ag surface diffusion there is minimal densification, as determined by dimensional measurements upon sintering. The extent of neck formation can be estimated using a surface-diffusion sintering model established by Kuczynski et al. as applying to the sintering of Cu-Ag core-shell particles fabricated using these methods with the diffusion coefficient from Dannenberg et al. The sintered neck size, x, can be determined by Equation 1. [29,30]

$$x^7 = \frac{56\, D_s\, \delta_s\, \gamma_s\, V_m\, a^3}{RT} t$$ **Equation 1**

where the surface diffusion coefficient $D_s = 4\mathrm{x}10^{-12}$ (exp (-0.61eV/kT)) m^2/s, δ_s: characteristic surface diffusion layer thickness, 0.5 x 10^{-9}m, γ_s: surface energy, 1.2 J/m^2, molar volume, V_m 1.027 x $10^{-5}m^3$/mol, [30]: a: particle radius (m), t: time (s), R: gas constant, 8.314 J/molK, and T: sintering temperature (K). As originally set out by Herring, with self-similar structures assumed in a simple two particle model, the time to achieve the same x/a ratio with different particle sizes allows a comparison of sintering kinetics when a single mechanism dominates neck formation. The time and particle size dependence of absolute and relative neck formation at 200°C by Ag surface diffusion (Eqn. 1) is shown in Figure 7 for 500 nm and 1 μm diameter particles. For an annealing time of 60 minutes, a time cited by our OEM advisory team as the maximum annealing time to target, the x/a values are 0.287 for 500 nm diameter particles, and 0.18 for 1-μm diameter particles. These calculated values are used later in the analysis of modulus as a function of annealing time.

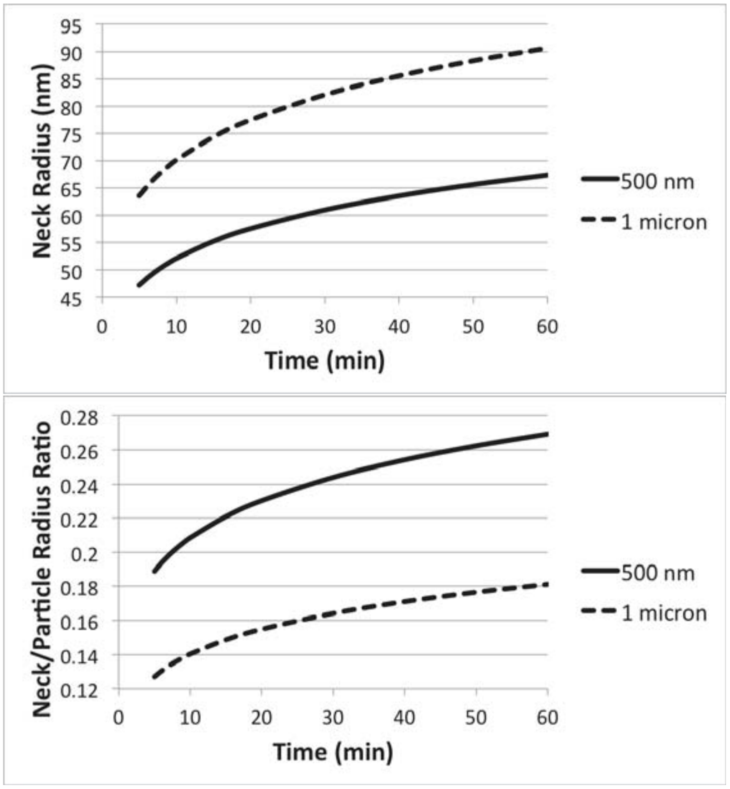

Figure 7. Calculated neck radius (x) and ratio of neck radius to particle radius (x/a) increase over time for 500nm and 1 μm particles annealed at 200°C

There is a limiting case for the extent of neck formation based on physical, geometrical constraints that must be explored: is there enough Ag in the particle shells to form necks with the expected geometries. The maximum possible neck radius formed from Ag can be estimated assuming that all of the silver shell diffuses to form sintered necks, the solid core particles touch at a single point and a cylindrical neck structure minus the excluded volume of the core particles.

Figure 8 details the assumed geometry. (For this simple model, the effect of the wetting angle of Ag on Cu is ignored.)

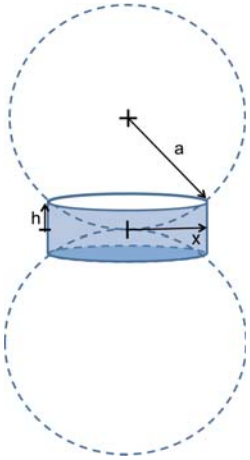

Figure 8. Assumed geometry for calculating limiting neck radius for Ag neck formation on Cu cre particles. The wetting angle of Ag on Cu is not being considered

For a known particle radius and silver shell thickness a geometric relationship was developed in order to determine neck radii, detailed in Equation 2. Equating the volume of the cylindrical neck to the volume of two equivalent hemispherical caps and the total volume of silver from the shells, the maximum possible neck radius for a simple two-particle geometry for PAC 1005 (500nm core radius, 9nm Ag shell thickness) was estimated to be 360 nm. For the case of maximum packing of spheres, assuming 12 nearest neighbors, the maximum possible neck radius was calculated to be 310 nm and an x/a of 0.6. These radii are more than a factor of three larger than the radii predicted from surface diffusion calculations for 60 minutes of annealing at 200°C. Therefore, silver supply will not limit the extent of neck formation for the targeted maximum annealing time of one hour.

$$Volume\ of\ Silver = 2h\pi x^2 - 2\left(\frac{\pi h}{6}(3x^2 + h^2)\right)$$ **Equation 2**

2.3.3 Mechanical Properties of Core-Shell Particle Compacts

Modulus and yield strength data obtained from compression tests are presented in Figure 9. Modulus and yield strength are directly correlated to the number and diameters of necks formed between particles during sintering. Higher annealing temperatures resulted in compacts with more neck formation, higher moduli and yield strengths.

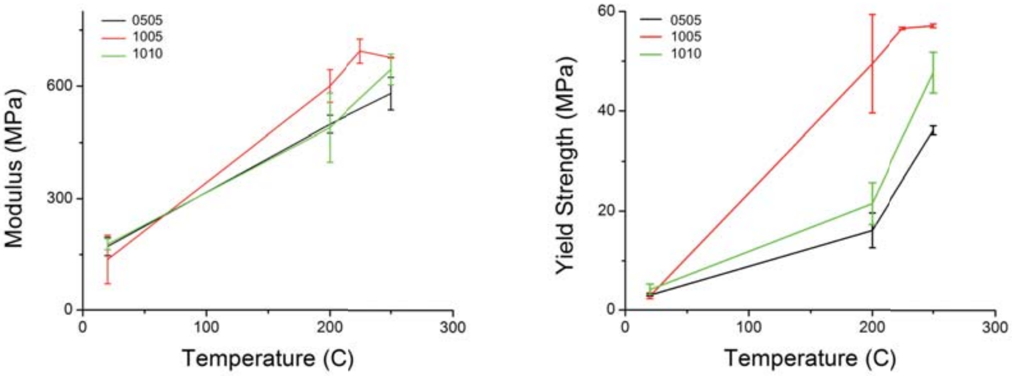

Figure 9. Modulus and yield strength data for the particle formulations

After sintering at 200°C, the maximum compression modulus of 620 MPa was obtained for PAC1005, with PAC1005 outperforming both PAC0505 and PAC1010. Similarly, PAC1005 exhibited higher yield strengths with values ranging from 40-60 MPa. In terms of suitability for electronic interconnects and die attachment, the yield strengths for as-sintered PAC1005 compacts are similar to the 40 MPa yield strength reported by Hamasaki et. al. for Sn-3.5Ag-0.75Cu for the same strain rate [31]. Of equal importance to joint stability is the maximum elastic strain allowable in the joint before yielding. With a significantly lower modulus than Cu, Si, or SAC solders and a yield stress of 45 MPa, the maximum strain in the joint before yielding is estimated to be 0.07. In thermal cycle testing for a typical ΔT of 180°C, the typical thermal expansion mismatch between glass-fiber reinforced FR-4 circuit boards and Si is estimated to produce a shear strain of 0.003. By comparison, the porous Cu-Ag core-shell sintered particle compacts can experience more than an order of magnitude greater strain before yielding that expected due to the imposed thermo-mechanical stresses.

The bulk moduli of copper and silver are 110 GPa and 83 GPa, respectively, with 620 MPa as the maximum modulus measured for the porous sintered PAC1005 core-shell compacts. The non-linear dependence of modulus on porosity and neck formation in porous powder compacts is well known. A modified form of the elastic modulus for open-cell metal foams, Equation 3, appears to be most appropriate for the case of a partially sintered compact at early stages of neck formation, in which the effective modulus Ef is determined by the bulk modulus, E_0, the foam density, ρ_f, and the theoretical density, ρ_{th}. [32]

$$Ef = E_0\left(\frac{\rho_f}{\rho_{th}}\right)^2 \qquad \text{Equation 3}$$

If the as-sintered geometry is modeled as a 3-D cubic foam of metal ligaments of radius x, equal to the neck size, with a fixed spacing of 2a, the particle diameter, the effective density as a function of time becomes a function of only the neck radius. The calculated effective moduli for the PAC1005 particles based on sintering by surface diffusion become 600 MPa, 900 MPa and 1300 MPa after 60 minutes of sintering at 200°C, 225°C and 250°C, respectively. The overall trends for PAC1005 moduli for different annealing times and temperatures are detailed in Figure 10. Mechanical property measurements of PAC1005 compacts shown in Figure 9 correlate to a 20-minute annealing time. The calculated moduli values noted in Figure 10 correspond to the theoretical moduli for the experimental results shown in Figure 9. While higher densities and moduli were expected for PAC0505 on the basis of the effect of particle size on sintering kinetics, the degree of agglomeration and the resulting lower initial density of the unsintered PAC0505 compacts likely led to fewer sintered necks and the observed poorer overall mechanical behavior. The reasons underlying the poorer mechanical behavior of PAC1010 are not known.

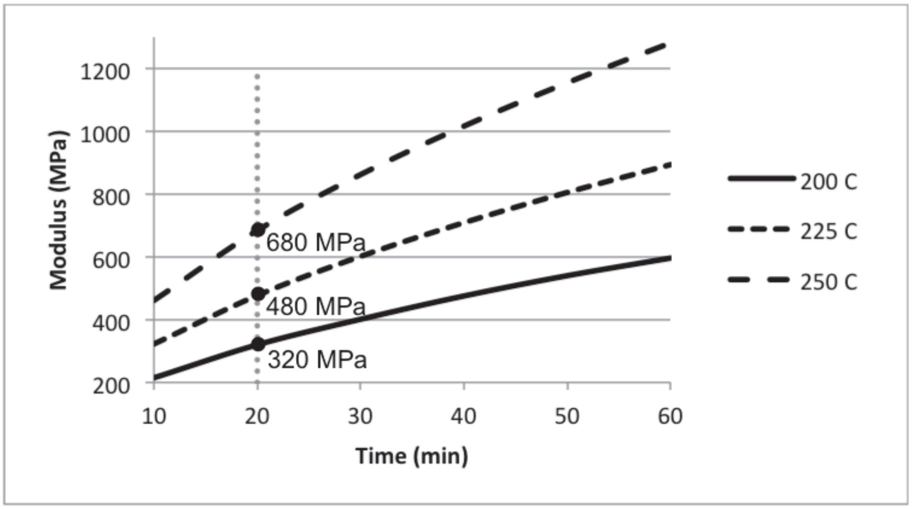

Figure 10. Calculated modulus for PAC1005 particles annealed at 200C, 225C, and 250C with values for the 20 minutes annealing time that correlates to the experimental data reported in Figure 9

Based on modulus and yield strength, PAC1005 was selected as the most promising powder for producing mechanically stable interconnects and was used for paste and process development.

2.3.4 Flux Formulation

In contrast to conventional solder pastes used for reflow which contain ~40 μm [15] particles, the use of 0.5-1 μm particles and the need to produce connections via particle-particle contact without melting and coalescence complicate paste formulation. In addition, two key stability factors during paste storage were identified: phase separation of the constituents and excessive drying and hardening.

Four test matrices covering 35 compositions were assessed and the fluxes that did not exhibit phase separation or excessive drying were combined with core-shell particles and evaluated as pastes. As detailed in Table 4, Matrix 1 evaluated the rheology of fluxes with a variety of rosins and rosin combinations.

Table 4. Matrix 1: Flux formulations 1A-1I focused on determining rosin or rosin combinations that provide the best rheology

Component	**1A**	**1B**	**1C**	**1D**	**1E**	**1F**	**1G**	**1H**	**1I**
Diethylene Glycol Dibutyl Ether	22.85	22.85	22.85	22.85	22.86	22.86	22.86	22.86	22.86
Tridecylalcohol	24.53	24.53	24.53	24.53	24.53	24.53	24.53	24.53	24.53
Teckros D85	52.62								
Teckros D95		52.62							
Pinecrystal KE-604			52.62						
Teckros D140					52.62	42.09	42.09		
R101 Rosin Ester						10.52			
SL102 Rosin Ester							10.52		
Teckros HX				52.62				42.09	42.09
Teckros RL60								10.52	
Teckros RL									10.52
Viscosity (cps) Brookfield RV5 spindle 5; speed 100	356	436	1024	Very Low	3488	1584	1528	1976	228

Within this first matrix (1A-1I), viscosity was assumed to be a key factor, however, this characteristic was determined to be discriminatory due to the ability to incorporate other flux agents to modify overall system behavior. Both single and dual rosin formulation properties could be altered with the addition of thickeners to increase viscosity, the addition of acid activators would increase particle and substrate surface activity and the volatility of the system could be more stable by using different solvents.

As detailed in Table 5, Matrix 2 (1J-1Q) evaluated the effects of adding dipropylene glycol (DPG) solvent, Troythix XYZ thickener, and succinic and adipic acid activators using the same base compositions as Matrix 1 (with the exception of 1D which was deemed not viable due to its very low viscosity). The combination of adipic and succinic acid helps to activate the surfaces of the particles, leads, and pads, by removing oxide and increasing the fluxing activity. These formulations were also mixed with SAC305 particles to 80 weight percent loading and reflowed in order to evaluate general flux performance. All SAC305 formulations mixed and reflowed well, according to industry standards.

Table 5. Matrix 2: Flux formulations 1J-1Q assessed the impact of acid activators on promoting oxide reduction and therefore particle interactions using rosin formulations from Matrix 1

Component	1J	1K	1L	1M	1N	1O	1P	1Q
Diethylene Glycol Dibutyl Ether	20.5	20.5	20.5	20.5	20.5	20.5	20.5	20.5
Tridecylalcohol	22	22	22	22	22	22	22	22
Teckros D85	47.2							
Teckros D95		47.2						
Pinecrystal KE-604			47.2					
Teckros D140				47.2	37.75	37.75		
R101 Rosin Ester					9.44			
SL102 Rosin Ester						9.44		
Teckros HX							37.75	37.75
Teckros RL60							9.44	
Teckros RL								9.44
Dipropylene Glycol (DPG)	1	1	1	1	1	1	1	1
Succinic Acid	1	1	1	1	1	1	1	1
Adipic Acid	3.5	3.5	3.5	3.5	3.5	3.5	3.5	3.5
Troythix XYZ	4.8	4.8	4.8	4.8	4.8	4.8	4.8	4.8
Viscosity	Medium	Medium	Very High	Very High	High	High	Medium	High
Mixed with SAC 305	Mixed well	Mixed well	Mixed well	Mixed well	Mixed well	Mixed well	Mixed well	Mixed well
Reflowed with SAC 305	Reflowed well	Reflowed well	Reflowed well	Reflowed well	Reflowed well	Reflowed well	Reflowed well	Reflowed well

After evaluation of Matrices 1 and 2, Teckros D85 was selected as the rosin for further optimization. The adipic and succinic acid combination was determined to be unacceptable because the volume of acid needed to promote activity in the high surface area 1µm particle system was deemed to be too large and was replaced by a malonic acid activator.

Table 6 lists the compositions of Matrix 3 (2A-2I) that evaluated the effects of a different set of solvents, and the malonic acid activator with Teckros D85 rosin. The goal of this matrix was to evaluate pastes with reduced rosin content in order to decrease the amount of residual flux after reflow/annealing and to produce fluxes with low enough viscosity to promote particle-particle contact during heating and high enough viscosity during heating to limit paste slumping during heating. Note that only low MEK paste formulations (2F-2I) remained stable after mixing, without any apparent phase separation.

Table 6. Matrix 3: Flux formulations 2A-2I focused on reducing the rosin content and understanding the effects of the transition to Malonic acid on the rheology, and particle loading

Component	2A	2B	2C	2D	2E	2F	2G	2H	2I
Methyl Ethyl Ketone	34	29	29		34	17	10	10	10
i-propanol				29			10		5
N Methyl Pyrrolidone								10	5
Cellosolve	40	40	35	35		34			
Butyl Cellosolve					30		30	30	30
Terpineol	10	10	10	10	10	10	20	20	20
Teckros D85	10	15	20	20	20	20	20	20	20
Malonic Acid	1	1	1	1	1	1	3.5	3.5	3.5
Phase Separation	Yes	Yes	Yes	Yes	Yes	No	No	No	No

Based on the results from Matrix 3 that suggested using Butyl Cellosolve along with low MEK content produced stable fluxes, the design program Stat-Ease was used to develop a design of experiments matrix (Matrix 4) to evaluate the interactions of the components and determine the optimal composition for our performance needs, as specified in Matrix 4 (3A-3I), detailed in Table 7. These nine fluxes qualitatively evaluated based on viscosity during the heating and cooling stages of flux preparation; all were found to be acceptable

These final nine flux formulations (3A-3I) were then evaluated based on five qualitative levels of three processability parameters: ease of mixing during particle incorporation, adhesion to the substrate during paste application, and adhesion to the substrate after annealing. The adhesion and mixability for each of these formulations were ranked between 1-5 (Good-Bad) and are detailed in Table 7. The mixability rankings were based on apparent ease of incorporation for producing pastes with approximately the same particle loading (50 vol%, 88 wt%). Some fluxes showed poor particle wetting and resulted in separation of flux and particles regardless of mixing duration and speed, while other flux compositions showed rapid particle wetting and formation of stable, uniform pastes.

Pastes that did not easily wet the surface of the copper substrate and required multiple attempts to adhere during paste application were given poor adhesion rankings (where lower is better). Pastes that exhibited delamination during annealing were assigned a low sintered adhesion ranking. Pastes that could not be removed from the substrate with scraping using a spatula after annealing were assigned given good adhesion rankings. The rankings in Table 7 were used to reduce the number of candidate pastes for manufacturability assessments. The adherence to the substrate after annealing was more heavily weighted due to its importance in creating a stable mechanical and electrical connection.

These nine pastes were also evaluated for weight loss during annealing. Annealing experiments were performed in forming gas (5%H, 95%N) at 205°C for 5-60 minutes. The percent flux weight loss was normalized relative to the amount of flux in each sample in order to compensate for the slight variations in particle loading in the individual paste formulations. Weight loss for each composition after 60 minutes of annealing is detailed in Table 7. Samples that experienced delamination during annealing were not evaluated for weight loss and are denoted by N/A. The results of these weight loss experiments were compared to results from fluxes in previous matrices and the results showed similar behavior, ranging from 8-13 percent.

Table 7. Matrix 4: Flux formulations 3A-3I focused on determining the impact of component interactions as well as promoting sinterability (Mixability and adhesion rankings 1-5 Good-Bad)

	3A	3B	3C	3D	3E	3F	3G	3H	3I
Methyl Ethyl Ketone	10	10	10	10	10	10	10	10	10
i-propanol	5	7	5	7	5	7	7	6	5
N Methyl Pyrrolidone	5	3	5	3	5	3	3	4	5
Butyl Cellosolve	30	32	35	35	32	37	30	33.5	37
Terpineol	20	20	20	20	20	20	20	20	20
Teckros D85	20	20	15	15	20	15	20	17.5	15
Troythix XYZ	6.5	6.5	6.5	6.5	6.5	6.5	6.5	6.5	6.5
Malonic Acid	3.5	1.5	3.5	3.5	1.5	1.5	3.5	2.5	1.5
Hot Viscosity	Low	Low	Low	Low	Low	Low	Low	Low	Low
Cold Viscosity	High	High	High	High	Medium	Low	Medium	Medium	Medium
Flux Density (g/cc)	0.81	1.04	0.76	0.94	0.87	0.9	1.07	0.95	0.88
Volume Percent Particles	47	54	48	53	50	51	56	53	51
Paste mixability	2	2	5	1	4	1	3	5	4
Adhesion before annealing	2	5	3	3	1	5	4	3	1
Adhesion after annealing	4	4	3	1	5	3	2	1	5
Weight Loss % (60 min)	7.6	12.3	11.2	12.1	N/A	11.3	11.4	11.7	N/A

Evaluation of the flux burn-off during annealing, along with the mix-ability, and adhesion evaluations resulted in the selection of paste formulations 3D and 3H. These pastes exhibited flux burn off percentages greater than the 10.8% average as well as the best ranking adhesions after annealing. Both compositions contained 8 components, with five solvents, one rosin, one thickener, and an acid activator, as detailed in Table 8. These pastes were chosen for further testing that included sinterability, a rheological assessment, and printability testing.

Table 8. A list of components and ratios for the best performing flux systems, 3D and 3H

	Methyl Ethyl Ketone	i-propanol	N Methyl Pyrollidone	Butyl Cellosolve	Terpineol	Teckros D85	Troythix XYZ	Malonic Acid
3D	10	7	3	35	20	15	6.5	3.5
3H	10	5	4	33.5	20	17.5	6.5	2.5

2.3.5 Pastes – Particles in Flux

Using paste formulation 3D, the extent of neck formation during annealing was investigated. Figure 11 shows SEM micrographs of neck formation for a sample of PAC1005 powder in 3D flux annealed for 5, 30, and 60 minutes. Figure 11A shows no visible neck formation and the sample contained residual flux as indicated within the white circle. Figure 11B shows a neck connecting two particles after 30 minutes of annealing as indicated by the white circle. Figure 11C depicts a network of particles are connected through neck formation as contained within the circle. Figure 11 depicts increased neck formation with annealing time. These images are proof of concept and confirm that the presence of flux promotes interparticle connection during annealing and that with increased annealing time a continuous network of particles and necks is formed.

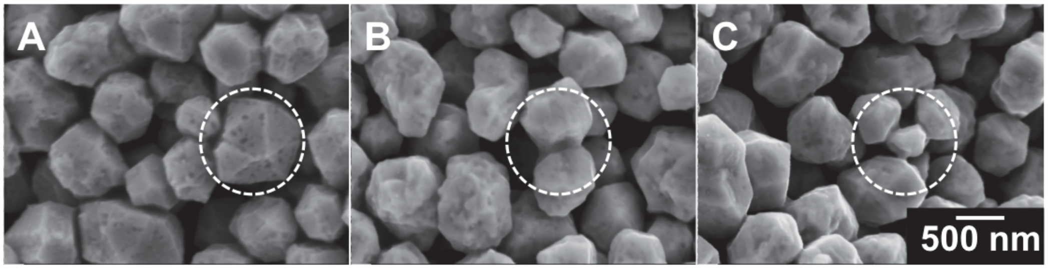

Figure 11. SEM micrographs showing the progression of increased neck formation wiht annealing time (A-5min, B-30min, C-60min)

2.3.6 Rheology and Printability

Conventional solder paste shows non-Newtonian, shear-thinning behavior, which is essential for successful printing. Rheological data were obtained in order to verify the desired shear-thinning properties of the as-fabricated pastes. Plate-on-plate rheological measurements were performed for flux formulation 3H using 0.5mL of 53.3 volume percent loading. As shown in Figure 12, the viscosity decreases with increasing shear rate validating that paste 3H is shear-thinning.

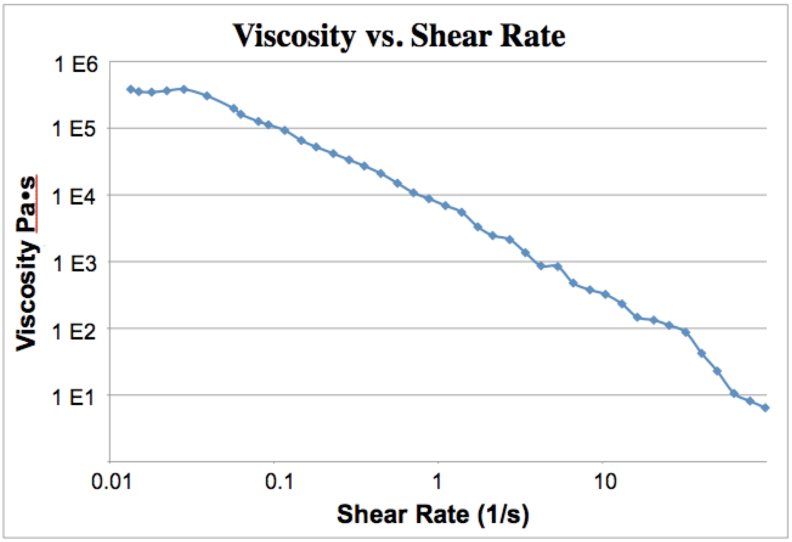

Figure 12. Viscosity vs. shear rate plot for paste formulation 3H showing the desired shear-thinning properties

Stencil printing assessment of both the 3D and 3H paste formulations was carried out at Speedline Technologies to determine if the Cu-Ag core-shell paste formulation could be successfully applied to circuit boards using conventional solder paste deposition techniques. Pastes were printed on test boards containing a wide variety of pad shapes, sizes, and pitches using an MPM stencil printer manufactured by Speedline Inc. Initial parameters of a 30mm/sec speed and 6.8 kgp squeegee pressure, based on traditional lead-free solder pastes, resulted in poor coverage for the Cu-Ag core-shell particle pastes. The coverage exhibited slumping, dog-ears and incomplete pad fill. The squeegee pressure and speed were optimized in order to produce consistent coverage.

For formulation 3H, flat coverage with no dog-ears was acquired using a pressure of 7 kgp and a speed of 25mm/sec, however, there was still visible slumping and some incomplete fill. It should be noted that paste 3H dried very rapidly and was only capable of running 3 prints before the paste began to slide instead of roll behind the squeegee.

For formulation 3D, 9.5 kgp of pressure and a 30mm/sec speed produced pads with good coverage and minimal visible defects after 6 consecutive depositions however, similar to paste 3H, it was clear that paste 3D was thickening with time. It is important to note that printing tests were run with the system hood open in order to be able to observe the behavior of the paste line during deposition. Running the printing process in a closed printing system will reduce drying. Testing also shows the need to adjust solvent rations in order to control evaporation rates during board manufacturing. Images of the smallest and largest pads printed with paste formulation 3D can be seen in Figure 13.

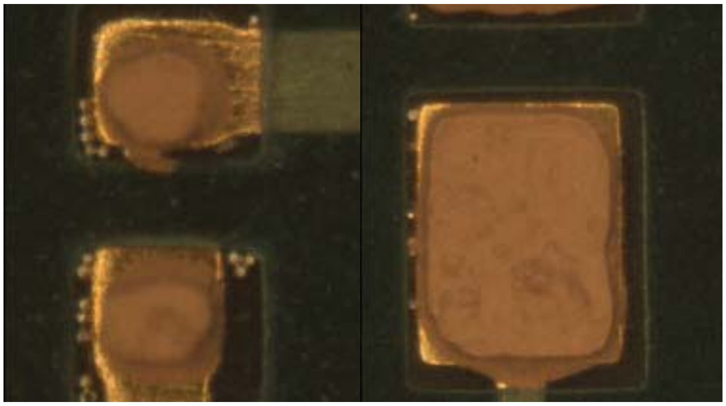

Figure 13. Images of pads exhibiting good coverage. Left: 01005 pad (0.4 mmX0.2 mm) Right: 0402 pad (1 mmX0.5 mm)

2.4 Conclusions

The use of Cu-Ag core-shell nanoparticles was validated as a Pb-free interconnect technology. Upon annealing, the Ag shell dewets the copper surface and forms Ag necks between Cu core particles at particle-particle contacts creating an electrically, thermally, and mechanically stable, porous sintered network. Particle characteristics and paste formulation were optimized with respect to sinterability; mechanical strength and processability for typical surface mount assembly and reflow technologies. This optimization was carried out using three core-shell powder configurations and over fifty flux formulations. The combination of 1 μm diameter core-shell particles with 9nm Ag shells, and fluxes containing methyl ethyl ketone, isopropanol, methyl pyrrolidone, butyl cellosolve, Terpineol, Teckros D85, Troythix XYZ, and malonic acid were determined to be the best performing. These pastes exhibited the targeted shear thinning behavior and promoted neck formation with acceptable flux residues after annealing. Using commercial board assembly equipment, optimization was performed based on squeegee speed and pressure. The two best performing pastes showed coverage and paste rheology comparable to commercial Pb-free solder pastes validating Cu-Ag core-shell nanoparticles as a Pb-free interconnect technology.

CHAPTER 3. SCIENCE

3.1 Science Introduction

3.1.1 Thin Films

Thin films are used for a variety of engineering applications and have been broadly implemented to fill a variety of roles in electronics processing. Thin films experience a broad range of stresses that can be the result of growth mode, deposition process, misfit with the substrate material, and thermal influences. Relaxation of these stresses during subsequent heating that may occur during device lifetime can result in the formation of a variety of microstructural changes. Stress relaxation can result in grain growth, abnormal grain growth, boundary grooving, hole formation, dewetting, hillock formation, whisker formation, popped grains, sunken grain, voids, bubbles, and delamination. In order to understand the formation of defects that result from stress relaxation the causes of film stress must first be understood. [33]

3.1.1.1 Growth Modes

There are several growth modes through which thin film formation can occur. These growth modes are Frank – van der Merwe (FV), Volmer – Weber(VW), and Stranski – Krastonov (SK) which refer to layer-by-layer, island growth, and a combination of both layer-by-layer and island growth respectively. Figure 14 shows schematic representations of each of the growth modes described. The mode of growth that occurs is dependent on the particular system and set of processing parameters. One key influential factor is the lattice mismatch of the film and substrate material. Smaller misfits will result in FV growth due to the ability of the atoms to arrange themselves into a matrix without the formation of a large interface strain. A larger misfit will result in SK growth due the formation of large interface strain as the thickness is increased. These various growth modes will influence the grain structure of the thin film and therefore the stress relaxation mechanisms available to the microstructure. [34]

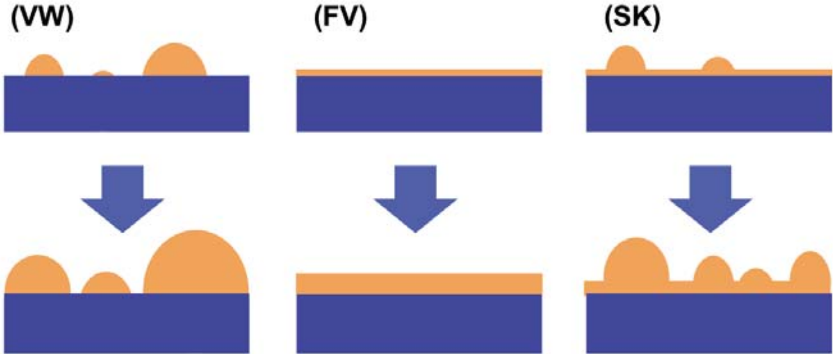

Figure 14. Schematic representations of the three growth modes, (VM) Volmer-Weber, (FV) Frank - van der Merwe, and (SK) Stranksi – Krastonov

3.1.1.2 Deposition Stresses

As thin films are deposited they experience a variety of intrinsic stress behavior associated with the film formation and thickening process. The intrinsic stress behavior of a metal film begins with the development of compressive stresses. These stresses are present prior to the formation of a continuous layer of film material. Upon coalescence of the film into a continuous layer, the film experiences a rapid decrease in compressive stresses and eventually exhibits a tensile stress state during thickening. As film growth progresses and film thickness is increased, these tensile stresses can be further accommodated by defects in the system, thus reducing the tensile stresses. The resulting stress state of metallic thin film system is often a slight compressive stress. A graphical representation of the stress progression of metallic thin films can be seen in Figure 15. [35]

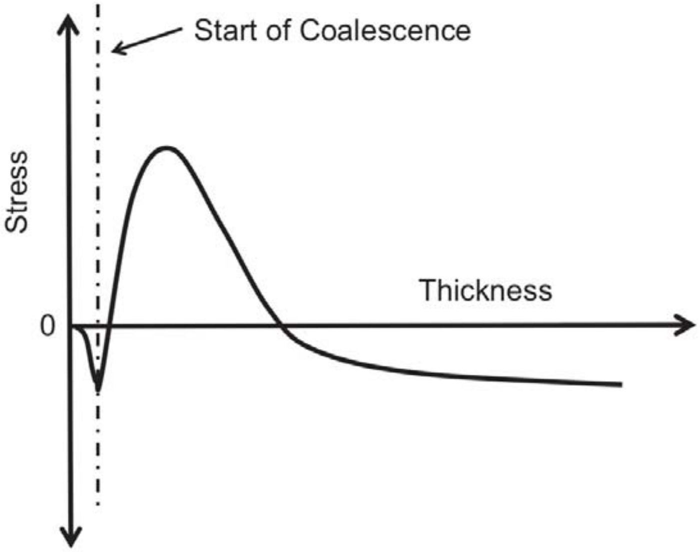

Figure 15. A schematic plot showing the changes in stress that a film experiences as its thickness is increased during deposition

Upon reaching a critical thickness, metallic thin films can accommodate inherent stresses and strains by the formation of a variety of defects specifically, through the formation of misfit dislocations at the film-substrate interface. Along with the intrinsic stresses a film acquires during deposition additional thermal stresses may be imposed on the system.[35]

3.1.1.3 Misfit Stresses

In the case of a thin film on a substrate, some strain will be present due to the film-substrate interface. Assuming the film thickness is sufficiently thinner than the substrate, the film material will take on the lattice parameter of the substrate material. When the film thickness is beyond some critical value dislocations form at the interface in order to accommodate for the strain. These dislocations that help accommodate for the misfit strain are often referred to at misfit dislocations. Equations 4-6 define the misfit strain between the film and substrate material. [34,36]

$$\varepsilon_{mf} = \frac{(a_s - a_f)}{a_s}$$

Equation 4

Overall film strain can then be defined by

$$\varepsilon = \varepsilon_{mf} - \frac{b}{s}$$

Equation 5

And the strain per unit area thus becomes

$$\varepsilon_s = M\left(\varepsilon_{mf} - \frac{b}{s}\right)^2 t$$

Equation 6

3.1.1.4 Thermal Stresses

The difference in the CTE between the film and substrate materials can have a great influence on the film dewetting. Annealing of a thin film on a substrate of much greater thickness will result in expansion or contraction of the sample. The value of the CTE determines if the material will expand or contract and to what degree this deformation will occur. There are effects that may result from differences in CTE between the film and substrate. For an annealed film that is well adhered to the substrate surface the dimension of the film will be constrained by the in-plane dimensions of the substrate. This constraint will induce a stress between the film and substrate affected by the difference in CTE. Table 9 contains thermal expansion coefficients for common film and substrate materials. [34]

Table 9. List of thermal expansion coefficients [37]

Material	CTE (10^{-6}/K)
Quartz	0.6
Silicon	3
YSZ	10
Gold	14
Copper	17
Silver	18

Table 10. List of thermal expansion differences [37]

System	CTE Difference
Silver-Copper	1
Gold-YSZ	4
Gold-Silicon	11
Silver-Silicon	15
Silver-Quartz	17.4

3.1.2 Dewetting Overview

The word dewetting is used to describe a broad range of phenomenon in literature but in this case we use the term dewetting to define film evolution as a result of capillarity. Dewetting is the process a film undergoes in order to evolve from its flat-plane non-equilibrium shape to the equilibrium island shape (a hemispherical cap for isotropic materials).

3.1.2.1 Thermodynamics of Dewetting

The thermodynamic driving force that causes a system to tend toward the lowest energy state, minimizing surface energy, provides the driving force for dewetting. In the case of an isotropic thin film the equilibrium shape of the film is dependent on the contact angle between the substrate and film materials, as determined by the interfacial energy. For a contact angle of θ=0°, a film completely wets the substrate, resulting in a continuous flat film at equilibrium. For a contact angle of θ=180°, a film is considered non-wetting and in equilibrium will form a spherical island atop the substrate. The system geometry of a film on a substrate is composed of three distinct interfacial energies that can be related by the contact angle between the film and substrate materials. This relationship is defined by Young's equation, Equation 7, derived from the surface tension force balance at a film edge, Figure 16. [38]

$$\gamma_s = \gamma_i + \gamma_f \cos\theta \qquad \text{Equation 7}$$

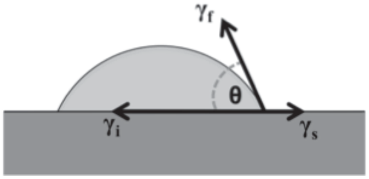

Figure 16. Figure showing the geometry association with Young's equation

In the case of a continuous thin film where the contact angle is greater than zero, the thin film is not stable. Because the equilibrium shape of the material system is dependent on the contact angle, any system where the contact angle is greater than zero will be metastable. The inherent driving force to minimize interfacial energy leads to the formation of hemispherical caps containing the equilibrium contact angle, and thus the term dewetting.

When a film breaks up, or dewets, it creates a triple phase point between the atmosphere, substrate, and film material that contains a local curvature. This curvature leads to a difference in chemical potential, providing a driving force for diffusion that is dependent on the magnitude of the contact angle. The Gibbs-Thompson Equation can define the excess chemical potential, [39]

$$\mu(s) = \mu^0 + \Omega\gamma\kappa(s) \qquad \text{Equation 8}$$

where $\mu(s)$ is the surface chemical potential, μ_0 is the chemical potential at a flat surface, Ω is the atomic volume, γ is the surface energy and $\kappa(s)$ is the average surface curvature at surface location s. This convention leads to a convex, positive, surface having a higher chemical potential than a concave, negative, surface. This potential difference leads to atom flux from surface hills (hillocks, agglomerations, etc.) to valleys (dewet regions).

The equilibrium state of any dewetting system can be stable by creating either a single island on a substrate containing the equilibrium contact angle or an array of smaller islands that each make the equilibrium contact angle with the substrate. Srolovitz and Goldiner determined that there is a minimum island radius that results in a system more stable than a flat film.[40] This minimum radius for which an array of islands is more stable than a flat film for a given film thickness, h_f is given by

$$r_{\min} = \frac{3\sin\theta_w}{1-\cos\theta_w} h_f$$ Equation 9

This result defines the existence of multiple stable islanded geometries for a dewetting system. Specifically, geometries ranging from a single large island to an array of small islands with radii slightly larger than $r_{\min}$ will be more stable that a flat film

3.1.2.2 Nucleation of Holes

Mullins was the first to study the stability of initially flat films by focusing on the influence of thermal grooving. Mullins evaluation showed that in the case of an isotropic continuous solid film, thermal fluctuations that lead to surface perturbations were stable regardless of transport mechanism. [41] Thus, thermal fluctuations do not result in the formation of substrate-exposed regions, instead such perturbations spontaneously decay back to form a flat film. In terms of surface area and energetics it makes physical sense that this process is metastable, because surface perturbations will result in an increase in surface area and energy without the destruction of any. In order for surface fluxuations to amplify and result in exposed substrate there must be some energetic advantage associated with the film breakup. [41] Thus, using Mullins analysis a pre-existing void or formation of a substrate-exposed region is required in order for a film to experience spontaneous dewetting.

Mullins solid film work only considered the interactions between the film and atmosphere, assuming any interactions with the substrate were negligible. Vrij performed a similar analysis on dewetting of liquid thin films. Through the incorporation of substrate-film interactions Vrij determined that thermal fluctuations can penetrate the film thickness leading to the film to spontaneously dewet.[42]

Srolovitz and Safran determined through thermodynamics that for a solid thin film, not only must the void be pre-existing in order for spontaneous wetting to occur but the void must be larger than some critical radius for dewetting to be energetically favorable. In particular, the critical void radius was determined to be dependent on the film thickness via

$$r_{crit} = \frac{h_f}{\sin\theta_w} \qquad \text{Equation 10}$$

Grain boundary grooving and penetration at triple junctions are the most common mechanisms for hole formation in polycrystalline films. Mullins determined that for an isolated grain boundary that both evaporation-condensation and surface diffusion resulted in an infinite groove deepening with time. Specifically, evaporation-condensation has a time dependence of $t^{1/2}$ while surface diffusion has a time dependence of $t^{1/4}$. [41] Mullins also determined that the shape of groove depth profiles were dependent on the transport mechanism. As seen in Figure 17 grooves formed by evaporation-condensation smoothly decrease from the initial film height, while grooves formed by surface diffusion develop a build up of material above the initial film height. These differences in depth profiles will be a relevant part of hole and edge retraction discussed in another section. [41]

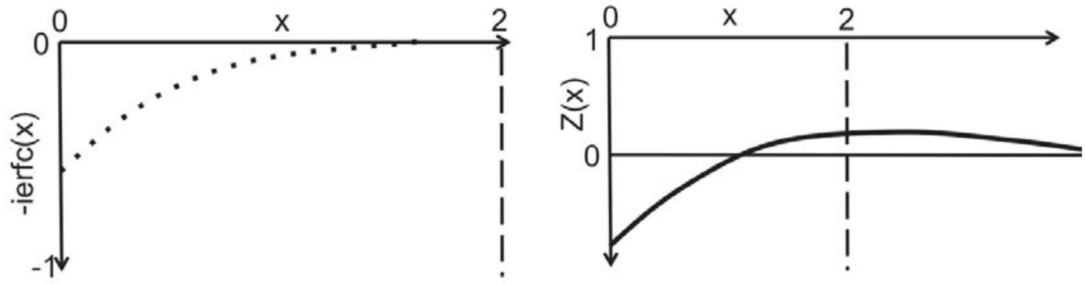

Figure 17. Schematics of normalized groove profile shapes caused by (left) evaporation-condensation and (right) surface diffusion. Showing the edge build-up that results from surface diffusion. Adapted from Mullins, W. W. Theory of Thermal Grooving. *J. Appl. Phys.* 28, 333 (1957). [41]

Genin et. al. compared grooving between grain boundaries and triple junctions, determining that triple junction grooving occurred much more quickly than grooving a boundary between two grains. This result implies that critical void formation for dewetting to occur in a polycrystalline film should occur at triple junctions in the microstructure. [43] Genin et. al. also determined that forces acting on a boundary can greatly influence the depth of the groove. Grooves under tension experience more deepening than stress-free grooves while grooves under compression experience less deepening than stress-free grooves. These results can be easily translated to the amount critical dewetting nuclei formed based on the stress state of a thin film. Films under tension should create critical nuclei for dewetting quicker than films under compression.

Films can also experience spontaneous dewetting nucleated by methods other than grain boundary grooving. Strain instabilities at the film-substrate interface, [44] the creation of bubbles in the film [45,46], and void formation at the substrate-film interface [45] can lead to dewetting of a system.

3.1.3 Isotropic Dewetting Models

Once a film has developed a hole, dewetting can begin. There are two notable sets of work that propose kinetic models for the dewetting mechanisms of a continuous thin film once a void has been formed. First, Brandon and Bradshaw developed a model for void growth through surface diffusion causing continuous thickening and withdrawal. Second, Jiran and Thompson expanded on the same framework noting that void edges did not remain uniform but instead experienced non-uniformities that affect the curvature and thus the driving force for diffusion.

3.1.3.1 Brandon and Bradshaw

The goal of the Brandon and Bradshaw research was to acquire data for the mobility of atoms in a metallic thin film deposited by evaporation. Brandon and Bradshaw used the tendency of a film to dewet to determine the surface self-diffusion coefficient, D_s, and surface energy, γ_s. Large grain polycrystalline silver films were deposited on both Pyrex and mica through evaporation in vacuum. Film thicknesses ranged from 27nm to 1000nm. Samples were annealed at temperatures between 175°C – 375°C and the structure of the film was monitored through microscopy. Experimental results were used to develop a model for the growth of holes in metallic thin films dependent on the film thickness and annealing time. [47]

The model proposed by Brandon and Bradshaw begins with three assumptions (1) a circular void geometry, (2) mass conservation of the material that would have filled the void into the thickened edges surrounding the void, and (3) a 90° contact angle between the substrate and the thickened film at the void edge.

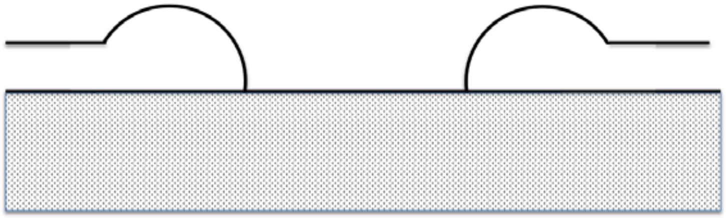

Figure 18. A cross-sectional view of a circular void showing a thickened edge as described by Brandon and Bradshaw. Adapted from Brandon, R. & Bradshaw, F. J. The Mobility of the Surface Atoms of Copper and Silver Evaporated Deposits. *Royal Aircraft Extablishment* 1–162 (1966).

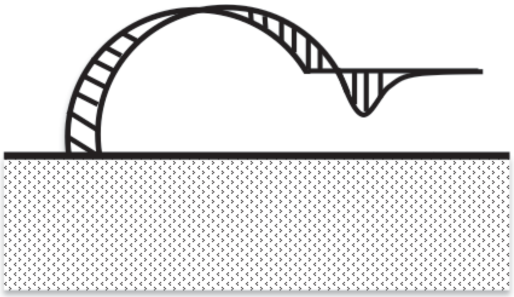

Figure 19. Schematic of a hole edge showing the regions of volume change that occur during surface diffusion. Adapted from Brandon, R. & Bradshaw, F. J. The Mobility of the Surface Atoms of Copper and Silver Evaporated Deposits. *Royal Aircraft Extablishment* 1–162 (1966).

In this model, as the void continues to grow, the edged continue to thicken causing a decrease in curvature and thus reducing the driving force for diffusion. As the void grows, the diffusion rate continuously decreases and eventually stops. Brandon and Bradshaw derived this relationship to be

$$r^{5/2} = \frac{5\pi^{1/2}Bt}{2d^{3/2}}$$ Equation 11

with,

$$B = \frac{D_s\gamma\upsilon\Omega^2}{kT}$$ Equation 12

where r is the void radius, d is the film thickness, D_s is the surface diffusivity, γ is the surface energy, v is the number of atoms per area, Ω is the atomic volume and k is Boltzman's constant. The key relationships that can be taken away from this are the void growth velocity dependence on time and film thickness. The void growth rate is proportional to 2/5 the power of time and -3/5 the power of film thickness.[47]

3.1.3.2 Jiran and Thompson

The goal of the Jiran and Thompsons research was motivated by the disconnect between the Brandon and Bradshaw model and experimentally determined dewetting kinetics and structures. Specifically, voids seen in practice are not simply shaped (spherical) but instead grow into complicated shapes and the growth rate model does not accurately predict system kinetics. Jiran and Thompson deposited thin gold films onto amorphous silicon nitride membranes for TEM studies and fused silica for laser light transmission via evaporation in vacuum. [48]

Unlike the model proposed by Brandon and Bradshaw, void edges exhibited instability and developed a morphology that was dependent on the local film thickness. As Brandon and Bradshaw predicted there was material accumulation at the void edges however, the accumulation was not uniform. The curvature difference between the thick and thin regions causes a difference in driving forces leading to faster void growth in thinner regions. The faster growth in thinner regions leads to non-uniform almost fractal-like void formation.

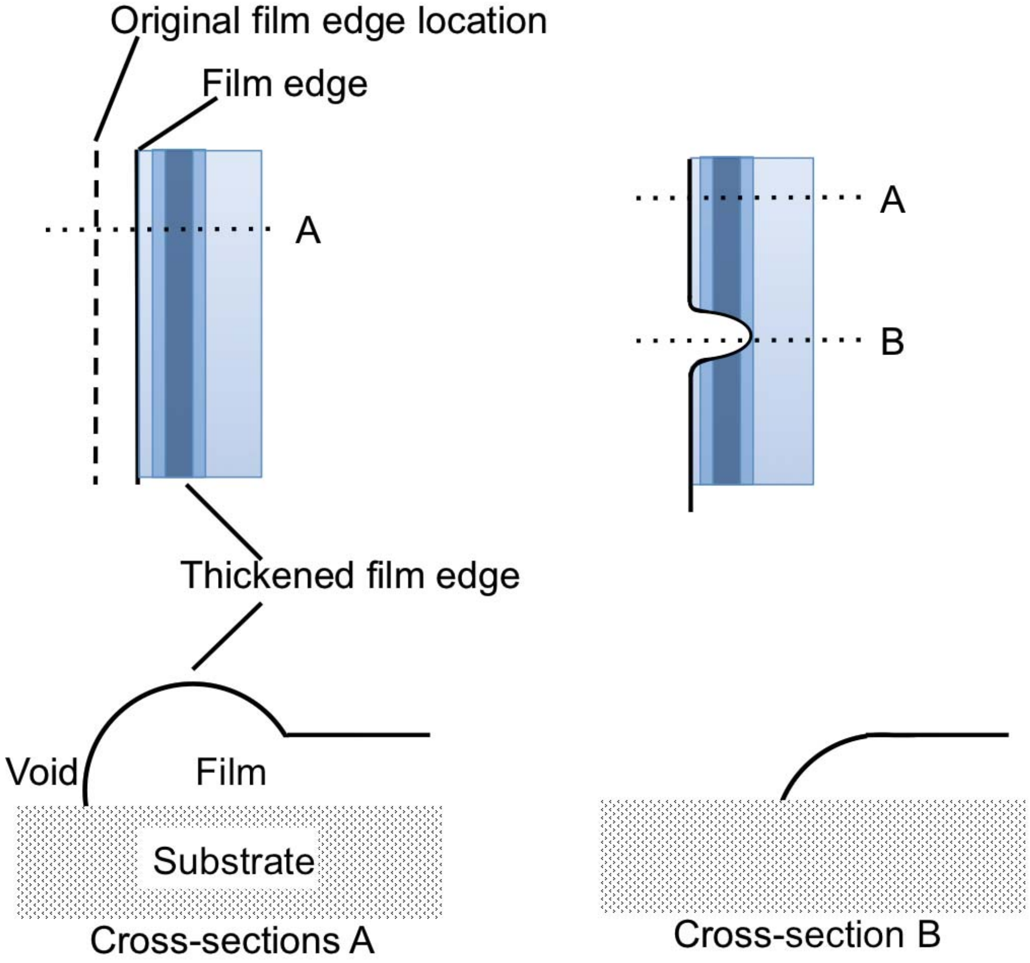

Figure 20. Schematic showing the difference in void edge movement between regions of thick and thin film edge. Adapted from Jiran, E & Thompson, C.V. Capillary Instabilities in thin films. Journal of Elec. Materi. 19, 115-1160 (1990).

Jiran and Thompson went on to develop a model that accounts for the non-uniformities in edge thickness and void growth while maintaining Brandon and Bradshaw’s assumption that the contact angle of the film edge with the substrate is ninety degrees and determined that the growth rate of the void is constant with time. The relationship they derived is defined by

$$\frac{\Delta x}{\Delta t} = 2\frac{D_0\gamma\Omega^2}{kT\pi h^3}\exp\left(-\frac{Q_s}{kT}\right)$$ Equation 13

where D_0 is the pre-exponential for surface diffusivity, γ is surface tension, Ω is the atomic volume, h is the film thickness, and Q_s is the activation energy for surface diffusion.

Jiran and Thompson's model predicted the growth rate to be constant and proportional to -3 power of film thickness. While Jiran and Thompson's model accounts for the complex structures seen experimentally during dewetting experiments it is not clear if the predicted trends can be assumed or adapted to any material system. For this reason, several research groups developed their own kinetic predictions and equations based on the work of both Brandon and Bradshaw and Jiran and Thompson but accounting the specifics of their material system and geometries of interest. [48]

3.1.3.3 Other Velocity Predictions

Mullins showed that the boundary velocity through surface diffusion could be described by

$$V_n = -B\nabla_s^2\kappa$$ Equation 14

where V_n is the surface normal velocity, $\nabla_s^2\kappa$ describes the curvature of the surface, and $B = D_s\gamma_v\Omega^2 v / kT$. Where D_s is the surface diffusion coefficient, γ_v is the surface energy per unit area, Ω is an atomic volume, v is the number of atoms per unit area, and kT is the thermal energy.[41,46] Srolovitz and Safran later adapted this equation and predicted that through surface diffusion boundary kinetics asymptotically decays to zero. These results differ from those of Jiran and Thompson that predict a constant rate of boundary motion. Srolovitz and Safran also predicted, that the film thickness influenced the velocity but in the case of surface diffusion the influence is not a simple scale as seen by the works of Brandon, Bradshaw, Jiran and Thomspon. Instead for the case of surface diffusion there is no perfect scaling as described by

$$\dot{\rho} = VB^{1/4} t^{-3/4} \left\{ \log^3 \left[Bt(\alpha / a \right]^4 + \ldots \right\} \qquad \text{Equation 15}$$

where V is a constant of the order 10^{-3}. This complex relationship suggests the influence of more than one length scale in the system.[46,49]

Eventually, the features that were once holes grow large enough that they impinge on each other creating a collection of islands separated by regions of exposed substrate. The initially formed islands are not yet at their equilibrium size or shape. Islands larger than the equilibrium size will change diameter with velocities defined by their transport mechanism. Based on the assumptions made pertaining to dewetting in the systems of interest surface diffusion is the transport mechanism of interest.

Over time the velocity will reduce until motion stops and the islands reach their equilibrium shape of a spherical cap in contact with the substrate at the equilibrium contact angle. Srolovitz and Safran determined the equilibrium island radius to be described by

$$\rho_{eq} = \left(4\Omega/\pi\alpha\right)^{1/3} \qquad \text{Equation 16}$$

where Ω is the volume of the material contained in the island, $\alpha = \tan(\theta)$, with θ being the equilibrium contact angle as defined by the Young-Dupree equation.[46]

Lastly, Ghaleb and Perraillon examined the surface diffusion of 1-2 monolayers of silver deposited on (331) and (110) copper surfaces. Diffusion coefficients were determined based on the concentration profiles after annealing and results suggested that surface diffusion occurred at different rates on the different copper faces. The possibility of anisotropic diffusion in the silver on copper system may influence the onset and progression of dewetting. [50]

3.1.4 Polycrystallinity and Anisotropy Influence on Defect Formation

The descriptions developed by Brandon and Bradshaw and Jiran and Thompson are only valid for thin continuous single crystal films that contain no grain boundaries, and all relationships defined assume no anisotropy. These descriptions simply describe the effect of surface diffusion at the edge of a film but do not consider any outside effects. Thin films in engineering applications are often polycrystalline with a variety of anisotropy and wetting effects influencing the stress relaxation behavior and therefore more factors must be taken into consideration. Dewetting is one example of the kind of defect morphologies that can result from thin film stress relaxation. Thin film relaxation can also manifest in the formation of a variety of other heterogeneous defects such as holes, popped grains, sunken grains, hillocks, whiskers, surface faceting, delamination, voids, and bubbles. In many cases more than one type of defect is found in a single set of experimental parameters. Due to the complex interactions of localized film thickness, texture, and diffusion paths, deconvoluting the individual impacts can be quite complicated. The structure that a film acquires upon stress relaxation, for our study this happens through annealing, is dependent on the specifics of the materials system and relaxation parameters. Analysis of thin film dewetting literature suggests that the amount of time that the sample is allowed to relax, the temperature it is exposed to, and film thickness will greatly influence the final structure of the film. Along with this, there are several studies where the annealing structure is influenced by the formation of hillocks and the presence of local texture or orientation relationships. In order to correlate the influence of the annealing parameters, sample geometry, and material system to the final dewet microstructure we must first examine the literature. The following sections will discuss the current state of literature that addresses defect formation models, correlations to dewetting, and other effects that may influence the onset and progression of these processes.

As previously mentioned, hillock formation is a known stress relaxation mechanism for thin films. Assuming that stress relaxation (or strain minimization) is a driving force for dewetting of thin films, the stress relieved by the formation of hillocks will reduce the driving force for dewetting to occur. This reduction in driving force will lower the required annealing temperature and time to achieve the various stages of dewetting and may inhibit the dewetting process. In many of the silver films studied in this work both dewetting and hillock formation occurs. Therefore, familiarity with the growth models and structural relationships associated with hillock formation will be crucial in developing and understanding of silver thin film stress relaxation mechanisms.

3.1.4.1 Hillock Growth - Relevant Literature

Sarobol et al developed a physics-based model that relates the ability of a grain to grow out of the plane of a film to a force balance due to the accretion stress at the base of grain and the stress required to overcome grain boundary sliding friction. This model assumes that the grain of interest has a surface grain geometry with an inverted stepped cone structure and grain boundaries containing horizontal and vertical facets. Atoms will build up on the horizontal facets perpendicular to the direction of defect growth. This build up will result in a shear force along the vertical facets. This shear force will be competing with the grain boundary sliding friction. Grain boundary sliding will only occur when the shear force due to atomic accretion is greater than the resisting grain boundary friction. When grain boundary sliding occurs the grain will rise out of the plane of the film until the accretion stress is no longer greater than the sliding friction. The mathematical representation of this relationship is defined in Equation 17 r is the grain radius, σ is the accretion stress, t is the film thickness, and β is the sliding friction. Sarobol et al also extends this model to more complex geometries my manipulating the accretion parameters and starting grain shape. [51] This physics-based approach to modeling whisker and hillock growth out of the film plane does fundamentally cover growth. However, this model does not include considerations of film stress or other factors that are known to influence defect formation.

$$\pi r^2 \sigma > 2\pi r t \beta \qquad \text{Equation 17}$$

Kovalenko et al examined the correlation between dewetting and hillock formation for thin Fe films on sapphire annealed at 750°C. This group proposed that, during the formation of a single hole, a single surface defect grows out of the film plane, implying that atomic transport occurs only between these two areas. The diffusion path for this scenario is along the film-substrate interface and not surface diffusion as is suggested to be the dominant diffusion mechanism for dewetting. This work can be added as an extension of the Sarobol et al GB sliding limited model of out-of-plane defect formation. In this case, atomic diffusion takes place, moving material from the free surface to the film-substrate interface resulting in an accretion of atoms at the base of a grain. This accretion will result in the movement of the grain out of the plane of the film thus forming a popped grain, hillock, or whisker. [52]

3.1.4.2 Texture and Preferred Orientation Effects - Relevant Literature

Galinski et al showed that the minimization of surface energy and the minimization of strain density, which are normally autonomous, are the two governing factors in hillock evolution and kinetics in thin Pt films on YSZ. It was seen that at a critical transition temperature of 973 K, there is an evolution from strictly hillock formation to a combination of hillock formation and hole formation near hillock bases. Finite element simulations were combined with experimental results and indicated a minimization of film free energy occurs due to hillock formation and determined that the minimum free energy shape can be used to predict hillock aspect ratio. It was also determined that the locations where hole formation occurred, at the bases of hillocks, coincided with the location of local maximum stress. Galinski et al also noted that the deposition technique greatly impacted the chosen pathway of thermal instabilities in thin films. Identical thermal treatments of samples prepared by different methods can lead to different defect morphology formation when all other parameters are kept constant. This is of key importance because it clearly shows that the inherent properties of the film (grain boundary energy, localized texture and stress states) have a greatest impact on which instability mechanism will dominate and therefore the resulting defect morphology. [53]

Muller et al examined the dewetting of thin gold films on silicon. A 30nm gold film annealed at 600°C formed holes after 10 minutes of exposure. Analysis of the data shows a clear progression from holes to dewet structures containing finger-like projections. In this case, island formation is not seen. However, in a second study by Muller et al a 30nm gold film was annealed at 900°C for 72 hours and the system was able to reach the island formation regime. Through the use of XRD, the texture change of annealed gold films on silicon was studied. Muller et. al. determined that as dewetting occurred the texture of the film material increased as the dewetting progresses. The frequency of the (111) plane normal orientation increased with increasing annealing time and temperature. [54]

3.1.4.3 Other Influencing Factors - Relevant Literature

Sauter et al examined the effect of film thickness on hillock formation through the study of Au thin films on Si substrates with silicon nitride barrier layers. Samples were exposed to three thermal cycles from room temperature to 500°C and the structures and stress states were examined. Differences in film thickness will result in differences in film stress state and therefore different relaxation mechanism and defect morphologies. For this materials system, there was a critical film thickness of 300nm after which hillock formation occurred. Hillock diameter and density were measured and both were determined to increase with increasing film thickness. Gold film stress states were determined using wafer curvature measurements during cycling. As expected, the stress state of the film transitioned from tensile to compressive during heating and reverted back to tensile during cooling. For thicker films, the magnitude of the compressive biaxial stress was greater. [55]

Syarbaini examined hillock formation and growth during annealing for 500nm thick gold films on SiO2/Si and SixNy/Si substrates. Annealing took place at 500°C in a forming gas atmosphere. Based on rates of change in hillock surface area, results of the study suggested that the a combination of lattice and grain boundary diffusion were the dominate mechanisms behind hillock growth during annealing. However, the visible surface morphology changes (faceting and roughening) of hillocks also suggested that surface diffusion was active. This study focused on the differences in hillock morphology achieved with different annealing parameters. It was noted that the different stress states achieved through variations in annealing time and continuous versus interrupted annealing studies greatly influenced hillock structure. A variety of possible explanations for differences in hillock structure were proposed with the main focus being on the variation in stress states between continuous versus interrupted annealing studies and the influences these stress states will have on diffusion kinetics and defect formation. [56] Understanding the mechanism behind the differences in defect structures and densities seen for continuous versus interrupted annealing studies may help in understanding the progression of stress relaxation defect formation in the silver films studied in this dissertation.

3.1.5 Silver Film Relaxation Literature Review

The previously mentioned studies have provided insight into the processes and relaxation kinetics that take place during thin film relaxation and dewetting. However, it is also necessary to understand the state of research on the materials system of interest. This section will focus on results from silver film studies.

3.1.5.1 Silver Dewetting

Sharma and Spitz examined the dewetting of 50nm silver films on quartz and found that dewetting occurs to a higher degree with more elevated temperature. As previously mentioned, dewetting occurs through atomic diffusion and diffusion is faster at higher temperatures. Therefore, dewetting will occur faster at higher temperatures with all other variables being equal. However, there is minimal literature that quantifies the effect of temperature on expected rates from diffusion. Sharma and Spitz studied 500nm silver films on quartz annealed at 375°C for 20 hours, and 470°C for 76 minutes. In examining the resulting microstructures it is apparent that even with the shorter annealing time the sample annealed at 470°C contains more exposed substrate than the sample annealed at 375°C. A more comprehensive study could provide insight into the dominant diffusion mechanisms behind the onset and progression of Ag thin film dewetting. [57]

3.1.5.2 Silver Thickness Effects

Krishna et al. examined the influence of film thickness on dewetting of silver thin films on silicon exposed to irradiation via 10 laser pulses. The exposure to the same number of laser pulses was assumed to simulate the effect of identical annealing conditions for each sample. The 2 nm sample microstructure contained small silver islands, the 4.5, 7.4, ad 9.5 nm films resulted in varying degrees of dewetting all containing finger-like projections and the 11.5 and 20 nm microstructures only exhibited the onset of hole formation. This study shows the effect that thickness has on the dewetting structure, formation, and progression. As thickness is increased but annealing time is held constant, the microstructure is not provided with enough energy density (per film volume) to promote the same level of stress relaxation and therefore thicker films exhibit less change in microstructure for the same annealing parameters. [58]

Simrick et al studied the thermal stability of 100 – 820 nm thick silver films on YSZ. Annealing temperatures ranged from 250-550°C. As previously defined in the literature, dewetting progressed via hole formation and hole opening to eventually form isolated islands of film material. The hole size and exposed substrate area were tracked over a variety of temperature and thickness combinations. The resulting data was used to produce a structure map that can predict the predominant structure based on the known time and temperature for a specific anneal of the system. Simrick et al also used their experimental hole radius data and Brandon and Bradshaw's surface diffusion model for dewetting to back-calculate the effective diffusion coefficient for surface diffusion during dewetting of silver thin films on YSZ. Diffusion coefficient values ranged between 10^{-9} – 10^{-5} cm^2/s. [59]

3.1.5.3 Silver Hillock Formation

Thurmer et al studied the dewetting behavior of 1nm silver films on silicon annealed at 350°C. After 4 hours of annealing the 1nm films dewet to form islands. However, along with the traditionally seen progression of hole formation, continuous dewetting resulting in a finger-like projections, and island formation, the films also exhibited the formation of larger hillock-like features. [60] Similarly, Sharma and Spitz saw hillock formation on 500nm silver thin films on quartz annealed at 375 C for 20 and 120 hours. [57]

3.1.5.4 Silver Texture and Orientation Effects

Similar to the results of Galinski et al on Pt thin films where the minimum energy shape influenced the hillock shape, Thurmer et. al. reported hillocks of silver that appeared to exhibit preferential growth of certain facets (or orientations) during dewetting. The influence of this orientation effect will result in faceted island formation. This preferential growth may also influence the kinetics, as growth will likely not be limited by diffusion but instead by the availability of diffusing atoms to attach to a desired surface or interface. [60]

3.1.6 Implications for Silver on Silicon and Copper

All of the factors discussed in this introduction will play a role in the relaxation behavior of the silver films examined in this research. This section will discuss the implications of the key factors that may influence the stress relaxation defect formation and progression for silver films on silicon and copper.

While there isn't a vast amount of literature on silver thin film stress relaxation behavior, the work that is available suggests that both hillocks and solid state dewetting can be formed during relaxation. As previously mentioned stress relieved by the formation of hillocks will reduce the driving force for dewetting to occur and will therefore influence defect morphology progression.

It is also important to note that in 2002 Baletto et al reported that silver atom attachment behavior on copper can be influenced by the copper surface orientation. Specifically, adatoms of silver on copper (111) facets diffuse quicker than on (100) facets. [61] This difference in adatom diffusion will influence the structure that the film takes during deposition in terms of stress state, local microstructure, and local texture of the film. All of these factors will influence the stress relaxation defect formation and progression. Due to the anisotropic adatom attachment behavior defined by Baletto et al and orientation relationships between silver and copper the grain structure of the copper core particles (single crystal, polycrystal, textured, etc.) will influence the grain structure of the silver shell and thus affect the relaxation defect formation mechanism. Kim et. al. examined the interface between the copper seed and silver shell using high resolution transmission electron microscopy (HRTEM) and determined there was an epitaxial relationship between the copper core and silver shell that appeared to be dependent on shell thickness. Thick shells (>15nm) appeared rough and displayed a Ag(220)//Cu(220): Ag[-111]//Cu[-111] relationship while thinner (~5nm), faceted shells had a Ag(111)//Cu(220) relationship. [11] Figures 21 – 24 are schematics of what these relationships mean in terms of atomic positions.

For the thick shell relationship of Ag(220)//Cu(220): Ag[-111]//Cu[-111], the silver and copper 220 planes are parallel to each other. It is important to remember that the (220) plane is referenced because (110) planes do not diffract in FCC. The second half of the Ag(220)//Cu(220): Ag[-111]//Cu[-111] relationship states that the [$\bar{1}$11] within the (220) planes of both silver and copper are also parallel to each other. A schematic representation of this relationship can be seen in Figure 21 and a schematic of the each location in a reference crystal can be seen in Figure 22.

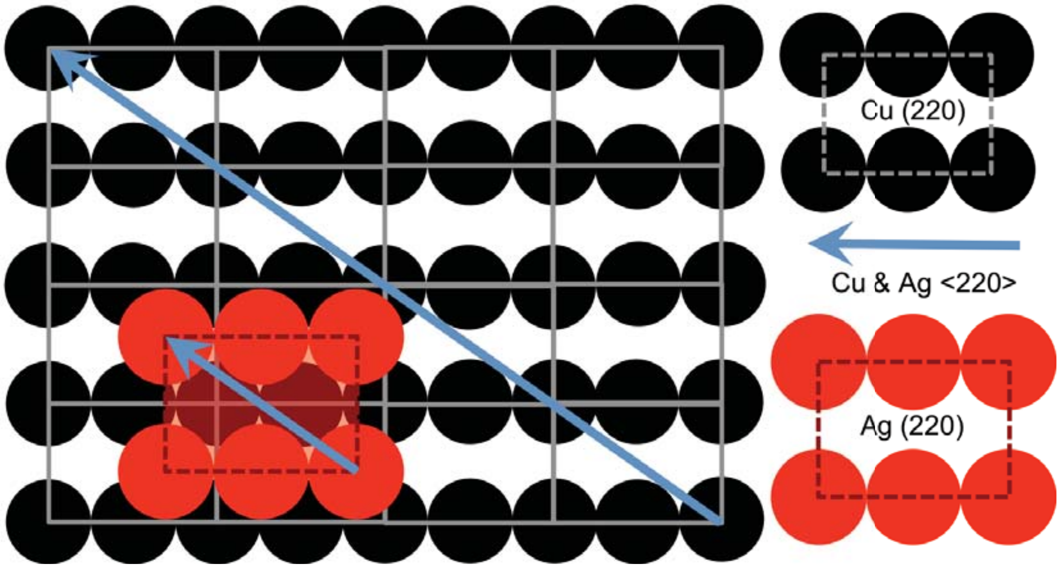

Figure 21. A schematic representation of the Ag(220)//Cu(220): Ag[-111]//Cu[-111] epitaxial relationship in terms of crystal structure showing an example of how the silver film may lay atop the copper substrate.

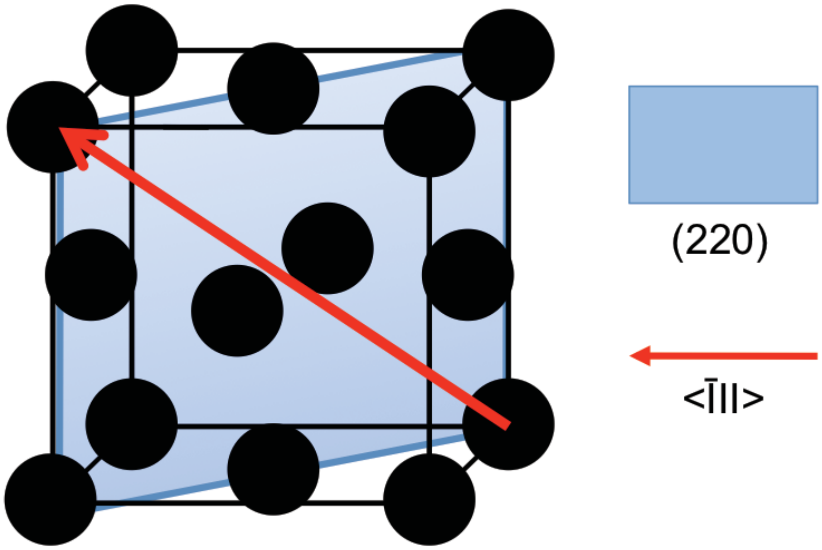

Figure 22. A schematic representation showing the (220) plane and <-111> direction location in an FCC crystal.

The second relationship, Ag(111)//Cu(220), describes that the silver (111) plane lies parallel the copper (220) (or 110) plane and states that there is no directly correlating relationship between any directions in the substrate and film. A schematic of this relationship and the associated planes within a reference crystal can be seen in Figure 23 and Figure 24.

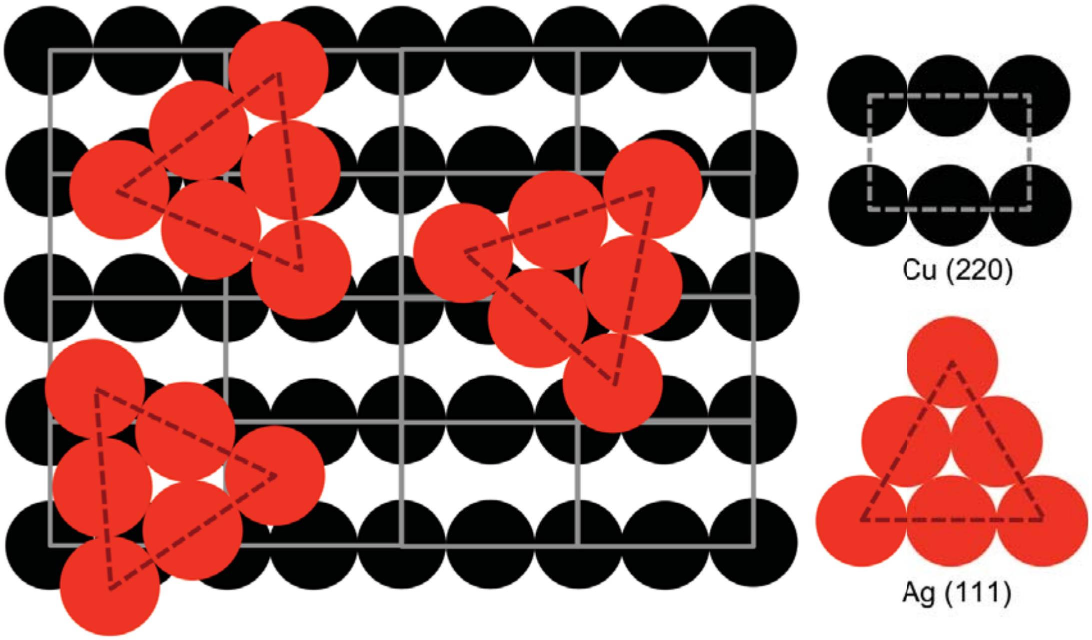

Figure 23. A schematic representation of the different planes and three possible orientation for the silver film.

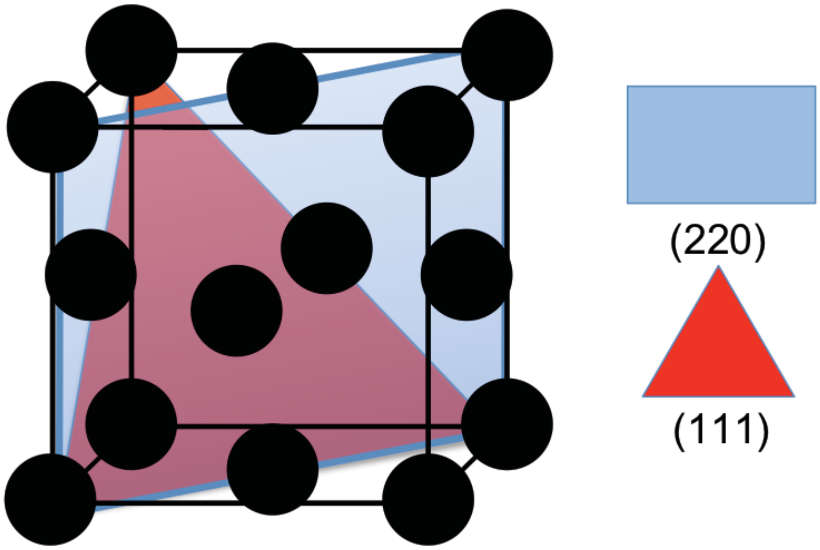

Figure 24. A schematic representation showing the (220) and (111) planes in an FCC crystal.

3.2 Experimental

3.2.1 Experimental Overview

The goal of this research was quantification of the kinetics and non-uniformity of dewetting through examination of the progression of microstructural changes during solid-state annealing of polycrystalline thin silver films. This chapter will focus on three key studies of 50nm silver films on silicon: the effects of film non-uniformity on dewetting kinetics during continuous annealing, local microstructure evolution during interrupted annealing, and the effect of capping layers on local dewetting kinetics and microstructure evolution. From these studies the dominant dewetting processes can be analyzed by comparing the average behavior with the quantitative local behavior of individual regions, including hole growth and coarsening of individual grains.

In the first study, the degree of non-uniformity in dewetting behavior is quantified through measurements of the average exposed substrate area fraction and hole densities of an annealed silver film. Possible causes of non-uniform relaxation behavior are discussed and the experimental results are compared to proposed relationships with differences in film thickness or annealing temperature. The surface diffusion coefficient for each identified region is also calculated and compared to literature values and expected trends.

In the second study, the effect of capping layers on local dewetting kinetics and microstructure evolution is investigated. Three locations with a carbon-based, organic capping layer induced by SEM imaging are tracked. SEM and AFM are used to track changes in surface structure and characteristics after anneals of 1, 9, 18, and 36 hours. The average behaviors as well as the local changes of each tracked location are quantified with measurements of changes in hillock area, hole area, and roughness. The surface diffusion coefficient associated with each anneal is then calculated. These results are compared to those from the previously defined non-uniformity study as well as literature values.

In the third study, global and local microstructure evolution during a series of interrupted annealing experiments is investigated. Six locations are tracked on the surface of a 50nm electron beam evaporated thin silver film on a (100) silicon substrate. Atomic force microscopy is used to track changes in surface structure and characteristics after anneals of 1, 9, 18, and 36 hours. The average behaviors as well as the local changes of each tracked location are quantified with measurements of changes in hillock area, hole area, and roughness.

3.2.2 Experimental Procedure

3.2.2.1 Substrate and Film Preparation

Single crystal silicon substrates were purchased from MTI Corporation, diced into 10mmX10mm squares (with standard wafer thickness), cleaned with piranha solution to remove residual organic material and subsequently cleaned with acetone, methanol, and ethanol. The native oxide layer was not removed.

For the first study, 99.99% purity silver was deposited onto (111) silicon at a rate of 1 nm per second via thermal evaporation physical vapor deposition (TEPVD) using a tungsten basket heater at Purdue University (Lafayette, IN, USA). Substrates were not heated or rotated during deposition. Similarly, instrument geometry only allowed for a 2-inch separation between the source and sample. Because of this, there were directional deposition effects influencing the uniformity of the film thickness and grain structure. Under SEM investigation, some regions of the sample surface exhibited what appeared to be solidified splatter patterns, suggesting that the Ag source material was boiling. The geometry of the thermal evaporation deposition chamber greatly affected the quality of film deposited. However, regions that appeared uniform were studied in order to determine the effects of non-uniformity on dewetting kinetics.

For the second study, 99.999% pure silver was deposited onto (100) silicon via electron beam physical vapor deposition (EBPVD) at The Technion – Israel Institute of Technology (Haifa, Israel) by Dr. Wayne Kaplan and Hadar (Bratt) Nahor. The as-deposited sample surfaces produced by EBPVD appeared to be more uniform than those from TEPVD. The 50nm film thickness, as determined by the in-situ quartz crystal microbalance, was confirmed via multiple Focused Ion Beam (FIB) cross-sections across the surface of the sample. As seen in Figure 25, the resolution of the microscope was limited at the 50nm scale but measurements show an approximate 60nm thickness, which is within reasonable error of the measurements taken. The image contains five different regions. The top section of the film is the free surface of the silver film, the large bright region below is ion-beam platinum that was used to protect the film surface from beam damage during cutting, the thin dark region below the ion-beam platinum is electron-beam platinum, the brighter region below the electron beam platinum is the silver thin film, and the large dark region at the bottom of the image is the silicon substrate. The tilt corrected measurement of the film thickness is, 63.5nm, as labeled on the image.

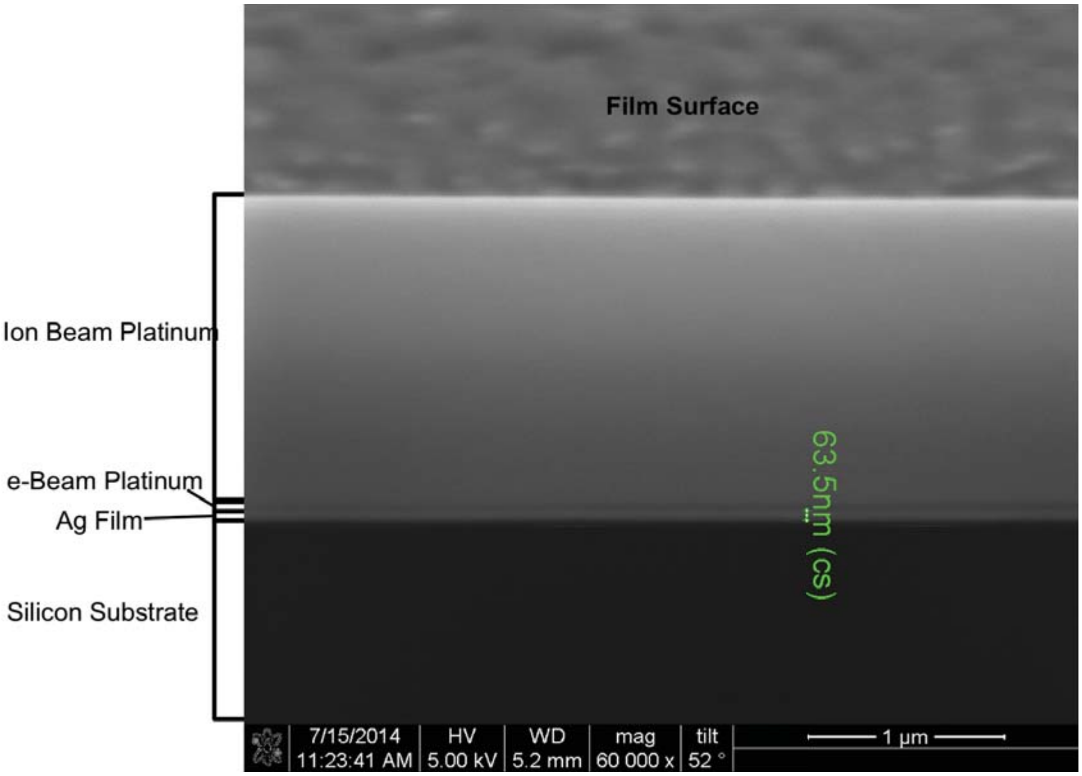

Figure 25. FIB cross-section of a Ag thin film on silicon deposited through electron beam evaporation and expected to be 50nm showing the approximate measured thickness of 60nm.

3.2.2.2 Annealing

Samples were annealed in a tube furnace at 200°C in a forming gas (95%N, 5%H) atmosphere at 100 standard cubic centimeters per minute (sccm). Thermal stabilization of the furnace was established 2 hours prior to sample insertion. Samples were placed face up into ceramic crucibles and loaded into the cold end of the furnace. The end cap was replaced and the tube furnace was purged with forming gas for 20 minutes prior to inserting the sample into the hot zone using a metal insertion rod. When annealing cycle was completed, the crucible was retracted into the cold end using the metal insertion rod and the sample/crucible pair was allowed to cool in the tube for 30 minutes under flowing forming gas prior to opening the furnace and removing the sample. Samples for the film uniformity study were annealed for 2 hours in order to investigate the early stage progression of hole formation during dewetting. For the microstructural evolution and capping layer effect studies, interrupted annealing experiments, a sample was annealed for 1, 1, 9, 18, and 36 hours in order to capture the onset and progression of relaxation behavior.

3.2.2.3 Microstructural Characterization

In order to evaluate the microstructural evolution of the stress relaxation and dewetting structures produced, several regions of the sample surface were monitored over time after continuous and interrupted annealing studies.

Two microscopy techniques were employed in order to analyze the microstructures accompanying silver thin film dewetting and stress relaxation. Following the same areas of the sample(s) using an FEI XL-40 Scanning Electron Microscope (SEM) and a Veeco Dimension 5000 Atomic Force Microscope (AFM), microstructural changes were monitored. All AFM scans were taken with Vistaprobes contact mode long cantilever tips with a spring constant of 0.2 N/m, and a resonant frequency of 12 kHz. Scans were taken in contact mode using scan rates at or below 0.8 Hertz (Hz) and collecting at least 640 samples per line. In the second study, a 200μm square grid array of Vickers hardness indents were used as fiduciary marks to aid in repeatedly locating and measuring the same regions. Impressions were made with a 25kg load and indents clearly depressed not only the film material but the silicon substrate as well. It should be noted that the indents did not appear to influence the formation or progression of relaxation structures during annealing experiments beyond the indent buildup at edges. Therefore all measurements were taken at least 1.5 μm away from indents. Details of the number of areas analyzed are presented below in the results section.

Two microstructure analysis software tools, Nanoscope v140r3sr3 and Image J 1.48v Analysis, were used to quantify changes in sample roughness, grain size, exposed substrate area, hillock area, film thickness and defect density.

3.2.2.4 Capping Layer

During SEM analysis of the films, a carbon-based, organic capping layer was deposited on to the silver thin film. The presence of the capping layer was validated through a combination X-ray Photoelectron Spectroscopy (XPS) and post-annealing SEM analysis. XPS is a microscopy technique used to measure the elemental composition of the first 8-10 nm of a sample surface.

XPS results indicated the presence of Silver (30%), Carbon (33%), Oxygen (12%), and Silicon (25%). Based on the assumption that our films are truly uniformly thick, and otherwise defect free, it can be assumed that we have a silicone contaminate (poly dimethylsiloxane, PDMS).

The presence and effect of the capping layer can be clearly seen in both the AFM and SEM after the sample has been annealed and the microstructures have begun to progress. AFM/SEM images showing the effect of the capping layer on the microstructure can be seen in Figures 26 and 27.

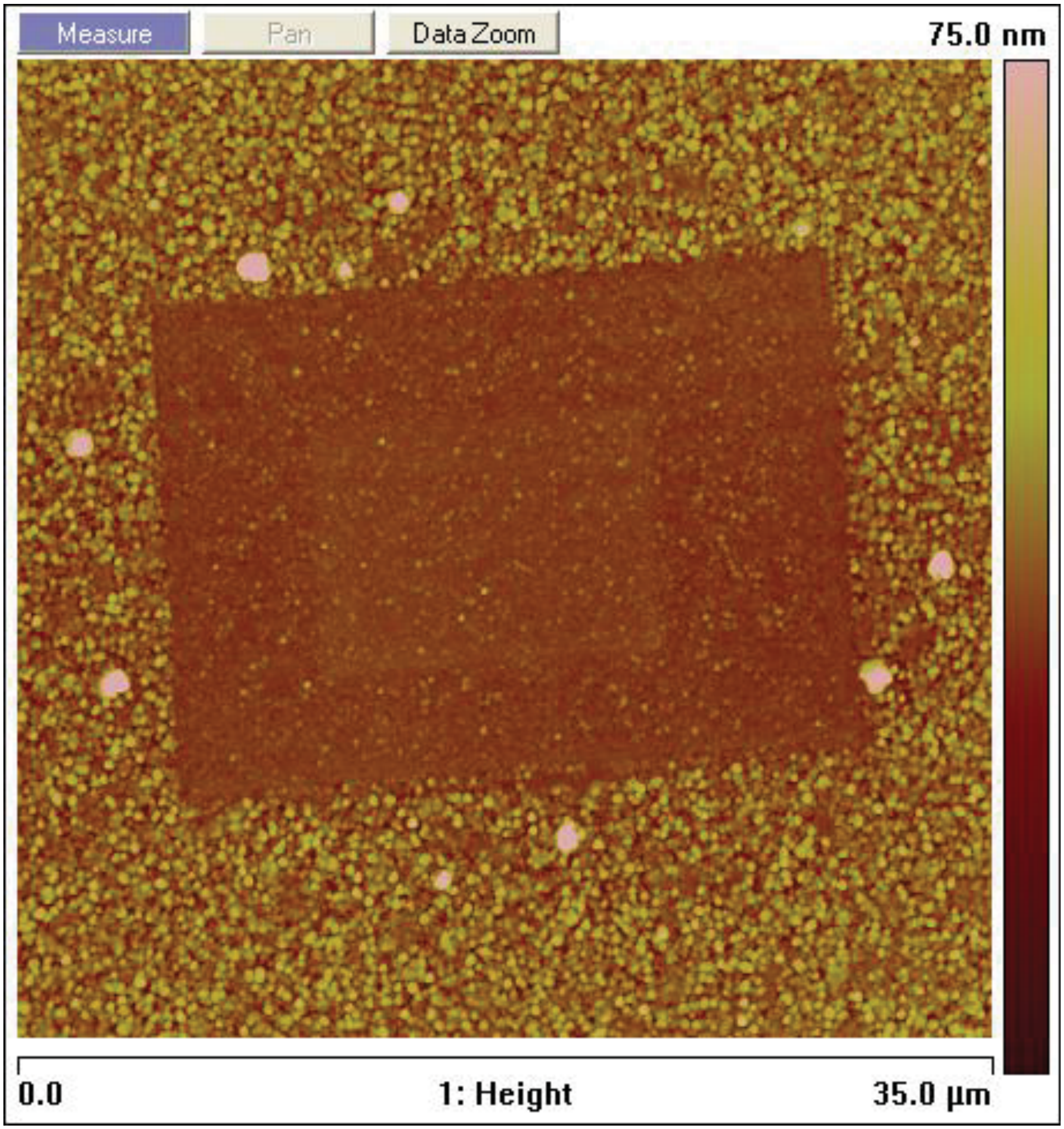

Figure 26. AFM scan of a region of silver film that was SEM'd prior to annealing showing the impact of the capping layer on the surface morphology.

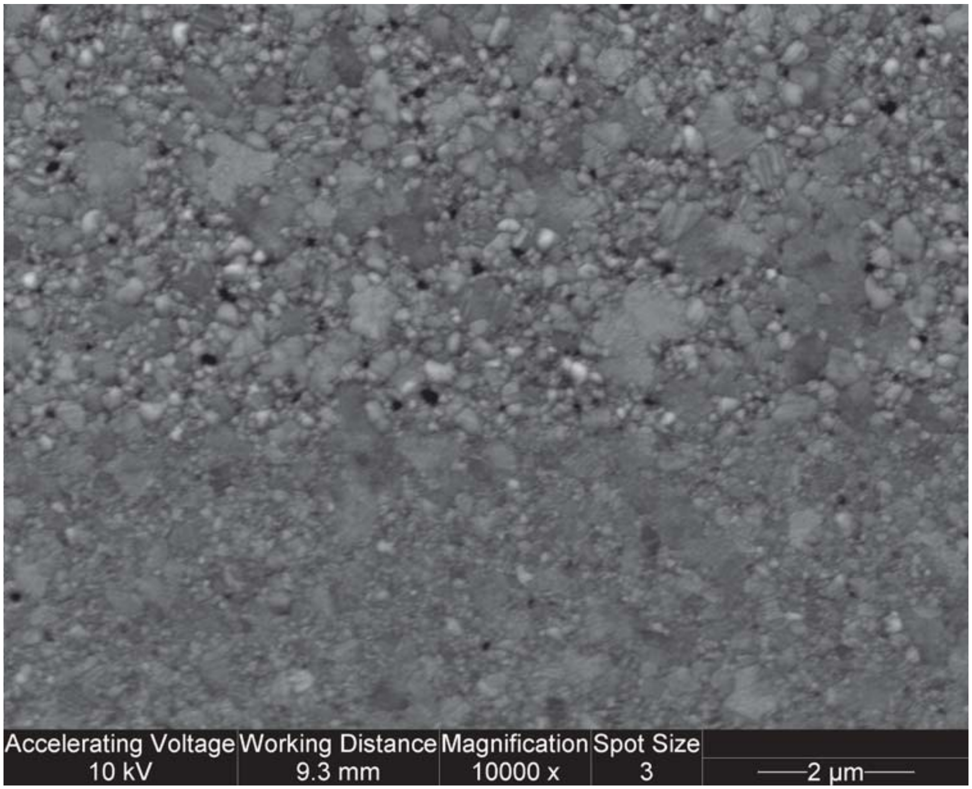

Figure 27. SEM micrograph of a region of silver film that was SEM'd prior to annealing (bottom ½ of the image) showing the impact of the capping layer on the surface morphology relative to non-capped regions (top ½ of the image).

The effect of the capping layer on the microstructure, its evolution and diffusion kinetics during dewetting of thin silver films is quantified within the scope of this dissertation. The results of dewetting with a capping layer are also compared to free surface dewetting without a capping layer.

3.3 Results and Discussion

3.3.1 Study 1: Film Non-Uniformity Effects on Dewetting

Microstructural characteristics of 50nm thick silver films thermally evaporated on (111) silicon were examined after being continuously annealed at 200°C in a forming gas atmosphere for 2 hours.

After annealing, grain growth, hole formation, dewetting, coarsening, faceting, and localized crystal growth out of the film plane were present to different degrees across the film surface. This broad variation in relaxation is clearly portrayed in the non-uniformity within and microstructural differences between the SEM images in Figure 28. These micrographs were taken at the same scale on the surface of the same sample that experienced the same annealing profile. From this image, it is apparent that the dewetting behavior is non-uniform and there are regions that exhibit drastically different defect densities, sizes, etc.

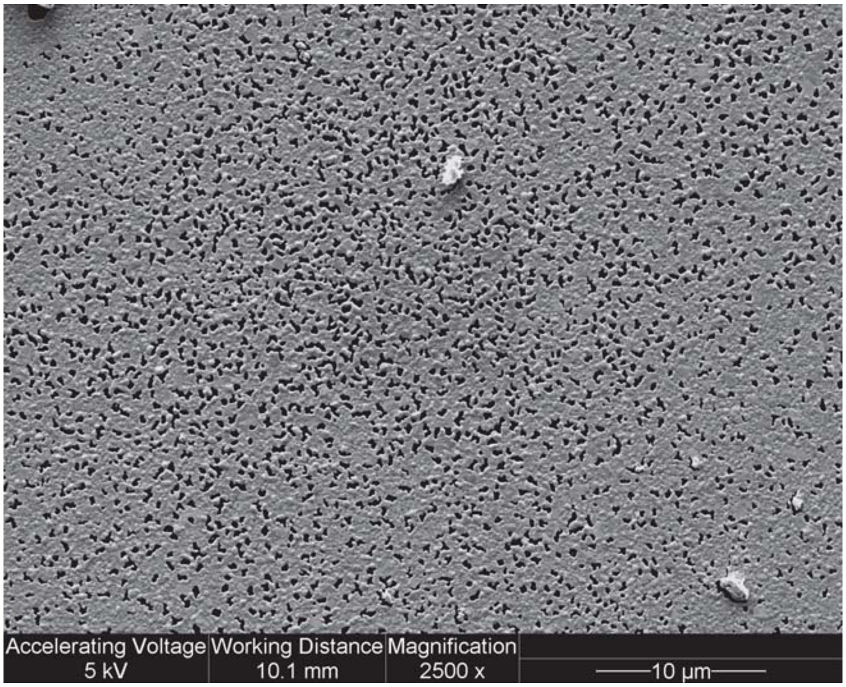

Figure 28. SEM micrograph of a 50nm thick silver film thermally evaporated on (111) silicon annealed at 200°C in a forming gas atmosphere for 2 hours showing the non-uniformity of dewetting behavior across the sample surface.

Upon closer investigation of the structures seen by SEM, there are 5 distinct dewetting regions and microstructures present within the overall film. Figure 29 shows a representative microstructure from each of these 5 defect regions. These five distinct regions re categorized as (1) a low density of small, isolated pinholes, (2) a higher frequency of larger holes of approximately the same size as the average grain size, (3) a solid state finger-like dewetting with multiple grains disappearing to form irregular holes, (4) rougher finger-like dewetting combined with hillock formation, or (5) more extensive finger-like dewetting with extensive hillock formation, few remaining small grains and with similar edge shapes of the irregular holes and the interconnected grains.

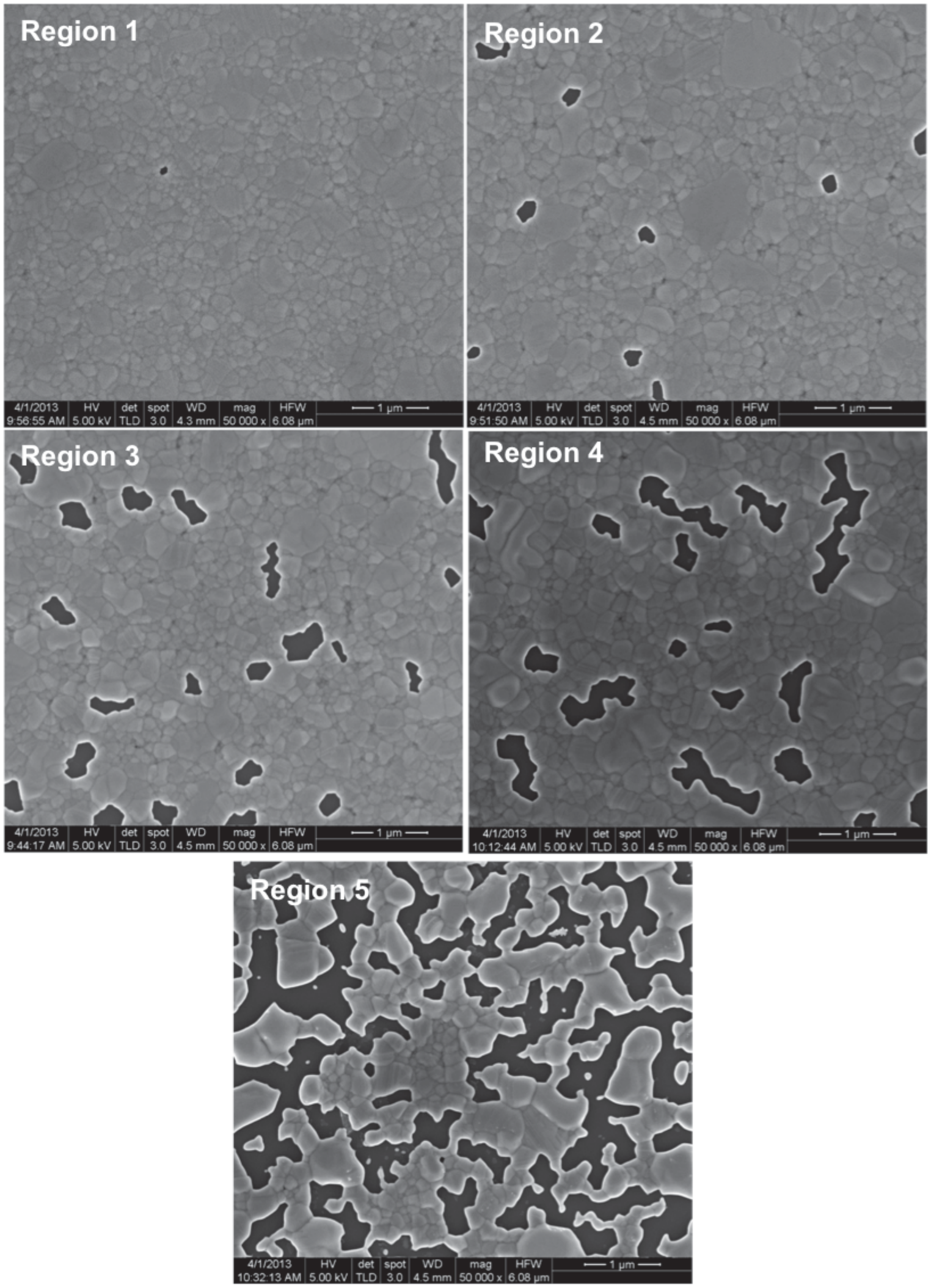

Figure 29. SEM micrographs showing the range of behavior as defined by five distinct regions showing (1) a low density of small, isolated pinholes, (2) a higher frequency of larger holes, (3) a solid state finger-like dewetting with multiple grains disappearing to form irregular holes, (4) rougher finger-like dewetting combined with hillock formation, and (5) extensive finger-like dewetting and hillock formation, with remaining small grains and some isolated island formation.

In order to quantify the extent of this variation, the hole density, (or number of separate regions where the substrate is exposed when the irregular holes connect), and average fraction of exposed substrate area were calculated. Measurements were acquired from all images taken within each region and averaged over the total area imaged for each region type. The results for average hole density and exposed substrate fraction can be seen in Figure 30. The extent of exposed substrate area ranges from zero to 30% and the average hole density ranges from 0.08 to 0.66 holes/μm^2. The plateau in hole density is due to holes impinging on each other creating fewer, larger holes in the microstructure. Holes in region 5 were so interconnected that it became difficult to accurately measure hole densities, therefore region 5 was not considered for the hole density evaluation.

The dewetting literature indicates that, for a film of constant thickness and annealing time, hole behavior across the sample surface should be relatively uniform. However, this film behaves more like a sample with variable thickness or annealing times. With uniform behavior, holes should progress as pin holes at triple junctions, followed by opening of the pinholes, formation of side branches (finger-like projections), and eventually a 2D interconnected network of exposed substrate.

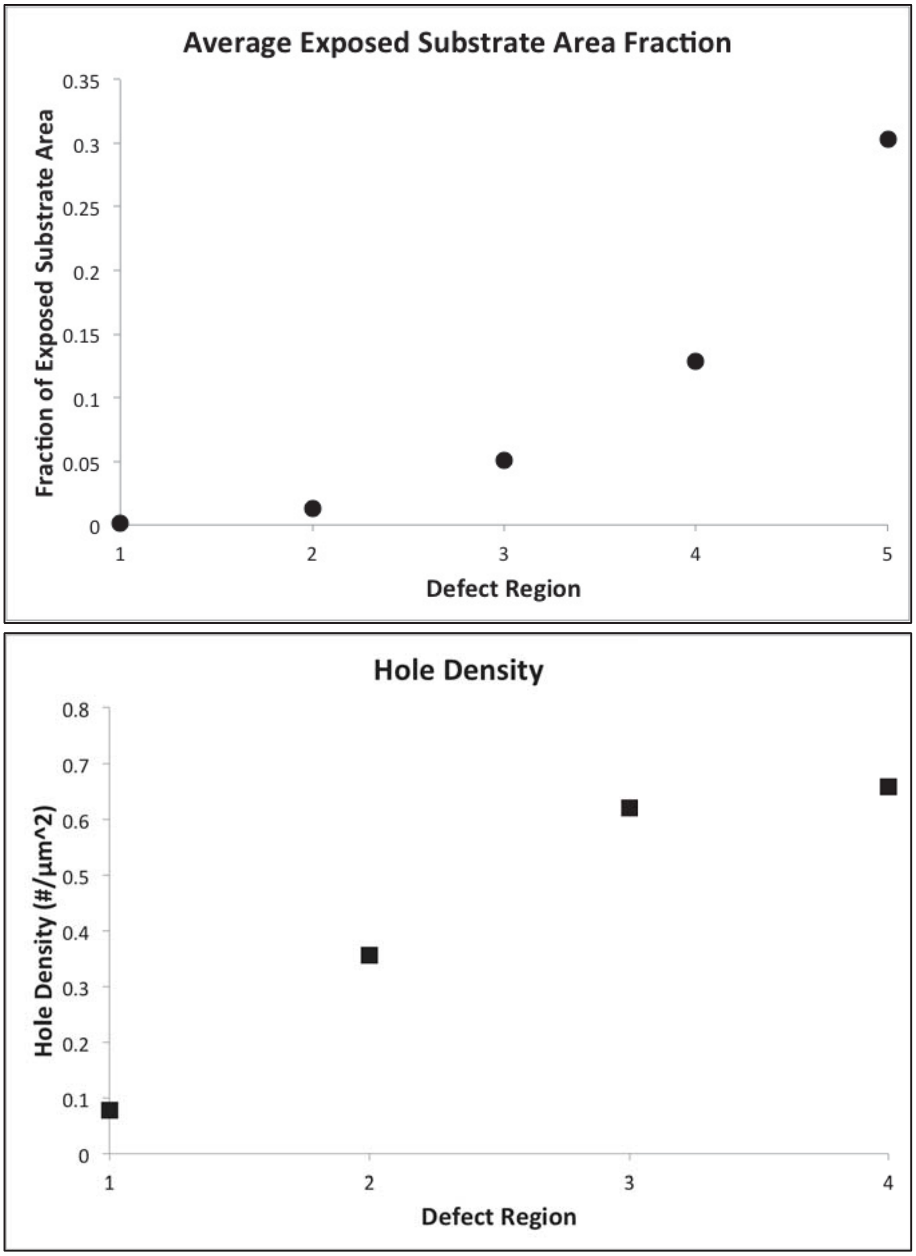

Figure 30. Average exposed substrate area fraction and hole density for the five distinct dewetting behavior regions.

Since these separate regions formed in a single sample after annealing, we hypothesized that the non-uniform behavior occurring within the 5 distinct defect regions for this experiment is associated with non-uniformities in the film structure created during deposition. Specifically, an inconsistent film thickness would result in regions that exhibit different amounts of exposed substrate and different stages of dewetting. Brandon and Bradshaw predicted film thickness and annealing time dependences on hole growth rates. The relationships as defined by Brandon and Bradshaw (Eqns. 11 and 12) show that void growth rate is proportional to 2/5 the power of time and -3/5 the power of film thickness for a single annealing temperature. [47] As seen in Figure 31, by comparing the apparent increase in exposed substrate area over different regions to the Brandon and Bradshaw models for thickness and annealing time dependence we can see that the exposed area spread matched both trends relatively well. It should be noted that the scale of the x-axis for either of these direct comparisons with time or thickness is unknown and therefore the relationships were simply scaled to provide data points that approximate the behaviors within the different defect regions.

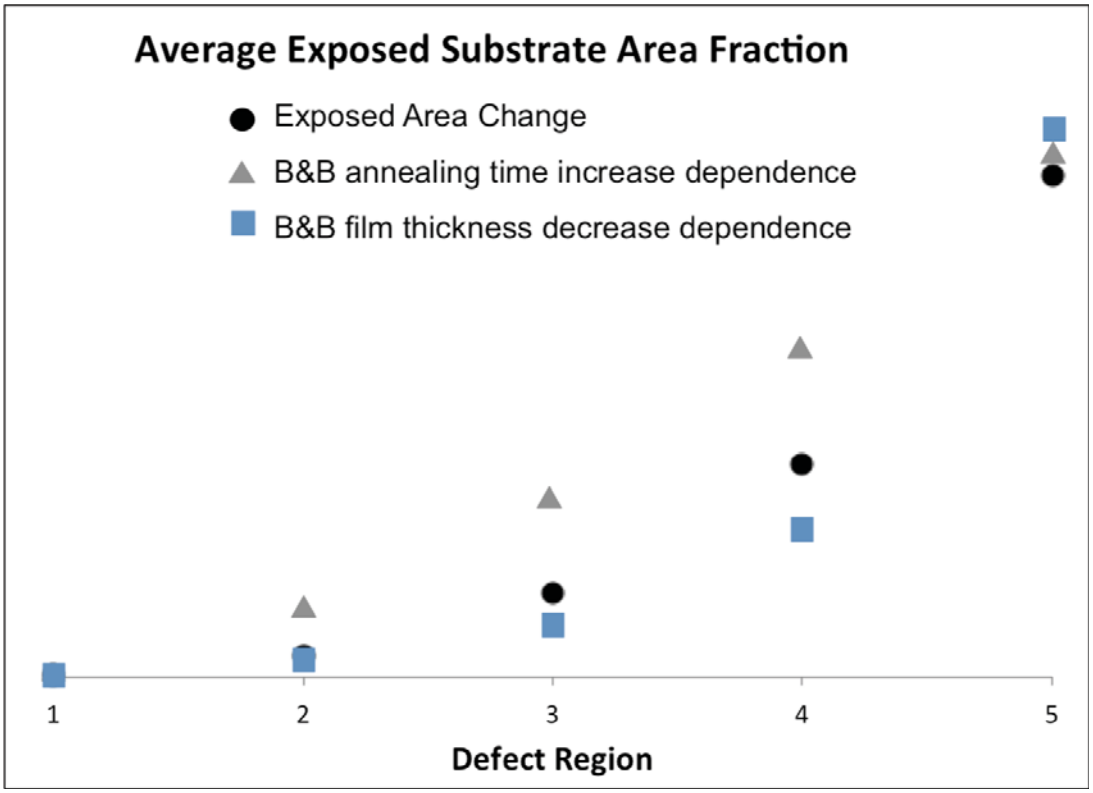

Figure 31. Average exposed substrate area in each defect region fitted with Brandon and Bradshaw's predicted dependencies on film thickness and annealing time showing that the experimental results fit closely with both.

Recall that this broad range of behavior that is non-uniform across the surface of the sample was unexpected. Typically, dewetting is described as a global phenomenon that behaves uniformly across a film subjected to consistent annealing parameters. However, the above comparison suggests one of three things, (1) the diffusion coefficient is constant and the distinct defect regions seen within this experiment varied in thickness (decreasing between Regions 1-5), (2) the diffusion coefficient is not uniform across the sample surface, or (3) the observed microstructure evolution is not controlled by surface diffusion. As previously mentioned, the nature of the deposition process used to produce this film may have produced non-uniform films and this comparison suggests that the deposition process did in fact produce a range of film thicknesses across the sample surface resulting in different dewetting behavior under uniform annealing conditions. However, under initial investigation of the as deposited films, no differences in the microstructure were visible across the surface of the film. This suggests that the variable thickness across the film surface is relatively minimal. A quantitative assessment of the expected film thickness based on the dewet areas associated with each region was calculated in order to determine the plausibility of thickness variation causing the broad range of behaviors in this sample.

Using the relationship Brandon and Bradshaw developed between hole radius and time as shown in Equation 18

$$D_s = \frac{2}{5}\frac{r^{\frac{5}{2}}h^{\frac{3}{2}}k_B T}{\pi^{\frac{1}{2}}t\gamma\omega^2\upsilon} \qquad \text{Equation 18}$$

where r is the hole radius, h=50nm, T=473.15 K, $\gamma=1.2\text{x}10^{-5}$ Jcm^{-2} [62], $\omega = 1.7\text{x}10^{-23}$ cm^3 (from FCC lattice parameter), and $v=1.5\text{x}10^{15}\text{cm}^{-2}$ [63]. The effect of film thickness or changing diffusion coefficients on the silver surface diffusion coefficient can be back calculated using the SEM image data. Assuming a uniform diffusion coefficient (correlating to a 50nm film thickness) for each of the 5 distinct defect regions, the film thickness variation needed to produce the structures seen in the SEM images can be calculated from the average hole radii.

The calculated thicknesses for each Region, 1-5, were used to better understand which region(s) correlate to the desired 50nm thickness. The correlating film thickness values and changes are detailed in Table 11. Assuming that Region 1 represented a region with 50nm thickness, the film coverage ranges from 1.7nm to 50nm. At 1.7nm the film would not be likely to completely cover the sample surface. Due to the previously described investigation of the as deposited film surface, we know this is not the case and therefore is scenario not representative. Similarly, while the thermal evaporation process used is expected to be slightly non-uniform due to the experimental set-up, thickness variations ranging from 200nm to 1µm are physically unreasonable, especially when considering that under initial investigation the sample surface did not exhibit any visible variations in starting microstructure.

Table 11. Calculated film thicknesses assuming the diffusion coefficients calculated and detailed in Table 11 for Regions 1-5

	Thickness (nm)				
Region 1	50.00	208.23	387.15	689.40	1489.99
Region 2	12.01	50.00	92.96	165.54	357.78
Region 3	6.46	26.89	50.00	89.04	192.43
Region 4	3.63	15.10	28.08	50.00	108.06
Region 5	1.68	6.99	12.99	23.13	50.00

The second possibility is that the diffusion coefficient is not uniform across the sample. Table 12 contains the range of calculated diffusion coefficients calculated when assuming each region is 50nm in film thickness, these values range from 6.3×10^{-9} to 1×10^{-6} cm^2/s. This range in diffusion coefficient data was not expected, as the diffusion coefficient is a constant in the Brandon and Bradshaw dewetting model. Historically, this diffusion limited kinetic model has been assumed to be representative of the dewetting kinetics for thin silver films. However, if the system fit the proposed Brandon and Bradshaw model, the calculated diffusion coefficient would remain constant across the sample surface. The calculated range in effective diffusion coefficient data indicates that for a uniform film thickness and annealing parameters, the diffusion behavior would have to vary 3 orders of magnitude across the sample surface in order to produce the range of structures seen throughout Regions 1-5. While mild changes in diffusion coefficient are likely across a sample surface, as the local structure and texture will influence atomic diffusion, a 3 order of magnitude range suggests that other factors are influencing the diffusion kinetics.

Table 12. Calculated diffusion coefficients assuming a 50nm thick film for each of the representative microstructures from Regions 1-5

	Diff. Coeff (cm2/s)
Region 1	6.33E-09
Region 2	5.38E-08
Region 3	1.36E-07
Region 4	3.24E-07
Region 5	1.03E-06

There are limited models of hole and hillock growth kinetics and behavior in the literature and a broad range of reported values for surface diffusion coefficients in silver ranging from 10^{-9} – 10^{-5} m^2/s at or near the temperature range of interest. It should be noted that there is limited literature available for surface self-diffusion coefficients of Ag, however, the values calculated from fitting our experimental data to Brandon and Bradshaw's proposed model, do fall within or near the large, 4 order of magnitude range, found within the literature for temperatures on the order of 200-250°C.

The results of this assessment make it clear that the non-uniformity in dewetting behavior for this experiment is not directly related to inconsistencies in film thickness. It should be noted that while the diffusion coefficient values calculated from this experiment falls within the known value range. This does not validate that surface diffusion is the key mechanism behind hole and hillock growth kinetics. Other factors are likely influencing the diffusion during relaxation. In fact, the broad range of diffusion coefficients calculated for the same experimental parameters suggests that Brandon and Bradshaw's surface diffusion limited based model does not address all of the influencing factors on dewetting kinetics. Specifically, the presence of interface-limited kinetics has been evident though the experiments within the scope of this thesis. The influence of interface-limited kinetics could also explain the non-uniform behavior present in this and subsequent experiments. Interface-limited kinetics don't proceed in the same uniform way that diffusion-limited kinetics would progress. Instead of system progression being limited by the speed that material can arrive at a sink, the system progression is limited by the availability of attachment sites at the sources or the sinks (at the free surfaces). This factor is likely influencing both the hole and hillock growth in the system of interest. The effects of this on calculations throughout literature and in determining kinetics for the system of interest will be discussed in more detail in the subsequent sections within this chapter of the dissertation.

3.3.1.1 Study 2: Capping Layer Effects on Dewetting

In order to investigate local changes in microstructure, holes that developed within regions with a capping layer were tracked between each anneal. The specific regions followed over time were selected from SEM images after all annealing was complete.

The starting microstructure after film deposition appeared uniform in surface structure containing no visible grain boundary grooves or holes. An SEM micrograph of the starting film structure can be seen in Figure 32. There are some large grains on the order of 1μm surrounded by regions where the grain size is indeterminable. There is a visible surface roughness across the film on the order of 10nm (quantified via AFM).

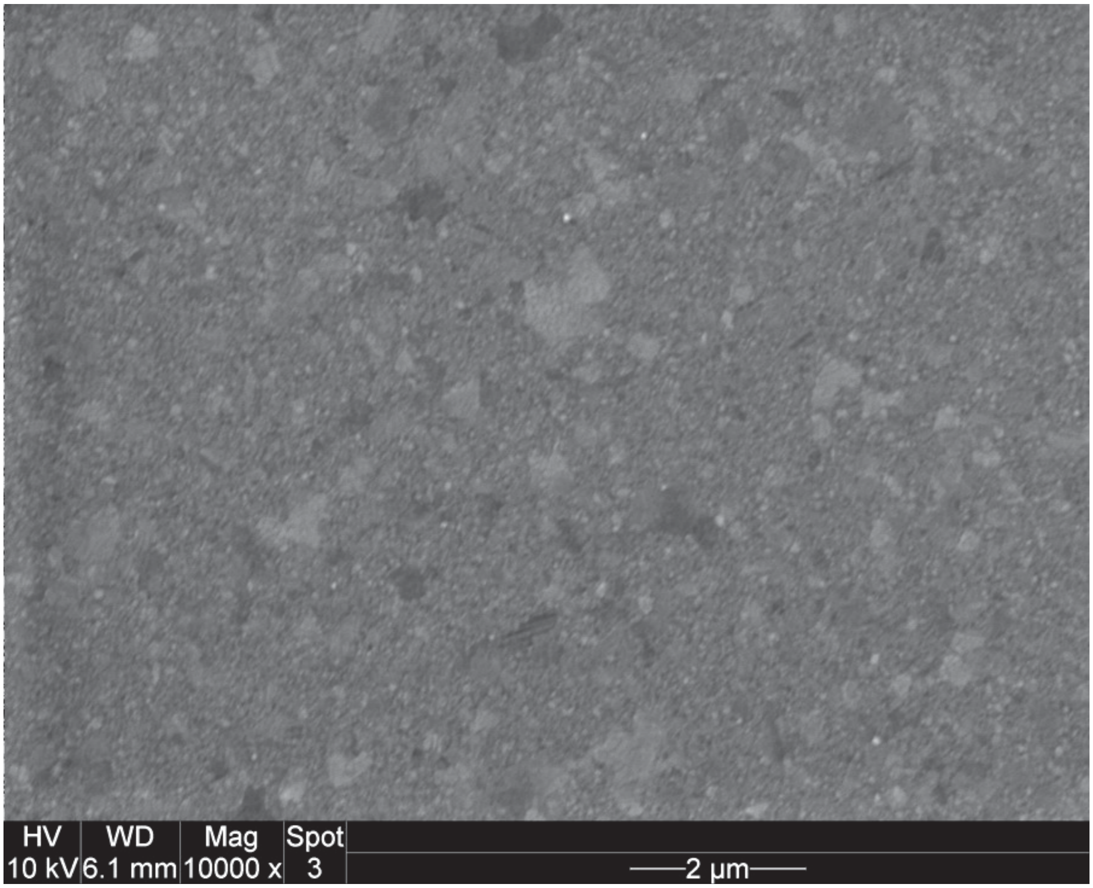

Figure 32. SEM micrograph showing a representative as-deposited microstructure for a 50nm Ag film.

After annealing, the microstructure exhibited grain boundary grooving, grain growth, and hole formation. As the interrupted annealing study progresses and the sample is annealed for longer times the details of these features (size and shape) change. Initial investigation the microstructural evolution was evaluated via SEM imaging.

3.3.1.1.1 Microstructural Investigation - SEM

In order to quantify the growth of holes during the series of anneals, the holes within each of these grain regions are investigated more closely. Visual inspection of the SEM microstructures also revealed the existence of 3 hole types: holes present between individual grains (10-50nm in diameter), holes on the order of the hillock grain size (250-300nm in diameter) that may or may not grow during subsequent anneals, and holes that formed after the 18-hour anneal from regions that previously contained visible grains. For the purposes of this study, 15 holes on the order of hillock size and 10 holes formed after the 18-hour anneal were selected for investigation. All holes were selected based on visibility within the 5 annealed microstructures. A representative location showing the microstructural progression between the first 1-hour anneal and the 36-hour anneal can be seen in Figure 33. From left to right, the image highlights an example of a hole formed after the 18 hour anneal, a hole present after 1 hour that did not grow with subsequent anneals and a hole present after 1 hour that grew with subsequent annealing.

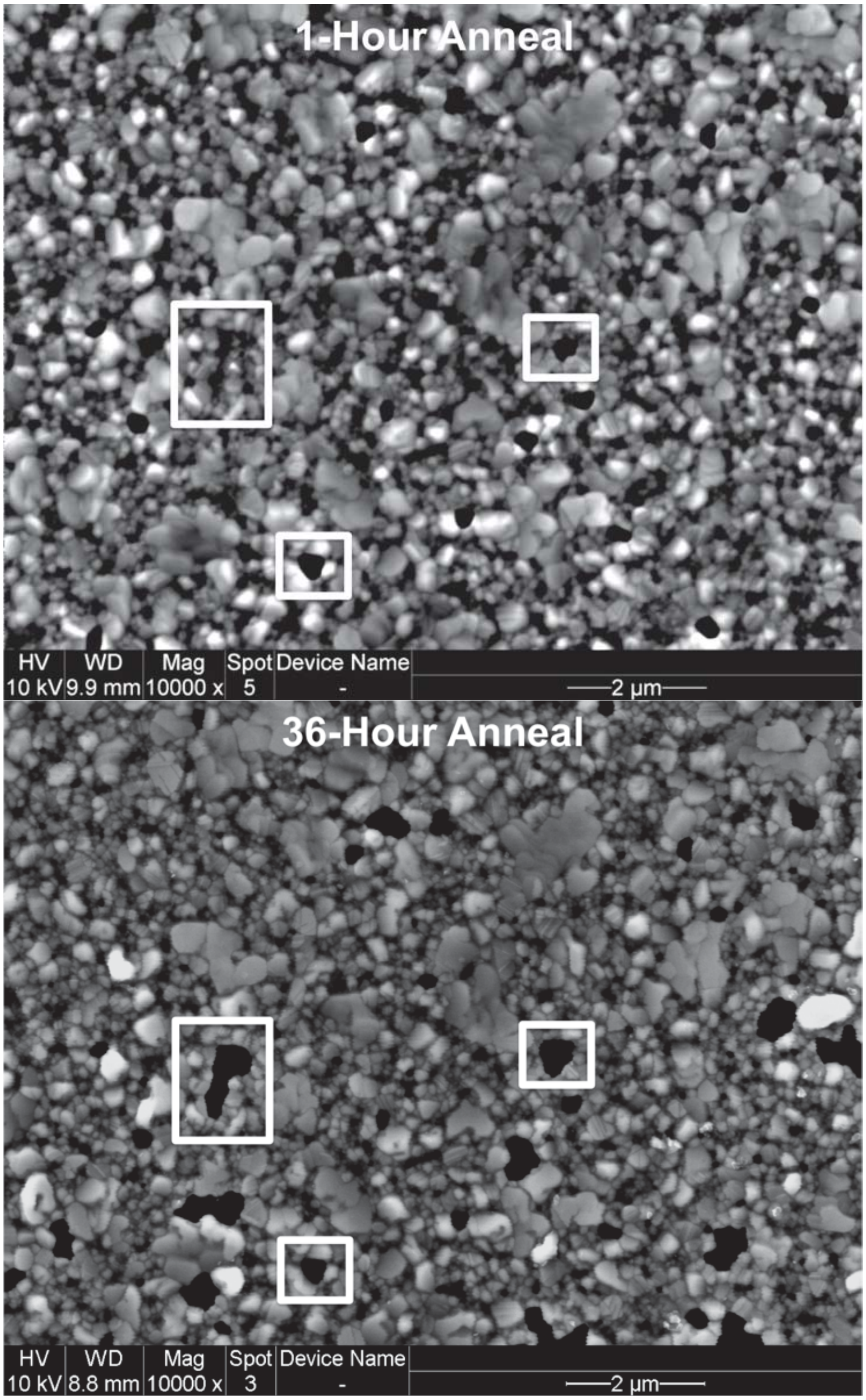

Figure 33. SEM micrographs showing changes in three types of holes formed during annealing. Left to right: a hole formed after the 18 hour anneal, a hole present after 1 hour that did not grow with subsequent anneals and a hole present after 1 hour that grew with subsequent annealing.

In order to better understand the changes in the microstructure, beyond just the formation and growth of holes, magnified regions of a representative microstructure after 1, 9, and 18 hour anneals can be seen in Figure 34. In this region, it appears that the larger holes present after the 1-hour anneal exhibit little to no visible change during annealing. However, there are regions where large hoes form after the 18-hour anneal. These regions appear to contain very fine grains that may or may not have holes between them that penetrate through the thickness of the film. Along with this, there appears to be little to no visible grain growth after any of the annealing experiments. This assessment is very localized and region specific but as seen in Figure 34 the microstructures of interest are complicated and contain a wide variety of grain shapes, grain sizes, hole shapes, hole sizes, and other microstructural features such as faceting, twinning, grain boundary grooving, and what appears to be single-grain localized height increases. However, the details of these changes are difficult to track using SEM imaging because the resolution of the details, especially hole and boundary details, is dependent on the imaging parameters and contrast. Another factor of key here is that some grains appear to be growing out of plane based on the contrast (brightness increase). However, this is not a quantifiable measurement of any height change. Because of the dependence of SEM imaging on contrast resolution and the inability to quantify some of the visible changes via SEM, AFM analysis was pursued as a complementary analysis technique.

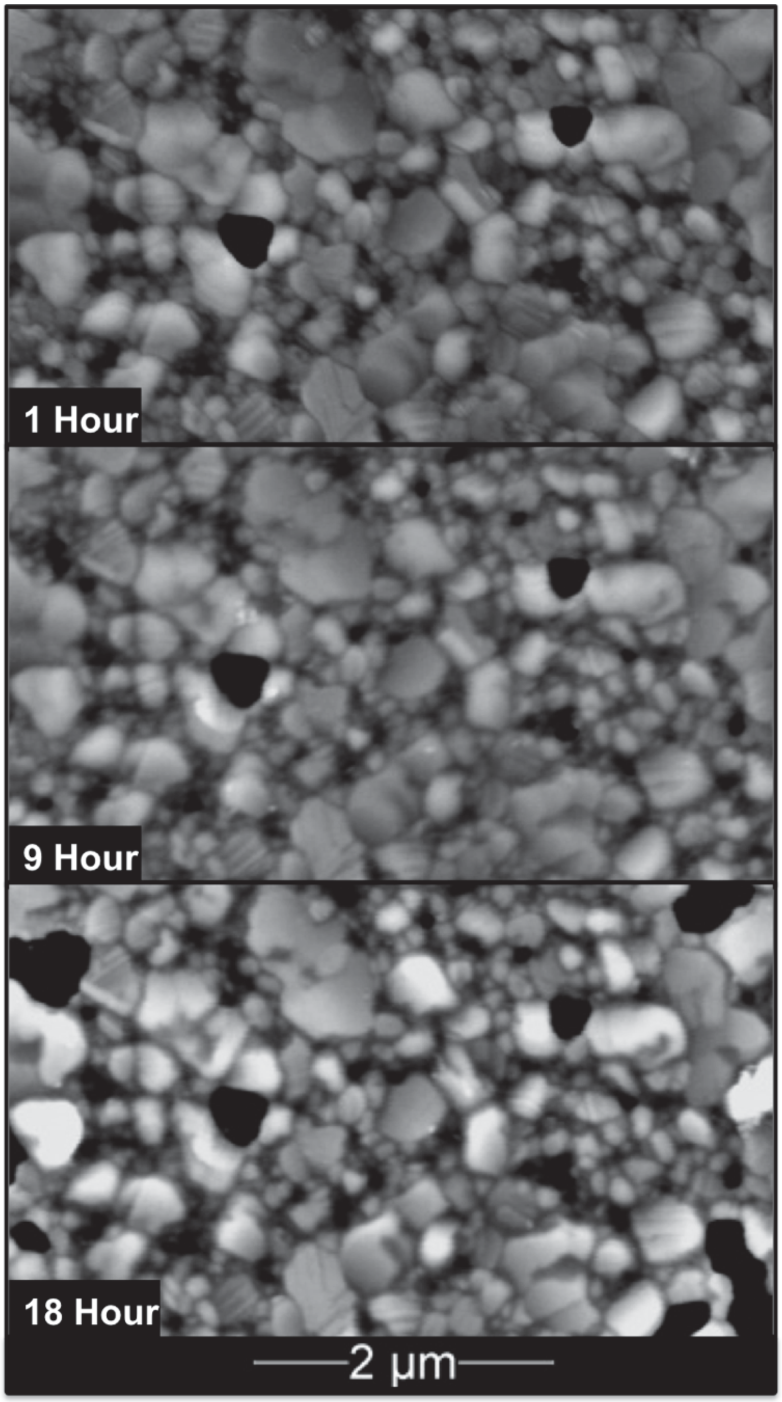

Figure 34. SEM micrographs showing the a wide variety of grain shapes, grain sizes, hole shapes, hole sizes, and other microstructural features such as faceting, twinning, grain boundary grooving, and what appears to be single-grain localized height increases that occur and change over the annealing study.

3.3.1.1.2 SEM Capping Layer Hole Tracking

In order to quantify the growth of holes that occurred during annealing in the capped regions the ImageJ Particle Analysis tool was used to measure the area of exposed substrate for each hole. The change in hole area was tracked after each anneal in order to determine size change and rate of change for hole growth. An example of the progression of a single hole can be seen in Figure 35. It should be noted that these measurements are based on the assumption that the contrast difference visible within the SEM microstructures are representative of the film depth. This assumes that the darkest image locations have either reached the substrate or are deep grain boundary grooves. In order to determine the area of a single hole after each anneal, SEM images were cropped, the threshold tool was used to eliminate pixels above the threshold (assumed to represent the substrate or grain boundary groove), and the particle analysis tool was used to trace and measure the area of the holes. It is important to note that the imaging parameters for each SEM micrograph will influence the details of the stigmation, brightness and contrast for these regions and interest. These factors can influence both the depth assessment and shape of features. Therefore, there is some human error associated with determining the threshold level for each image. This influence of these factors can be seen in the boundaries of the of the holes within both the thresholded image and the hole traces.

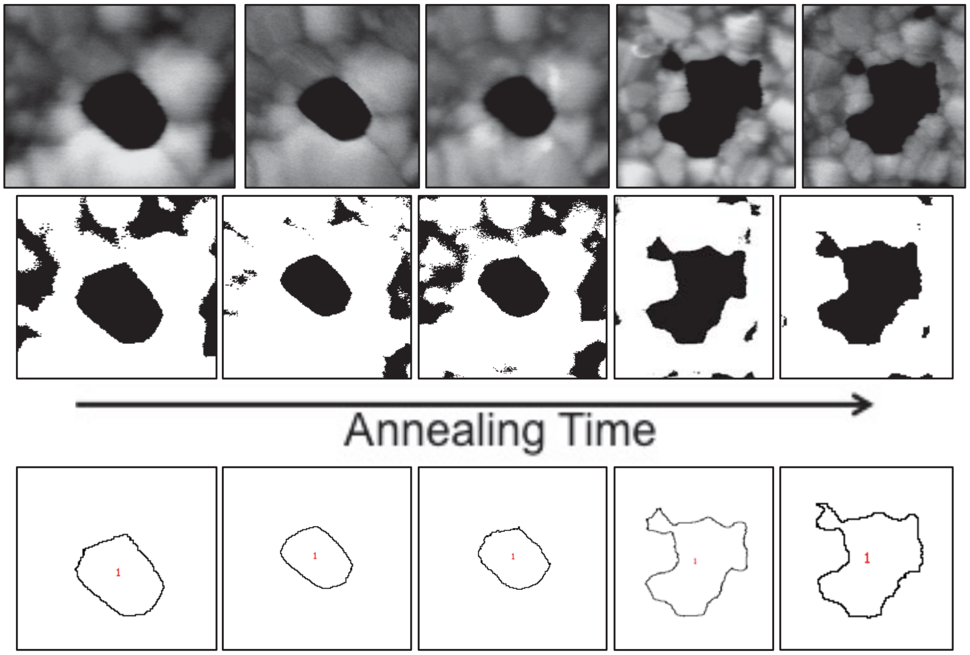

Figure 35. An example of the SEM micrographs, black/white thresholded images, and associated hole traces used to track the area change of holes after each annealing experiment.

Three regions that were subject to capping layer effects were tracked with both AFM and SEM between annealing experiments. Using the progression of SEM images over the series of annealing experiments. As previously described, individual holes were tracked in order to determine changes in exposed substrate over time. The behavior of these individual holes is summarized in Figure 36. While only 2 distinct behaviors are visible if holes are tracked from 1-hour to 36-hour anneals, visual inspection of the SEM microstructures reveals the existence of a third hole type: holes that formed between the 9-hour and 18-hour anneals from regions that previously contained visible grains. Therefore, there are three distinct hole types: holes that remain approximately the same size after subsequent anneals, holes that increase in area after the 18 hour anneal, and holes that appear after the 18 hour anneal from regions previously containing grains. These different hole types can be clearly seen in the plots of individual hole area in Figure 36.

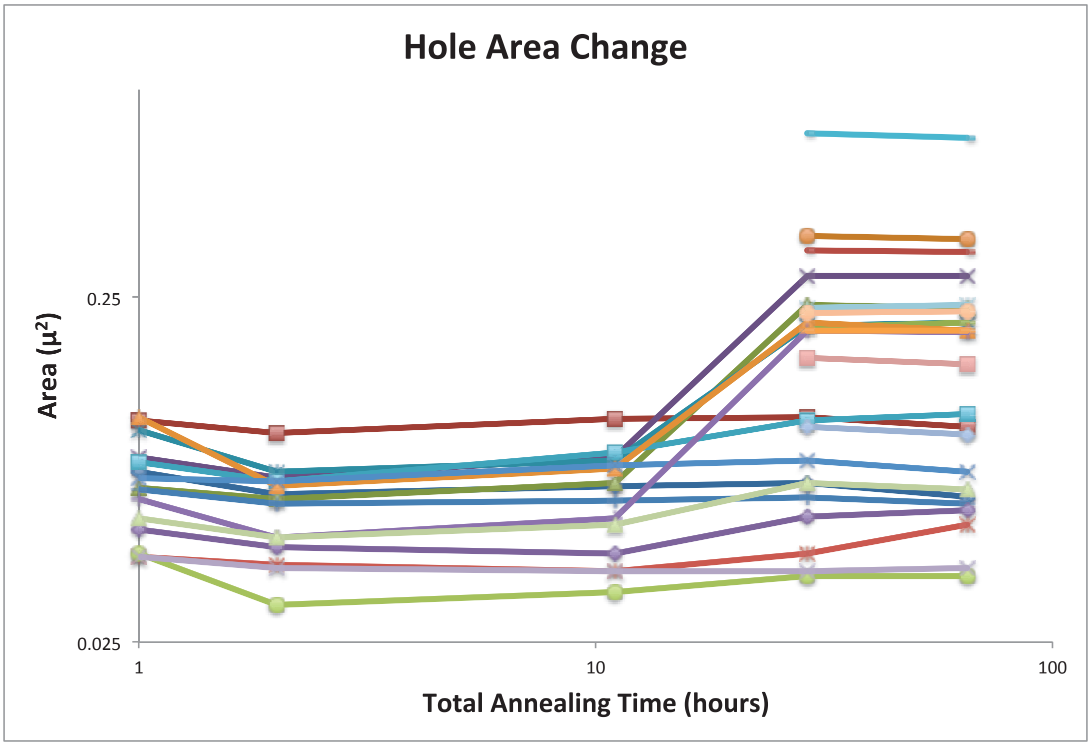

Figure 36. Plot of the hole area change after each annealing experiment for holes present after the first anneal and holes that formed after the 18-hour anneal showing three distinct behaviors (1) no hole area change, (2) hole area increase after the 18-hour anneal, and (3) hole formation after the 18 hour anneal.

As previously mentioned and clearly seen within the hole area tracking data, there are some holes that form after the 18-hour anneal (29 total hours of annealing) from regions that did not exhibit visible hole formation after prior anneals. An example of this hole type can be seen in Figure 37. This image set shows a late forming hole microstructure overlaid over the pre-existing microstructure. This pairing and overlay of microstructures after the 1-hour and

36-hour anneals shows a representative structure change for one of the late-forming holes described.

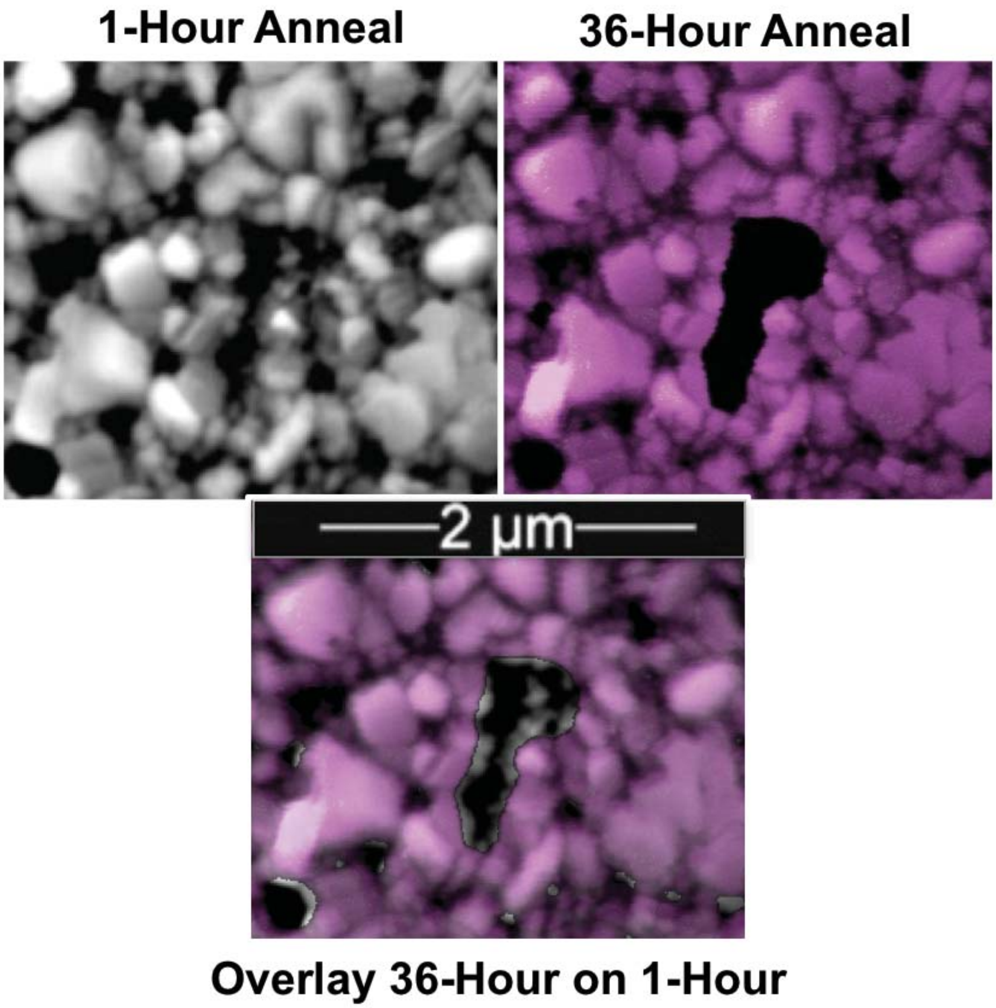

Figure 37. SEM micrographs after the 1-hour and 36-hour anneal for a hole that formed late in the annealing progression and the overlay of hole areas showing the grains and film material that were removed to form the hole.

3.3.1.1.3 Capped Region Hole Growth Analysis

Using the same image thresholding technique used to track hole area change for individual holes, the overall changes in hole area and hole density for each of the capped regions were assessed from SEM images of the second 1-hour anneal, 9-hour anneal, 18-hour anneal and 36-hour anneal. The data for each location after each anneal can be seen in Figure 38. The hole density for Location 1 and Location 2 decrease after every anneal, with the greatest decrease for both locations occurring after the 36-hour anneal. This decrease in hole density makes physical sense because we expect small holes to grow and eventually coalesce to form fewer, larger, holes as annealing progresses.

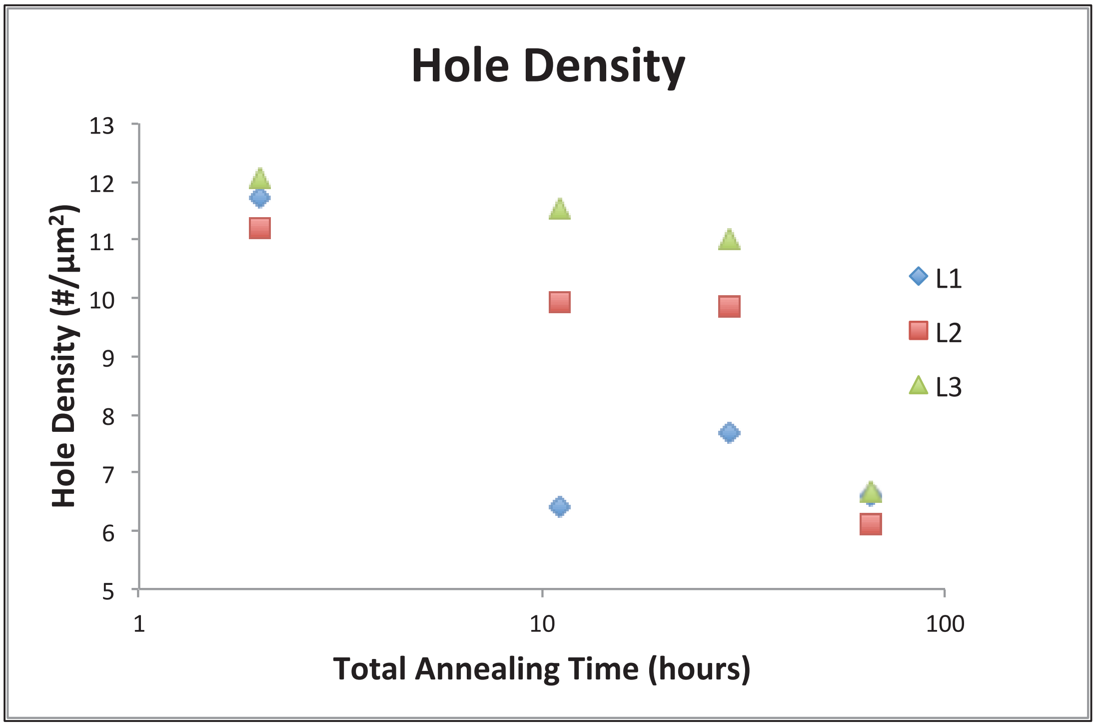

Figure 38. Plot of hole density after each anneal for Locations 1-3 (capping layer regions) showing the decrease in hole density as annealing time increases.

The hole density changes for capping layer regions were also averaged in order to provide a more global assessment of the behavior. The average hole densities, as determined by the local densities from Locations 1-3 can be seen in Figure 39.

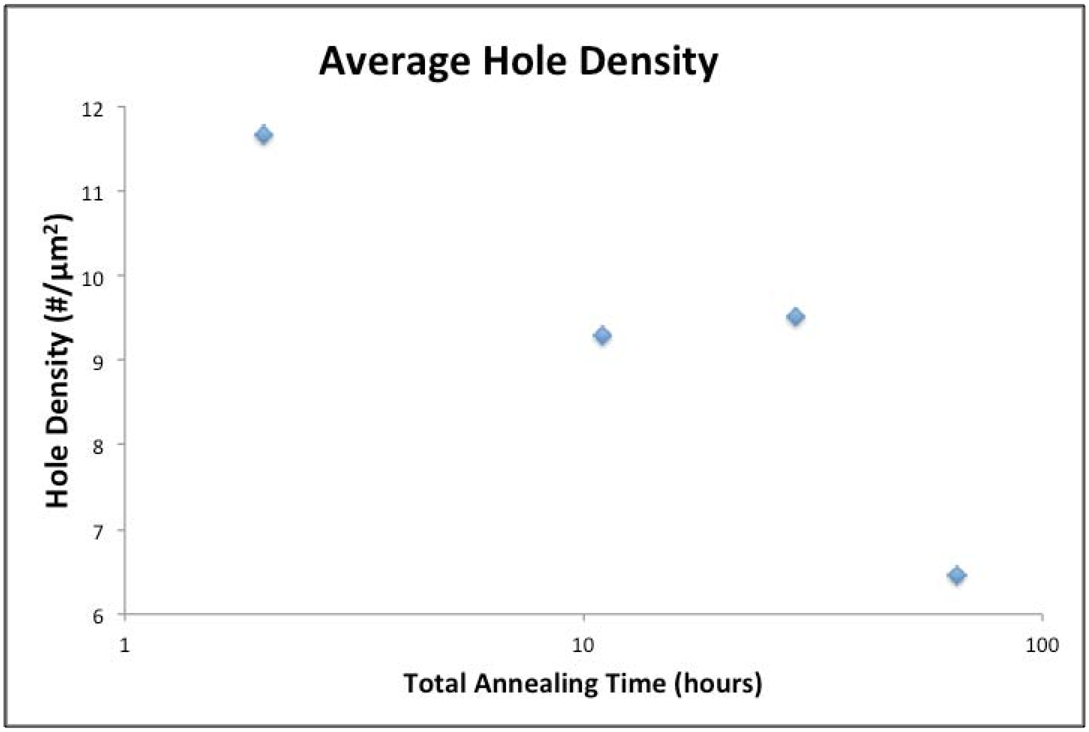

Figure 39. Plot of the average hole density after each anneal for Locations 1-3 (capping layer regions) showing the hole density decreasing with increasing annealing time.

Along with the hole density, changes in exposed substrate (or hole) area were also quantified. The hole area for each location is detailed in Figure 40. The hole area fraction within these regions is expected to increase with increasing annealing time. However, the data shows that all locations exhibit a large decrease after the 9 hour anneal and two of the studied locations also show an area decrease after the 36-hour anneal. While these decreases are not expected, they are representative of the images taken. Possible sources of error in the assessment technique are described at the end of this section.

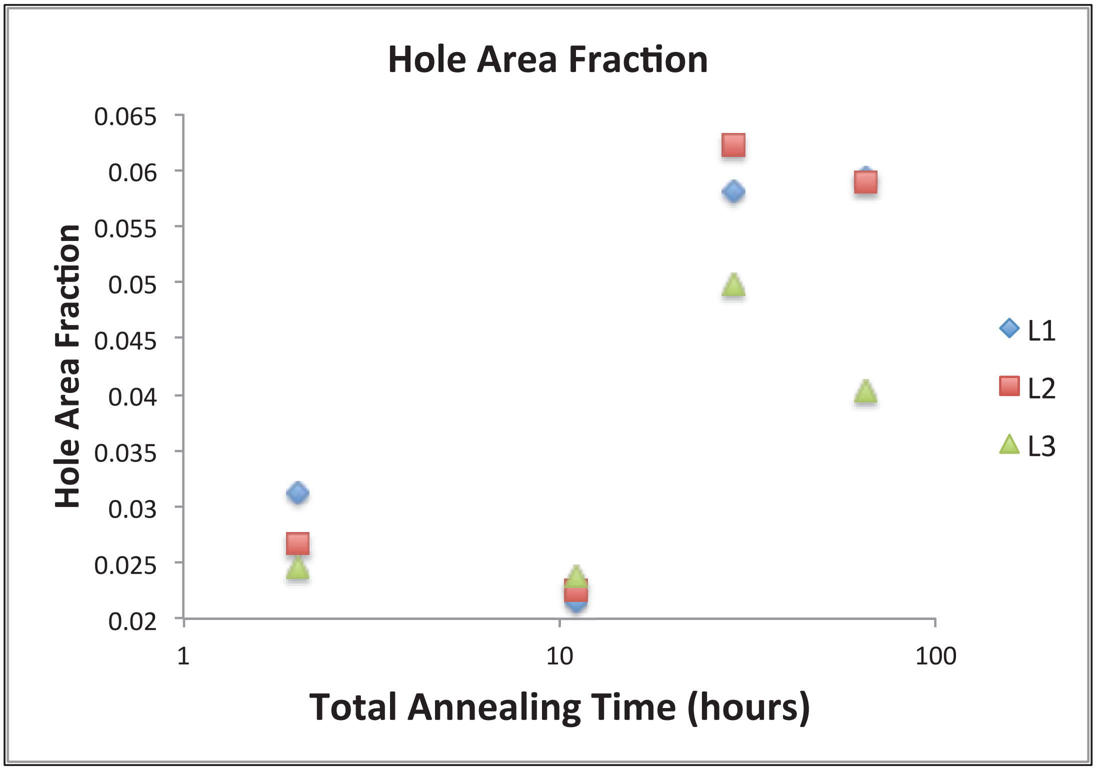

Figure 40. Plot of hole area fraction after each anneal for Locations 1-3 (capping layer regions) showing the overall increase in hole area fraction as annealing time increases

Along with the individual location data, the average hole area fractions from these three locations were determined in order to assess the overall behavior at a more global level of assessment. As with the individual data, the sample appears to experience a large decrease in the hole area fraction after the 9-hour anneal. But the overall trend of the hole area fraction with annealing time is increasing.

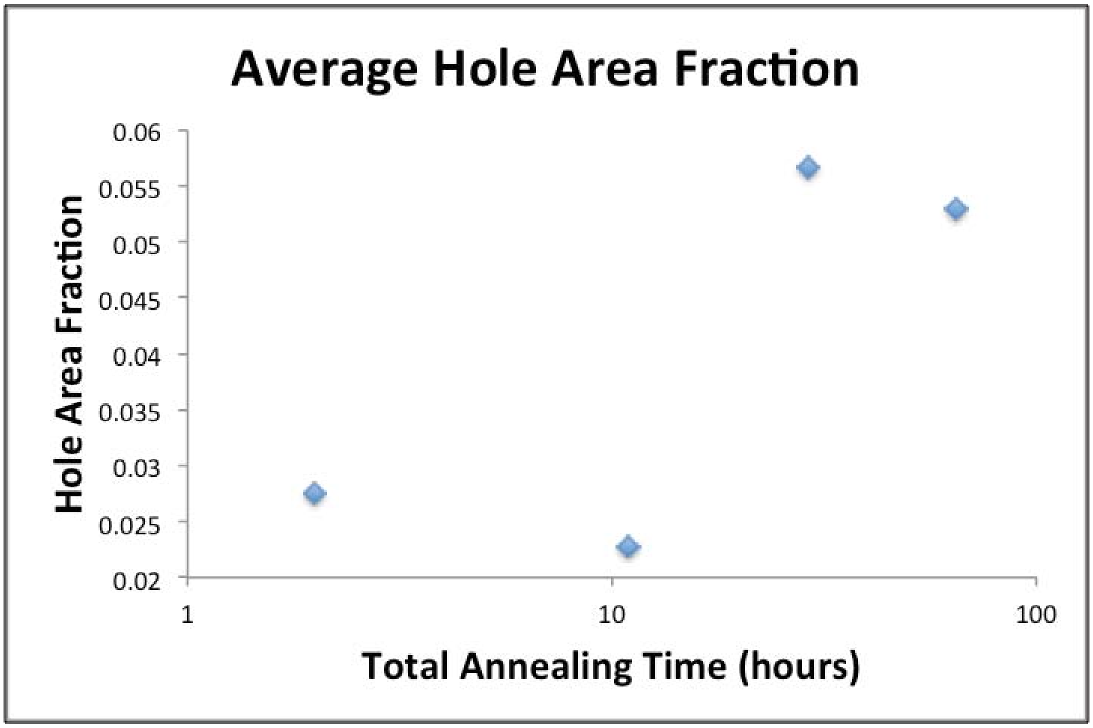

Figure 41. Plot of the average hole area fraction after each anneal for Locations 1-3 (capping layer regions) showing the hole area fraction increasing with increasing annealing time.

As previously mentioned, the hole growth rate is not expected to be linear, instead, Brandon and Bradshaw predicted a hole growth rate that correlates to 2/5 the power of time. However, this value was also calculated based on experiments that did not undergo any diffusion suppression or capping layer influences.

As with the individual hole tracking assessment, it is important to note that the imaging parameters for each SEM micrograph will influence the details of the stigmation, brightness and contrast for these regions of interest. These factors can influence both the depth assessment and shape of features, as well as with the operator determining the threshold level for each image. This influence of these factors can be seen in the boundaries of the holes within both the thresholded image and the hole traces. Similarly, the goal of each SEM assessment was to image the same area. However, there was some slight variation in the regions assessed. The influence of the imaging parameters could have greatly impacted the assessment. Figure 42 contains the images taken for each location after each anneal in order to more clearly depict the possible sources of error.

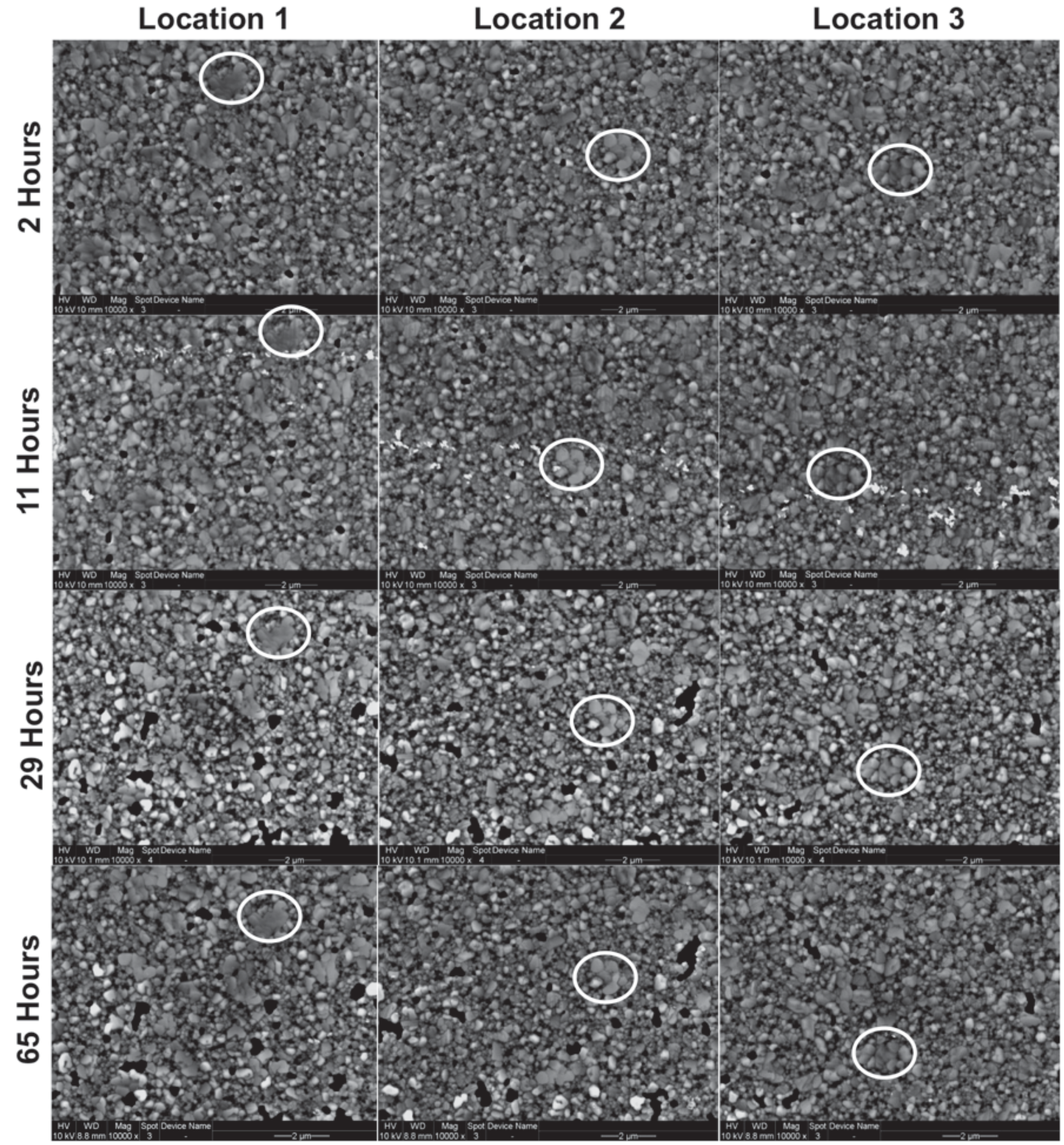

Figure 42. SEM micrographs of each location (1-3) after each anneal showing the changes in microstructure and the variation in sample area used for each assessment.

3.3.1.1.4 Capped Layer Roughness Analysis

Capped regions were also investigated using AFM in order to better quantify the microstructural evolution during the interrupted annealing experiments. Example images from the progression of annealing studies can be seen in Figure 43. These images are displayed with the same height scale, ranging from -150nm to 150nm, this allows for a comparison of the relative height change with increased annealing time. It is apparent that the film area surrounding the capped region is developing much taller also larger diameter features than within the capped regions. It is also apparent that in the upper right hand corner of the capped regions the behavior is different than in the remainder of the capped regions. AFM scans of each location were taken at a variety of size scales after each anneal. Of key importance here is that all of the AFM scans that were used to track the border between the capped and un-capped regions were taken in the upper right-hand corner of each location. Therefore, it is apparent that the AFM scanning influenced the behavior in these regions. This phenomenon is likely due to the tip is removing some of the capping layer during scanning and creating diffusion channels for material transport.

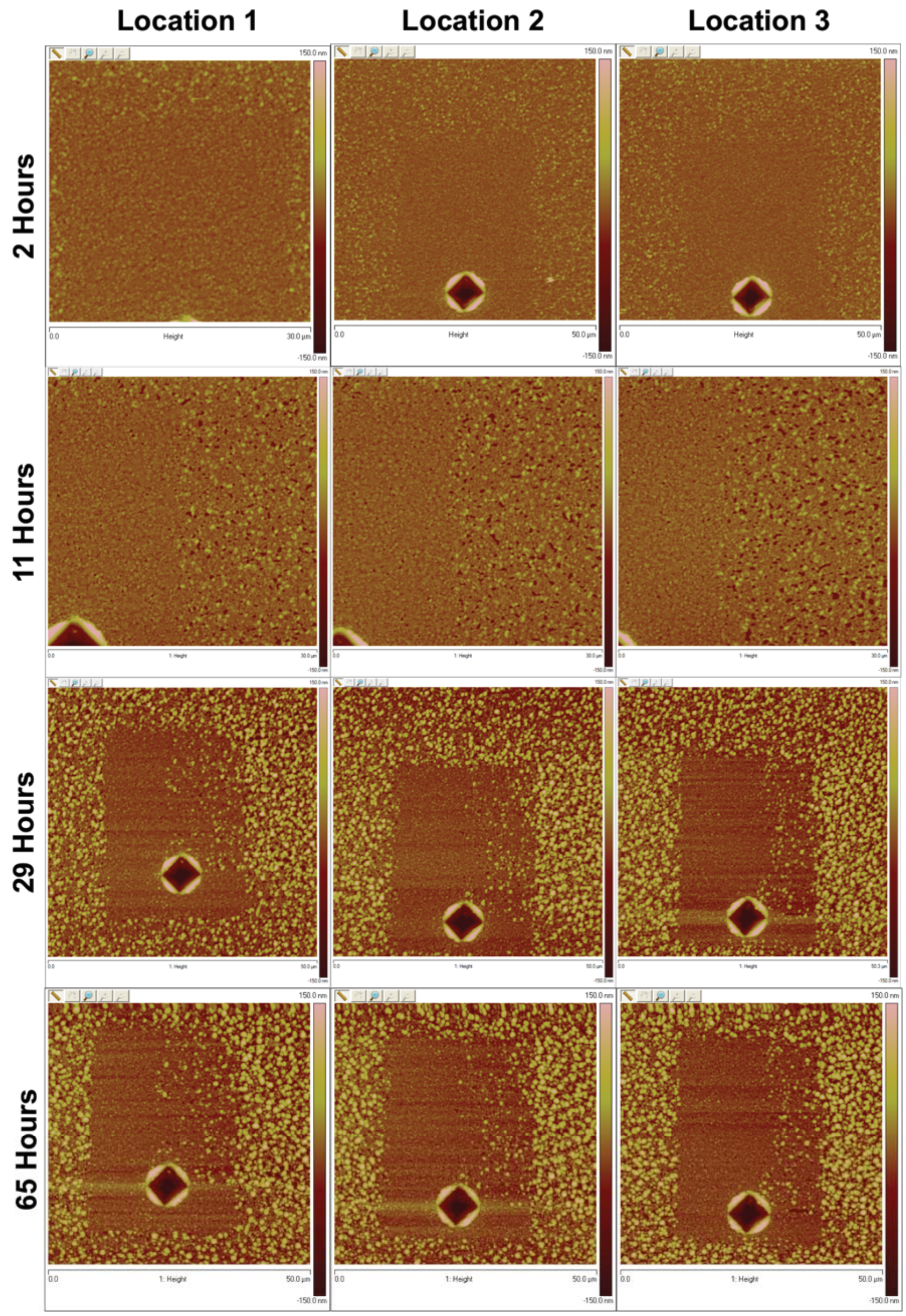

Figure 43. AFM micrographs of each location (1-3) after each anneal showing the changes in structure and feature height.

Using the AFM data, the roughness changes in the regions subject to the capping layer effects were investigated. The local averages and overall average roughness changes with annealing time are detailed in Figures 44 and 45. The roughness measurements are only for the regions that exhibit the fully capped behavior (the left ½ of the capped regions). The roughness plots show an increase in roughness with annealing time. This behavior is expected as relaxation progresses and the microstructures develop holes and hillocks to relax stresses. Figure 44 shows the local average roughness for each location after each anneal. All locations show an overall increase in roughness. However, location 3 shows a decrease in roughness after the 18-hour (29 total hours) anneal. This is likely due to the locations selected to average over. Including or excluding a single defect would greatly impact the roughness assessment in these regions due to the small scale.

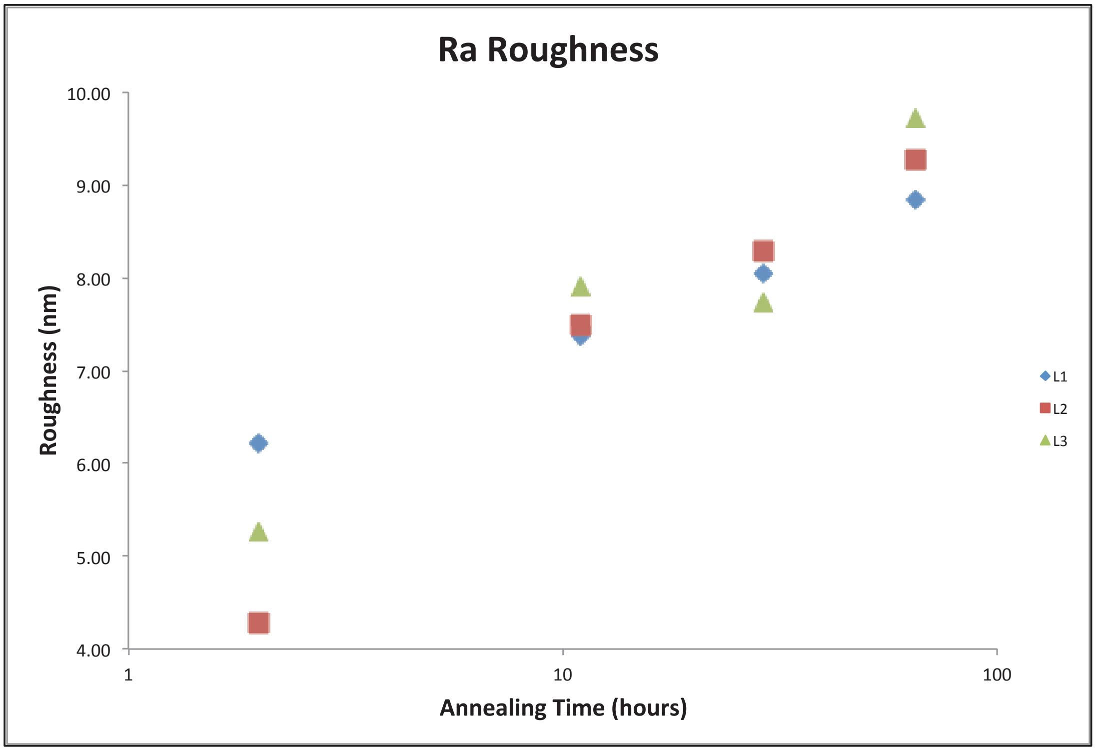

Figure 44. Plot of roughness within the capped regions after each anneal for Locations 1-3 showing the overall increase in roughness with annealing time

Similarly, the overall averages of the three locations after each anneal show a general increase in roughness. This data will later be compared with the change in roughness for locations that did not experience the diffusion suppression effects of the capping layer. The roughness is still expected to increase, however, the rate at which it increases will likely change (increase) because of the ability of the system to exploit a wider variety of diffusion paths that includes surface diffusion.

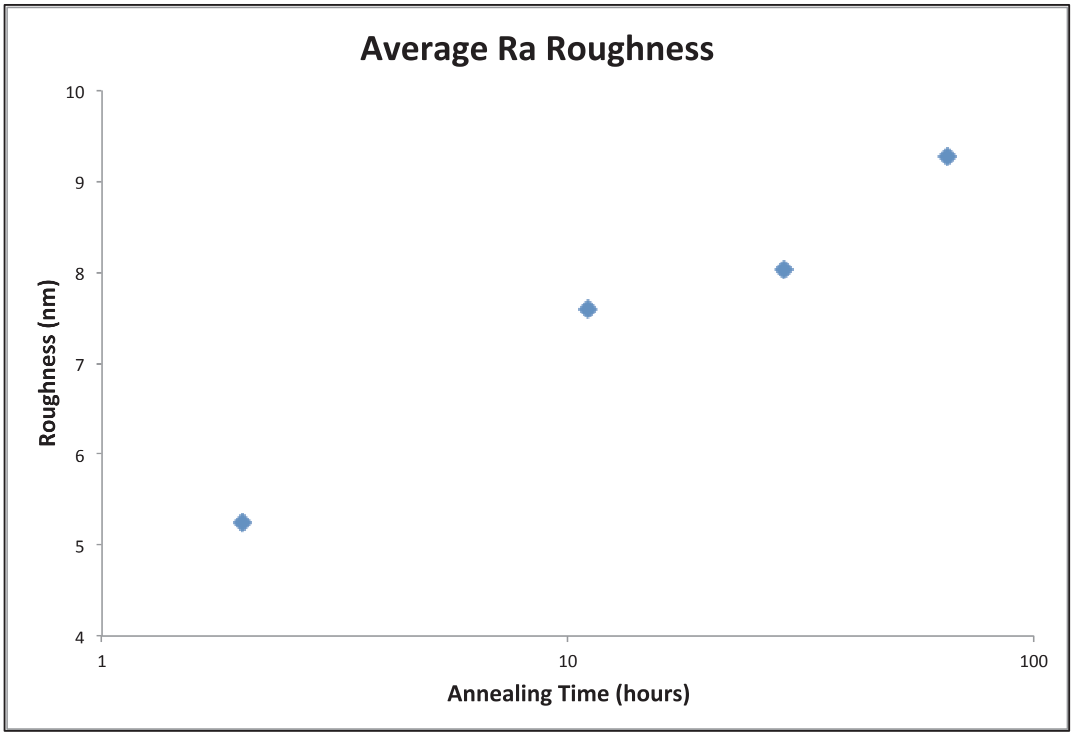

Figure 45. Plot of the average roughness within the capped regions after each anneal for Locations 1-3 showing the roughness increase with increasing annealing time.

For the same three locations, the roughness outside of the capping layer regions was also assessed in order to compare the roughness changes with and without the capping layer. Figure 46 depicts the local changes in roughness for Locations 1-3 outside of the capped region. A comparison of the scales between Figure 45 and Figure 47 shows that the average roughness started approximately 2X greater and by the final anneal the roughness outside of the capped regions were approximately 3.5X greater.

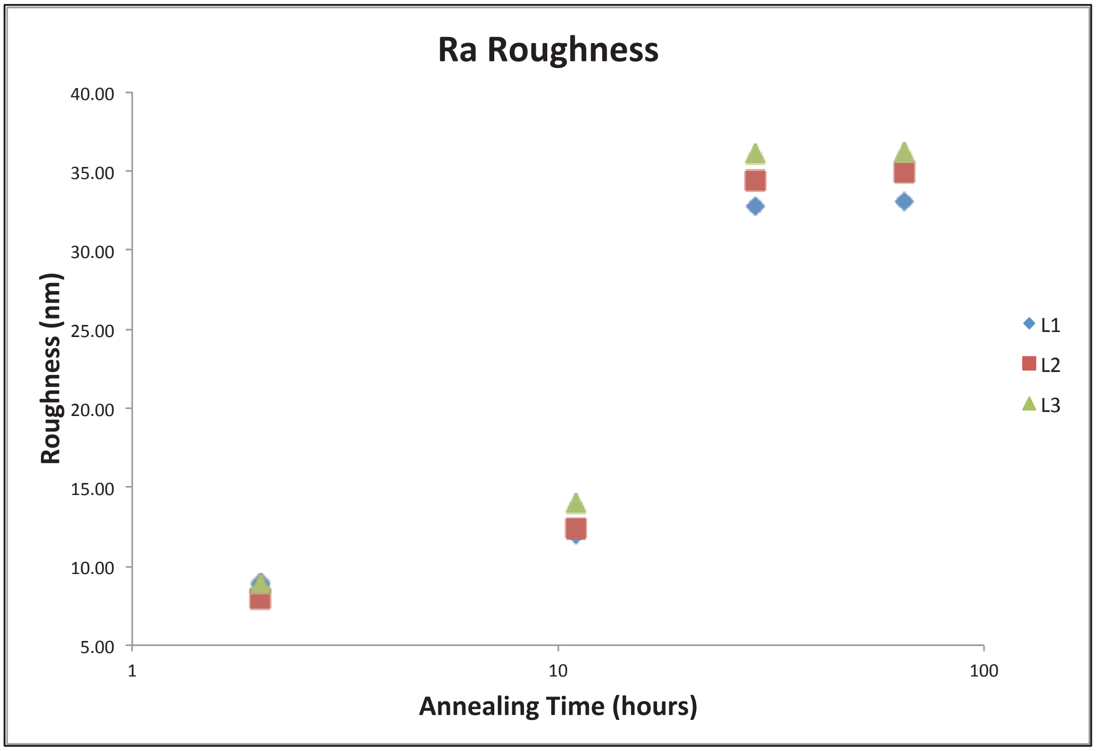

Figure 46. Plot of roughness outside of the capped regions after each anneal for Locations 1-3 showing the overall increase in roughness with annealing time

The overall averages of the three locations after each anneal still show the predicted increase in roughness. However, the rate of roughness change has also increased as predicted. By comparing the difference in the final roughness values for the capped (~10nm) and non-capped (~37nm) regions, an increase in the final roughness for the non-capped regions for the same annealing time is clear.

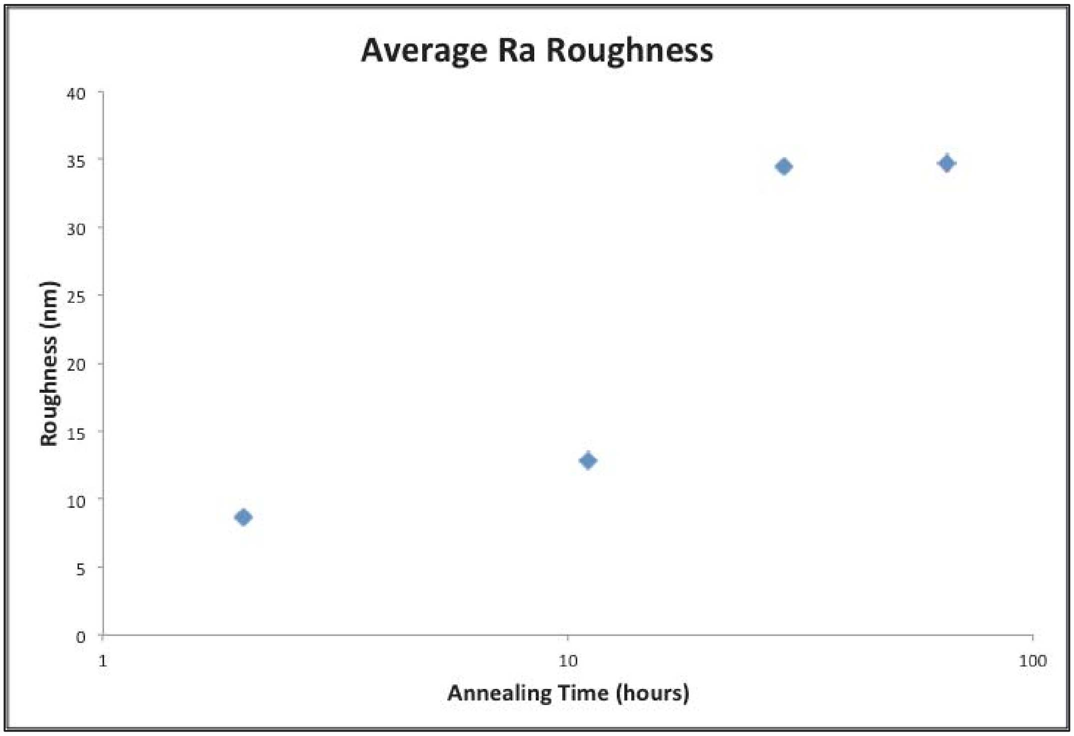

Figure 47. Plot of the average roughness outside of the capping layer area after each anneal for Locations 1-3 showing the roughness increase with increasing annealing time.

Combining both assessments onto a single plot allows for a direct comparison of the effect of the capping layer on film roughness changes with annealing. It is clear that the capping layer has impacted the roughness even after the 1-hour anneal study. Figure 48 shows both the capped and non-capped data for individual locations and averages showing the distinct trends.

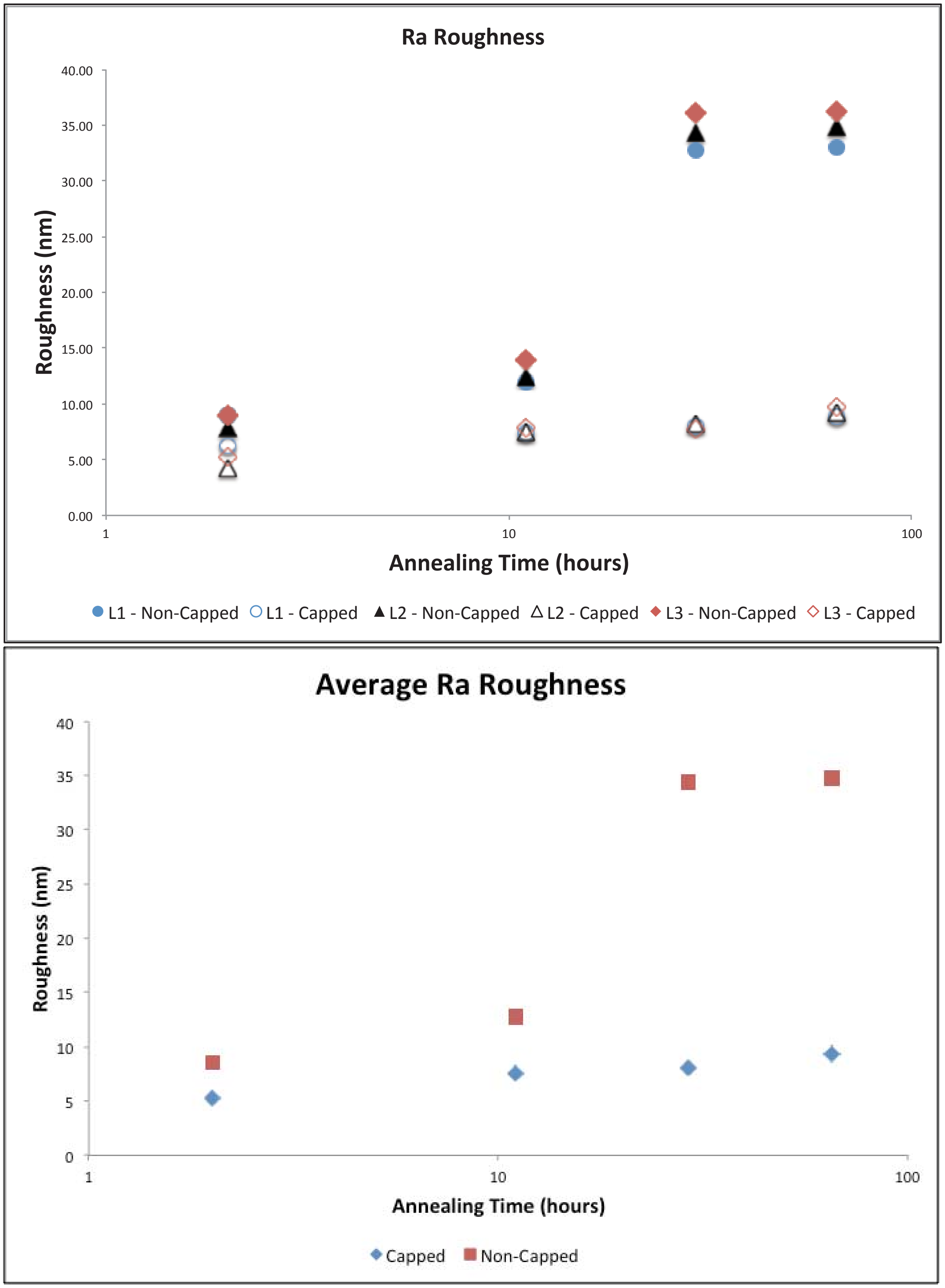

Figure 48. Comparison of the individual and average roughness changes for the capped and uncapped regions contained with Locations 1-3 quantifying the effect of the capping layer on roughness changes during annealing.

3.3.1.1.5 Capped Layer Surface Diffusion Calculations

Using Brandon and Bradshaw's surface diffusion model as described in the previous section, the effect of the capping layer on an effective "surface diffusion coefficient" for silver can be quantified using the SEM image data. The average hole radii after each anneal were determined from the total hole area and number of holes. Using the average hole radii for the four investigated annealing times, the effective diffusion coefficient, based on the data from each experiment, was determined. The measured average hole radius and calculated diffusion coefficients for each annealing time are detailed in Table 13.

Table 13. Table showing the range in diffusion coefficients calculated from the average holed radii measured from the SEM micrographs after each anneal

Total Annealing Time (s)	Hole Radius (cm)	Diffusion Coefficient (cm2/s)
7200	2.7 E-06	1.6 E-09
39600	2.9 E-06	3.3 E-10
104400	4.4 E-06	3.7 E-10
234000	5.1 E-06	2.4 E-10

The effective diffusion coefficient decreases 6.7X from the calculated value for 2 total hours of annealing (1.6 x 10^{-9} cm^2/s) to the value for the 65 total hours of annealing (2.4 x 10^{-10} cm^2/s). These results are for regions where surface diffusion has been suppressed by the presence of a capping layer and they still exhibit a factor of 6.7 difference.

Recall that in the non-uniformity study, assuming a 50nm silver film thickness annealed for 2 hours at 200°C, the diffusion coefficient ranged from of

6.3×10^{-9} cm^2/s to 1×10^{-6} cm^2/s. For the capping layer study, a 50nm film annealed for 2 hours at 200°C results in a diffusion coefficient of 1.6×10^{-9} cm^2/s. This comparison shows 4X decrease in the predicted diffusion coefficient for regions with the capping layer relative to the smallest diffusion coefficient calculated from the non-uniform film study. These suppressed values will also be compared to those from other tracked locations in the bearing analysis section of this chapter.

Clearly, the surface diffusion behavior of silver exhibits drastically non-uniform behavior for even slight changes in both physical and experimental parameters. This result is validated in the literature. As previously mentioned, the surface diffusion coefficient data reported in literature ranges over 20 orders of magnitude for similar temperature regimes. As with the non-uniformity study, the broad range of diffusion coefficients calculated for this capping layer experiment with the consistent experimental parameters suggests that Brandon and Bradshaw's surface diffusion limited based model does not address all of the influencing factors on dewetting kinetics.

3.3.2 Study 3: Local Microstructure Evolution During Interrupted Annealing

3.3.2.1 Newly Developed Bearing Analysis Technique - Procedure

Using a combination of the bearing analysis function in the NanoScope software and the particle analysis tool in Image J, the hillock density, hole density, total hillock area, and total hole area for regions examined by AFM were determined. Bearing analysis is a method for determining the distribution of features as a function surface height over a sample surface of a specific area. The bearing analysis tool was used first to impose a height threshold on the collected AFM data selecting (or eliminating) data above or below the threshold height. Typical scans for the microstructures examined contain data points ranging in height from exposed silicon substrate surface to the peaks of hillocks formed during annealing.

The bearing area percent versus bearing depth plots, as seen in the examples in Figures 49-51, were used to determine suitable height thresholds between the bulk of the film and holes or hillocks formed during annealing. The majority of the scan areas exhibited an S-shaped curve with two visible slope changes. Using the changes in slope on the bearing area versus bearing depth plot (highlighted in yellow in Figure 49) as a starting point, the depth threshold was adjusted for each data set until all defect regions appeared (by eye) to contain more than one pixel. This threshold was based on visual assessment of each image and was set at each slope change in order to produce black and white images that characterize the exposed substrate area and hillock area for each location.

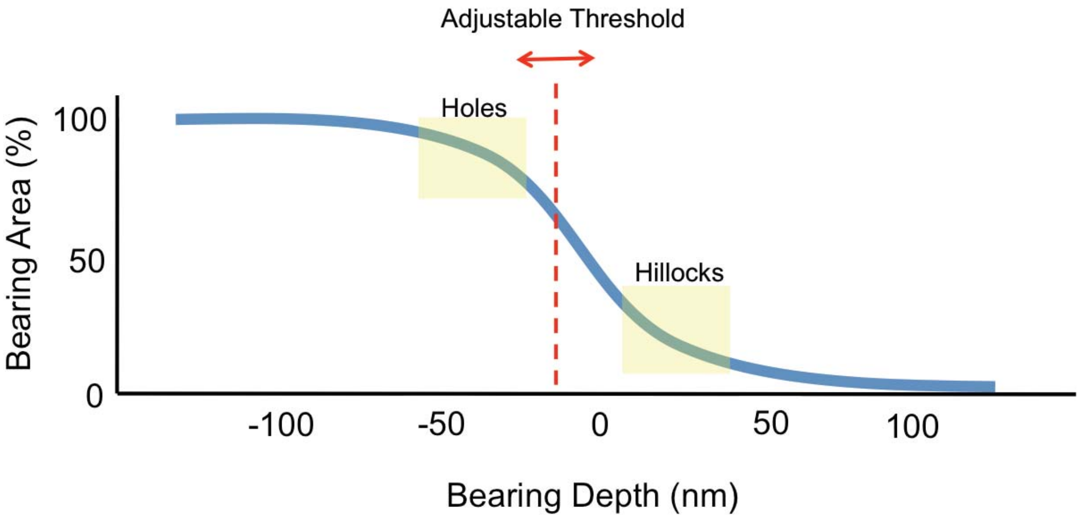

Figure 49. Bearing area versus depth plot showing the user-controlled adjustable threshold and the approximate locations of the cutoffs for both hillocks and holes

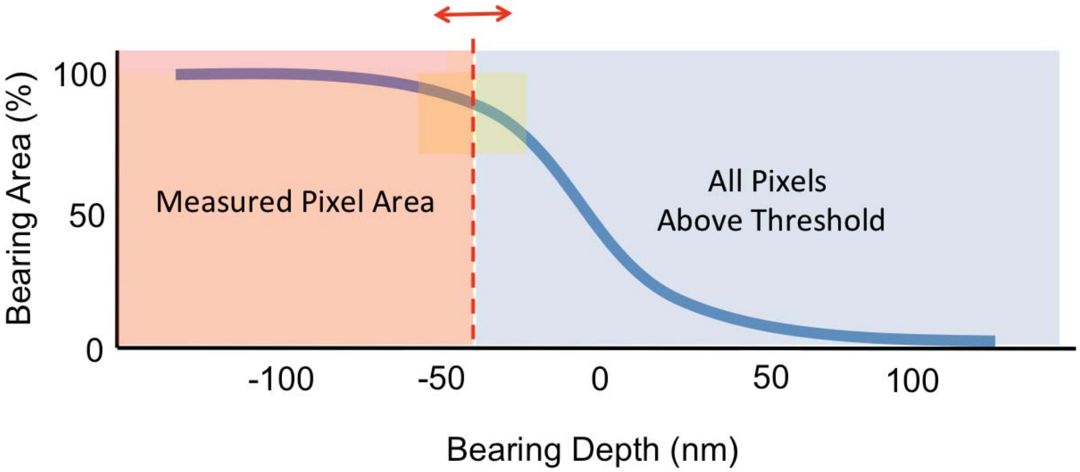

Figure 50. Bearing area versus depth plot showing an assessment of hole area. The area measured for the assessment and the area of pixels that the Nanoscope software is shown (the hole area does NOT coincide with the area above the chosen threshold).

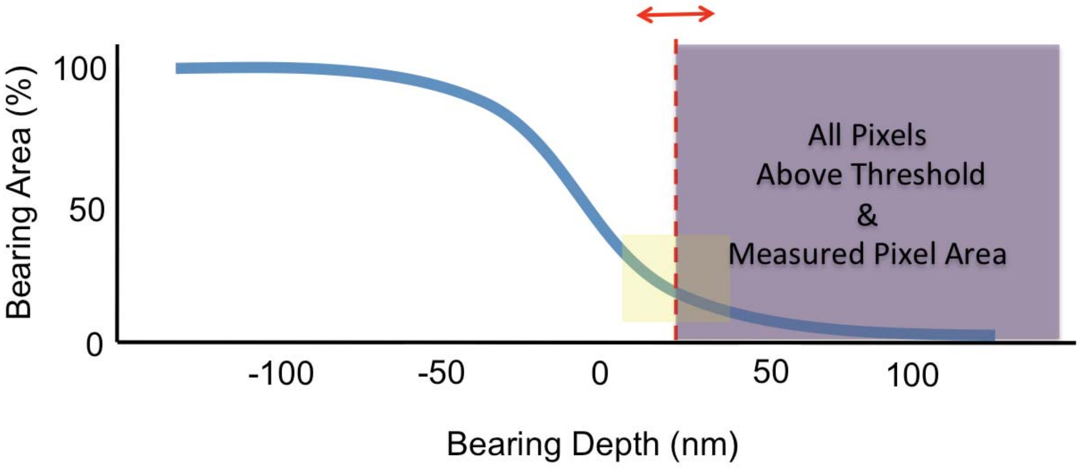

Figure 51. Bearing area versus depth plot showing an assessment of hillock area. The area measured for the assessment and the area of pixels that the Nanoscope software is shown (the hillock area DOES coincide with the area above the chosen threshold).

In order to quantify the variability of microstructure evolution at various length scales, a representative and reproducible measurement of the defect area is needed, not simply the area above or below the threshold. In order to determine the defect areas at various length scales, the defect images resulting from the bearing analysis were processed using ImageJ in order to determine the area associated with exposed substrate and hillocks for each data set. Area was determined through image processing. Images were converted to black and white, segmented into 9 equal areas and analyzed using the Particle Analysis function in ImageJ, as above. The Particle Analysis function in Image J measures the number and area of distinct regions in an image based on specific user-defined threshold criteria which in our case were set in the bearing analysis and reports the number and area within each region. The number of defects present in each segment and the area associated with each defect was then logged and totaled. Figure 52 is an example of an AFM image after the bearing analysis for hillock area has been completed. The AFM image was cropped in order to eliminate input from the fiduciary marks in the data analysis. Any regions of data with surface heights above the threshold have been replaced with blue pixels. For hillock area measurements these blue pixels are the regions of interest. Figure 53 contains the subsequent 9-segment images used for number and area analysis.

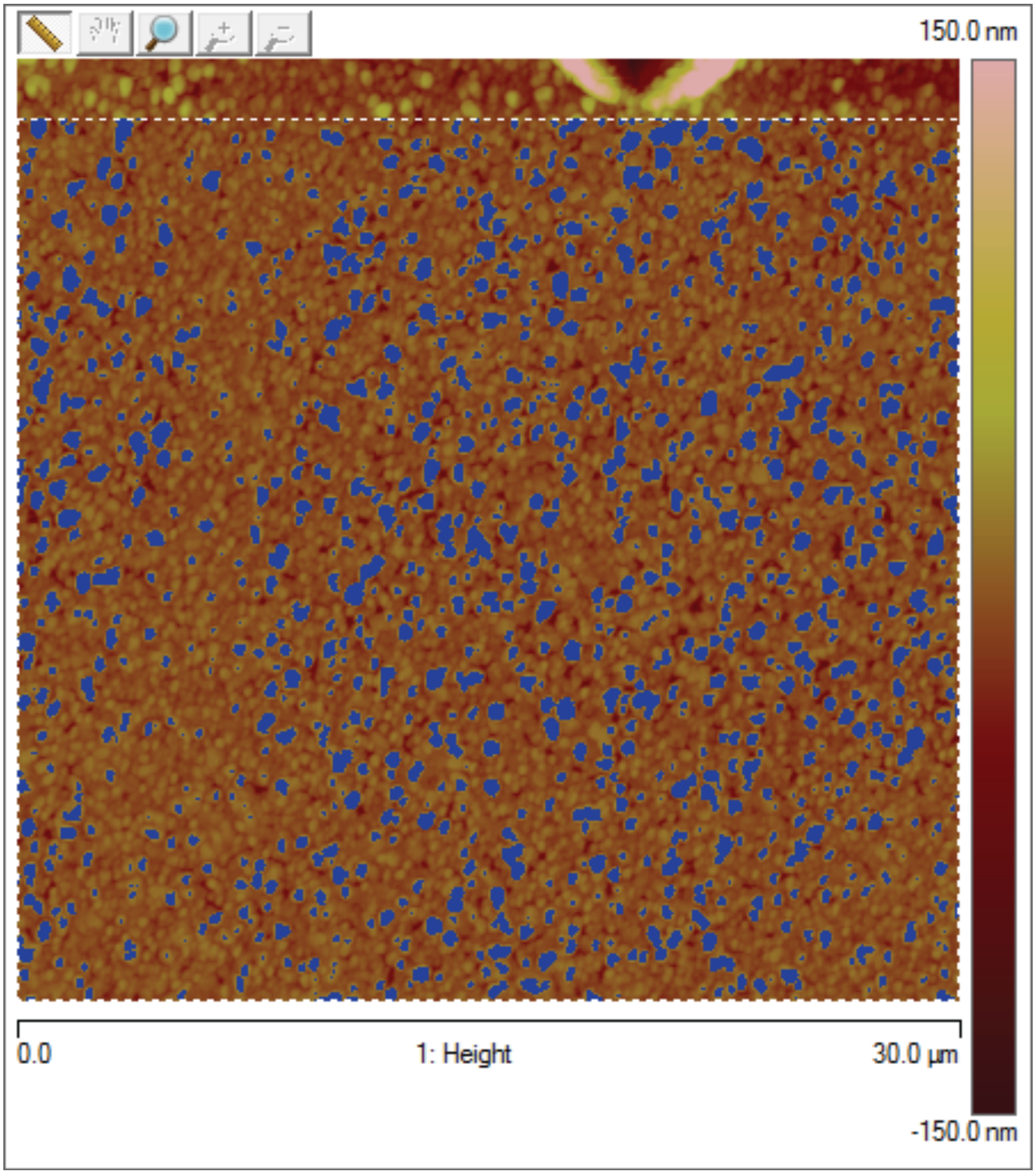

Figure 52. An AFM image after the bearing analysis for hillock area has been completed showing regions above the threshold in blue. The blue pixel area is the hillock area.

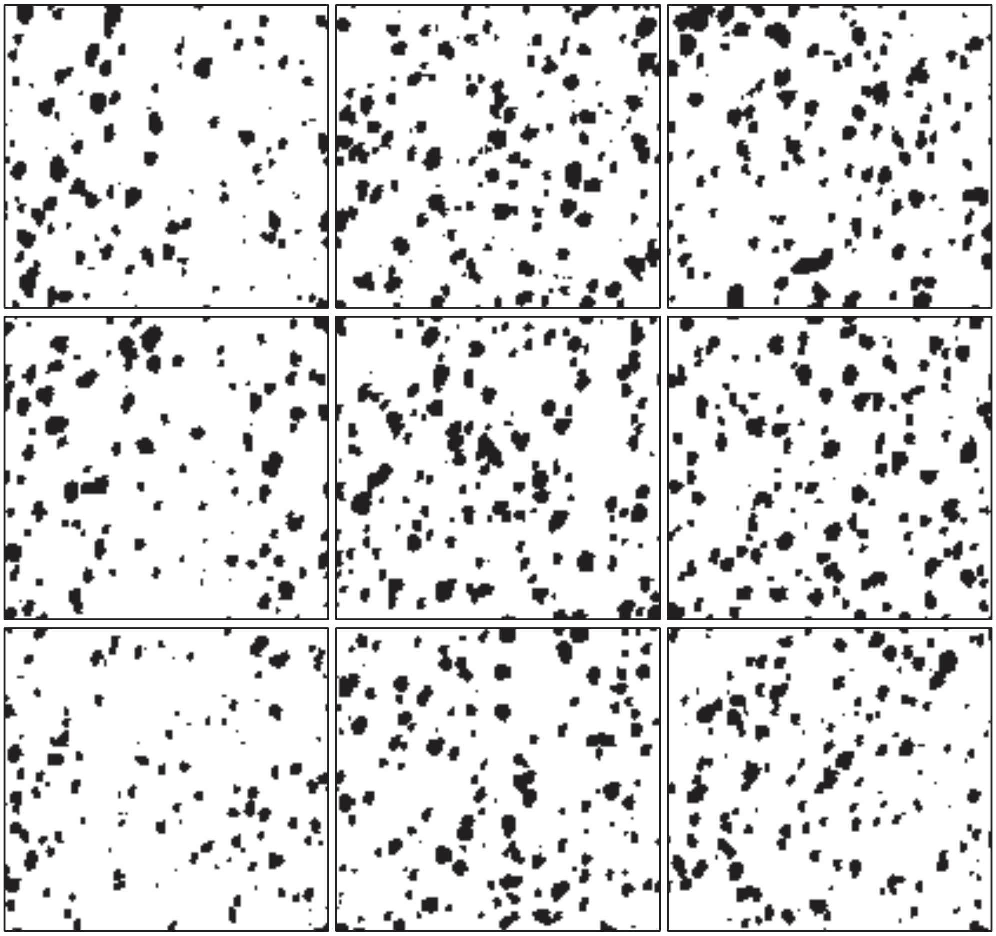

Figure 53. An example of a segmented image after the bearing analysis for hillock area has been completed (Figure 46) showing the hillock area in black and the nine image segments used for analysis.

Similarly, Figure 54 is an example of the same AFM image after the bearing analysis for exposed substrate area has been completed. The AFM image was once again cropped in order to eliminate data from the fiduciary marks. All regions of data with a surface height above the threshold have been replaced with blue pixels. In this figure the regions of interest for determining exposed substrate area are those regions that are not blue, or that are below the threshold. Figure 55 contains the subsequent 9-segment images used for area analysis.

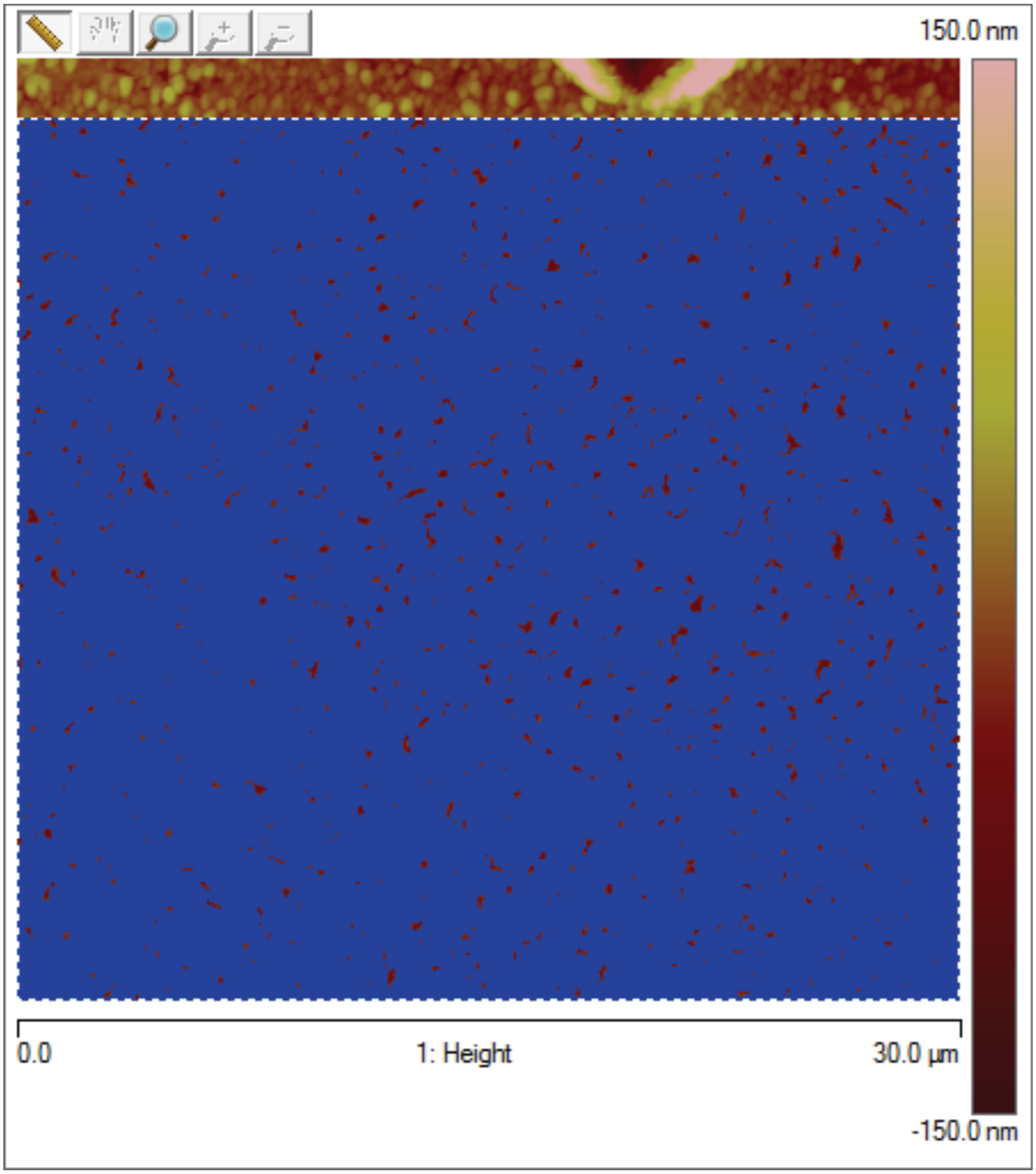

Figure 54. An AFM image after the bearing analysis for hole area has been completed showing regions above the threshold in blue. The non-blue pixel area is the hole area.

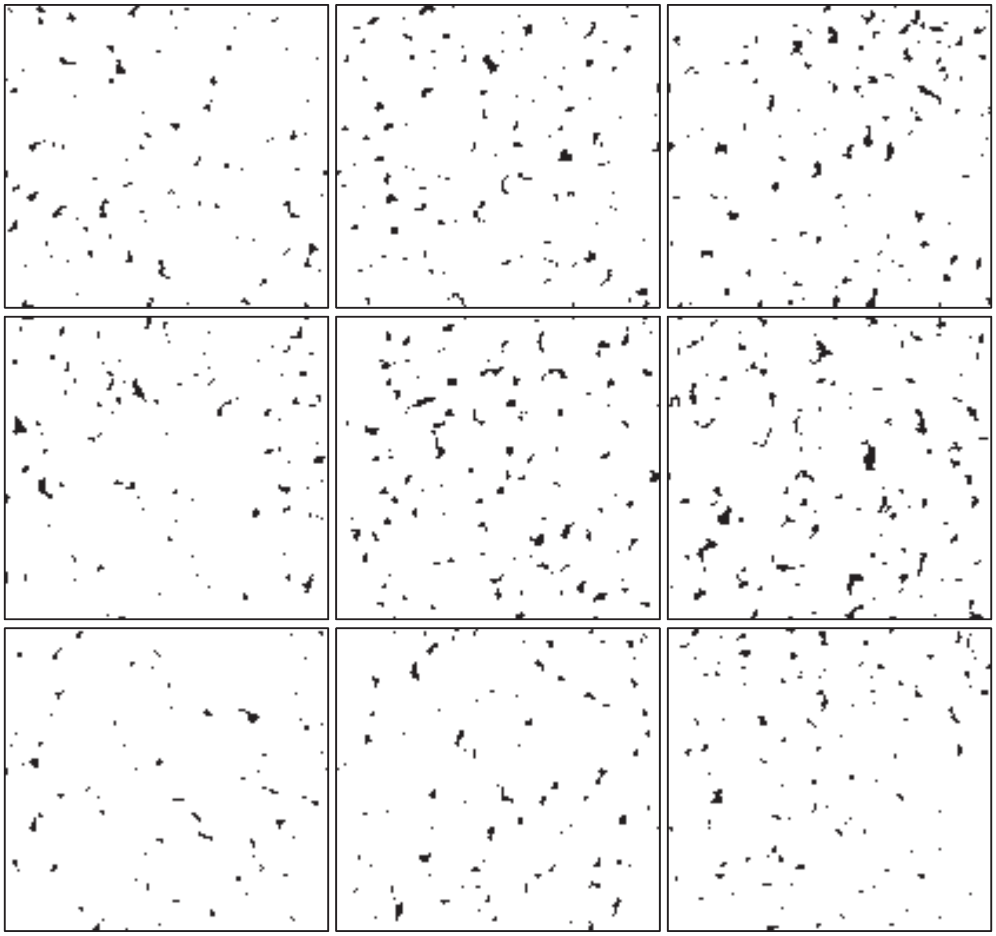

Figure 55. An example of a segmented image after the bearing analysis for hole area has been completed (Figure 48) showing the hole area in black and the nine image segments used for analysis.

The bearing analysis technique described is highly dependent on user judgment for determining the appropriate threshold level. As stated, the levels were chosen based on visual interpretation of the S-shaped area vs. depth curve and the location that appeared to contain the fewest single-pixel defects (by eye). However, the error associated with choosing a threshold +/- 1 can be quantified and therefore the error associated with the thresholding decision can be quantified.

3.3.2.2 Newly Developed Bearing Analysis Technique - Error Assessment

Using the representative region shown in Figure 56 an error assessment was performed. Figure 56 shows the AFM image from the scan, the depth histogram showing the distribution of height data from the scan, and the bearing area plot showing the percentage of area above each depth. As described above, changes in slope associated with the S-shaped bearing area plot were used to determine the threshold values for the bearing analysis based on a visual assessment of the location where single pixel holes or hillocks were minimized.

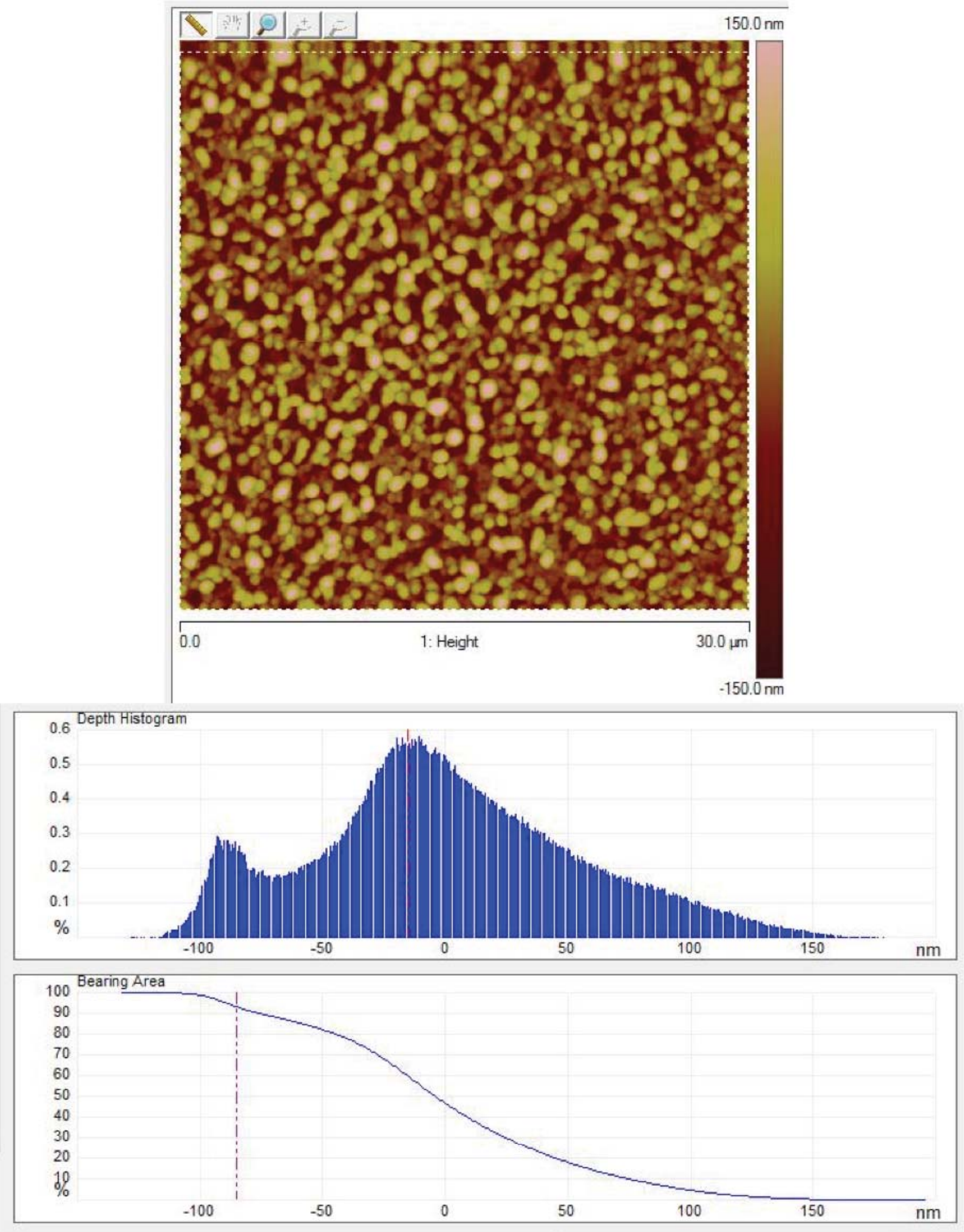

Figure 56. An example AFM scan, the corresponding depth histogram showing the distribution of height data from the scan, and the bearing area plot showing the percentage of area above each depth.

In order to determine the error associated with the threshold value choice, an assessment of the changes in total defect area and area percent for a one nm change in threshold height were assessed using a representative image. As previously described the majority of the scan areas exhibited an S-shaped curve with two locations of slope change. These slope changes are representative of the transition between the body of the film and the hillocks (above the body) and holes (below the body). However, in a few cases, there appeared to be another change in slope on the far left-hand side of the bearing area plot. Because of this feature being present in several of the scan areas a location containing this third slope change is also included in this comparison.

Figure 57 depicts the hillock and hole bearing analysis images of the threshold level selected for representative location as well as the images for +/- 1 nm. It is difficult to detect physical changes in the images by eye and therefore one region of change from each +/- pairing is highlighted. The changes in area (blue pixels) are seen in Table 14.

Table 14. The area above the selected threshold height showing the changes in area that correspond to 1nm changes in depth

	Hillock 34nm	**Hillock 35nm**	**Hillock 36nm**	**Hole -24nm**	**Hole -25nm**	**Hole -26nm**	**Hole -85nm**
Area (μm^2)	217	214	209	591	595	604	819
Area %	25	24.3	23.7	67	67.6	68.6	93

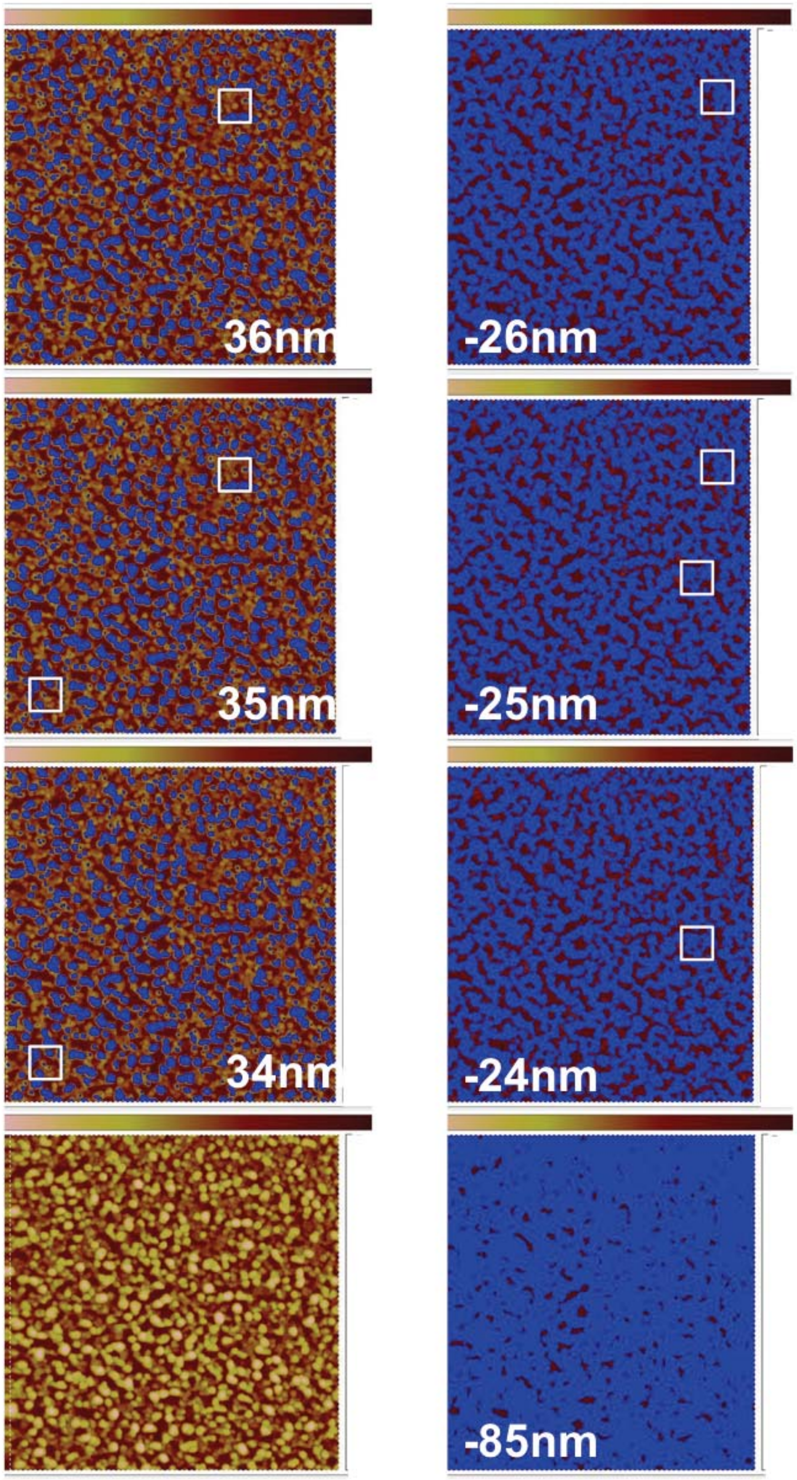

Figure 57. A series of AFM scans showing the original scan area, as well as the hillock and hole bearing analysis images for the error analysis threshold heights. The white boxes correlate to regions of change between the baseline images (35nm and -25nm) and the +/- 1nm images showing the small visible changes in the structure

As previously mentioned, some scans contained a third change in slope. Because the hole data are associated with the left-hand side of the plot it may be hypothesized that this slope change is associated with the presence of a different type or morphology of hole area. However, this is not the case. Examining the AFM scans in Figure 57 and comparing visible hole regions within the non-thresholded image and the 85nm thresholded image, shows that at this slope change there are still areas of the substrate that are exposed and not present in the data. Therefore, this third slope is not representative of hole formation. This slope change correlates to a large area of film being present at the same height. In this case, this height is below the height needed to show the representative area of exposes substrate. AFM scans have an arbitrary zero location assigned based on the scale the user provides and therefore the depth threshold needed to show the exposed regions may not correlate directly to the location of the substrate.

By comparing the differences in the hillock and hole area between the +/- 1nm data it was determined that the error associated with the area measurements for both holes and hillocks is on the order of +/- 5 μm^2 and a 0.005 area fraction. As determined from the 100 μm^2 scan areas used for assessment. This result gives an associated error of 5%.

For a few locations, data samples were also acquired from much smaller scans, on the order of 10 μm^2. For these smaller regions the associated error is 50% and therefore the resulting data are not useful for characterizing microstructure evolution. The impact of this error can be seen when comparing data for the same time and temperature combination gathered from the same location at different scales. For location five after the 36-hour anneal, the hole density and hole area fraction were calculated from two area scans, a 100 μm^2 area and a 10 μm^2 area, as detailed in Table 15. (Details about how these values were calculated are in the bearing analysis section of this dissertation.)

Table 15. The hole area fraction and hole density measured from 100 μm^2 and 10 μm^2 scan areas showing the impact of scan area on data collection

	Hole Area Fraction	**Hole Density**
10 μm2	0.13	3.12
100 μm2	0.19	0.69

The effect of this scale effect is even more clearly seen when comparing the plots and associated equations for each data set. Figure 58 shows the hole area fraction data for a single tracked location after each anneal, the top plot shows the results when all locations were scanned at approximately the same scale (100 μm^2); the bottom plot show the results when the 36 hour data were taken from 10 μm^2 scans. The plots show that smaller measured area fraction for the 10 μm^2 scan has impacted the calculated hole growth rate (as determined by a linear regression) by decreasing it from 0.0025 to 0.0016 hole μm^2 / scan area μm^2 / hour. This 40% increase in the growth rate change would greatly impact the overall averages determined for the data set.

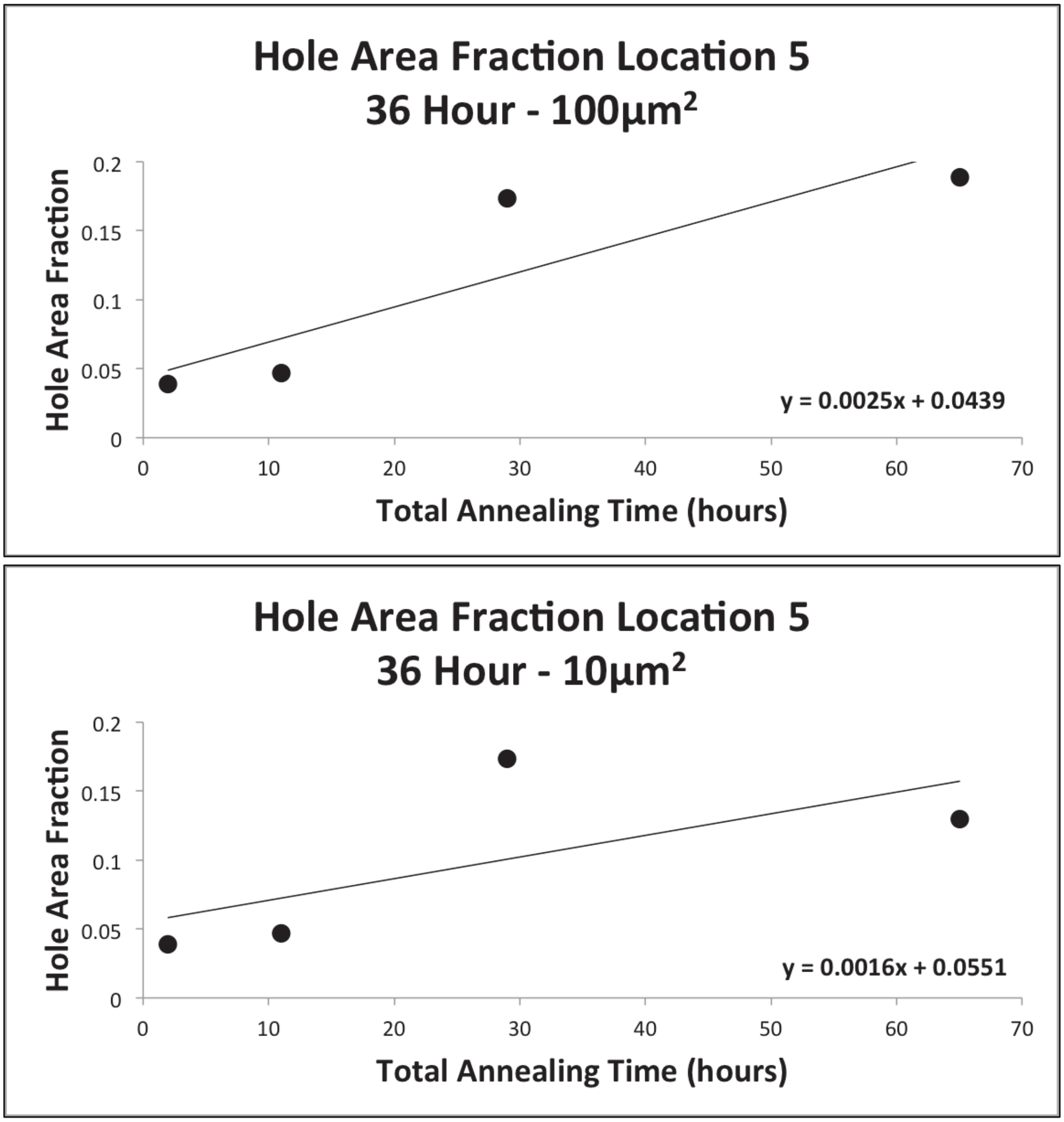

Figure 58. The measured hole area fraction data for Location 5 after each anneal showing the effect that scan area has on the measured hole growth rate. The top plot shows the results when all locations were scanned at approximately the same scale (100 µm^2); the bottom plot show the results when the 36 hour data was taken from 10 µm^2 scans.

Similarly, the scan area effects also impact the density data. Figure 59 shows the hole density data for a single tracked location after each anneal, the top plot shows the results when all locations were scanned at approximately the same scale of 100 µm^2, whereas the bottom plot shows the results when the 36 hour data was taken from a 10 µm^2 area. The plots show a larger measured hole density for the 10 µm^2 scan. This increase in apparent hole density is a result of the higher resolution of the AFM for smaller scan areas.

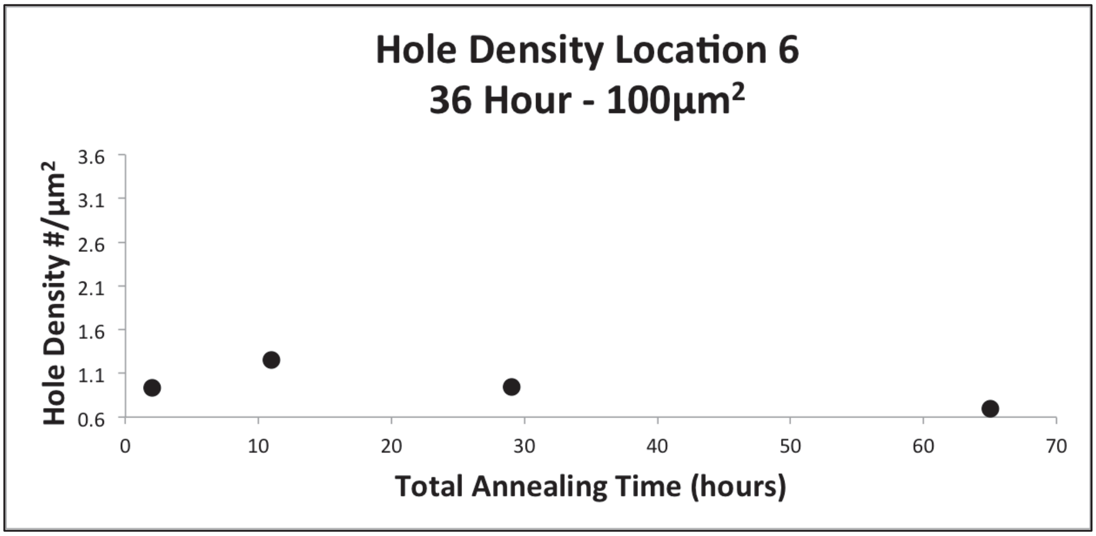

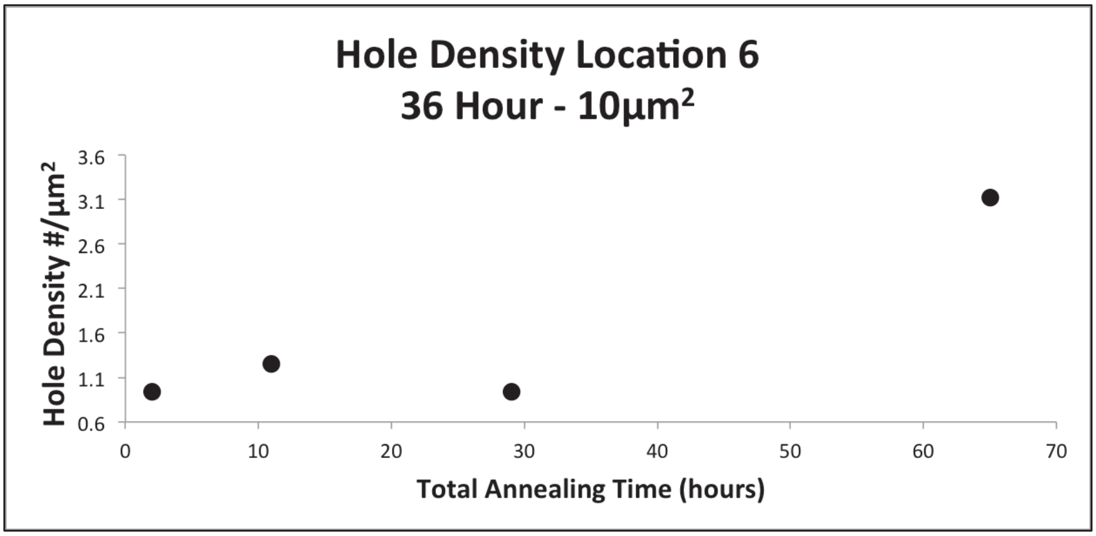

Figure 59. The measured hole density for Location 5 after each anneal showing the effect that scan area has on the data. The top plot shows the results when all locations were scanned at approximately the same scale (100 µm^2); the bottom plot show the results when the 36 hour data was taken from 10 µm^2 scans.

Because of the error associated with the bearing analysis technique and the effects of the scan area on providing representative data, it was determined that total scan areas of 30 X 30 μm or greater were necessary for a representative assessment of the film structure. This will be key for future studies, as this error had not been quantified prior to this investigation.

3.3.2.3 Bearing Analysis of Ag/Si

An interrupted annealing study was used to track individual locations through a series of anneals ranging from 1-36 hours. The structure of the film, changes in microstructure, and details about the defect formation between each anneal provide insights into how silver films dewet and relax. The experiment was conducted on a 50nm silver film on (100) Si substrate that was deposited through electron beam evaporation. The first and second anneals were conducted for 1 hour each, the third anneal for 9 hours, the fourth for 18 hours, and the final anneal was for 36 hours. All annealing took place at 200°C in a forming gas atmosphere. The surface morphology evolutions of six areas, referred to as Locations 4-9, were tracked after the 2nd 1-hour anneal, the 9-hour anneal, the 18-hour anneal, and the 36-hour anneal using AFM. The locations were chosen from within the fiduciary grid array as previously defined. These locations were centrally located on the sample surface in order minimize any edge effects.

The bearing analysis technique previously described was used to determine the average hillock and hole densities, area fractions, and the variation of each of these characteristics at each tracked location after the 1, 9, 18, and 36-hour anneals (2, 11, 29, and 65 total hours of annealing time). Recall that scans from each location, at each time, were segmented into 9 equal areas. The measurements of density and area for each of the 9 image segments were also averaged in order to determine the density and area for not only each segment but also each location. These values were also averaged over the sample surface in order to determine global behavior and the standard deviations were reported in order to quantify the non-uniformity at each location. It is important to note that while great care was taken to scan the same location for each assessment in some cases scan areas changed slightly and therefore there is some small error associated with variations in the scan areas reported.

3.3.2.3.1 Hillock Assessment

Figure 60 shows the average hillock density for each location. Within this data set, the changes in hillock densities for individual locations after each anneal are detailed. Average hillock density values for individual locations ranged from approximately 0.6 #/μm^2 to 1.9 #/μm^2. Dividing the initial scan area into 9 equal areas for assessment allows for an evaluation of the uniformity of defect formation across the sample surface. As described in the first study on the uniformity of hole formation in the continuously annealed silver film, relaxation behavior is a localized phenomenon therefore variation in the extent of hillock and hole formation across the sample surface is expected. The variation in hillock density between the 1-hour and 36-hour anneals, as determined by the standard deviation, decreases from 0.3 to 0.06 #/μm^2 showing that the hillock density becomes more uniform across the sample surface as annealing and relaxation progresses. This result suggests that the initial onset of hillock formation is non-uniform, however, as hillock growth and coarsening progresses the number of hillocks present across the sample surface not only decreases but the hillock density also becomes more uniform. Physically, this increase in uniformity suggests that initial hillock growth occurs to different extents across the surface of the sample. With more hillocks forming in some regions and fewer forming in others, However, as annealing time increases the average number of hillocks present within a given area become more uniform suggesting that eventually, the hillock behavior becomes more globally uniform across the sample surface.

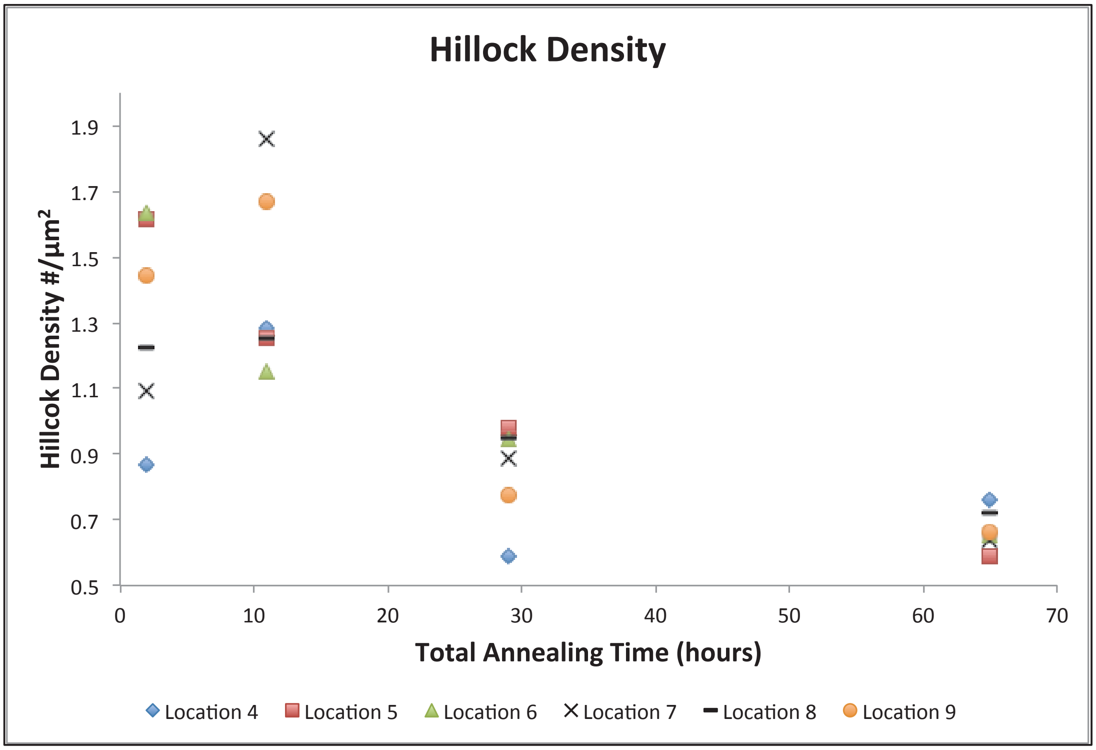

Figure 60. Plot of hillock density after each anneal for Locations 4-9 showing the decrease in hillock density as annealing time increases

A closer investigation of the hillock data shows that 4 of the 6 tracked locations (4,7,8,&9) show an increase in the hillock density after the 9-hour anneal while 2 of the tracked locations (5&6) show a decrease. It is expected that initially the film will form many defect sites to relax stresses and as annealing progresses these defect sites will grow and ultimately coarsen. Therefore, it is possible that at the local scale, the film within regions 5 & 6 had already formed the maximum number of hillocks needed within the section of the film to reduce the film stresses associated with deposition, mismatch, or thermal expansion as described in the introduction to this chapter. Another possible explanation is that the areas tracked were slightly different between anneals and therefore regions with slightly different behavior are being compared at the same location. As previously mentioned, great care was taken to scan the same location for each assessment however, in some cases scan areas changed slightly and therefore there is some error associated with variations in the scan areas reported. After the 18-hour anneal, all locations show a decrease in hillock density. This decrease is likely due to the continued growth of some hillocks at the expense of smaller hillocks (coarsening). If certain, more energetically favorable, hillocks grow while other hillocks that initially formed do not, then the bearing analysis may no longer account for all of those original hillocks in the hillock assessment. If the selected bearing height for the 18 hour anneal was above the selected bearing height for the 9 hour anneal then the hillocks present in the 9-hour scan that did not grow vertically will not be accounted for in the 18 hour assessment This is due to the height difference between the growing hillocks and the bulk of the film material being so much greater than the original difference between the bulk of the film material and earlier forming hillocks. Similarly, as hillock growth occurs, if two hillocks are growing next to each other and the boundary between them is not deep enough to fall below the bearing height selected as the threshold, the pair of hillocks will appear as a single hillock in the bearing analysis assessment. Lastly, all locations except Location 4 exhibit another decrease in hillock density after the 36-hour anneal. Location 4 shows an increase in hillock density after the 36-hour anneal.

By averaging the nine local averages from each location presented in Figure 60 above, the global change in hillock density over the sample surface was calculated for each annealing time. Figure 61 depicts the change in average hillock density with annealing time for the series of interrupted annealing experiments. The average hillock density decreases overall. However, the density increases after the 9-hour anneal. This is due to the four locations that exhibited the increase in hillock density locally. As previously mentioned, this may be due to residual stresses within the film structure that have yet to be relaxed and therefore lead to the formation of hillocks. A decrease in hillock density is expected, as hillocks formed after early anneals coarsen with increased exposure to elevated temperatures, thus decreasing the number of hillocks.

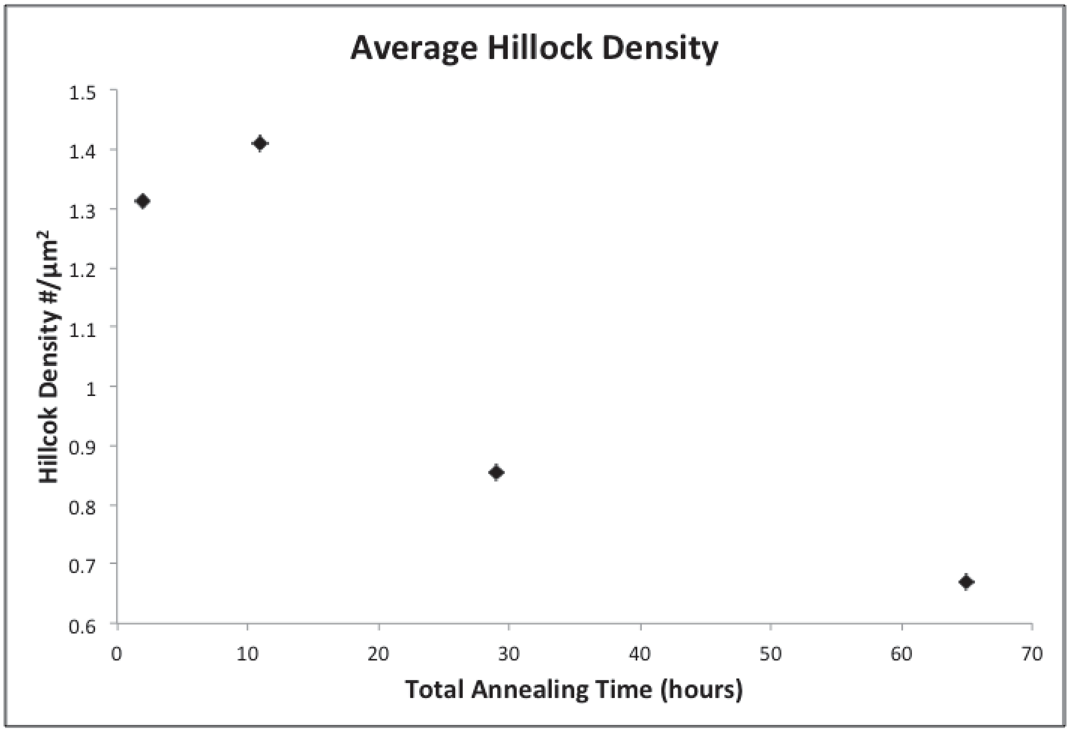

Figure 61. Plot of the average hillock density after each anneal for Locations 4-9 showing the density decreasing with increasing annealing time.

Using the same process of averaging for each location from the 9 image segments to determine local changes, followed by averaging over all locations to determine global values, the change in hillock area fraction with annealing time was assessed. The hillock area fraction was tracked by comparing the total projected area associated with hillocks (above the bearing analysis threshold) to the total imaged area at each location. The average hillock area fraction for each location, as determined by the hillock areas measured within the 9 image segments from each AFM scan, can be seen in Figure 62. Hillock area fraction increases with increased annealing time, showing that hillocks are either forming or growing across the sample surface as annealing and relaxation progresses. It should also be noted that the variation in data, as determined by the standard deviation between the results from the 9 image segments, increases with annealing time with a change in standard deviation from 0.01 to 0.05 showing that hillock area fraction becomes less uniform across the sample surface as annealing and relaxation progresses. The hillock area fraction increases for each anneal at each location, except for the 36-hour anneal at location 5. At location 5 there is a slight decrease in the hillock area fraction after the 36-hour anneal. However, this decrease of 3% is within the 5-8% error associated with the selection of a different bearing depth (+/- 1nm) and therefore is not statistically significant.

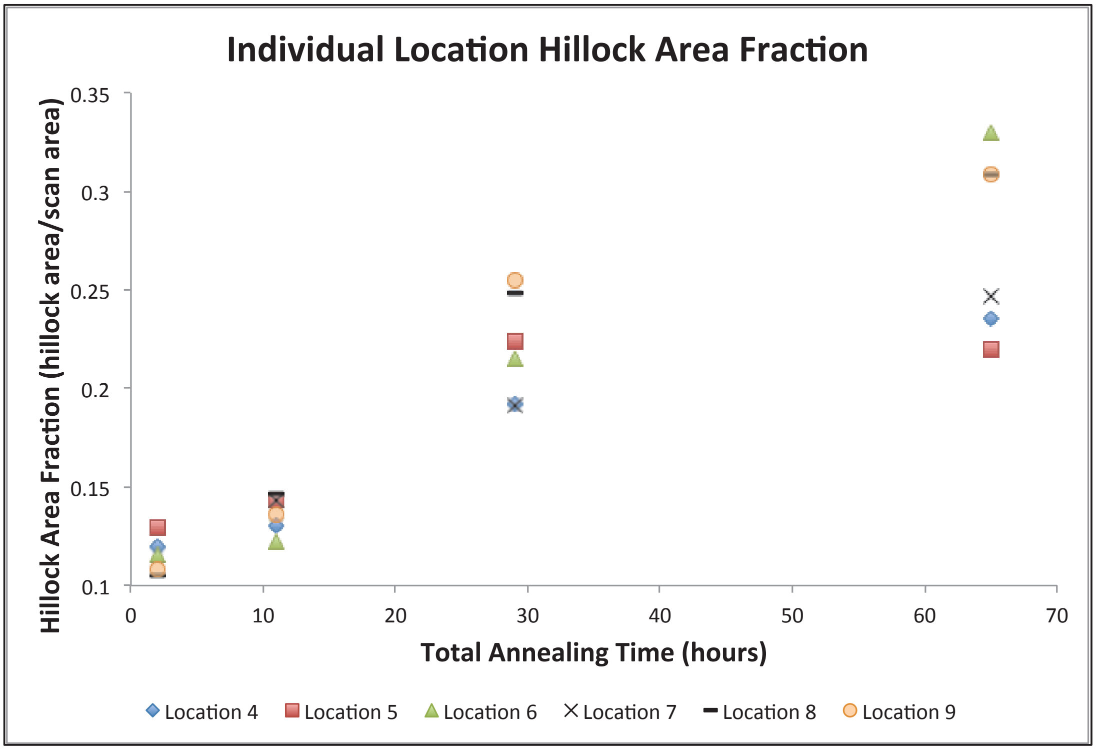

Figure 62. Plot of hillock area fraction after each anneal for Locations 4-9 showing the increase in hillock area fraction as annealing time increases

By averaging the local means at each location presented in Figure 56 above, the change in hillock area fraction over the sample surface was calculated. Figure 63 depicts the change in average hillock area fraction over annealing time for the series of interrupted annealing experiments. The average hillock area fraction increases with annealing time for all anneals. This overall increase in hillock area fraction combined with the decrease in hillock density seen in Figure 57 indicates that as relaxation progresses, hillocks are either coarsening as annealing progresses, or a smaller fraction of hillocks continues to grow after each anneal while the remainder do not.

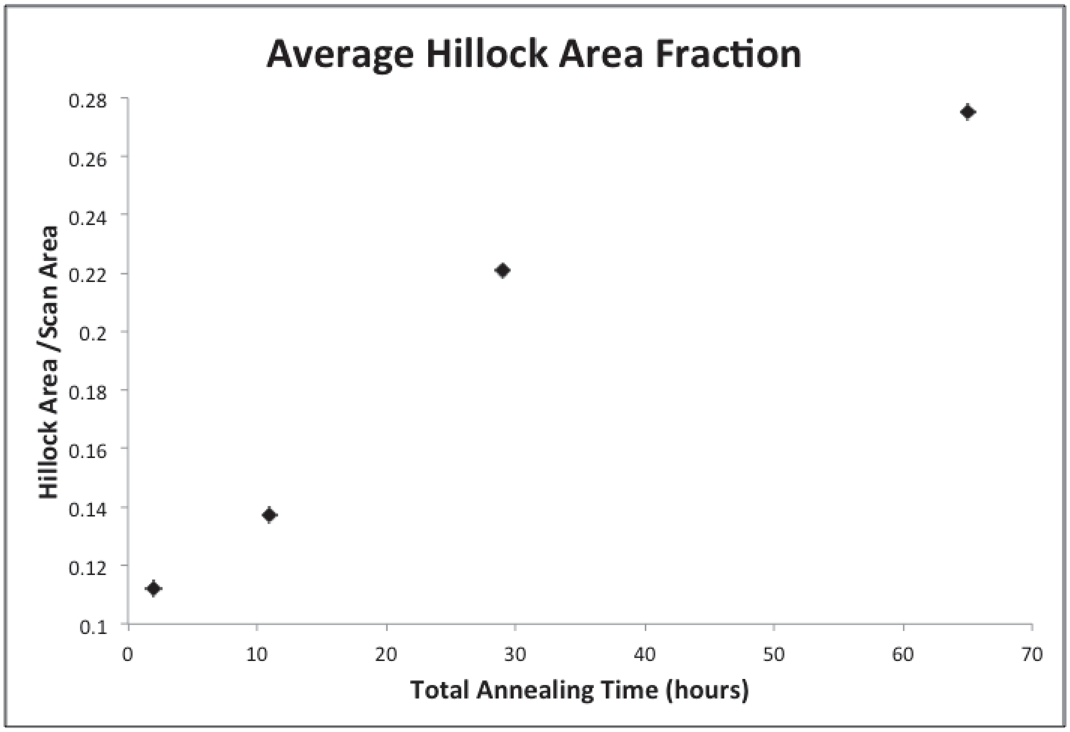

Figure 63. Plot of the average hillock area fraction after each anneal for Locations 4-9 showing the hillock area fraction increasing with increasing annealing time.

In order to better address changes in the distributions of defect sizes as a function of annealing time a histogram analysis of the frequency of defects in a range of area bins was assessed. In order to accurately compare non-normalized data (data that have not been scaled by the scan area) only locations with equal scan areas (or scan areas containing data within the known 5% error range) can be compared. The data from the 9, 18 and 36-hour anneals at locations eight and nine were chosen as representative samples for this assessment.

At each of these locations, a direct comparison of the number and size of defects present is completed by compiling all of the defect data (the number of hillocks/holes and hillock/hole area data) for each location after each anneal. The bin size for the total data assessments was set by producing 20 equal sized bins that ranges from the smallest and largest data points present between all 12 data sets addressed (3 anneals, 2 locations, 2 defect types). Equal binning between all data sets allows for a direct comparison. The goal of the histogram assessments, detailed in Figures 64 and 65, was to capture the distribution changes with annealing time for the smaller defects. It should be noted that the x-axis on the histogram plots are data ranges. Therefore, the frequency data account for any hillocks or holes that are less than or equal to the value listed but greater than the value of the previous bin. The frequency values for the 36-hour anneal data are labeled at the top of each column in order to make the data in the larger area bins visible. Data columns with only one or two data points present are too small to see even with the logarithmic scale on the y-axis. Comparing the Ag hillock area distribution after annealing for 9, 18 and 36 hours at 200°C reveals a broadening trend in distribution with some hillocks growing faster than the average. These faster growing hillocks are the clusters of hillocks that have achieved areas greater than 2μm^2. This type of non-uniform hillock growth is not expected for surface diffusion based models of hillock and hole growth. However, this local rapid hillock growth has been seen in silver dewetting literature and may represent the presence of other limiting factors. Specifically, the presence of interface limited growth kinetics would explain the increased growth of particular hillock relative to others. This plausible explanation of hillock and hole growth kinetics will be discussed in more detail throughout the remainder of this dissertation.

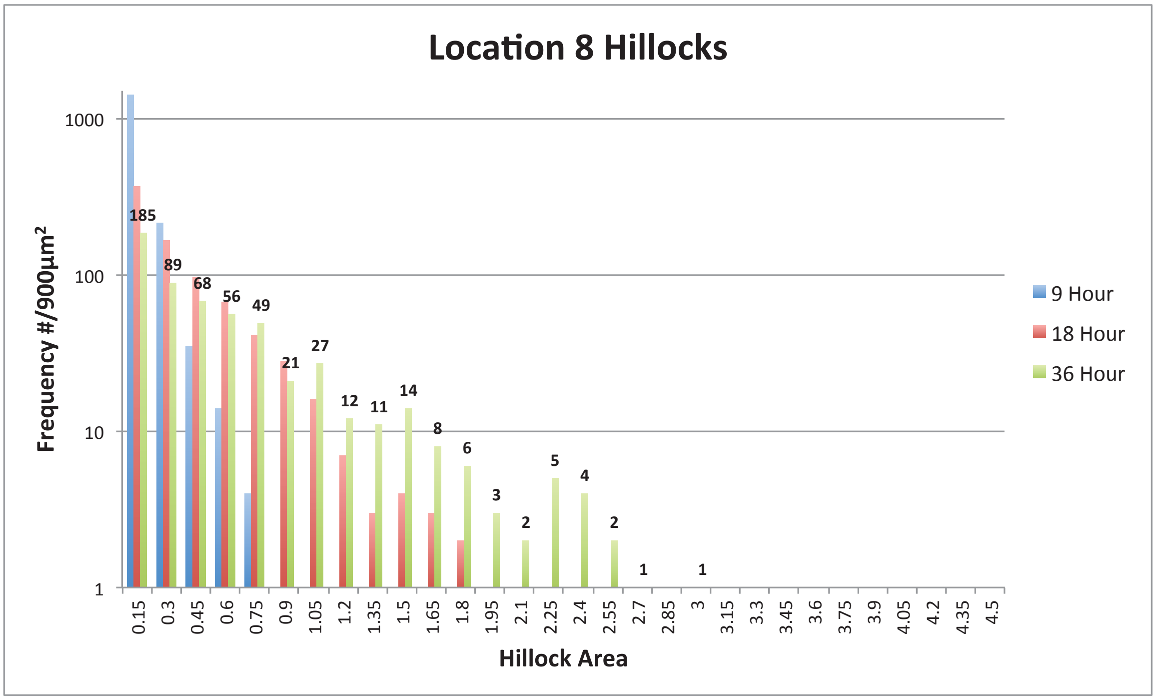

Figure 64. A histogram of the hillock frequency per hillock area bin for Location 8 showing a direct comparison of the number and size of defects present after the 9, 18, and 36-hour anneals and the changes in hillock area distribution.

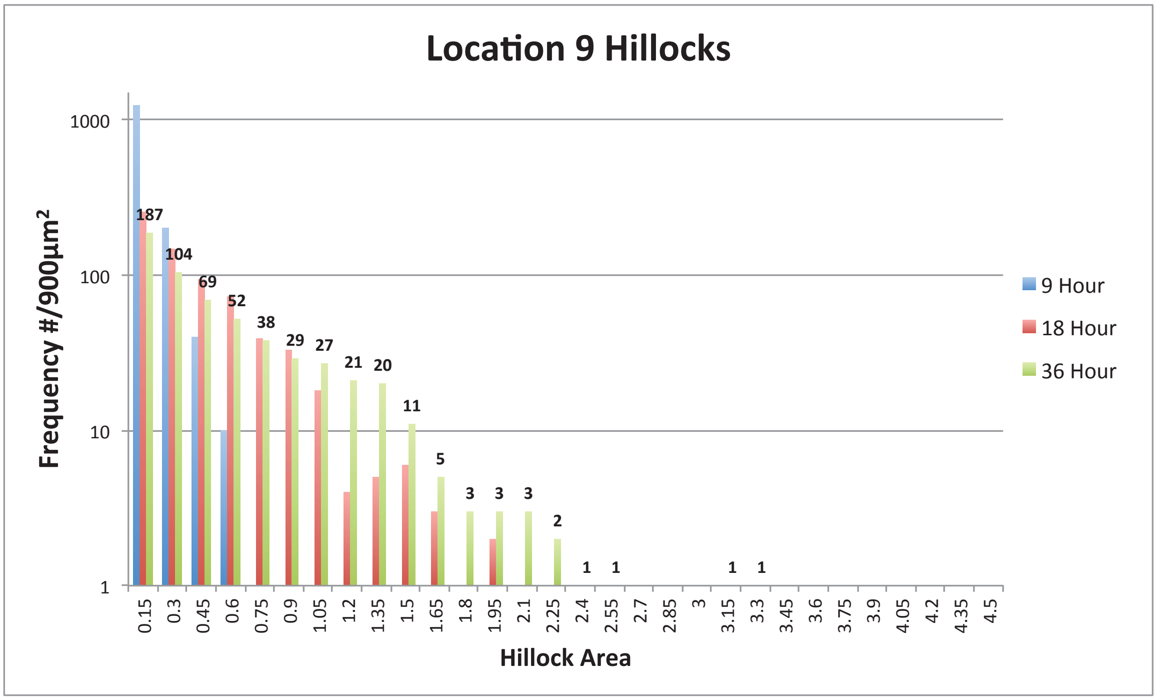

Figure 65. A histogram of the hillock frequency per hillock area bin for Location 9 showing a direct comparison of the number and size of defects present after the 9, 18, and 36-hour anneals and the changes in hillock area distribution.

Using the histogram data as a starting point, the average total area per bin was calculated in order to quantify changes in the distribution of defect sizes. The defect area data were sorted and the average defect area associated with each bin was determined. This average defect area per bin was then multiplied by the frequency of defects within that bin in order to determine the average total area per bin. The average total area per bin was then plotted and used to determine which area range contained the most defect area for both locations after each annealing time. The average total hillock area per bin plots in Figures 66 and 67 provide more detail into which area range contains the most defect area for both locations after each annealing time**.**

For Location 8, the bin containing the most hillock area after the 9-hour anneal is the 0-0.15μm^2 bin. This means that the majority of the hillock area after 9-hours is comprised of small hillocks with areas within this small range. After the 18-hour anneal, this peak has shifted slightly, with the maximum falling in the 0.15-0.3 μm^2 bin. However, the peak has also broadened and there are similar defect areas falling between 0.15-0.6 μm^2. This change in maximum hillock area per bin and broadening in the peak clearly show that hillocks are growing. This is once again the case after the 36-hour anneal, with the maximum area occuring for hillocks with diameters ranging from 0.6-0.75 and an even broader distribution.

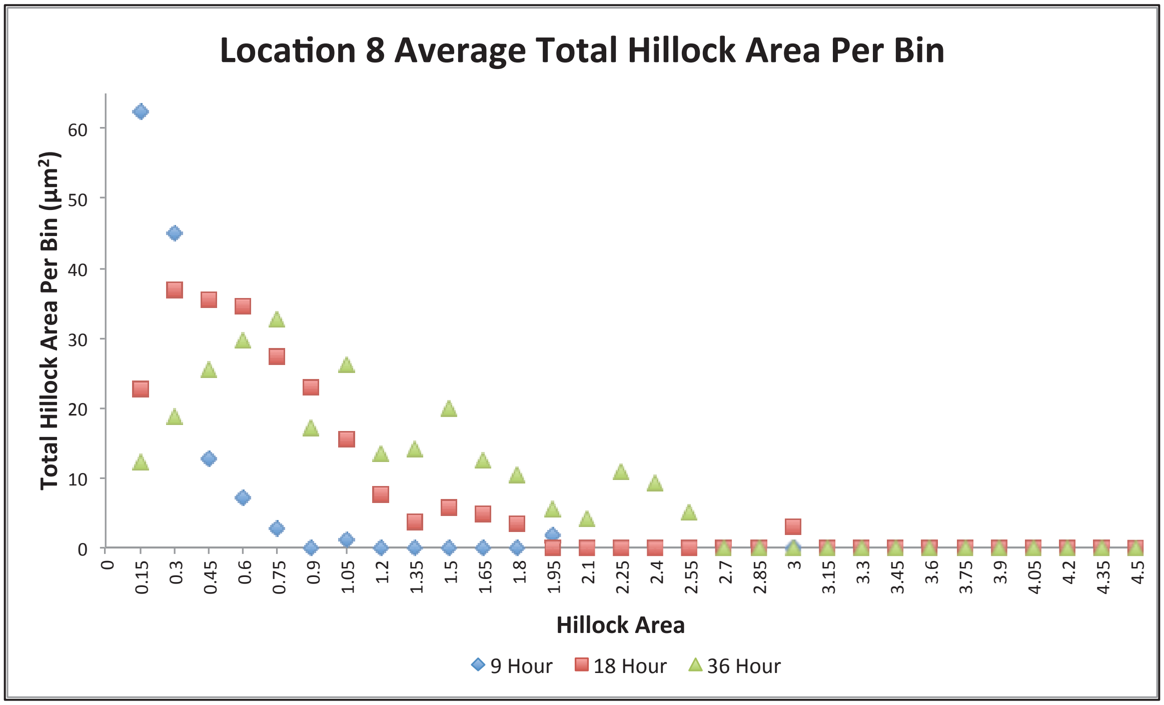

Figure 66. The average total hillock area per hillock area bin for Location 8 showing a direct comparison after the 9, 18, and 36-hour anneals and the changes in hillock area and size distribution.

A similar trend is seen for Location 9 with the bin containing the most hillock area after the 9-hour anneal being the 0-0.15μm^2 bin. After the 18-hour anneal, this peak has shifted slightly, with the maximum falling in the 0.45-0.6 μm^2 bin. Similarly, this peak has also broadened and there are similar defect areas falling between 0.15-0.6 μm^2. This is once again the case after the 36-hour anneal, with the maximum area occuring for hillocks with diameters ranging from 0.15-0.6 μm^2 and an even broader distribution with similar total areas in bins ranging from 0.15 -1.35 μm^2. This change in maximum hillock area per bin and continuus broadening in the peak depicted the hillock growth process taking place during subsequent anneals.

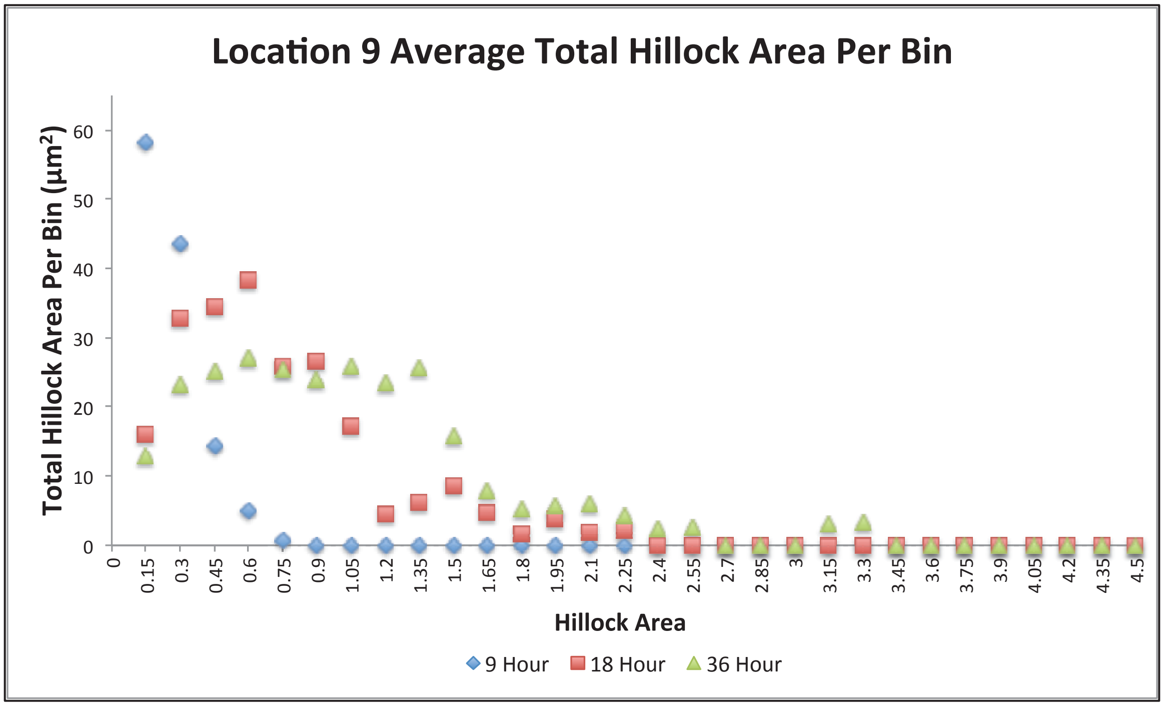

Figure 67. The average total hillock area per hillock area bin for Location 9 showing a direct comparison after the 9, 18, and 36-hour anneals and the changes in hillock area and size distribution.

In order to more closely address the bulk of the hillock data, which is heavily weighted in the smaller area bins, the hillock area data were cropped. The range of data present after a nine-hour anneal was used to define the cropped data maximum value therefore, these cropped plots only include hillocks with projected areas less than or equal to $0.75\mu m^2$. This data set will help to better capture the microstructural changes relating to the small hillocks present after each anneal. For both Location 8 and Location 9, a similar trend of distribution broadening is clear when comparing the 9 and 18-hour anneals. However, differences in distribution for the small holes present after the 18 and 36-hour anneals is not as aparent. It is important to note that the smallest area bins still see a decrease in frequency after the 36 hour anneal but a distinct change in behavior is not visible. This is likely due to the major structural changes being the formation of those much larger hillocks that grew faster than the average hillock structures within the locations of interest.

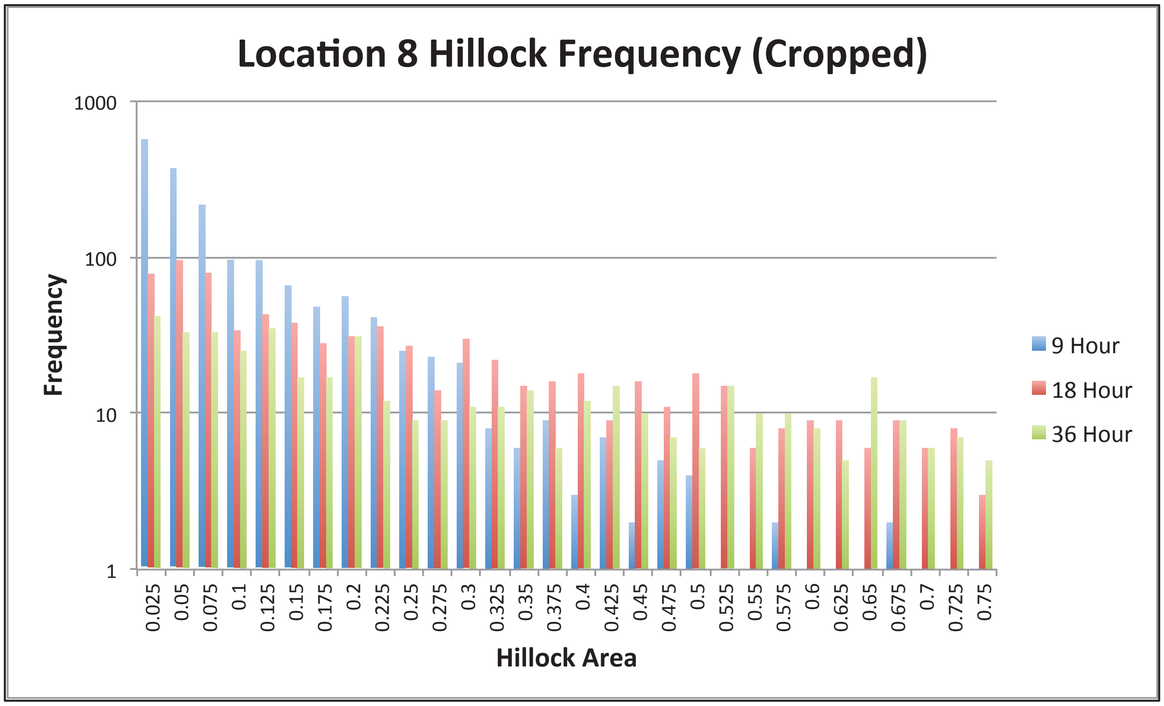

Figure 68. A cropped histogram of the hillock frequency per hillock area bin for Location 8 showing a direct comparison of the number and size of defects present after the 9, 18, and 36-hour anneals and the changes in hillock area distribution for small hillocks.

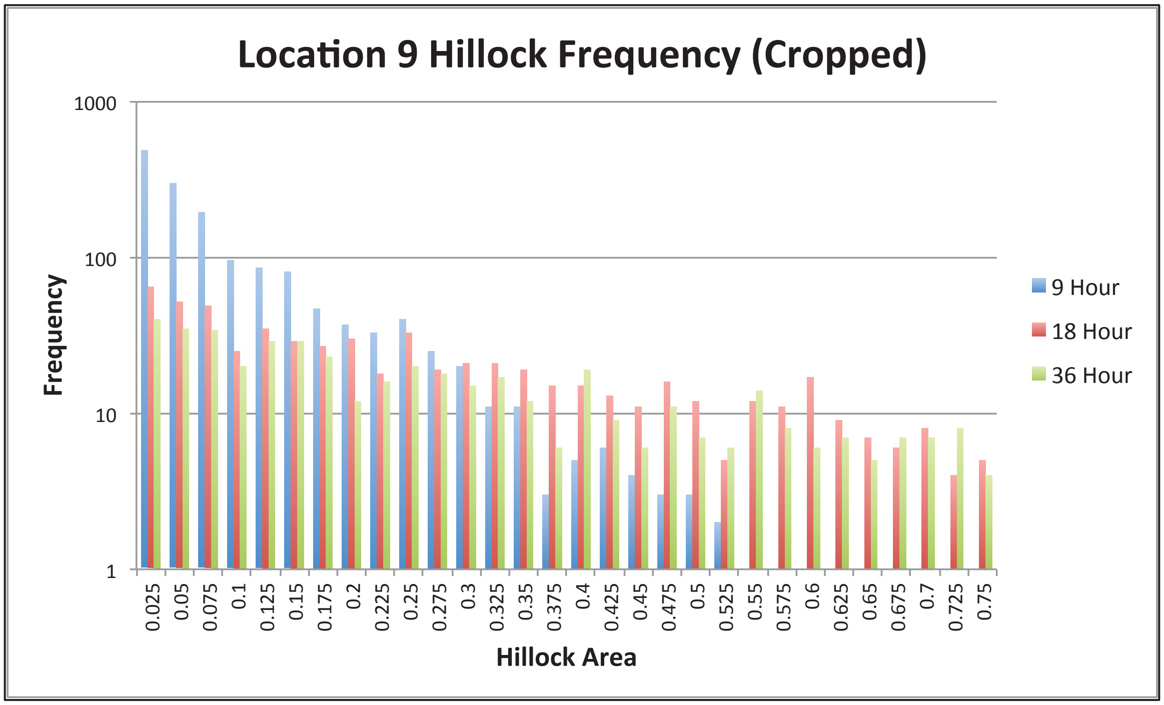

Figure 69. A cropped histogram of the hillock frequency per hillock area bin for Location 9 showing a direct comparison of the number and size of defects present after the 9, 18, and 36-hour anneals and the changes in hillock area distribution for small hillocks.

Again, the average total hillock area per bin plots in Figures 70 and 71 provide more detail into which area range contains the most defect area for both locations after each annealing time**.** For Location 8, the bin containing the most hillock area after the 9-hour anneal is the 0.05-0.75μm^2 bin. This means that the majority of the hillock area after 9-hours is comprised of small hillocks with areas within this range. After the 18-hour anneal, this peak has shifted, with the maximum falling in the 0.275-0.3 μm^2 bin. However, the area distribution has also broadened a great deal. This is once again the case after the 36-hour anneal, with the maximum area occuring for hillocks with diameters ranging from 0.625-0.65 μm^2 and an even broader distribution.

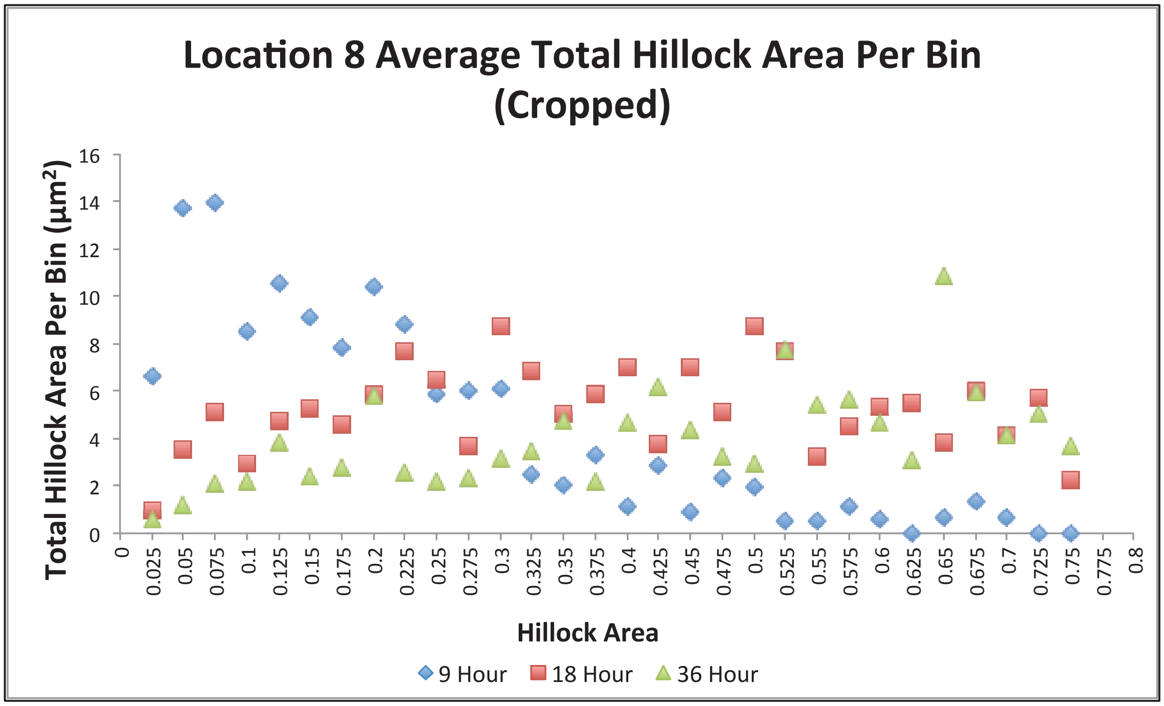

Figure 70. The cropped average total hillock area per hillock area bin for Location 8 showing a direct comparison after the 9, 18, and 36-hour anneals and the changes in hillock area and size distribution for small hillocks.

A similar trend is seen for Location 9 with the bin containing the most hillock area after the 9-hour anneal being the 0.05-0.75μm^2 bin. After the 18-hour anneal, this peak has shifted a great deal, with the maximum falling in the 0.575-0.6 μm^2 bin. However, after the 36-hour anneal, the maximum area occurs for hillocks with areas ranging from 0.525-0.55 μm^2 and an even broader distribution. This change in maximum hillock area per bin and continuous broadening in the peak depicts the hillock growth process taking place during subsequent anneals.

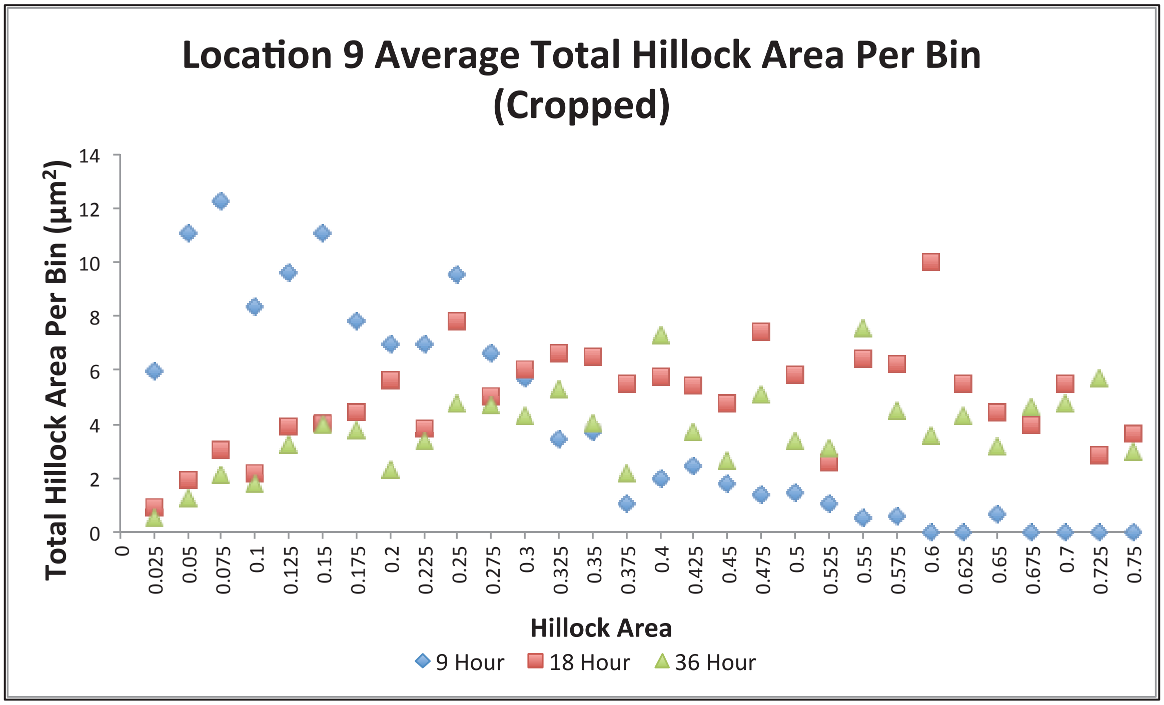

Figure 71. The cropped average total hillock area per hillock area bin for Location 9 showing a direct comparison after the 9, 18, and 36-hour anneals and the changes in hillock area and size distribution for small hillocks.

3.3.2.3.2 Hole Assessment

Along with tracking changes in hillock characteristics, the formation and progression of holes formed during annealing were tracked using the same techniques. Figure 72 shows the average hole density for each location, as determined by the hole densities within the nine area segments from each AFM scan. Average hole density values for individual locations ranged from approximately 0.38 #/μm^2 to 1.2 #/μm^2. The hole density is expected to initially increase during annealing. However, as relaxation progresses and holes continue to grow they will impinge, thus reducing the hole density. The variation in hole density between the 1-hour and 36-hour anneals, as determined by the standard deviation, increases from 0.2 to 1.4. This increase shows that the hole density becomes less uniform across the sample surface as annealing and relaxation progresses. A closer investigation of the hole data shows that 3 of the 6 tracked locations (6,7,&8) show an increase in the hole density after both the 9-hour and 18-hour anneals while the other 3 tracked locations (4,5,&9) show an initial increase after the 9-hour anneal followed by a decrease after the 18-hour anneal. It is expected that initially the film will form many defect sites to relax stresses and as annealing progresses these defect sites will grow. Therefore, it is possible that at the local scale, the film within regions 5 & 6 had already formed the maximum number of hole needed within the section of the film in to reduce the stresses associated with deposition, mismatch, or thermal expansion. Another possible explanation is that the areas tracked were slightly different between anneals and therefore regions with slightly different behavior are being compared at the same location. As previously mentioned, there is some error associated with variations in the scan areas reported. After the 36-hour anneal, all locations show a decrease in hole density. This decrease is likely due to the continued growth and impingement of holes.

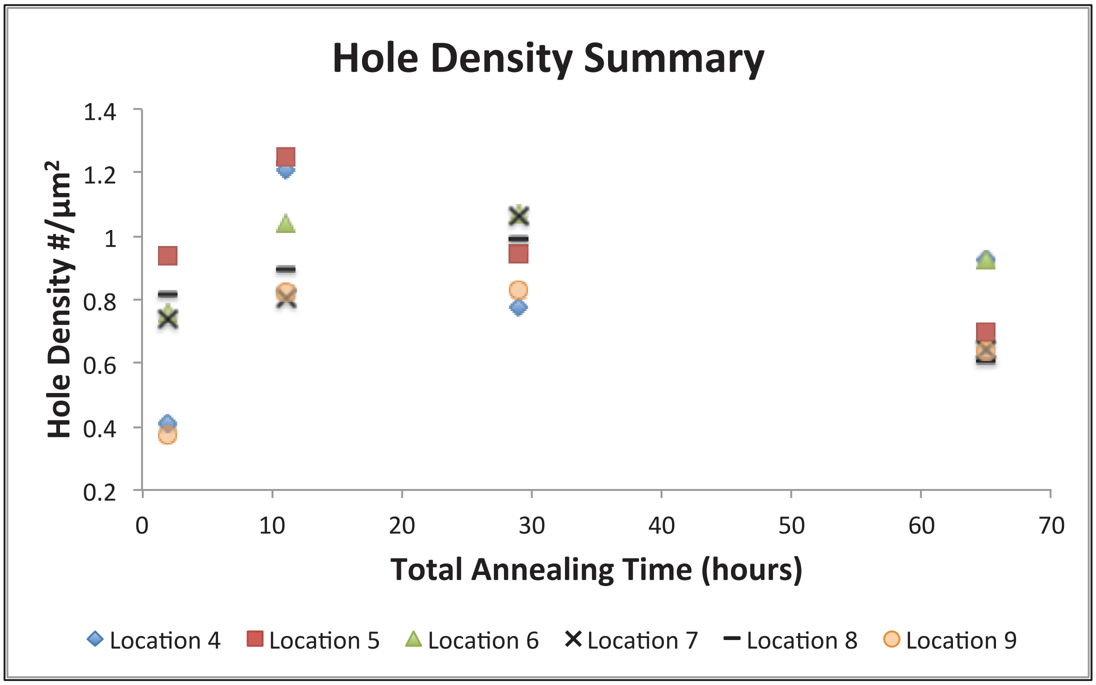

Figure 72. Plot of hole density after each anneal for Locations 4-9 showing the initial increase and overall decrease in hole density with annealing time.

The change in average overall hole density over the sample surface was calculated from the means at each location contained above. Figure 73 depicts the change in average hole density with annealing time for the series of interrupted annealing experiments. As expected, the hole density initially increases as they system creates holes at triple junctions in order to relax stresses and remove higher energy boundaries. As annealing progresses, the holes continue to grow and impinge reducing the number of distinct regions of exposed substrate (or holes).

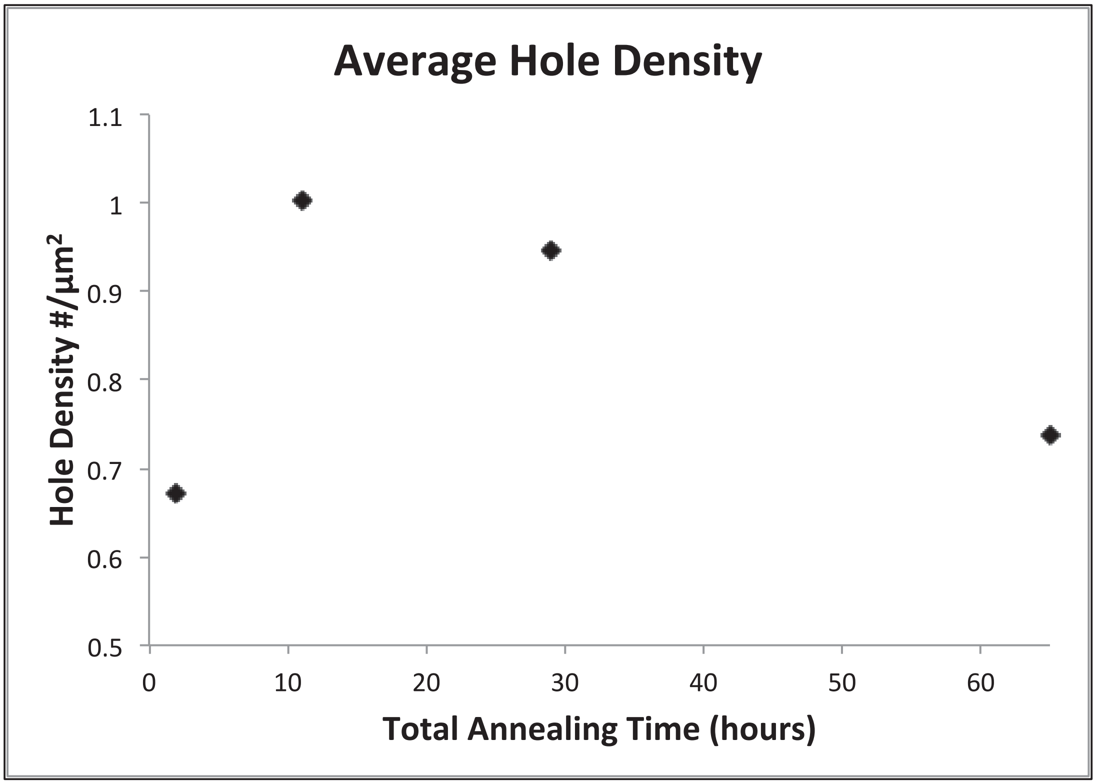

Figure 73. Plot of the average hole density after each anneal for Locations 4-9.

As with the hillock assessment that covered both density and area fraction, the hole area fraction of each location was tracked by comparing the total area associated with holes, as determined by the bearing analysis, to the total imaged area at each location. The average hole area fraction for each location, as determined by the hillock areas measured within the nine image segments from each AFM scan, can be seen in Figure 74. Hole area fraction increases with increased annealing time, showing that holes are growing and becoming more prevalent across the sample surface as annealing and relaxation progresses. It should also be noted that the variation in data, as determined by the standard deviation, also increases from the 1-hour to 36-hour anneals from 0.01 to 0.04. This change in data variation shows that hole area fraction becomes less uniform across the sample surface as annealing and relaxation progresses. The hole area fraction increases for each anneal at each location, except after the 9-hour anneal at location 7. At location 7 there is a slight decrease in the hillock area fraction after the 9-hour anneal. This decrease of 10% is only slightly outside of the known 5-8% error associated with the selection of a different bearing depth (+/- 1nm) and therefore may be a physically representative decrease in hole area. However, this could also be due to the slight variations in the areas tracked and is likely not representative of the film behavior.

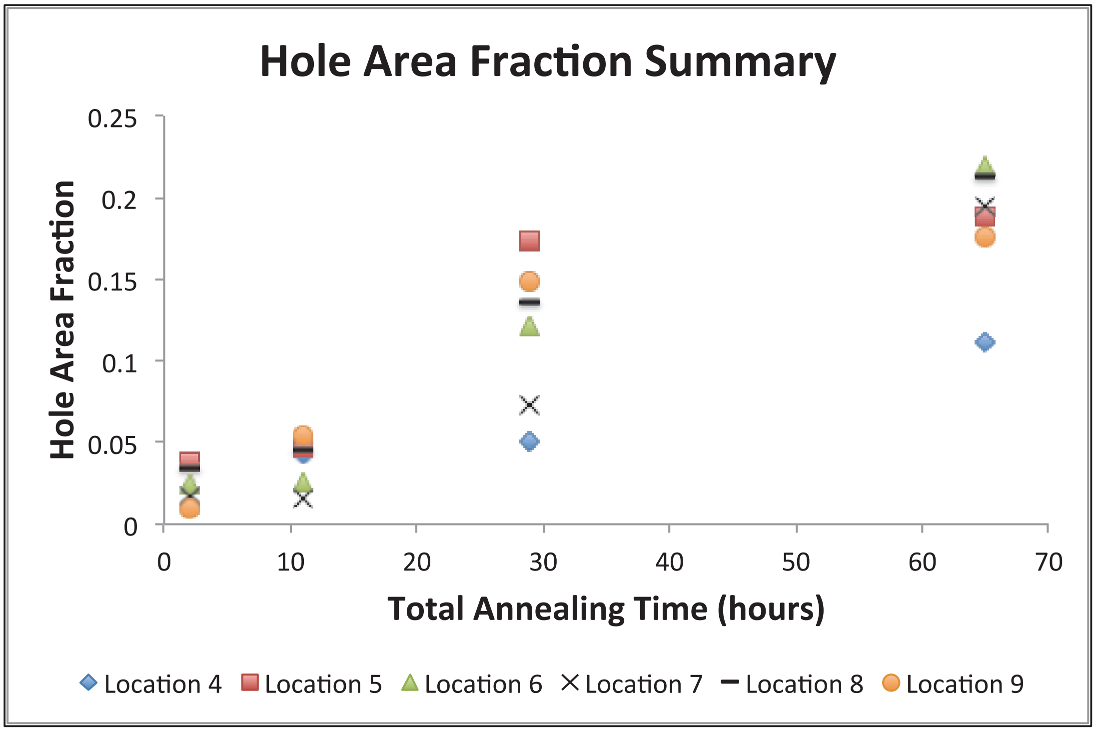

Figure 74. Plot of hole area fraction after each anneal for Locations 4-9 showing the overall increase in hole area fraction with annealing time.

The change in average overall hole area fraction over the sample surface was calculated from the averages at each location. Figure 75 depicts the change in average hole area fraction over annealing time for the series of interrupted annealing experiments. On average, the overall hole area fraction increases with increased annealing time. This increase in hole area fraction suggests that the holes are growing with increased annealing time.

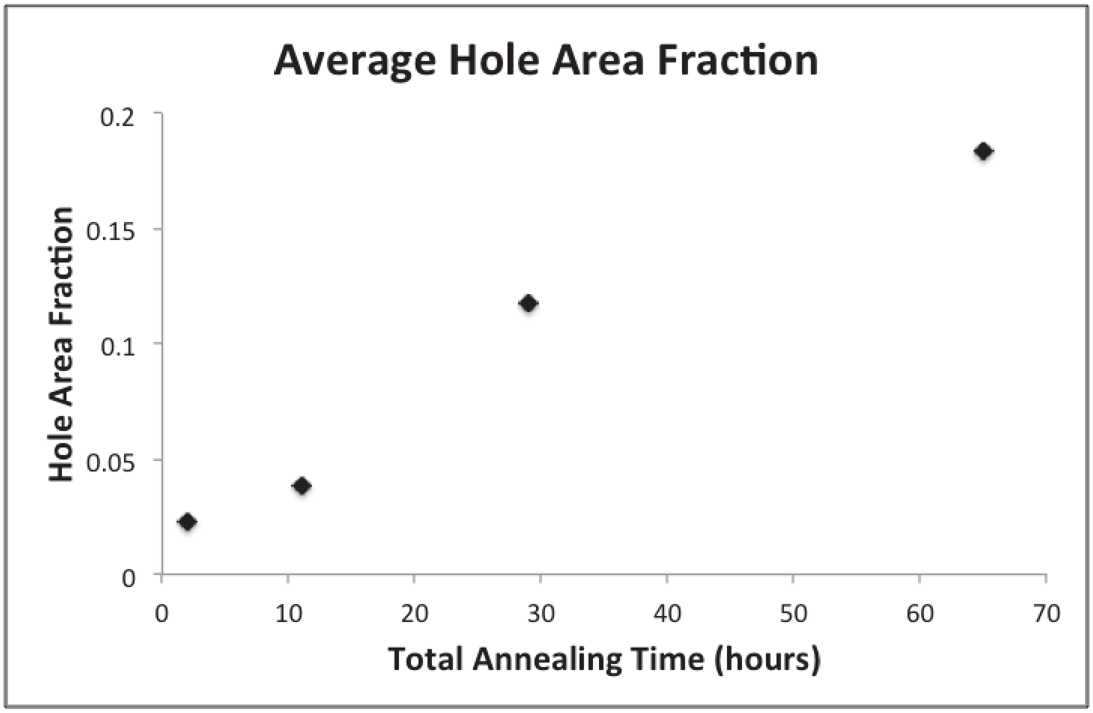

Figure 75. Plot of the average hole area fraction after each anneal for Locations 4-9 showing the area fraction increasing with increasing annealing time.

It should be noted that this rate of hole area fraction change is equivalent to the rate of change for hillock area fraction. The material diffusing away from the film to form holes is diffusing toward the diffusional sinks to form hillocks. Initially, it wasn't clear if this area-projection based bearing analysis technique of hillock and hole growth would be representative of the overall change because of the different conformations that volumes can take on when forming defects. However, the equivalent growth rates for both holes and hillocks in this analysis indicate that the data is representative.

The plots of the previously defined histogram and total area calculations for hole growth can be seen in the subsequent images (Figures 76 - 83). Comparing the Ag hole area distribution after annealing for 9, 18 and 36 hours at 200°C reveals a broadening trend in distribution with some holes growing faster than the average. These faster growing hole are the clusters of hole that have achieved areas greater than 1.5μm^2. This type of hole growth is expected as annealing and relaxation progresses with increased annealing time.

It is worth noting that Location 8 has a single hole with an area that between 4.35-4.5 μm^2. This hole is 10X larger than the largest hole present at this location after the 9-hout anneal. The formation of these larger defects is expected to continue to be present as annealing progresses. But of key importance here is that when comparing the local and global data presented for individual location hole area fractions and densities, the formation of this large hole did not influence the overall averages or global behavior of the film.

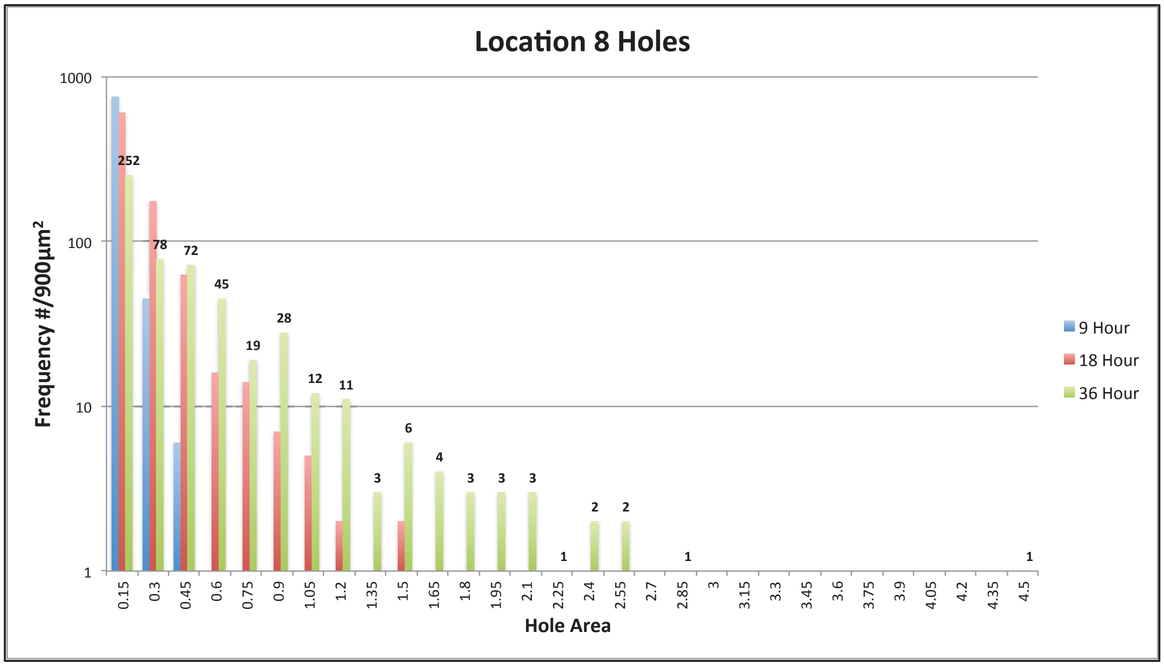

Figure 76. A histogram of the hole frequency per hole area bin for Location 8 showing a direct comparison of the number and size of defects present after the 9, 18, and 36-hour anneals and the changes in hole area distribution.

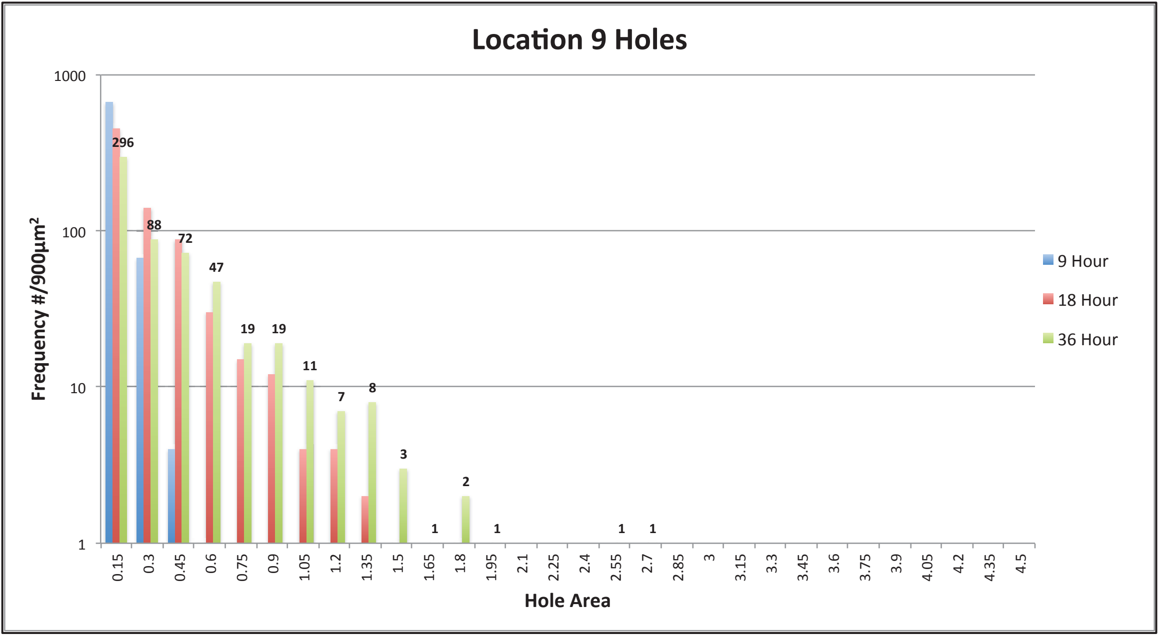

Figure 77. A histogram of the hole frequency per hole area bin for Location 9 showing a direct comparison of the number and size of defects present after the 9, 18, and 36-hour anneals and the changes in hole area distribution**.**

The average total hole area per bin plots in Figures 78 and 79 provide more detail into which area range contains the most hole area for both locations after each annealing time. These plots clearly depict the progression of hole area. For Location 8, the bin containing the most hole area after the 9-hour anneal is the 0-0.15μm^2 bin. This means that the majority of the hole area after 9-hours is comprised of small holes with areas within this small range. After the 18-hour anneal, this peak has shifted slightly, with the maximum falling in the 0.15-0.3 μm^2 bin. However, unlike the progression of hillocks that exhibited a laregly braodened distribution with several area bins surrounding the maximum containing similar total areas, the hole distribution maintains a distinct peak that has broadened relative to the 9-hour anneal but not to the extent seen in the hillock progression. After the 36-hour anneal, this peak has once again shifted slightly, with the maximum falling in the 0.3-0.45 μm^2 bin. However, the peak has also braodened and there are similar defect areas falling between 0.45-0.6 μm^2. This progression and continued broadening of the hole area distribution is characterisic of hole growth behavior.

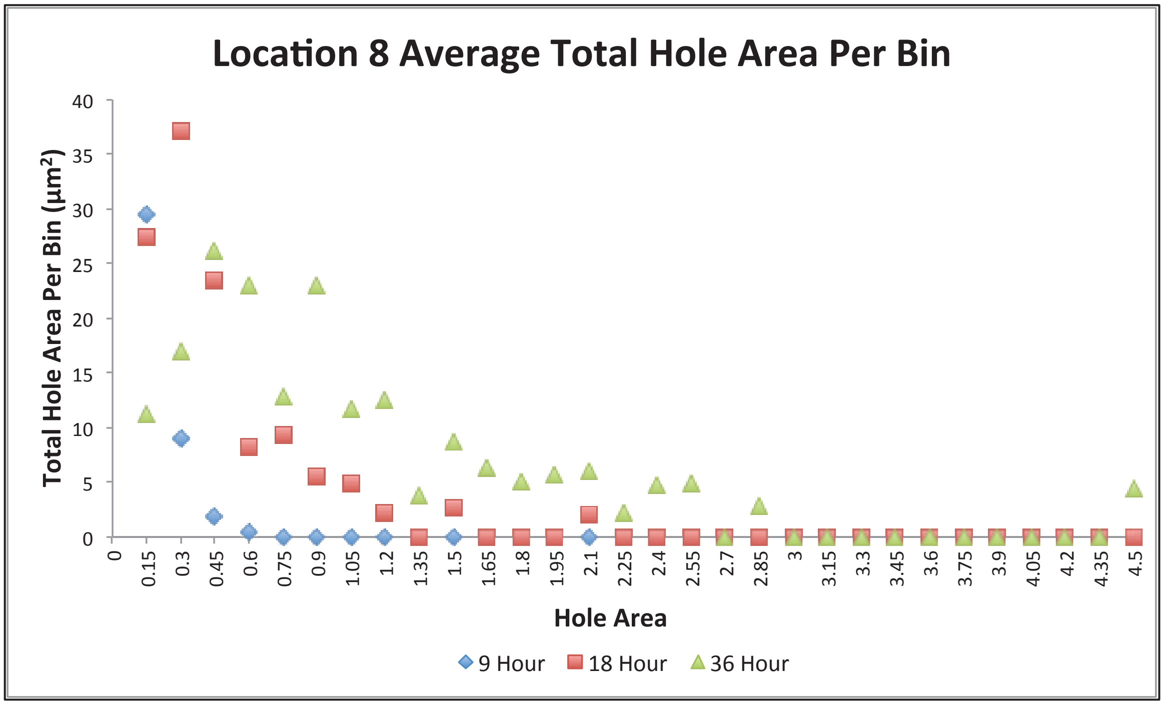

Figure 78. The average total hole area per hole area bin for Location 8 showing a direct comparison after the 9, 18, and 36-hour anneals and the changes in hole area and size distribution.

A similar trend is seen for Location 9 with the bin containing the most hole area after the 9-hour anneal being the 0-0.15μm^2 bin. After the 18-hour anneal, this peak has shifted slightly, with the maximum falling in the 0.3-045 μm^2 bin. Similarly, this peak has also braodened and there are similar defect areas falling between 0.15-0.45 μm^2. After the 36-hour anneal, the maximum area bin doesn't change but the peak is once again broadened and there are similar total areas ranging from 0.3-0.6 μm^2. This change in maximum hillock area per bin and continuus broadening in the peak depicted the hillock growth process taking place during subsequent anneals.

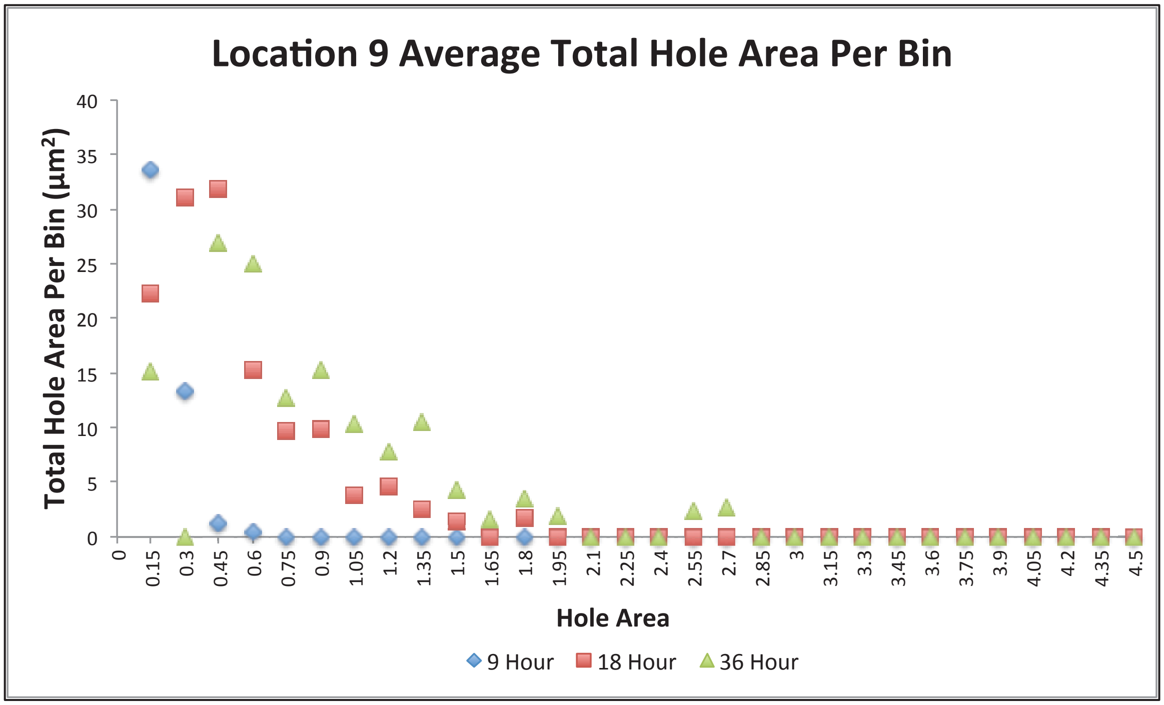

Figure 79. The average total hole area per hole area bin for Location 9 showing a direct comparison after the 9, 18, and 36-hour anneals and the changes in hole area and size distribution.

In order to more closely address the bulk of the hole data, which is heavily weighted in the smaller area bins, the hole area data was cropped to only include hole with areas less than or equal to 0.75μm^2. This data set will help to capture the microstructural changes relating to the small holes present after each anneal. For both Location 8 and Location 9, a similar trend of hole area distribution broadening is clear when comparing the anneals. It is important to note that the smallest area bins still see a decrease in frequency after the 36 hour anneal but a distinct change in behavior is not visible. Unlike the hillock behavior that exhibited a drastic decrease in the frequency of the smallest bin of hillocks after the 18 hour anneal, the distribution change for hole area appears more gradual. However, the same overall trend is present, an increase in larger defects and decrease in smaller defects. The freqeuncy of holes with smaller areas can be seen in the histrograms of Figure 80 and Figure 81. anneals.

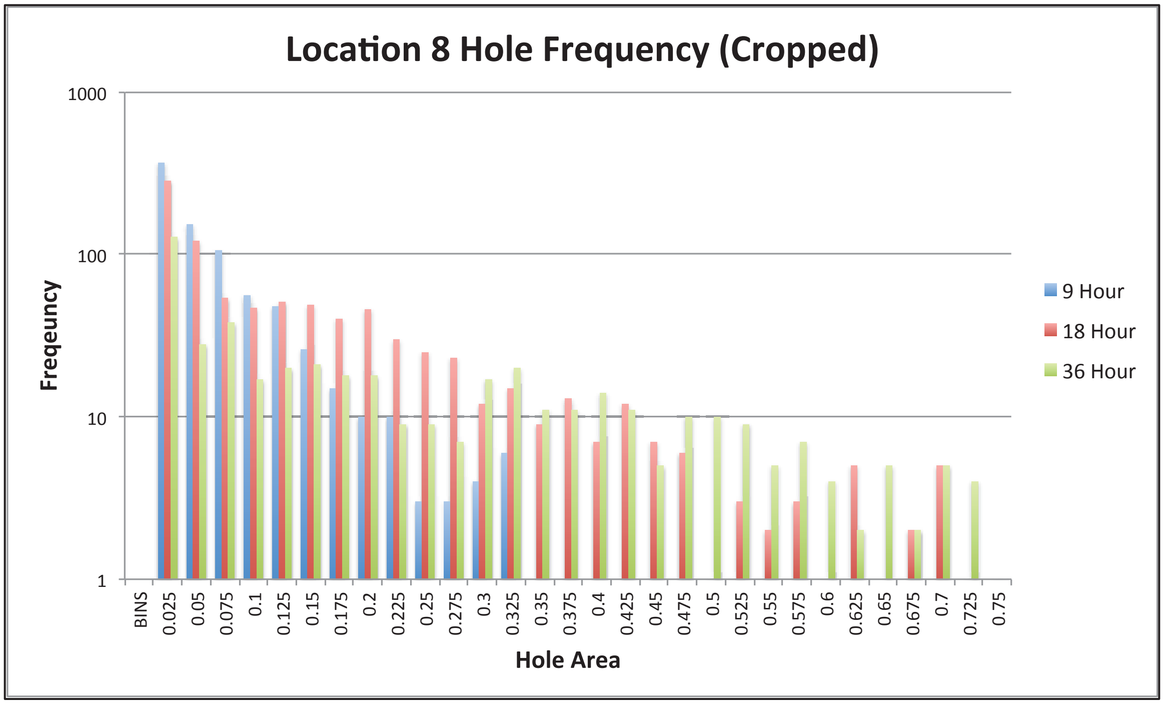

Figure 80. A cropped histogram of the hole frequency per hole area bin for Location 8 showing a direct comparison of the number and size of defects present after the 9, 18, and 36-hour anneals and the changes in hole area distribution for small holes.

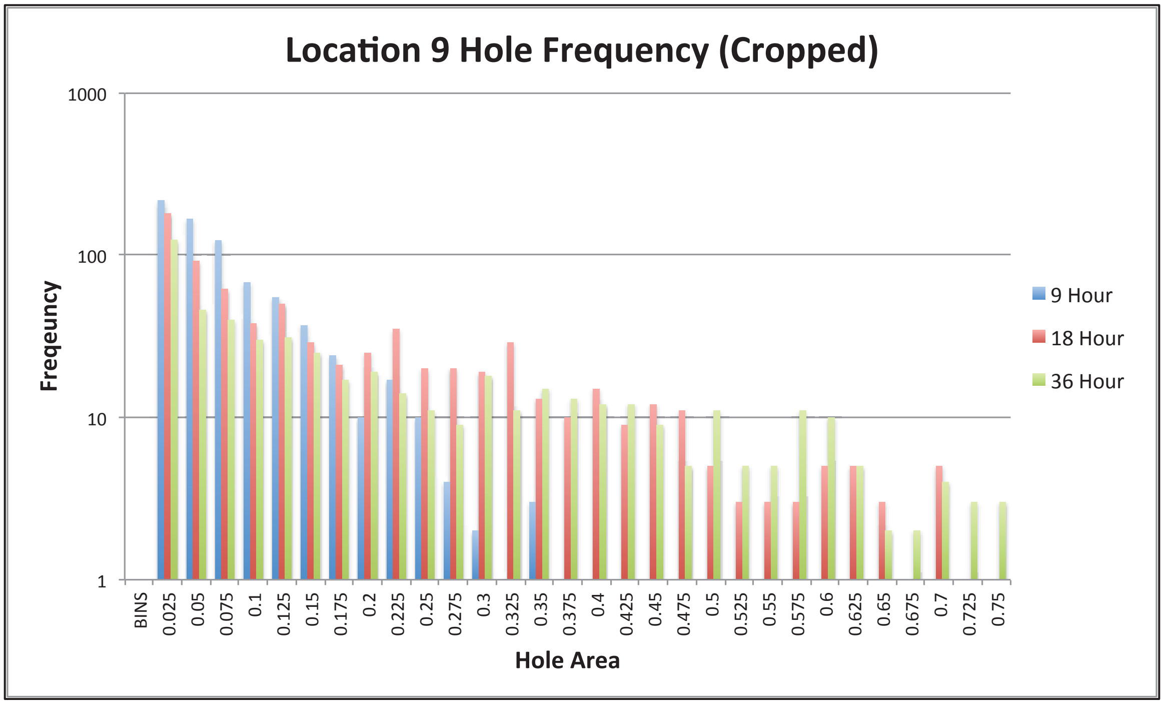

Figure 81. A cropped histogram of the hole frequency per hole area bin for Location 9 showing a direct comparison of the number and size of defects present after the 9, 18, and 36-hour anneals and the changes in hole area distribution for small holes**.**

Once again, the average total hole area per bin plots in Figures 82 and 83 provide more detail into which area range contains the most hole area for both locations after each annealing time. For Location 8, the bin containing the most hole area after the 9-hour anneal is the 0.05-0.75μm^2 bin. The distribution also shows that the majority (if not all) of the hole areas after 9-hours is comprised of small holes with areas below 0.35 μm^2. After the 18-hour anneal, this peak has shifted, with the maximum falling in the 0.175-0.2 μm^2 bin. However, the area distribution has also braodened a great deal. This is once again the case after the 36-hour anneal, with the maximum area occuring for holes with diameters ranging from 0.3-0.325 μm^2 and an even broader distribution.

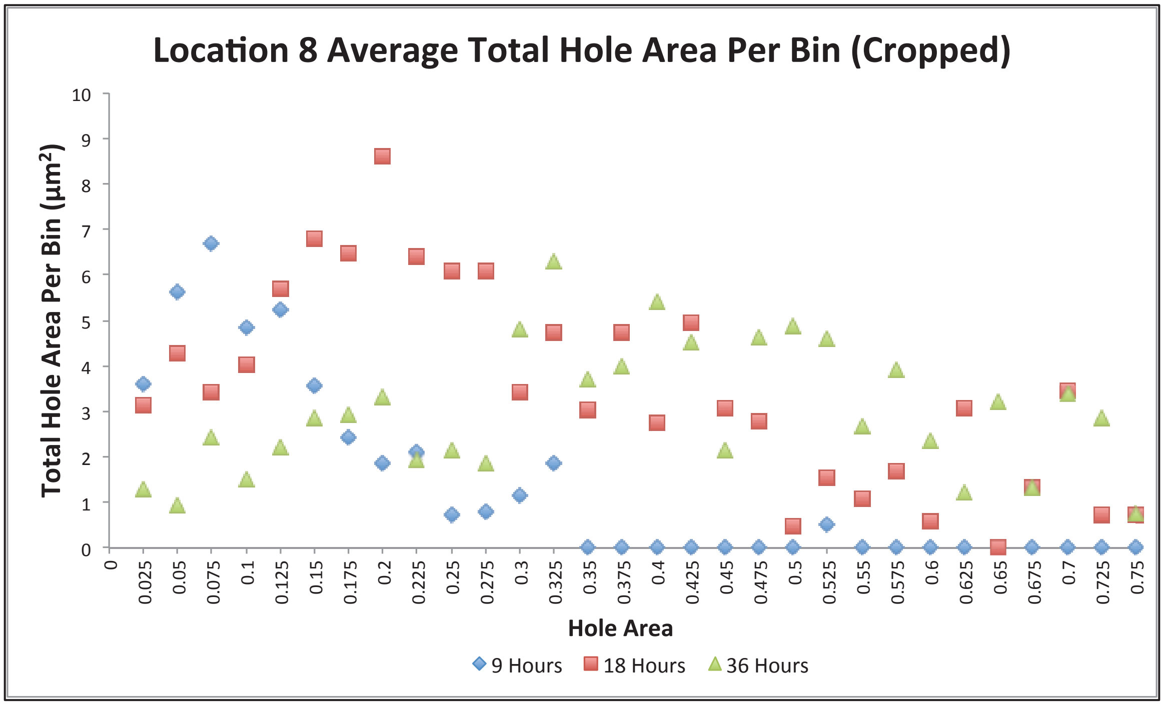

Figure 82. The cropped average total hole area per hole area bin for Location 8 showing a direct comparison after the 9, 18, and 36-hour anneals and the changes in hole area and size distribution for small holes.

A similar trend is seen for Location 9 with the bin containing the most hole area after the 9-hour anneal being the 0.05-0.075μm^2 bin. After the 18-hour anneal, this peak has shifted a great deal, with the maximum falling in the 0.3-0.325 μm^2 bin and the distribution broadening. After the 36-hour anneal, the maximum area occurs for holes with areas ranging from 0.55-0.575 μm^2 and an even broader distribution. This change in maximum hole area per bin and continuous broadening in the peak depicts the hole growth process taking place during subsequent anneals. occuring for holes with diameters ranging from 0.3-0.325 μm^2 and an even broader distribution.

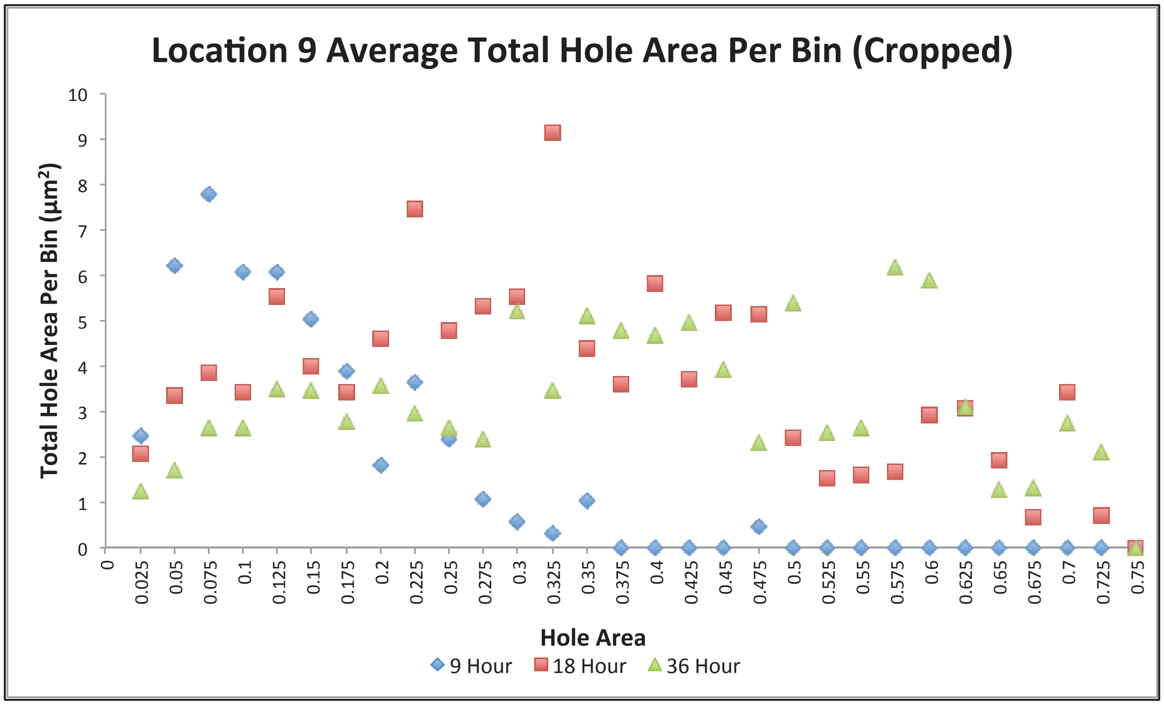

Figure 83. The cropped average total hole area per hole area bin for Location 9 showing a direct comparison after the 9, 18, and 36-hour anneals and the changes in hole area and size distribution for small holes.

3.3.2.3.3 Roughness

In order to better understand the global surface morphology changes the average roughness of each location was tracked using the Roughness analysis feature in Nanoscope at each location. Figure 84 shows the arithmetic average roughness for each location, as determined by the roughness measured within at least 3 AFM scans for each location and time combination.

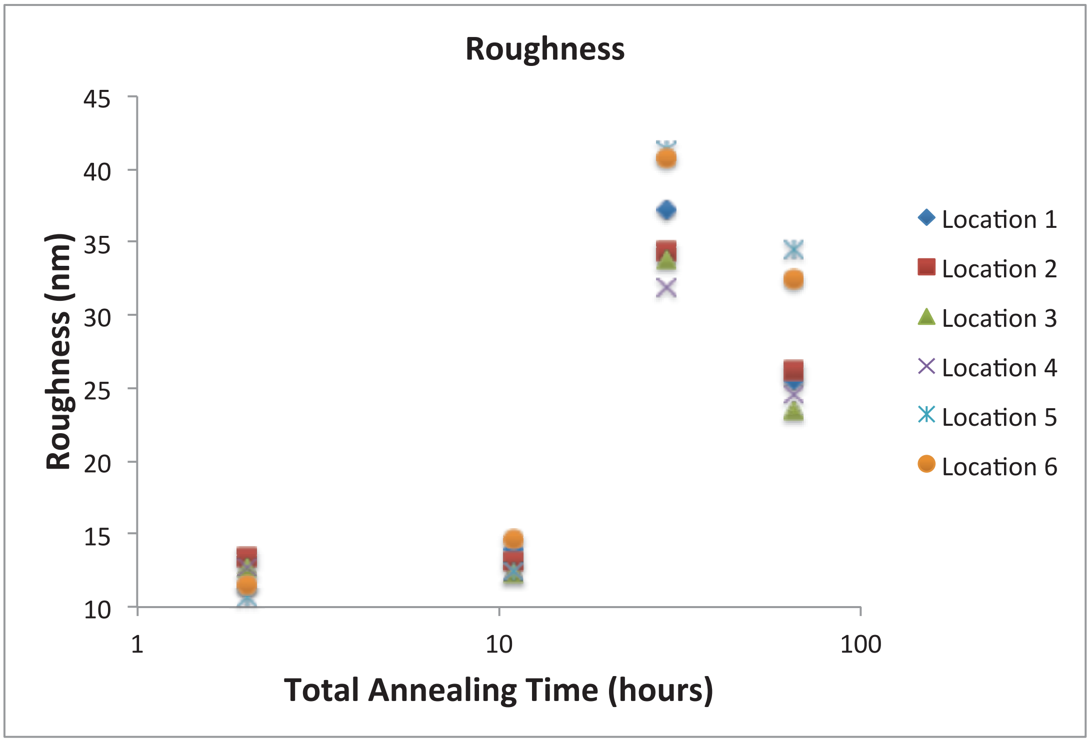

Figure 84. Plot of roughness changes after each anneal for Locations 1-3 showing an overall increase in roughness with annealing time and a decrease after the 36-hour anneal**.**

The data shows an overall trend of increased roughness with annealing time. Specifically, there is a slight increase in roughness after the 9-hour anneal, a drastic increase in roughness after the 18-hour anneal and a slight decrease in roughness after the 36-hour anneal. The decrease in roughness for every location after the 36-hour anneal was not expected. However, it is possible that the microstructure has become more uniform in its height distribution as dewetting has progressed and hillocks growth occurs.

The average roughness over the sample surface was calculated from the averages at each location. Figure 85 depicts the change in roughness over annealing time for the series of interrupted annealing experiments. The average roughness increased from the 1 to 18-hour anneals. However, after the 36-hour anneal the roughness decreased from 37 nm to 28 nm. Similar to the assessment done for the roughness data from the regions surrounding the capped regions (Locations 1 – 3), a logarithmic fit was used to determine the roughness change behavior. The trend line shows and R^2 value of 0.6 and a roughness rate change of 6.1 ln(time).

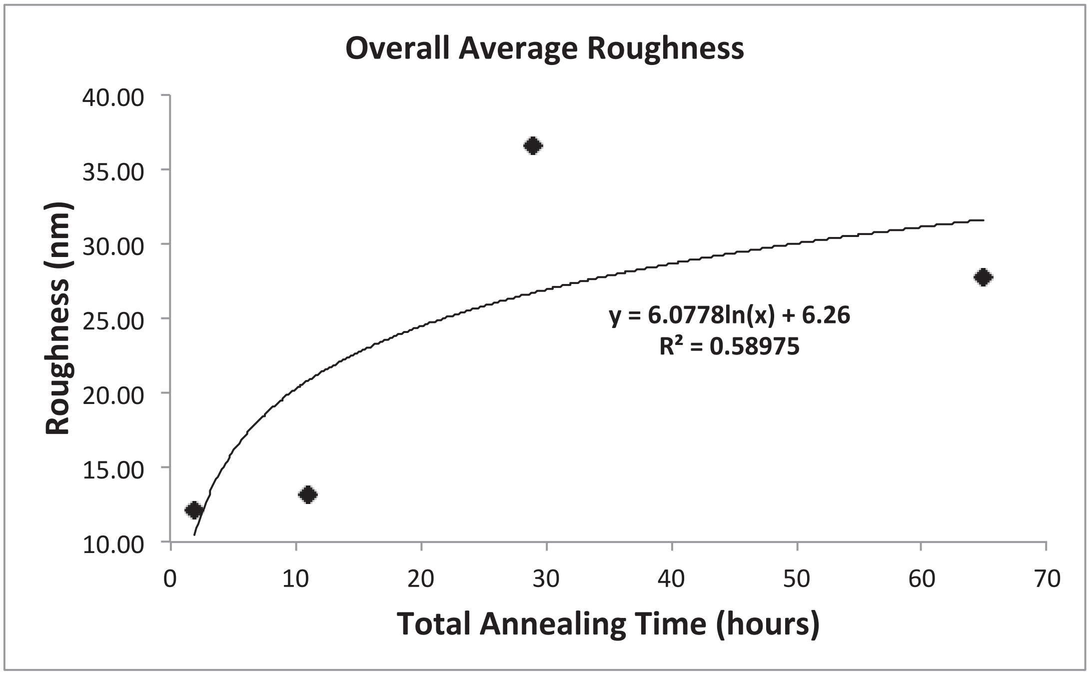

Figure 85. Plot of the average roughness after each anneal for Locations 4-9 showing the roughness rate of change of 6.1 ln(time).

Upon closer investigation, this data trend is similar to the data reported for the regions outside of the capped areas from Locations 1-3. A direct comparison of the two data sets can be seen in Figure 86.

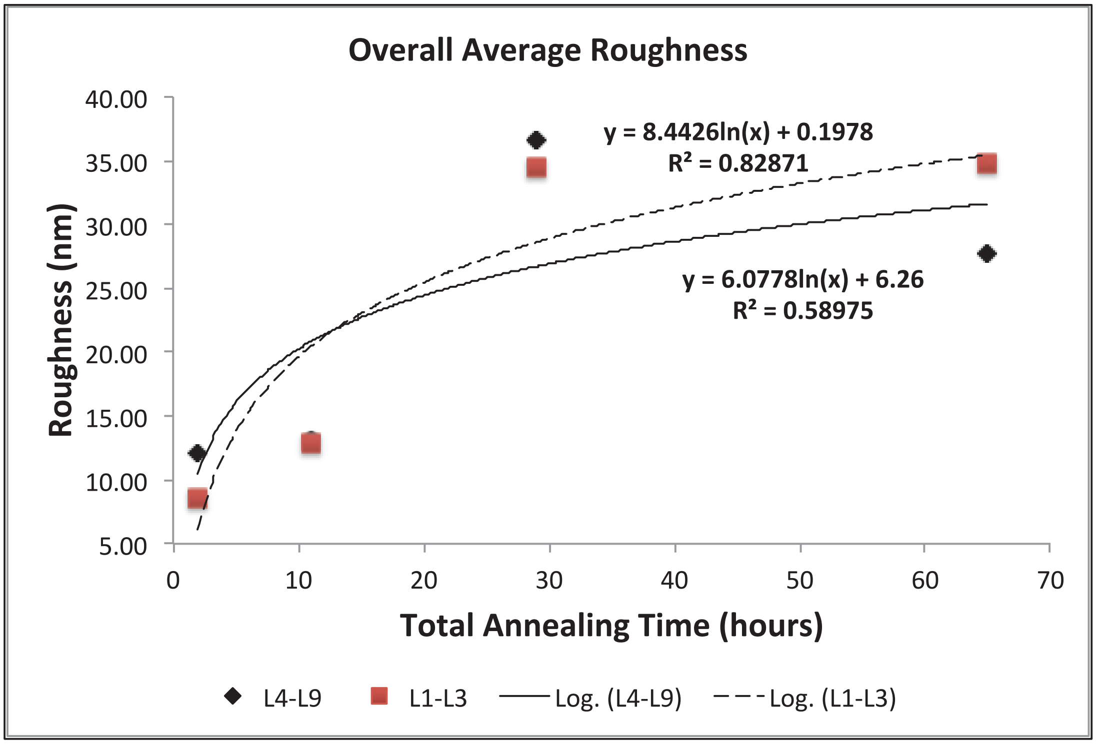

Figure 86. Comparison of the average roughness changes for the non-capped regions in Locations 1-9 (Recall: L1-L3 had data from both capped and non-capped) showing relatively good agreement but indicating that the capping layer likely influenced location kinetics surrounding the capped regions.

While the logarithmic trend line appears to represent the behavior well, the dewetting growth predictions of Brandon and Bradshaw are power-law based relationships. Specifically, void growth rate is proportional to 2/5 (0.4) the power of time and -3/5 (-0.6) the power of film thickness. Therefore, the roughness data trends for capped and non-capped regions were also fitted with power trends. The non-capped regions exhibited roughness change behavior with trends proportional to 0.3-0.44 the powder of annealing time. Capped regions exhibited suppressed behavior with roughness change trends on the order of 0.16 the power of annealing time.

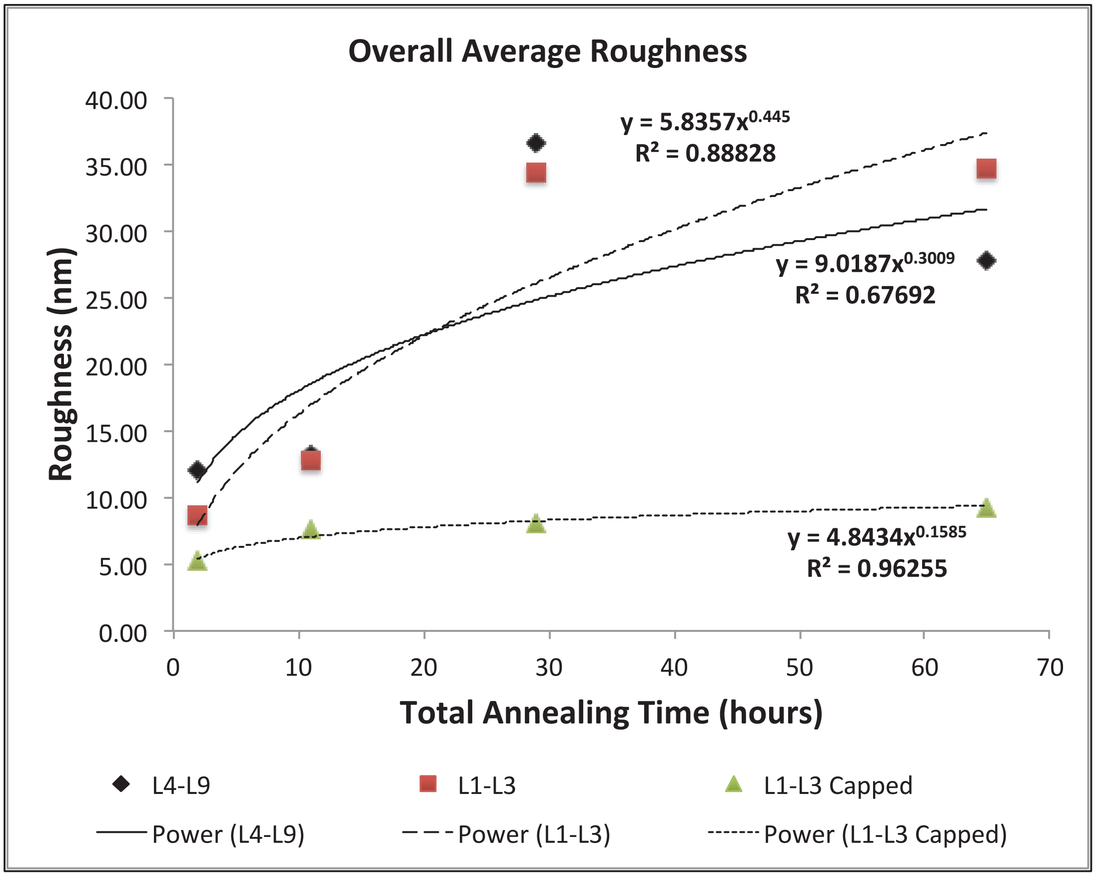

Figure 87. Comparison of the average roughness changes for the capped and non-capped regions in Locations 1-9 (Recall: L1-L3 had data from both capped and non-capped) quantifying the effect of the capped layer on roughness changes.

3.3.2.4 Surface Diffusion Calculation

As previously described, Brandon and Bradshaw developed a kinetic relationship between the surface diffusion coefficient of silver and the annealing time. If we assume that dewetting is controlled by surface diffusion and driven by capillarity for our system, the average surface diffusion coefficient for each annealing time can be calculated using Equation 16 using the average hole radius measured over all six tracked locations where h=50nm, T=473.15 K, $\gamma=1.2\text{x}10^{-5}$ Jcm^{-2} [62], $\omega = 1.7\text{x}10^{-23}$ cm^3 (from FCC lattice parameter), and $v=1.5\text{x}10^{15}\text{cm}^{-2}$ [63]. The data can be seen in Table 16.

Table 16. Table showing the range in diffusion coefficients calculated from the average holed radii measured from the AFM scans after each anneal

Annealing Time (s)	**Average Hole Radius (cm)**	**Diffusion Coefficient (cm^2/s)**
7200	1 E-05	4.3 E-08
39600	1.1 E-05	9.7 E-09
104400	2 E-05	1.6 E-08
234000	2.9 E-05	1.8 E-08

The effective diffusion coefficient decreases 2.4X from the calculated value for 2 total hours of annealing (4.3 x 10^{-8} cm^2/s) to the value for the 65 total hours of annealing (1.8 x 10^{-8} cm^2/s). Performing a 95% confidence interval, it was determined that this array of data, while appearing narrow in range, is statistically significant. Results at both 39,600 seconds and 7,200 seconds are beyond the upper and lower bounds. As predicted, the effective diffusion coefficients calculated for non-capped regions are larger than those for the capped regions. Specifically, the non-capped regions effective diffusion coefficients are nearly a factor of two larger than those for regions with the capping layer. A comparison of the diffusion coefficients calculated for the capped and non-capped regions can be seen in Figure 88.

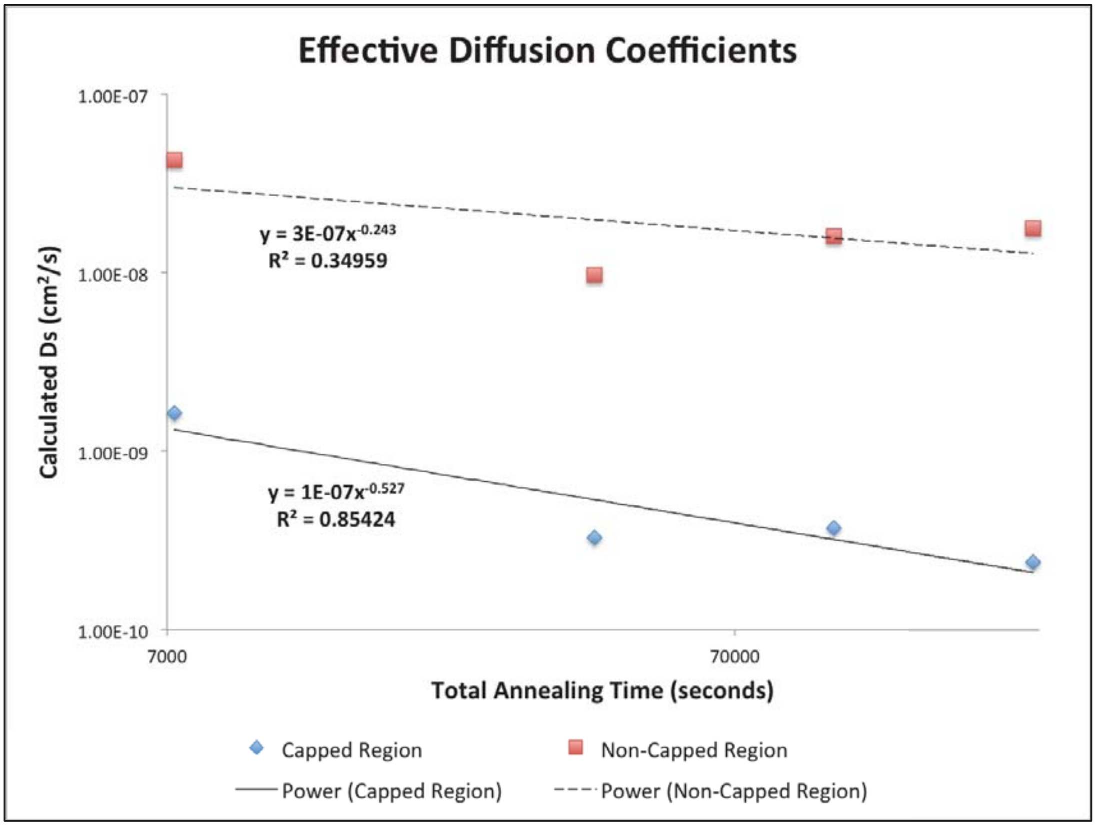

Figure 88. Comparison of the effective diffusion coefficients calculated for the capped and non-capped regions quantifying the effect of the capping layer.

For a direct comparison to recent literature, it can be seen that our calculated silver surface diffusion coefficient values are in good agreement with the reported measurements from Simrick et al, when extrapolated to our experimental temperature. Simrick et al reported a 10^{-7} cm^2/s surface diffusion coefficient for a 275°C anneal.

As another comparison, recall that in the non-uniformity study, assuming a 50nm silver film thickness annealed for 2 hours at 200°C, the diffusion coefficient ranged from of 6.3×10^{-9} cm^2/s to 1×10^{-6} cm^2/s. For the capping layer study, a 50nm film annealed for 2 hours at 200°C results in a diffusion coefficient of 1.6 x 10^{-9} cm^2/s. For the non-capped study, a 50nm film annealed for 2 hours at 200°C results in a diffusion coefficient of 4.27 x 10^{-8} cm^2/s. This comparison shows 27X difference in the predicted diffusion coefficient for regions with and without the capping layer.

As previously mentioned, the non-uniformity present in the first study is likely due to non-thickness related effects. Influences from the film and/or substrate condition, texture, local behavior, stress state, etc. can all greatly influence the formation and progression of dewetting.

Recall that in the Brandon & Bradshaw dewetting model, the surface diffusion coefficient is a constant. As seen within the literature and our experimental results, silver surface diffusion exhibits non-uniform behavior for even slight changes in both physical and experimental parameters. Of key importance for all of the studies presented in this dissertation is that while the diffusion coefficient values calculated from these experiments fall within the broad data range in literature. This does not verify or indicate that surface diffusion is the limiting mechanism behind hole and hillock growth. As previously mentioned, the surface diffusion coefficient data reported in literature ranges over 20 orders of magnitude for similar temperature regimes. The data reported for the scope of the experiments presented in this dissertation sees a change of 2 orders of magnitude. For samples processed similarly and with identical annealing parameters.

This range in reported diffusion coefficients may be directly related to the use of models that assume the wrong kinetic limits. Other factors are likely influencing the diffusion during relaxation. Specifically, the presence of interface-limited kinetics has been evident throughout the literature and the experiments within the scope of this thesis.

The presence of interface-limited kinetics explains the non-uniform behavior present in the literature and these experiments. Interface-limited kinetics don’t follow the same kinetic models as diffusion-limited kinetics. Instead, of system progression being limited by the speed that material can arrive at a sink, the system progression is limited by the availability of attachment site at the sink (interface). This factor is likely influencing both the hole and hillock growth in the system of interest. The effects of this on comparisons, measurements, and calculations of diffusion coefficients throughout literature has resulted in the broad, 20 order of magnitude range of data for silver surface diffusion coefficients.

3.3.2.5 Location Zero

When interface-limited kinetics plays a role in microstructural evolution, the growth of holes and hillocks will be non-uniform across time, which is the case for our results. This is non-uniformity is due to the limited ability of diffusing atoms to find an appropriate interface to attach to. Similarly, if interface-limited growth kinetics are present, growth will not depend on traditionally considered curvature based chemical potential differences but instead will depend on available attachment sites. One tracked location not previously discussed provides even more evidence of the existence of interface-limited kinetics in the dewetting of thin silver films.

Location Zero was SEM'd to deposit a capping layer prior to the first 1-hour anneal, SEM'd and AFM'd after the first anneal, and only AFM'd after the subsequent 1, 9, 18, and 36-hour anneals in order to monitor structure changes surrounding regions with a capping layer. After the first anneal, the AFM scans revealed the formation of large hillocks surrounding the capped region, as seen in Figure 89.

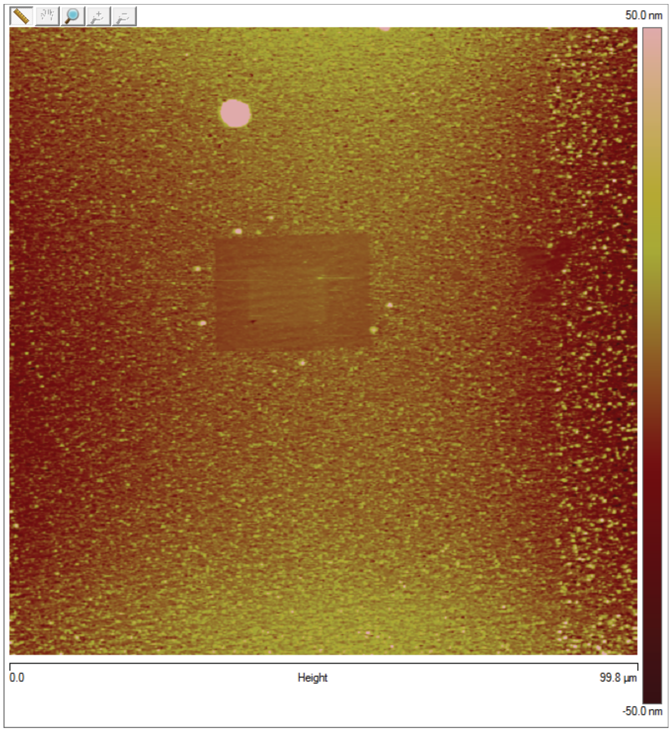

Figure 89. AFM scan of Location 0 showing the formation of large hillocks surrounding the capped region (box).

Using the bearing analysis tool, the height thresholds for the highest sets of data were captured after each scan, as seen in Figure 90. These images clearly show that with continued annealing, the hillocks that formed initially (shown within the white circles) do not remain the highest hillocks within the structure. These initially formed hillocks do not grow vertically at the same rate as the remainder of the structure or they would maintain their status as the tallest features present in the microstructure. Instead, as dewetting progresses and the microstructure develops more hillocks and holes, other regions of the sample form taller hillocks after the 18 and 36-hour anneals.

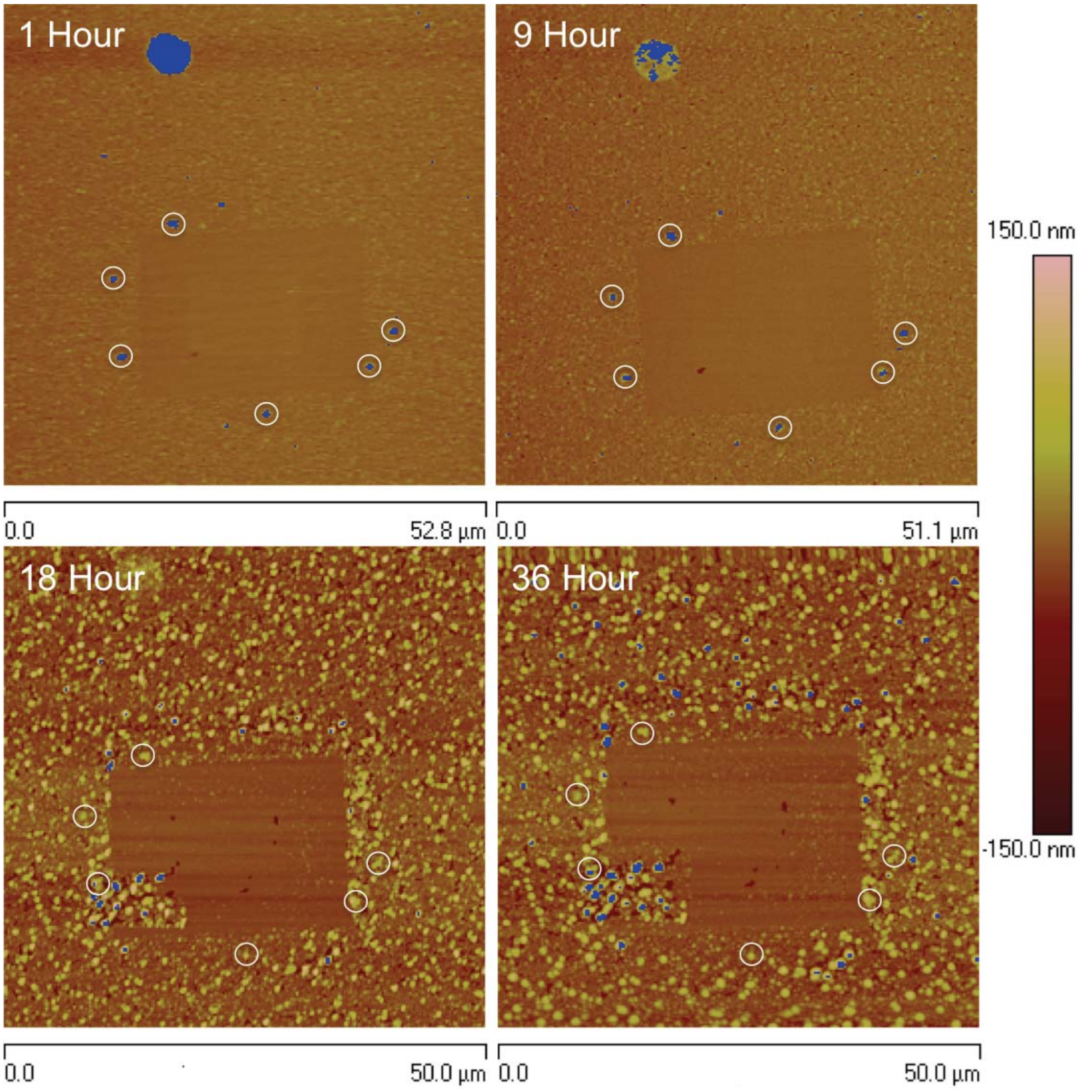

Figure 90. AFM scans from Location 0 showing the highest regions above the bearing analysis threshold with blue pixels

The results from Location 0 combined with the non-uniform diffusion over time, clearly show the presence of interface-limited kinetics in the dewetting of thin silver films. The kinetics of silver thin film dewetting are only sometimes limited by surface diffusion and therefore the traditional experiments for determining the diffusion coefficient of a system may not provide representative data for the silver thin film system. Therefore, a new approach to determining dewetting kinetics is needed in order to accurately describe the behaviors seen.

3.3.2.6 Conclusions

For the thin film dewettting behavior from these experimental results to fit the Brandon & Bradshaw diffusion-limited growth model, the calculated diffusion coefficient at each time for a given temperature would be constant. Because the values reported here both with and without the addition of a capping layer are not constant, the results from this dissertation show the likely presence of interface-limited kinetics during the dewetting of thin silver films. This hypothesis is further validated through the experiments at Location 0 that show if attachment sites for growth are blocked by the addition of a capping layer, dewetting progression is drastically retarded. Similarly, if surface diffusion was the controlling mechanism behind the formation and progression of the microstructural evolution there should be visible build up along the hole edge as predicted by Mullins, Brandon and Bradshaw, and validated in a variety of thin film dewetting studies on other material systems. However, this edge build-up during hole growth and film retraction is not seen in the experiments of silver thin films presented in this body of work. This is another key indicator that other rate-limiting mechanisms are controlling the dewetting progression in silver thin films.

These variations in results from the historically assumed diffusion-limited kinetic models for thin film dewetting could directly explain the broad range of silver surface self-diffusion coefficients reported in literature. The results of these experiments show that the kinetics of silver thin film dewetting may only sometimes be limited by surface diffusion. Because of these results, there is a need to develop a more physically realistic model to identify the contributions of multiple mechanisms to dewetting. In particular, there are times that interface (attachment)-limited growth dominates the dewetting kinetics. Therefore, the traditional experimental methods for calculating surface diffusion coefficients may provide invalid data for the silver thin film system. In the future work section I will propose new experimental methods for determining growth kinetics that will provide more representative data about the diffusion behavior for thin silver films.

3.3.2.7 Future Work

As previously mentioned, in order to properly determine the controlling mechanism for diffusion kinetics of silver thin film dewetting, new sets of experiments are needed. There are a variety of techniques and experiments that can assist in minimizing system variables allowing for more accurate determination of kinetic behavior.

First, the effects of imaging methods on the structural progression need to be quantified and minimized. In order to address the influence of imaging on system behavior in-situ experiments are necessary. As mentioned, regions within the samples studied that were imaged with an electron beam using SEM exhibited different kinetic behavior. Specifically, regions imaged prior to and between anneals exhibited the presence of a carbon-based organic capping layer and the kinetic behavior within these regions was suppressed. These results were reproducible in multiple microscopes, on samples produced through both thermal evaporation and electron beam evaporation, and for different beam settings. Because of the beam effects, atomic force microscopy was used to track microstructural changes, in order to minimize the external influences on growth kinetics. Atomic force microscopy eliminated the presence of any capping layer. However, examination of the final film structure (after all annealing experiments were completed) revealed that regions that were tracked with the atomic force microscope still exhibited minor differences in structure when compared to regions that had never been imaged. Because both scanning electron and atomic force microscopy appeared to influence the structural progression of dewetting, in-situ experimentation is strongly recommended. Additionally, the use of ultra high vacuum imaging equipment will minimize the formation and influence of any organics on the film surface allowing for a better representation of the thin film growth kinetics. The combination of ultra high vacuum scanning electron microscopy and in situ imaging during annealing would allow for direct quantification of the onset and progression of dewetting in the silver thin film system.

Second, the use of controlled geometry structures during annealing will help quantify the influence of interface-limited kinetics on the dewetting progression. Specifically, tracking the structural progression of isolated regions with different orientations during in-situ heating will allow for quantification of the extent of interface-limited growth. This could be the tracking of lines, islands, or other isolated shapes with distinct orientation differences relative to each other and/or the substrate. This type of experiment will allow for determination of specific faces (orientations) that grow or shrink at inconstant rates due to interface-limited kinetics. Recall that under the traditionally assumed diffusion-limited kinetic models, growth of all faces should be constant and uniform. This experimental data will be crucial in better predicting the kinetic behavior of silver thin films and may allow for kinetic engineering (i.e. designing a film with a particular dominate orientation or texture in order to control the kinetic behavior of dewetting).

Lastly, in order for the results of these experiments to be adapted to the Cu-Ag core-shell interconnect system defined in Chapter 2; a study of silver thin film dewetting behavior on copper is necessary. As previously mentioned, there are well-known orientation relationships present between silver and copper. The effect of these orientation relationships on dewetting has not yet been quantified. However, in introductory experiments performed on 50nm silver thin films thermally evaporated on to large grain polycrystalline copper, it was seen that dewetting progressed differently on grains of different orientation. These preliminary results suggest that orientation relationships will greatly impact the dewetting kinetics of the Cu-Ag core-shell system. A comprehensive design of experiments monitoring the dewetting structures and progression of silver thin films on a variety of copper orientations would allow for quantification of these effects. Similar to the controlled geometry experiments previously discussed, the results from orientation relationship experiments would allow for kinetic engineering of the Cu-Ag core-shell system. It is possible that the copper core could be manufactured with a specific surface orientation prior to silver deposition. This could allow for faster, more uniform, or controllable dewetting behaviors resulting in differences in the processing and behavior of the final interconnect. Factors such as interconnect formation time, formation temperature, mechanical strength, or electrical performance could be influenced if the structure and kinetics of dewetting could be better controlled.

In summary, there are a variety of next-step experiments that would allow for better quantification of silver thin film dewetting structure and kinetics. Understanding the influential variables on dewetting kinetics would allow for kinetic engineering of metallic thin films in a variety of applications.

CHAPTER 4. ENVIRONMENTAL IMPACT ASSESSMENT

4.1 Environmental Impact Introduction

4.1.1 Life Cycle Assessment

According to the Environmental Protection Agency, a Life Cycle Assessment (LCA) is: “a technique to assess the environmental aspects and potential impacts associated with a product, process, or service, by: compiling an inventory of relevant energy and material inputs and environmental releases, evaluating the potential environmental impacts associated with identified inputs and releases, and interpreting the results to help you make a more informed decision.” [64] For a comprehensive overview of the Life Cycle Assessment technique please reference the LCA101 document, titled “Life Cycle Assessment: Principles and Practice”. [65] The importance of life cycle assessment is the ability to determine the advantages or disadvantages associated with a proposed technological or materials transition prior to its implementation. In this case, we can determine the human health and environmental impacts associated with the transition of traditionally used lead-free solder to our proposed lead-free solderless interconnect technology.

4.1.2 Solder Interconnects and Their Alternatives: A Comparison

The decision to replace Pb-Sn eutectic solder with SAC-based solders was made based on the presence of Pb in the former, and the absence of Pb in the latter. The terms of the Restriction of Hazardous Substances (RoHS) initiative were drafted in 1999 to be implemented in 2006. The specific materials restrictions were based on human toxicity and concerns about contamination of landfills, and limited lead (Pb) < 1000 ppm, cadmium (Cd) < 100 ppm, Mercury (Hg) < 100 ppm, hexavalent chromium (Cr VI) < 1000 ppm, polybrominated biphenyls (PBB): 1000 ppm, and polybrominated diphenyl ethers (PBDE) < 1000 ppm. It was only after this legislation was enacted, that a formal LCA of impacts other than toxicity were made for Pb-free solder alloys. In 2005, an LCA of Pb-free and Sn-Pb solders by Geibig and Socolof illustrated the issues pertaining to the decision to ban Pb in electronics. [66] Geibig reported that the SAC-based lead-free alternatives had more negative environmental impacts in 10 of the 16 evaluated impact categories when compared to Pb-Sn. [66] However, the majority of these impacts are environmental in nature and not related to human health, which was the motivating factor behind the ban on Pb. In this case, for the EU, a pass-fail criterion on the human health related impact factors trumped any impact associated with other environmentally focused categories. This illustrates the complexity of decision-making based on LCA analysis. There is no single metric that is used as a standard in determining a good or bad performance in an impact category. In the case of the RoHS initiative, a single metric, human health impacts, was predefined as a pass-fail criterion for assessment. However, there is a broad range of impact categories assessed through LCA and individuals, manufacturers, and suppliers, often have differing opinions about how the impact categories should be weighted. For this reason, it is critical to clearly define any weighting or pass-fail criteria used in the evaluation a life cycle assessment.

As seen in table 3-106, from the Gaibig assessment of SnPb and three Pb-free alloys, the difference between impact in any given category ranges from a factor of 40 to a few percent, and are sensitive to the models, boundary conditions and assumptions and input data as clearly articulated in the report. Furthermore, this assessment illustrated that the benefit of going Pb-free becomes greater if an alternative process for silver extraction is used. This example demonstrates the importance of quantifying the impacts of individual life cycle stages as new technologies are being developed rather than inadvertently making choices that, while convenient, may create higher ultimate impacts.

The impacts of using a new technology compared with the existing solution and other alternatives should be explicitly assessed, minimized through possible changes in formulation, and acknowledged when introducing a new technology into the electronics. Taking a forward looking approach, the research study presented in this Chapter addresses these issues by comparing the LCAs for fabrication of the now ubiquitous SAC305 alloy powder and circuit board final assembly with fabrication and assembly using the new technology we have been developing based on the sintering of Cu-Ag core-shell particles.

4.1.3 Comparative LCA of SAC 305 and Cu-Ag Core-Shell Interconnects

4.1.4 Solder and Alternative Comparison – The Scope

As with all LCAs, defining the scope and system boundaries is critical in determining both the relevance and the accuracy of the comparison. For example, if the system boundaries are too narrow, important aspects of the system that influence the environmental impacts may be overlooked, and if they are too wide the assessment may be too broad and with too much uncertainty to be useful in comparison to other assessments.

The flow chart in Figure 91 details the processing steps for manufacturing both SAC305 and core-shell powders, printed circuit board population, and system annealing to produce a functional circuit board. The boxes contained within the region labeled “materials” account for the raw materials needed for production. The diamonds that follow raw materials input account for each processing step needed in order to produce the metal powders associated with each technology. The purple rectangles represent three steps necessary to produce a populated circuit board for both technologies, including: producing a paste out of manufactured powders via flux incorporation, deposition of the paste via screen or stencil printing, and board population or component attachment. The last two diamonds within the “energy consumption” region represent the differences in thermal processing needed to produce a functional PCB from each technology. The system boundaries for this LCA are marked within the materials and energy consumption regions of Figure 91. The manufacturing steps for producing both SAC 305 and Cu-Ag core-shell metal powders are not considered for this assessment. A discussion about their potential impacts and the proper procedure for assessing them will be discussed in the discussion section of this chapter. The raw materials and thermal processing for each technology are the key system differences considered within the scope for this assessment.

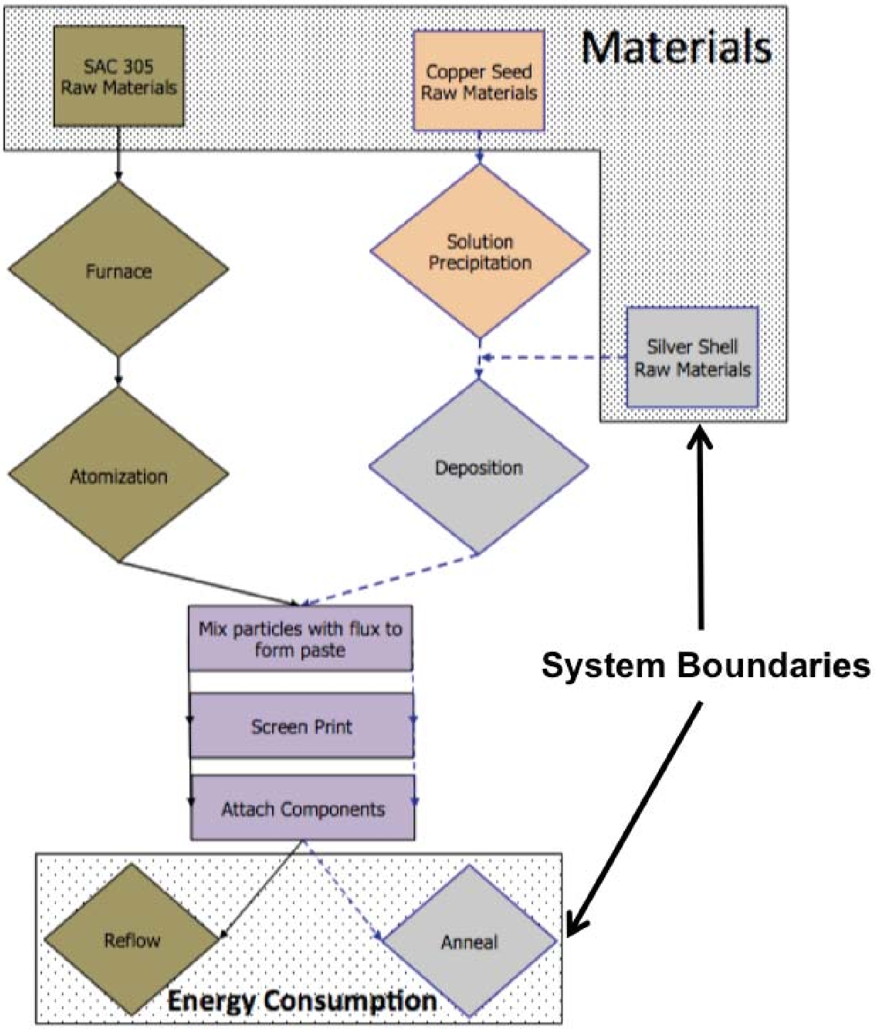

Figure 91. A schematic showing the manufacturing processes for both SAC305 powder and core-shell technology highlighting the system boundaries (Materials for metal production and energy consumption during connection formation)

The compared functional unit will be the production of mechanically stable and conductive interconnects for 360mL of solder paste, enough for component attachment on 180 boards, with the appropriate processing parameters and heating profiles assessed for each technology. Note that the appropriate comparison is by volume of the selected functional unit, not by weight. The densities of the base materials and the interconnect structures themselves are different and interconnects require a specific geometry, hence; a specific volume is necessary for a functional unit comparison not a weight. Due to the difference in thermal profiles required for the two technologies increments of 180 boards are useful for a direct comparison. Assembly using the core-shell technology requires rapid heating to 205°C, an isothermal anneal for 1 hour of annealing, followed by rapid cooling, all in an inert atmosphere. For PCB applications, SAC305 solder joints are traditionally created through the use of a reflow soldering profile that takes 8-15 minutes to solder a circuit board. Based on the oven length, zone dwell times, and conveyor speed, a standard reflow oven produces 180 boards an hour. Annealing for the core-shell technology will likely be a batch process rather than the traditional continuous process of reflow soldering. In order to anneal the core-shell technology in a reflow oven, assuming the entire length is 205°C with a one hour processing time, the length of the furnace would need to be at least 4X longer. Therefore, comparing 180 boards manufactured through reflow to 180 boards annealed in a large walk-in furnace allows for a more realistic direct comparison of the impacts at the industrial scale.

The reference flows assessed include material processing (metal) and the energy required to attach the same number of components to 180 boards using 360mL of solder paste. The volume of metal for each paste system is equivalent and therefore assumed to be 50 volume percent, an industry standard. [15] The fluxes associated with each paste system were not taken included. In this analysis we assumed that the fluxes would be the same, but this is not necessarily true. Based on the Cu-Ag core-shell paste development discussed in Chapter 2, the flux formulation necessary to produce a viable paste for this solder alternative varies slightly in chemical makeup when compared to a traditional SAC 305 solder paste. However, there are still many unknowns for core-shell flux development. Note that the flux formulations in Chapter 2 were selected based on stability, rheology, adhesion, and processability in a circuit board assembly environment, and not based on environmental implications for this LCA. If we were to develop this technology further for commercialization, we would need to reevaluate the candidate flux formulations, based on LCA considerations. It is certain that some possible flux ingredients, such as thiols, would increase the impacts and therefore would need to be included in the assessment before formulation would be done. Along with this, in order to compare the core-shell flux to SAC 305 we would first need to compare the variety of fluxes currently used with SAC305 for reflow applications. However, this assessment may not be useful at this early stage of the technology development.

This assessment does not include the printed circuit board itself nor any of the components attached to the system because they are the same for both technologies. Similarly, it does not include the solder paste deposition or component attachment methods, since we demonstrated in Chapter 2 that the core-shell paste may be processed with the same equipment, i.e. in terms of these steps, the core-shell paste is a “drop-in” replacement for SAC305 paste. Therefore, as noted in Figure 91, this LCA covers only the fabrication of the metal powders and the heating of the populated PCB assemblies with each paste type.

4.1.5 Solder and Alternative Comparison – The Inventory

4.1.5.1 Metal Fabrication Processes

Solder powders, including SAC305 solder powder, are fabricated through a centrifugal atomization process where the input metal is melted, the resulting liquid alloy is dispensed through a rotating atomizer in order to produce metal droplets, and the droplets solidify into metal powders as they cool.

In contrast, Cu-Ag core-shell particles are produced through chemical processing. The copper core particles (500nm-2 um) are fabricated via a solution precipitation reaction and the silver film is deposited onto the preformed copper cores through an electroless deposition process. While there are many processes for making larger diameter copper powder, the processes for forming fine polycrystalline copper particles (<1.5 μm) are more limited. One representative process for manufacturing such fine powders is through a reaction between solutions of Copper (I) Chloride (CuCl) and Iron (II) – citrate. [67,68] The copper particles are then dispersed in an alkaline solution that activates the surfaces for electroless deposition. The activated copper particles are immersed in a solution containing a high concentration of silver ions along with a reducing agent and the surfaces of the copper particles are coated with a uniform silver film. [69,70,71] A material inventory for the fabrication of Cu-Ag core-shell particles using this process can be found in Tables 18 and 19.

4.1.5.2 Materials Inventory

The metals inventory for the processing of 1,328 grams SAC305, the amount needed to fabricate 360mL of solder paste for assembly 180 populated circuit boards, is detailed in Table 17.

Table 17. Material and process inventory for SAC305 particle processing

Materials	Quantity (grams)	Reference
Copper	6.6	Calculated
Silver	40	Calculated
Tin	1282	Calculated

The materials inventory for the processing of 1,852 grams of the Cu-Ag core-shell particles, the amount needed to fabricate 360mL of solder paste for assembly 180 populated circuit boards, is detailed in Table 18. The materials inventory to coat 1760 grams of copper seed particles with 5-wt% Ag is detailed in Table 19. The quantities listed in the table are based on the molar masses of the Eco-Invent Database materials listed and the moles per liter provided in the noted references.

Table 18. Material and process inventory for the copper core formation of Cu-Ag core-shell particle technology

Processing Material	Eco-Invent Database Material	Quantity (grams)	Reference(s)
Copper (I) chloride (CuCl)	Copper (I) Oxide	163	Calculated from the Halaciuga [67]
	Hydrochloric Acid (HCl)	83	
Trisodium citrate dihydrate ($Na_3C_6H_5O_7$-$2H_2O$)		2.2	Halaciuga [67]
Iron (II) sulfate heptahydrate ($FeSO_4$-$7H_2O$)	Iron (II) sulfate ($FeSO_4$)	322	Halaciuga [67]

Table 19. Material and process inventory for the silver shell of the Cu-Ag core-shell interconnect technology

Processing Material	Eco-Invent Database Material	Quantity (grams)	Reference(s)
Ammonium sulfate ($(NH_4)2SO_4$)	Ammonium sulfate ($(NH_4)2SO_4$)	1284.4	Low from Xu range [70]
Ammonium hydroxide (NH_3H_2O)	Ammonium in solution	330.5	Low from Xu range [70]
Silver Nitrate ($AgNO_3$)	Silver	92.62	Calculated assuming only enough Ag for 5wt%
	Nitric Acid	71.64	
Tartaric Acid Potassium Salt (($C_4H_4O_6KNa$)		7.29	Xu [70]

4.1.5.3 Interconnect Formation

The processing method for creating electronic interconnects is different for each of the proposed systems. SAC305 solder paste creates connections by flux activation, solder melting and wetting of the component leads and circuit board pads, and solidification during cooling. This overall process is known as “solder reflow“, in electronics manufacturing. As described in greater detail in Chapter 2, these process steps are carried out in a well-controlled multi-zone furnace where the circuit boards are transferred from zone to zone on a continuous conveyor belt. This reflow process typically takes minutes (8-15min) and a traditional reflow oven can output approximately 180 boards in an hour. [15] The Cu-Ag core-shell technology requires annealing at 205°C for an hour in an inert atmosphere. [11,72] To compare these technologies the Cu-Ag batch furnace must be capable of holding 180 boards in order to provide the same hourly production rate.

Table 20. **Energy consumption each technology furnace**

Solder Type	Oven Type	Avg. Power Consumption	Reference
SAC305	Reflow Oven	10	Average from Kazinca [73]
Core-Shell	Inert Gas Oven	5*	*Approximated

*NOTE: This value is based on the energy ratings provided for a variety of similar inter gas ovens

4.1.5.4 Assumptions

The silver film electro-less deposition process for the sourced core-shell particles is proprietary and therefore the electro-less deposition method was assumed to be comparable to a well documented method from literature, i.e., it was assumed that this process is representative of the one used to manufacture the Cu-Ag core-shell particles. Furthermore, the literature references for the processes for fabricating both the copper core and silver shell are for lab-bench scale manufacturing in terms of quantity and production. Therefore, we assume that the scale to industrial manufacturing is linear in this case. This is likely an overestimate due to the economy of scale.

To develop assessments for materials, SimaPro v7.1 and the Ecoinvent 2.0 database are used in conjunction with TRACI impact factors. Due to lack of material availability in the database, substitution was required for some reagents for both the copper seed particle precipitation and silver electro-less deposition reactions. These substitutions were either chemically similar materials that are expected to be representative of the environmental impacts of the original reagent while maintaining the function of the reaction system, or a combination of chemicals needed to produce the required material, for example, copper chloride and silver nitrate were replaced by the components used to manufacture them.

Silver nitrate is often manufactured by dissolving silver in nitric acid. Using the reaction listed below, and an assumption that the amount of silver needed is only that needed to produce a 5wt% Ag shell, the amount of nitric acid was calculated.

$$4Ag + 6HNO_3 \rightarrow 4AgNO_3 + NO + NO_2 + 3H_2O$$

Copper chloride is often manufactured by dissolving copper (I) oxide in hydrochloric acid. Using the reaction listed below and a simple conversion the amount of copper oxide and hydrochloric acid needed to produce the known amount of copper chloride needed for the reaction was calculated.

$$2HCl + CuO \rightarrow CuCl_2 + H_2O$$

Currently, the impacts of tartaric acid potassium sodium salt ($C_4H_4O_6KNa$) and trisodium citrate dihydrate ($Na_3C_6H_5O_7$-$2H_2O$) are not included in the assessment of the impacts. However, based on the typical uses and toxicology data for both of these constituents, available through the National Institute of Health, it can be assumed that their impacts will be negligible in comparison to the other raw materials. Tartaric acid potassium sodium salts are commonly used for a variety of medicinal and baking applications. Specifically, tartaric acid potassium sodium salts are found as ingredients in medical laxatives, baking powders, cake mixes, a variety of leavening agents, and even in the manufacturing process for hard candy. [74] Similarly, trisodium citrate dihydrate (trisodium citrate), is also commonly used in a variety of medical and food applications such as a blood anti-coagulant, an expectorant, a nutrient to prevent curdling of milk, and even an additive in soft drinks. [75] Because of their common use in widely consumed food products and ingested in medicines, it can be assumed that the impacts associated with tartaric acid potassium sodium salts and trisodium citrate are negligible when compared the impacts of the other raw materials, such as silver.

4.2 Results and Discussion

Using the TRACI impact assessment outputs the environmental impact of the materials used in manufacturing both SAC305 and Cu-Ag core-shell particles was evaluated. Results on the outputs are detailed in Table 21. The comprehensive analysis of the impacts associated with each constituent is available in the Appendix .

Table 21. TRACI Impacts for the materials used to manufacture SAC305 solder and Cu-Ag core-shell particles. The table also shows the core-shell breakdown in terms of core particle precipitation and shell deposition impacts**.**

Impact Category	SAC 305	Cu-Ag core-shell total	Core Particle	Shell Deposition
Global Warming (Kg CO2 eq)	39.4	45.8	0.57	45.2
Acidification (H+ moles eq)	43.8	35.1	0.93	34.2
Carcinogenics (Kg benzene eq)	0.1	0.33	0.21	0.12
Non-Carcinogenics (Kg toluene eq)	2002	2684	186	2497
Respiratory Effect (Kg PM2.5 eq)	0.34	0.13	0.006	0.12
Eutrophication (Kg N eq)	0.03	0.04	0.0004	0.03
Ozone Depletion (Kg CFC-11 eq)	2.89E-06	4.01E-06	1.72E-07	3.84E-06
Ecotoxicity (Kg 2,4-D eq)	688	922	10.5	911
Smog (Kg NOx eq)	0.35	0.44	0.003	0.43

According to our results, the environmental impact of the core-shell technology is higher than that for SAC305 for all but two categories, acidification and respiratory effect.

Visual representations of the human health and environmental impact data detailed Table 22 can be seen in Figures 92 and 93.

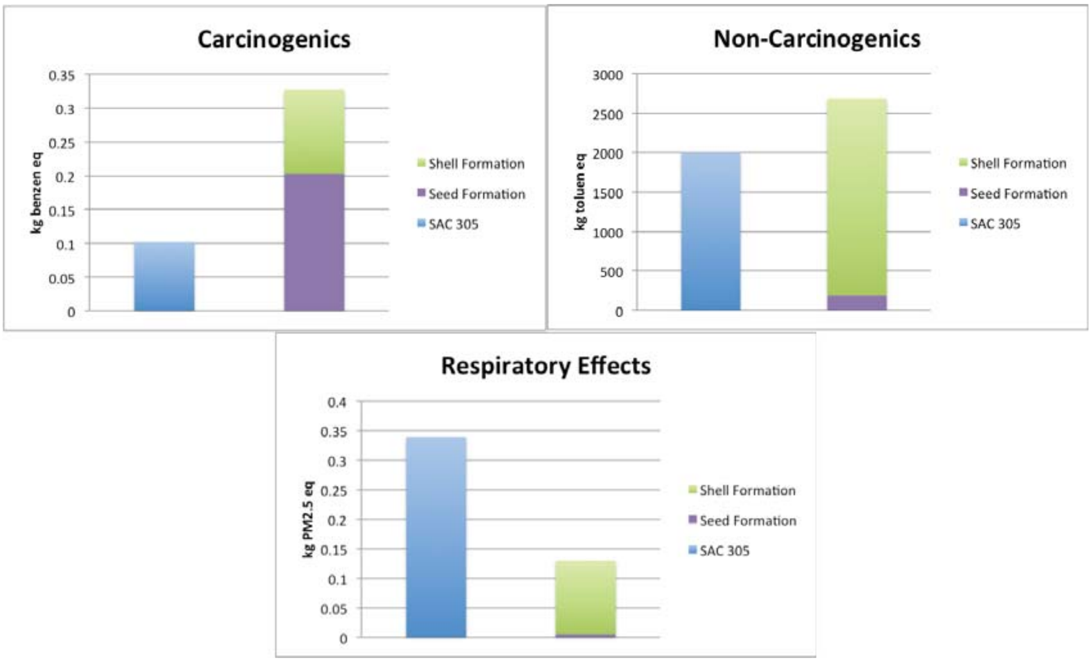

Figure 92. Plots of the human health TRACI impacts associated with the materials needed for manufacturing of SAC305 and Cu-Ag core-shell particles (separated by seed formation and shell formation)

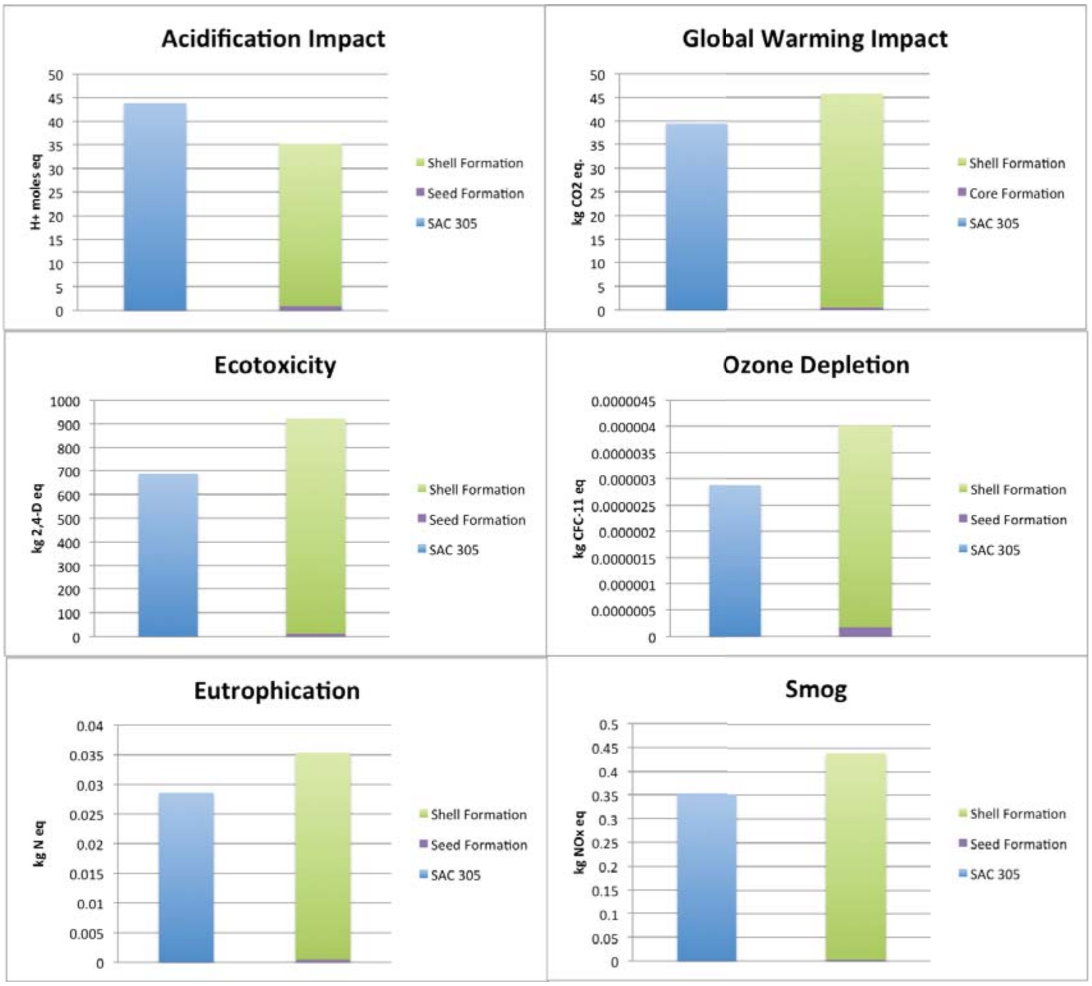

Figure 93. Plots of the environmental TRACI impacts associated with the materials needed for manufacturing of SAC305 and Cu-Ag core-shell particles (separated by seed formation and shell formation)

The results presented here suggest that the overall environmental impact of the material inputs for manufacturing Cu-Ag core-shell solderless interconnect system is greater than SAC305. In seven of the nine categories, the impacts associated with the materials to fabricate the core-shell technology are greater than those of the materials needed for SAC305 production.

The majority of the impact associated with the core-shell system comes from the amount of silver needed for the electroless deposition of the silver shell. In six of the nine categories the impacts associated with the silver for the shell deposition account for more than 90% of the total core-shell impact. As noted in the assumptions section, it was assumed that the bench-top processing method found in literature was not only representative of the proprietary industrial process used to produce our research materials but could also be linearly scaled to mass production. However, a direct comparison of the amount of silver needed for both systems based only on weight percent, 40 grams for SAC305 and 93 grams for core-shell, suggests that the assumptions made will have little impact on the presented results. Of key importance here is that fact that this assumption is based on an equal volume of dispensed paste. However, if we consider the details of the final interconnect geometry we may be able to reduce the amount of core-shell particles needed to produce the same number of interconnects thereby reducing the impacts associated with each functional unit. The core-shell system creates interconnects through sintering via surface diffusion of the thin silver film and therefore little to no densification takes place during annealing. For an equivalent interconnect geometry and assuming a particle loading of 50 volume percent, the total volume of Cu-Ag core-shell powder needed is ½ that for an equivalent SAC 305 solder joint. A schematic representation of this interconnect geometry assessment is depicted in Figure 94.

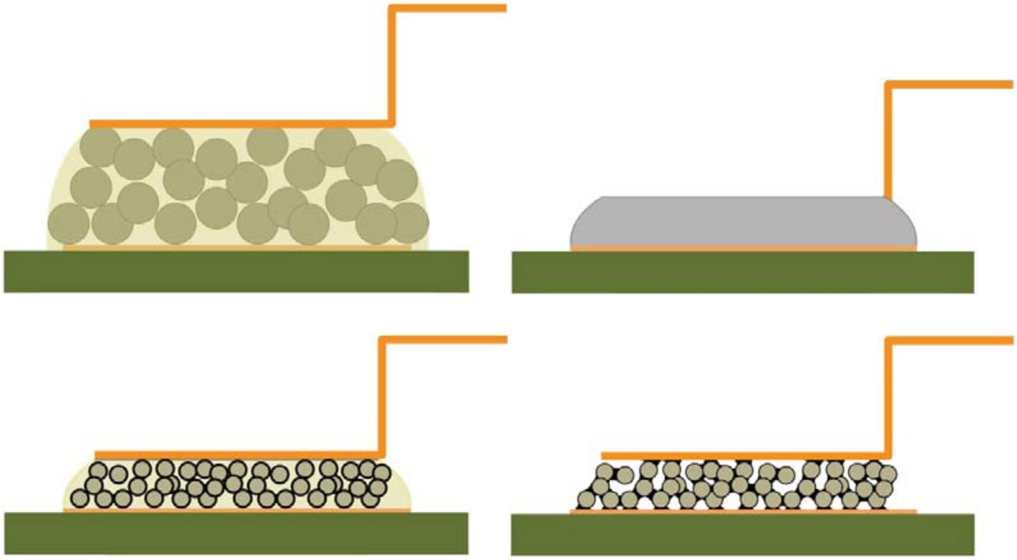

Figure 94. A schematic representation of the interconnect geometry showing that for an equivalent interconnect geometry and assuming a particle loading of 50 volume percent, the total volume of Cu-Ag core-shell powder needed is ½ that for an equivalent SAC 305 solder joint. TOP: SAC 305; BOTTOM: Core-Shell; LEFT: Before heating; RIGHT: After heating

As mentioned above, the majority of the impacts associated with the core-shell system come from the quantity of silver needed processing. If the same interconnect geometry is achievable with half the volume of powder, we can halve the impacts associated with the core-shell technology without changing the compared functional unit, thus making the core-shell technology impacts less than SAC 305 in all categories except for carcinogenic effects due to the copper core. This negative impact is associated with the use of copper (I) oxide, which was used in conjunction with hydrochloric acid to form copper (I) chloride. It is not clear if the use of an alternative method for producing copper (I) chloride would reduce these impacts. However, because copper (I) chloride is most commonly produced using the copper (I) oxide and hydrochloric acid, it is likely a good representation of the true impacts.

The Cu-Ag core-shell technology is versatile in its design and can remain functional with a variety of particle sizes and shell thicknesses, thus providing other possible routes for reducing the impacts associated with the silver content. [72] It should be noted that system performance has not been directly evaluated for less than 5wt% Ag, i.e. 10 nm thick shell for a 1 micrometer spherical Cu core. However, there is a limiting case for the extent of neck formation based on physical, geometrical constraints that can be used as proof of concept. As described in Chapter 2 we can calculate if there is enough Ag in the particle shells to form necks with the expected geometries. The maximum possible neck radius formed from Ag can be estimated assuming that all of the silver shell diffuses to form sintered necks, the solid core particles touch at a single point and a cylindrical neck structure minus the excluded volume of the core particles. By equating the volume of a cylindrical neck to the volume of two equivalent hemispherical caps and the total volume of silver from the shells, the maximum possible neck radius for a simple two-particle geometry for a 2 wt% shell (approximately 3.5nm thick) was estimated to be 240 nm. This radius is more than a factor of two larger than the radius predicted from surface diffusion calculations for 60 minutes of annealing at 200°C. Therefore, silver supply will not limit the extent of neck formation for the proposed equivalent silver weight percent. Similarly, if a smaller core particle size is used, the required sintering temperature and/or time can be reduced, however, the total amount of silver will depend upon the core size/surface areas and the required shell thickness,

The impacts associated with the core-shell system using the same amount of silver needed for the SAC305 production (resulting in a 2wt% shell) is detailed in Figures 95 and 96. This assessment allows for a direct comparison of the impacts associated with the non-silver components of each system. Because the impacts of the silver were so great it was difficult to compare the effects of the chemical production process used in core-shell manufacturing versus simple metal alloying for SAC305.

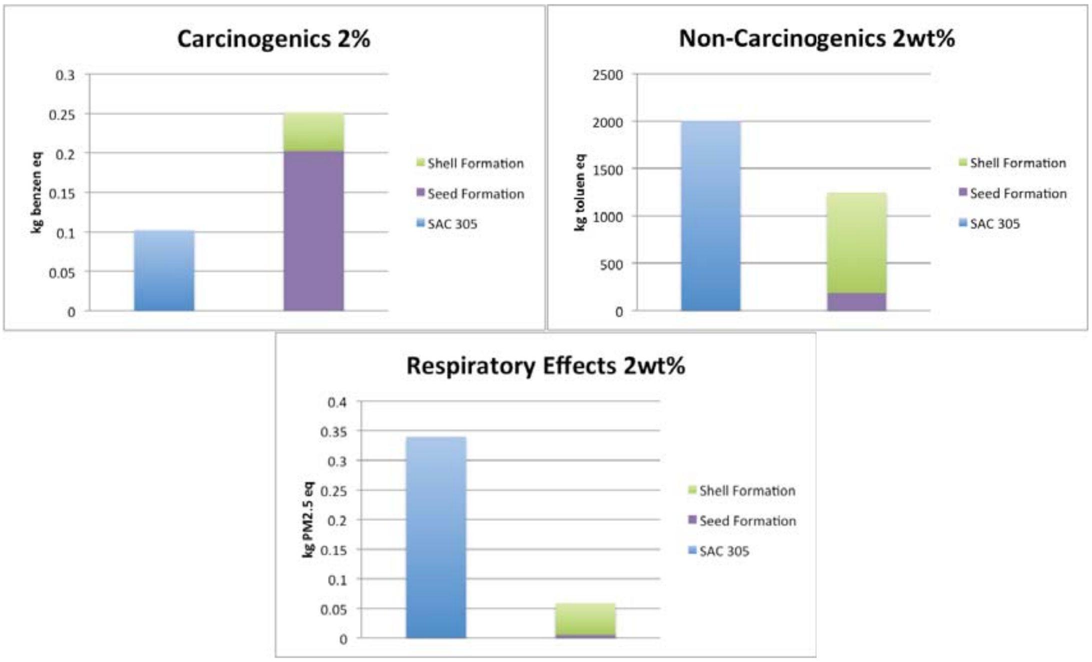

Figure 95. Plots of the human health TRACI impacts associated with the materials needed for manufacturing of SAC305 and Cu-Ag core-shell particles assuming equal amounts of silver for both systems.

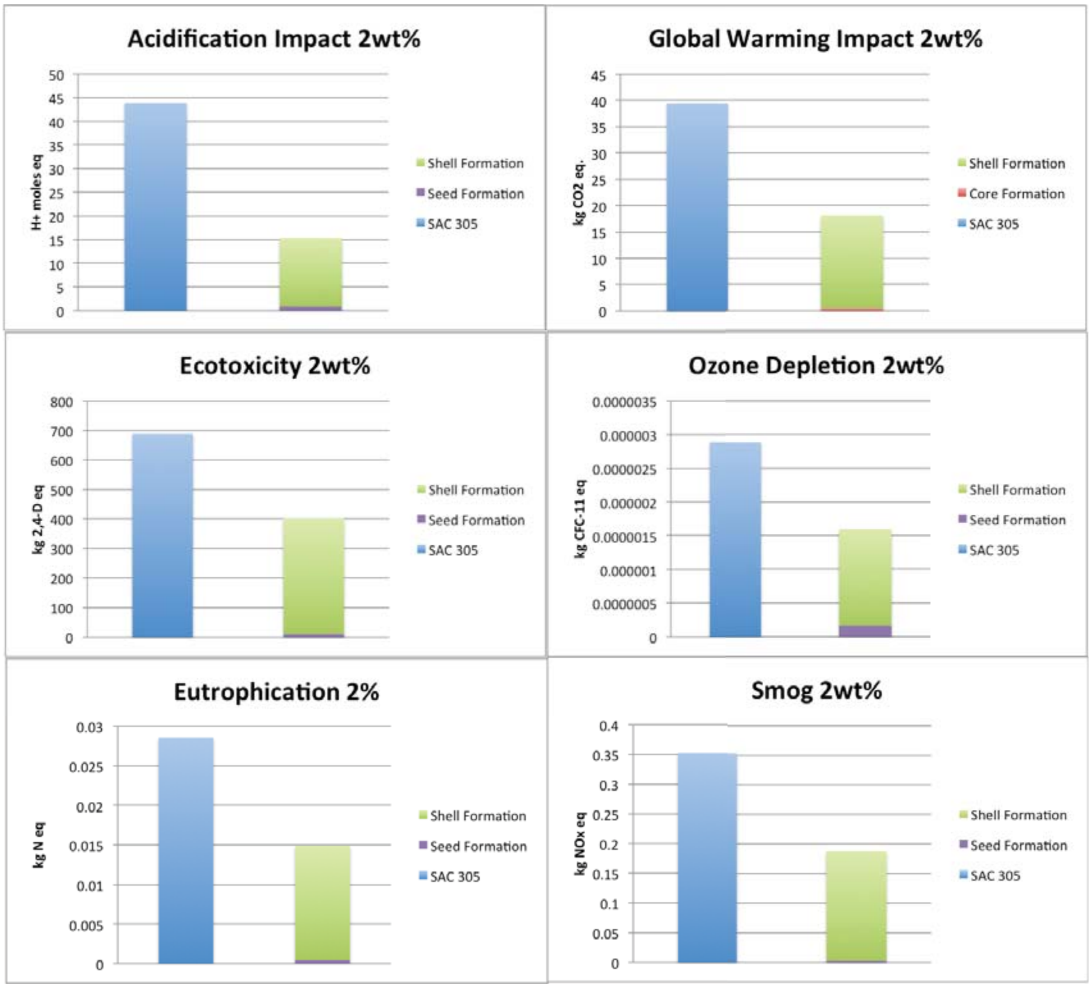

Figure 96. Plots of the environmental TRACI impacts associated with the materials needed for manufacturing of SAC305 and Cu-Ag core-shell particles assuming equal amounts of silver for both systems.

Analyses of the impacts associated with the reduced silver core-shell system clearly show that impact of core-shell chemical processing is not greater than the impact of the metals needed for SAC305 alloying. This is important because it this shows that with a simple geometry change in the core-shell system we may be capable of reaching or going beyond the break even point in terms of impact for eight of the nine categories. A table detailing the impacts associated with equal silver content system is detailed in the Appendix .

As previously mentioned, the energy consumption associated with the processing methods for producing both SAC305 and the Cu-Ag core-shell interconnect technology was not included in the assessment. However, we did attempt to extend the scope to include energy consumption associated with metallic atomization and solution processing methods. The results of the initial assessment will be presented however, it is important to note that in order to properly address this component of manufacturing, the functional unit needs to be adjusted. As it stands, the functional unit was chosen based on the output of a typical reflow oven. The value of 180 boards requires so little metal powder relative to the output of the metal processing methods that there are likely large errors associated with scaling.

4.3 Conclusion

In conclusion, we have shown that the environmental impacts associated with the material inputs for manufacturing of copper-silver core-shell particles containing 5wt% silver are slightly greater in seven of the nine TRACI impact categories than SAC305. The increased impact is directly related to the amount of silver needed to produce 360mL of solder paste containing 5wt% silver shells on 1μm particles versus 3wt% silver in 30μm alloyed solder particles. We have also shown that with a reduction in silver content, the core-shell system is capable of being equivalent to or out-performing SAC305 in eight of the nine TRACI impact categories.

REFERENCES

REFERENCES

[1] C. Idnani, Impact of New Materials and Processes on Manufacturing: Green (Pb and halide free), RoHS experience. Electronics Manufacturing Technology Symposium, p332, 2007

[2] F. P. McCluskey, M. Dash, Z. Wang, & D. Huff , Reliability of High Temperature Solder Alternatives. Microelectronics Reliability, 46, p1910, 2006

[3] K. N. Tu, A. M. Gusak, and M. Li, Physics and materials challenges for lead-free solders. Journal of Applied Physics **93** (3) p1335 (2003).

[4] P. Borgesen, T. Bieler, L. P. Lehman, and E. J. Cotts, Pb-Free Solder: New Materials Consideration for Microelectronics Processing. Mrs Bulletin **32,** (4) p360 (2007).

[5] K. W. Moon, W. J. Boettinger, U. R. Kattner, F. S. Biancaniello, and C. A. Handwerker, Experimental and thermodynamic assessment of Sn-Ag-Cu solder alloys. JOURNAL OF ELECTRONIC MATERIALS **29** (10) p1122 (2000).

[6] W. Yang, R. W. Messler, and L. E. Felton, Microstructure evolution of eutectic Sn-Ag solder joints. Journal of Electronic Materials **23** (8) p765 (1994).

[7] W. J. Boettinger, C. E. Johnson, L. A. Bendersky, K. W. Moon, M. E. Williams, and G. R. Stafford, Whisker and Hillock formation on Sn, Sn-Cu and Sn-Pb electrodeposits. Acta Materialia **53,** 5033 (2005).

[8] S. Choi, K. N. Subramanian, J. P. Lucas, and T. R. Bieler, Thermomechanical fatigue behavior of Sn-Ag solder joints. Journal of Electronic Materials, 29, 10, p1249 (2000)

[9] What is RoHS. https://www.bis.gov.uk/nmo/enforcement/rohs-home, 2012

[10] K.J. Puttlitz, G.T. Galyon. Imact of the RoHS Directive on high-performance electronics systems – Part II: key reliability issues preventing the implementation of lead-free solders. Journal of Materials Science-Materials in Electronics, 18, p347 (2007)

[11] S. J. Kim, E. A. Stach, and C. A. Handwerker, Fabrication of conductive interconnects by Ag migration in Cu–Ag core-shell nanoparticles. Applied Physics Letters **96,** 144101 (2010).

[12] C. Lea. A Scientific Guide to Surface Mount Technology, Electrochemical Publications Limited, Ayr, Scotland 1988

[13] Lee, Ning-Cheng. *Reflow Soldering Processes: SMT, BGA, CSP and Flip Chip Technologies*. Boston: Newnes, 2002. Print.

[14] Whitaker, Jerry C. *The Electronics Handbook*. Boca Raton, FL: CRC, 1996. Print

[15] K.J. Puttlitz and K.A. Stalter, Handbook of Lead-Free Solder Technology for Microelectronic Assemblies, New York, NY, Marcel Dekker, Inc., 2004

[16] "PROPERTIES OF SOLDERS." Multicore Solders, Aug. 2000. Web. <http://www.farnell.com/datasheets/315929.pdf>.

[17] D. Shangguan, “Leading the Lead-free transition”, Circuists Assem., March 2004

[18] D. Shangguan, “Understanding compatability and clarifying the issues in Lead-free transition”, Electronics Manufcaturing China, April, 2004, pp. 20-24

[19] D. Shangguan, A. Achari, “Evaluation of Lead-free eutectic Sn-Ag solder for automotive electronics packaging applications”, Proceedings of the International Electronics Manufacturing Technology Symposium, September, 1994, pp. 25-37

[20] D. Shangguan, A. Achari, “Lead-free solder developments for automotive electronics packaging application”, Proceedings of the Surface Mount International Conference, September, 1994, pp. 25-37

[21] P. Vianco, General soldering. Welding, Brazing, and Soldering: ASM Handbook: D. Olsen, T. Stewart, S. Liu, G. Edwards, Eds. ASM International: Materials Park, OH, 1993 Vol 6 964-984

[22] T.T. Nguyen, D. Yu, and S.B. Park, Characterizing the Mechanical Properties of Actual SAC105, SAC305, and SAC405 Solder Joints by Digital Image Correlation. Journal of Electronic Materials, 40 (6), p1409, 2011

[23] X. Cao, T. Wang, K. D. T. Ngo, and G. Lu. Characterization of Lead-Free Solder and Sintered Nano-Silver Die-Attach Layers Using Thermal Impedance. IEEE Transaction on Components, Packaging and Manufacturing Technology, 1, 4, 495 (2011)

[24] K.-S. Moon, H. Dong, R. Maric, S. Pothukuchi, A. Hunt, Y. Li., et al. Thermal Behavior of Silver Nanoparticles for Low-Temperature Interconnect Applications. Journal of Electronic Materials, 34 (2), 168, 2005

[25] J. G. Bai, J. Yin, Z. Zhang, G.-Q. Lu, and J. D. van Wyk, High-Temperature Operation of SiC Power Devices by Low-Temperature Sintered Silver Die-Attachment. IEEE Transactions on Advanced Packaging, 30 (3), 506, 2007

[26] F. G. Yost et al., *The Mechanics of Solder Alloy Wetting and Spreading,* Van Nostrand Reinhold, New York, 1993, ISBN 0442017529.

[27] G. Leonida, *Handbook of Printed Circuit Design, Manufacture, Components & Assembly,* Electrochemical Publications Limited, Scotland, 1981, ISBN 0901150096.

[28] F.A.L. Dullien, "Porous Media. Fluid Transport and Pore Structure", 2nd edition, Academic Press Inc., 1992Dannenberg.

[29] G. C. Kuczynski, Transactions of the American Institute of Mining and Metallurgical Engineers **185,** 169 (1949).

[30] J.M Howe, *Interfaces in Materials*, New York, John Wiley & Sons, Inc. 1997

[31] H. Hamaski, K. Shinbata, and F. Yoshida, Viscoplastic Parameter Identification for Lead-Free Solder Alloy by Micro-Indentation, FE Simulation and Optimization, Materials Transaction of the Japan Society for Technology of Plasticity, 49 (3), p. 532, 2008

[32] L.J. Gibson, Mechanical Behavior of Metallic Foams, Annu. Rev. Mater. Sci., 30, p.191-227.

[33] Freund, L. B., and S. Suresh. *Thin Film Materials: Stress, Defect Formation, and Surface Evolution*. Cambridge: Cambridge UP, 2003. Print.

[34] Tu, K.-N. *Electronic Thin-Film Reliability*. 396 (Cambridge Univ Pr: 2010)

[35] Cammarata, R. C. & Trimble, T. M. Surface stress model for intrinsic stresses in thin films. *J. Mater. Res.* **15**, 2468–2474 (2000).

[36] Hirth, J. P. *Theory of dislocations*. 857 (John Wiley & Sons: 1982).

[37] Committee, A. I. H. *ASM Handbook: Properties and selection*. (1990).

[38] Israelachvili, J. N. *Intermolecular And Surface Forces*. 600 (Academic Pr: 2010).

[39] Gibbs, J. *On the equilibrium of heterogeneous substances*. (1874).

[40] Srolovitz, D. The thermodynamics and kinetics of film agglomeration. *JOM Journal of the Minerals* (1995).

[41] Mullins, W. W. Theory of Thermal Grooving. *J. Appl. Phys.* **28**, 333 (1957).

[42] Vrij, A. Possible mechanism for the spontaneous rupture of thin, free liquid films. *Discuss Faraday Soc* (1966).

[43] Genin, F. Y., Mullins, W. W. & Wynblatt, P. The Effect of Stress on Grain Boundary Grooving. *Acta Metall. Mater.* **41**, 3541–3547 (1993).

[44] Jiran, E. & Thompson, C. V. Capillary instabilities in thin, continuous films. *Thin Solid Films* **208**, 23–28 (1991).

[45] Shaffir, E., Riess, I. & Kaplan, W. D. The mechanism of initial de-wetting and detachment of thin Au films on YSZ. *Acta Materialia* **57**, 248–256 (2009).

[46] Srolovitz, D. J. & Safran, S. A. Capillary instabilities in thin films. II. Kinetics. *J. Appl. Phys.* **60**, 255 (1986).

[47] Brandon, R. & Bradshaw, F. J. The Mobility of the Surface Atoms of Copper and Silver Evaporated Deposits. *Royal Aircraft Extablishment* 1–162 (1966).

[48] Jiran, E. & Thompson, C. V. Capillary instabilities in thin films. *Journal of Elec Materi* **19**, 1153–1160 (1990).

[49] Srolovitz, D. J. & Safran, S. A. Capillary Instabilities in thin films 1. Energetics. *J. Appl. Phys.* 247–254 (1986).

[50] Ghaleb. Anisotropy of surface diffusion of silver on the (331) and (110) clean copper surface at low temperature. *Surface Sciene* **162**, 103–108 (1985).

[51] Sarobol, P., J.e. Blendell, and C.a. Handwerker. "Whisker and Hillock Growth via Coupled Localized Coble Creep, Grain Boundary Sliding, and Shear Induced Grain Boundary Migration." *Acta Materialia* 61.6 (2013): 1991-2003.

[52] Kovalenko, O.; Greer, J.R.; Rabkin, E., “Solid-dewetting of thin iron films on sapphire substrates controlled by grain boundary diffusion,” *Acta Materialia*, vol.61, pp. 3148-3156, 2013.

[53] Galinski, H., T. Ryll, P. Stender, G. Schmitz, and L.J. Gaukler. "Hillock Formation of Pt Thin Films on Yttria Stabilized Zirconia Single Crystals." *Phys. Rev. B* 85 (2012): 125408.

[54] Müller, C. M. & Spolenak, R. Microstructure evolution during dewetting in thin Au films. *Acta Materialia* **58**, 6035–6045 (2010).

[55] Sauter, Linda, T. John Balk, Gerhard Dehm, Julie A. Nucci, and Eduard Arzt. "Hillock Formation and Thermal Stresses in Thin Au Films on Si Substrates." *MRS Proceedings* 875 (2005)

[56] Syarbaini, Luthfia. *Microstructural Evolution during Stress Relaxation of Gold Thin Films.* Diss. Purdue U, 2013.

[57] Sharma, S. K. & Spitz, J. Hillock Formation, Hole Growth, and Agglomeration in Thin Silver Films. *Thin Solid Films* **65**, 339–350 (1979).

[58] Krishna, H. *et al.* Thickness-dependent spontaneous dewetting morphology of ultrathin Ag films. *Nanotechnology* **21**, 155601 (2010).

[59] Simrick, N.j., J.a. Kilner, and A. Atkinson. "Thermal Stability of Silver Thin Films on Zirconia Substrates." *Thin Solid Films* 520.7 (2012): 2855-867.

[60] Thürmer, K., Williams, E. & Reutt-Robey, J. Dewetting dynamics of ultrathin silver films on Si(111). *Phys. Rev. B* **68**, (2003).

[61] Baletto, F., Mottet, C. & Ferrando, R. Growth simulations of silver shells on copper and palladium nanoclusters. *Phys. Rev. B* **66**, (2002).

[62] Dannenberg, R., E.A. Stach, J.R. Groza, and B.J. Dresser, *In-situ TEM observations of abnormal grain growth, coarsening, and substrate dewetting in nanocrystalline Ag thin films.* Thin Solid Films, 2000. **370**(1-2): p. 54-62

[63] J.M Howe, *Interfaces in Materials*, New York, John Wiley & Sons, Inc. 1997

[64] Socolof, M.L., Geibig, J.R., Life-Cycle Impacts of Lead and Lead-Free Solder Used in Wave Soldering of Electronics. IEEE 2005. ISEE. 96-101.

[65] Horne, Ralph, Tim Grant, and Karli Verghese. *Life Cycle Assessment: Principles, Practice and Prospects*. Collingwood: CSIRO, 2009.

[66] *Solders in Electronics: A Life-cycle Assessment Summary*. Washington, D.C.: Environmental Protection Agency, 2005.

[67] Halaciuga, S. LaPlante and D.V. Goia. Method for preparing dispersed crystalline copper particles for electronic applications. Journal of Materials Research, 24, 2009, pp 3237-3240.

[68] D. Andreescu, C. Goia, D.V. Goia, K.A. Blakely, R.B. Donn, and E. Groat. Novel Copper Powders and Flakes for Electronic Applications. 18th Annual Passive Components Conference Preceedings. 2004, p. 15

[69] D. Stojan, M. Dubois, and R. H. Lepard. Process for the Production of Silver Coated Particles. N.V. Union Miniere S.A., Brussels, Belgium, assignee. Patent 5,945,158. 31 Aug. 1999.

[70] X. Xu, X. Luo, H. Zhuang, W. Li, and B. Zhang, Electroless silver coating on fine copper powder and its effects on oxidation resistance. Materials Letters, 57, (24–25), 2003, Pages 3987–3991

[71] X. Shengqi, Z. Kexiong, and W. Hongjing. Enhanced Oxidation Resistance of Cu/Ag Composite Powder with a Compact Silver Shell Structure.

[72] Kim, Suk Jun. *An Influence of Crystal Structure and Interface Formation on the Electrical Properties of Nanoparticle Printed Thin Films.* Diss. Purdue U, 2010.

[73] P. Kaźnica. The Effect of Energy Use from an Optimized Reflow Oven Recipe in Lead-Free Applications. Flextronics and KIC. < http://kicthermal.com/download/Flextronics-Case-Study.pdf >

[74] "POTASSIUM ACID TARTRATE." *National Library of Medicine HSDB Database*. <http://toxnet.nlm.nih.gov/cgi-bin/sis/search/a?dbs+hsdb:@term+@DOCNO+1264>.

[75] "TRISODIUM CITRATE." *National Library of Medicine HSDB Database*. <http://toxnet.nlm.nih.gov/cgi-bin/sis/search2/f?./temp/~lh7LLu:4>.

APPENDIX

APPENDIX

Impact Category	Copper	Silver	Tin	SAC 305 TOTAL
Global Warming (kg CO2 eq.)	0.0361	17.5130	21.8551	39.4041
Acidification (H+ moles eq.)	0.1465	14.4026	29.2927	43.8418
Carcinogenics (kg benzene eq.)	0.0019	0.0486	0.0515	0.1019
Non-Carcinogenics (kg toluene eq.)	5.3082	1,060.6642	935.6429	2,001.6153
Respiratory Effects (kg PM2.5 eq.)	0.0009	0.0535	0.2849	0.3394
Eutophication (kg N eq.)	0.0001	0.0145	0.0140	0.0285
Ozone Depletion (kg CFC-11 eq.)	0.0000	0.0000	0.0000	0.0000
Ecotoxicity (kg 2,4-D eq.)	1.6904	390.6382	296.3305	688.6590
Smog (kg NOx eq.)	0.0006	0.1846	0.1674	0.3526

Impact Category	SAC 305 TOTAL	SAC with Cu-Ag Equal Silver content
Global Warming (kg CO2 eq.)	39.4041	17.5130
Acidification (H+ moles eq.)	43.8418	14.4026
Carcinogenics (kg benzene eq.)	0.1019	0.0486
Non-Carcinogenics (kg toluene eq.)	2,001.6153	1060.6642
Respiratory Effects (kg PM2.5 eq.)	0.3394	0.0535
Eutophication (kg N eq.)	0.0285	0.0145
Ozone Depletion (kg CFC-11 eq.)	0.0000	0.0000
Ecotoxicity (kg 2,4-D eq.)	688.6590	390.6382
Smog (kg NOx eq.)	0.3526	0.1846

Impact Category	Hydrochloric Acid	Copper Oxide	Iron Sulphate	Seed Formation Total
Global Warming (kg CO2 eq.)	0.1126	0.3369	0.1229	0.5724
Acidification (H+ moles eq.)	0.0275	0.8729	0.0317	0.9320
Carcinogenics (kg benzene eq.)	0.0004	0.2012	0.0010	0.2026
Non-Carcinogenics (kg toluene eq.)	1.7942	181.9341	2.6880	186.4164
Respiratory Effects (kg PM2.5 eq.)	0.0002	0.0051	0.0002	0.0055
Eutophication (kg N eq.)	0.0000	0.0003	0.0001	0.0004
Ozone Depletion (kg CFC-11 eq.)	0.0000	0.0000	0.0000	0.0000
Ecotoxicity (kg 2,4-D eq.)	0.2839	9.8398	0.3615	10.4852
Smog (kg NOx eq.)	0.0002	0.0030	0.0002	0.0035

Impact Category	Ammonium sulphate	Ammonia	Nitric acid	Silver	Film Deposition Total
Global Warming (kg CO2 eq.)	3.5751	0.6979	0.2305	40.7019	45.2053
Acidification (H+ moles eq.)	0.5945	0.1080	0.0392	33.4731	34.2147
Carcinogenics (kg benzene eq.)	0.0108	0.0011	0.0002	0.1129	0.1249
Non-Carcinogenics (kg toluene eq.)	26.7803	4.7233	0.5078	2465.0887	2497.1001
Respiratory Effects (kg PM2.5 eq.)	0.0038	0.0006	0.0001	0.1244	0.1289
Eutophication (kg N eq.)	0.0009	0.0003	0.0001	0.0336	0.0349
Ozone Depletion (kg CFC-11 eq.)	0.0000	0.0000	0.0000	0.0000	0.0000
Ecotoxicity (kg 2,4-D eq.)	3.0448	0.2446	0.0367	907.8819	911.2079
Smog (kg NOx eq.)	0.0054	0.0009	0.0004	0.4290	0.4357

Impact Category	Core-Shell Total	Core-Shell with SAC Equivalent Ag	SAC 305 TOTAL	SAC with Cu-Ag Equal Silver content
Global Warming (kg CO2 eq.)	45.7777	45.7777	39.4041	17.5130
Acidification (H+ moles eq.)	35.1468	35.1468	43.8418	14.4026
Carcinogenics (kg benzene eq.)	0.3276	0.3276	0.1019	0.0486
Non-Carcinogenics (kg toluene eq.)	2683.5165	2683.5165	2,001.6153	1060.6642
Respiratory Effects (kg PM2.5 eq.)	0.1345	0.1345	0.3394	0.0535
Eutophication (kg N eq.)	0.0353	0.0353	0.0285	0.0145
Ozone Depletion (kg CFC-11 eq.)	0.0000	0.0000	0.0000	0.0000
Ecotoxicity (kg 2,4-D eq.)	921.6931	921.6931	688.6590	390.6382
Smog (kg NOx eq.)	0.4392	0.4392	0.3526	0.1846

VITA

VITA

Milea J. Kammer was born on May 1st, 1986 in Indianapolis, Indiana. After graduating from Carmel High School in 2004 Milea went on to attended Purdue University in West Lafayette, IN, where she was President of Delta Zeta Sorority and an active member of the Purdue Materials Advantage chapter. Milea graduated with her Bachelors degree in Materials Engineering in May of 2008. In January of 2008, while completing her final semester of her bachelor degree requirements, she enrolled as a graduate student and began pursuing her graduate degree. Milea worked under the guidance of Carol A. Handwerker on the development and characterization of a novel lead-free solderless interconnect technology. Milea has since accepted a Senior Product Design Engineer position at Honeywell Aerospace in Clearwater, Florida.